Optical and Fiber Communications Reports 8

Zhongmin Yang
Can Li
Shanhui Xu
Changsheng Yang

Single-Frequency Fiber Lasers

Springer

Optical and Fiber Communications Reports

Volume 8

Series editors

Arun K. Majumdar, China Lake, USA
Anders Bjarklev, Lyngby, Denmark
Shibin Jiang, Tucson, USA
Gerd Marowsky, Göttingen, Germany
Carlo Someda, Pontecchio Marconi, Italy
Masataka Nakazawa, Sendai-shi, Japan

The Optical and Fiber Communications Reports (OFCR) book series provides high-quality monographs, edit volumes and textbooks in the multidisciplinary areas of optics, information science and electrical engineering. Each book is contributed from leading research scientists that gives an up-to-date and broad-spectrum overview of various subjects.
The main topics of this series will include, but not restricted to:

fibers and fiber-based devices
information optics, optical and quantum communication
optoelectronic imaging and multimedia technology
optical metrology and testing
virtual reality and display technologies
broadband lasers
optical switching (MEMS or others)
polarization and chromatic mode dispersion and compensation
long-haul transmission
optical networks (LAN, MAN, WAN)
further topics of contemporary interest.

Including both general information and a highly technical presentation of the results, this series satisfies the needs of scientists and graduates in the academic community as well as professionals and experts from industry. Books in this series establish themselves as comprehensive guides and reference texts following the impressive evolution of this area of science and technology.

More information about this series at http://www.springer.com/series/4810

Zhongmin Yang • Can Li • Shanhui Xu
Changsheng Yang

Single-Frequency Fiber Lasers

Springer

Zhongmin Yang
State Key Laboratory of Luminescent Materials and Devices and Institute of Optical Communication Materials
South China University of Technology
Guangzhou, China

Shanhui Xu
State Key Laboratory of Luminescent Materials and Devices and Institute of Optical Communication Materials
South China University of Technology
Guangzhou, China

Can Li
Department of Electrical and Electronic Engineering
The University of Hong Kong
Hongkong, China

Changsheng Yang
State Key Laboratory of Luminescent Materials and Devices and Institute of Optical Communication Materials
South China University of Technology
Guangzhou, China

ISSN 1619-1447 ISSN 1619-1455 (electronic)
Optical and Fiber Communications Reports
ISBN 978-981-13-6079-4 ISBN 978-981-13-6080-0 (eBook)
https://doi.org/10.1007/978-981-13-6080-0

Library of Congress Control Number: 2019930047

© Springer Nature Singapore Pte Ltd. 2019
This work is subject to copyright. All rights are reserved by the Publisher, whether the whole or part of the material is concerned, specifically the rights of translation, reprinting, reuse of illustrations, recitation, broadcasting, reproduction on microfilms or in any other physical way, and transmission or information storage and retrieval, electronic adaptation, computer software, or by similar or dissimilar methodology now known or hereafter developed.
The use of general descriptive names, registered names, trademarks, service marks, etc. in this publication does not imply, even in the absence of a specific statement, that such names are exempt from the relevant protective laws and regulations and therefore free for general use.
The publisher, the authors, and the editors are safe to assume that the advice and information in this book are believed to be true and accurate at the date of publication. Neither the publisher nor the authors or the editors give a warranty, express or implied, with respect to the material contained herein or for any errors or omissions that may have been made. The publisher remains neutral with regard to jurisdictional claims in published maps and institutional affiliations.

This Springer imprint is published by the registered company Springer Nature Singapore Pte Ltd.
The registered company address is: 152 Beach Road, #21-01/04 Gateway East, Singapore 189721, Singapore

Contents

1 Introduction 1
1.1 Brief History of Fiber Lasers 1
1.2 Main Components of Fiber Lasers 2
1.3 Current Development Status of Fiber Lasers 5
1.4 The Importance of Single-Frequency Fiber Lasers 6
References 8

2 Fundamental Principle and Enabling Technologies of Single-Frequency Fiber Lasers 11
2.1 Principle of Single-Frequency Lasing 11
2.2 Properties of Single-Frequency Lasers 13
2.2.1 Single Longitudinal Mode Operation 13
2.2.2 Intensity Noise 14
2.2.3 Frequency Noise 17
2.2.4 Linewidth 21
2.3 Cavity Design of Single-Frequency Fiber Lasers 26
2.3.1 Typical Cavity Structures 26
2.3.2 Other Schemes to Achieve Single-Frequency Lasing . . . 28
2.4 Single-Frequency Fiber Laser Design with Advanced Performances 30
2.4.1 Linearly Polarized Operation 30
2.4.2 Linewidth Suppression 31
2.4.3 Frequency and Intensity Noise Suppression 33
2.4.4 Continuous Wavelength Tuning 42
2.4.5 Fast Frequency Modulation 44
References 48

3 Single-Frequency Active Fiber Lasers 55
3.1 Introduction of Rare-Earth Ions Doped Multicomponent Glass Fiber 55
3.2 High-Power Operation from Fiber Oscillator 57

3.3 Thermal Effects in High-Gain Single-Frequency Fiber Lasers . . . 64
3.4 Noise Properties of High-Gain Single-Frequency Fiber Lasers . . . 71
3.4.1 Self-Heating Noise . . . 71
3.4.2 Coupling Between Frequency and Intensity Noise . . . 74
3.4.3 Amplified Spontaneous Emission Noise . . . 77
References . . . 79

4 Fiber Nonlinear Single-Frequency Lasers . . . 85
4.1 Nonlinear Effects in Optical Fibers . . . 85
4.2 Raman and Brillouin Fiber Lasers . . . 86
4.3 Random Distributed Feedback Fiber Lasers . . . 90
4.4 Fiber Optical Parametric Oscillator . . . 92
References . . . 93

5 Single-Frequency Pulsed Fiber Lasers . . . 97
5.1 Principle of Q-Switching . . . 97
5.2 Q-Switched Single-Frequency Fiber Lasers . . . 99
5.3 Other Single-Frequency Pulsed Fiber Lasers . . . 102
References . . . 102

6 Amplification Technologies of Single-Frequency Lasers . . . 105
6.1 The Significance of Amplifying Single-Frequency Lasers . . . 105
6.2 Basic Principles of MOPA Fiber Laser . . . 106
6.3 Structure of MOPA Fiber Laser . . . 107
6.3.1 Double-Clad Fiber Technology . . . 107
6.3.2 Cladding Pump Coupling Technology . . . 108
6.4 Limitation Factors of High-Power Single-Frequency MOPA Laser . . . 109
6.4.1 Nonlinear Effects . . . 110
6.4.2 Thermal Lens Effect . . . 111
6.4.3 Fiber End-Face Damage . . . 111
6.4.4 Pump Coupling Method . . . 112
References . . . 112

7 Amplification of CW Single-Frequency Lasers . . . 115
7.1 Amplification of CW Single-Frequency Lasers at the 1.0 μm Region . . . 115
7.1.1 Spectral Features of Yb^{3+} Emission . . . 116
7.1.2 Theoretical Model of Yb^{3+}-Doped Fiber Amplifier . . . 117
7.1.3 Experimental Study of Single-Frequency MOPA Laser Below 1030 nm . . . 118
7.1.4 Experimental Study of Single-Frequency MOPA Laser at 1064 Nm . . . 122
7.1.5 Experimental Study of CW Single-Frequency MOPA Laser at 1083 Nm . . . 126

7.2 Amplification of CW Single-Frequency Lasers at 1.5 μm Regions . . . 129
7.2.1 Characteristics of Er^{3+}/Yb^{3+}-Codoped Fiber . . . 129
7.2.2 Theoretical Model of Er^{3+}/Yb^{3+}-Codoped Fiber Amplifier . . . 130
7.2.3 Experimental Study of Core-Pumped 1.5 μm Single-Frequency MOPA Laser . . . 133
7.2.4 Experimental Study of Cladding-Pumped 1.5 μm Single-Frequency MOPA Laser . . . 135
7.3 Amplification of CW Single-Frequency Lasers at 2.0 μm Regions . . . 138
7.3.1 Theoretical Model of Tm^{3+}-Doped Fiber Amplifier . . . 139
7.3.2 Experimental Study of 2.0 μm Single-Frequency MOPA Laser . . . 140
References . . . 143

8 Amplification of Pulsed Single-Frequency Lasers . . . 149
8.1 Amplification of Pulsed Single-Frequency Lasers in 1.0 μm Regions . . . 150
8.2 Amplification of Pulsed Single-Frequency Lasers in 1.5 μm Regions . . . 153
8.3 Amplification of Pulsed Single-Frequency Lasers in 2.0 μm Regions . . . 158
References . . . 161

9 Representative Applications of Single-Frequency Fiber Lasers . . . 163
9.1 Next-Generation Optical Communication . . . 163
9.2 High Precision Optical Sensing . . . 164
9.3 Laser Coherent Beam Combining . . . 165
References . . . 165

10 Conclusion and Outlook . . . 169

Chapter 1
Introduction

Nowadays fiber lasers are the first choice for diverse scientific and industrial applications, thanks to their excellent beam quality, high efficiency, flexible and compact structure, and being engineerable to operate in various regimes through leveraging linear and nonlinear effects in optical fiber. One of the most important operating manners of fiber laser is the single longitudinal mode oscillation, which has been intensively studied over the past three decades, owing to the crucial demands of a laser source with high-stable single-frequency operation, narrow linewidth, low noise, scalable to high-output power, and compact and robustness structure. In this chapter, we first give a brief introduction of the development history of fiber lasers, as well as the main components that form a typical fiber laser. Then the current development status of fiber lasers is discussed, and in the last part, the importance of single-frequency fiber lasers is emphasized.

1.1 Brief History of Fiber Lasers

In 1960, Theodore Maiman demonstrated the world's first laser from a lamp-pumped ruby crystal at Hughes Research Laboratories [1]. Subsequently, laser emission from different host mediums like gas, liquid, semiconductor and other solid-state materials has been discovered [2]. Solid-state lasers are those "having ions introduced as an impurity in an otherwise transparent dielectric-host material (in crystalline or glass form)" [3]. Accordingly, Maiman's laser can also be recognized as the first solid-state laser, in which the dopant is chromium. Pioneer demonstration of lasing from glass was carried out in 1961 by Elias Snitzer, who used a flushtube to pump a millimeter-scale neodymium glass rod and realized laser emission at 1 μm [4]. In fact, this is essentially the first prototype of fiber laser, as the glass rod was intended to be designed to have a high index core and low index cladding to provide optical mode selection. After that, Snitzer and coworkers also demonstrated the first fiber amplifier on the basis of neodymium glass [5].

© Springer Nature Singapore Pte Ltd. 2019

Z. Yang et al., *Single-Frequency Fiber Lasers*, Optical and Fiber Communications Reports 8, https://doi.org/10.1007/978-981-13-6080-0_1

Although at the birth of laser, its importance and scientific significance have been fully realized, people did not find out the practical application for this special light and deemed it as "a solution looking for a problem." Under this circumstance, fiber lasers did not attract much research attention until two decades later, when the rapid development of telecommunication fueled the growth of fiber technology. Scientists found that fiber amplifiers on the base of erbium-doped single-mode fiber can be an ideal regenerator that has the combination of broad bandwidth and low cross talk for optical multiplexing transmission system at the communication window of 1.55 μm [6, 7]. In the 1990s, the rapid growth of Internet data traffic attracted vast investments to optical fiber technologies and as a result provided advantageous opportunity for the big development of fiber lasers. With the multiple demonstrations of laser performances such as wavelength diversity, different operation regimes, and power increase, researchers have identified a vast number of applications for fiber lasers outside of the communication field. Nowadays, while still being a research hotspot in the laser community, fiber lasers hold firmly the leading position in applications like telecommunications, material processing, spectroscopy, medicine, and directed energy weapons. Even so, there is still much work to do to fully bring to light the versatility of this special laser type.

1.2 Main Components of Fiber Lasers

Optical fiber has a special waveguide structure that consists of a core which is surrounded by a cladding whose refractive index is slightly lower than that of the core and guides light through total internal reflection. Generally, there is an extra protective polymer coating outside the cladding, and this buffer coating can improve the mechanical strength and moisture resistance of the fiber. Figure 1.1 demonstrates the visualized cross section and corresponding refractive index profile of a typical optical fiber. Under a given refractive index profile, the electromagnetic field solution of the transmitting light is discrete, and this yields different transverse modes, corresponding to different light intensity distribution in optical fiber. The

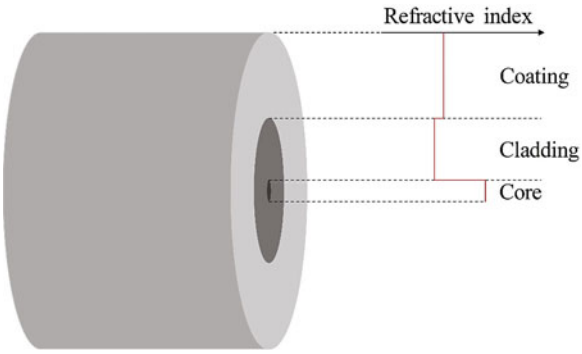

Fig. 1.1 Visualized cross section and corresponding refractive index profile of a typical optical fiber

simplest or lowest order mode structure is also referred to as fundamental/single mode, where the intensity profile is similar to that of a Gaussian beam [8]. The popular and extensively used single-mode silica (quartz glass) fiber can be manufactured with ultralow scattering, impurity losses and material imperfections, and transmission loss as low as 0.2 dB/km at the telecommunication band. This has helped the flourishing growth of fiber laser sources at the near-infrared (near-IR) and short-wave infrared (SWIR) band, via facilitating various functional fiber-coupled components. When going deeper into the mid-infrared (mid-IR) band, the intrinsic loss of silica glass significantly raised owing to its high maximum phonon energy. Fortunately, the creation of fluoride and chalcogenide fiber has offered alternatives for the mid-IR fiber lasers, although it is still in its infancy state as compared to its near-IR counterpart [9, 10]. After doping in the core with rare-earth (RE) ions, a fiber can then offer optical amplification when activated with a proper pump source and thus serve as the gain medium of fiber laser. Up to now, RE ions that have been doped into optical fibers consist of neodymium (Nd^{3+}) [11], erbium (Er^{3+}) [12], ytterbium (Yb^{3+}) [13], thulium (Tm^{3+}) [14], bismuth (Bi^{3+}) [15], holmium (Ho^{3+}) [16], dysprosium (Dy^{3+}) [17], and praseodymium (Pr^{3+}) [18] and their luminescence spectra have substantially ranged from ultraviolet to mid-IR band.

To construct a fiber laser, the RE ions doped fiber is utilized to implement a fiber cavity in which the emitted photons can undergo oscillation and obtain net gain in a single round trip while providing laser output at the same time. Typical cavity configuration includes linear fiber Fabry-Pérot resonator and fiber ring traveling wave resonator. Figure 1.2 shows the typical configuration of a linear fiber resonator, in which the reflective and the partial reflective mirror compose the Fabry-Pérot cavity. At present, fiber Bragg gratings (FBGs) are intensively adopted as the reflective mirror for fiber lasers, owing to its merits of all-fiber form and flexible wavelength selectivity [19]. For a given length of resonator, only the optical components at certain discrete frequencies that experience a phase shift of an integer multiple of 2π in one round trip can realize oscillation. These discrete frequencies are also referred to as longitudinal (axial) modes of the laser. Nevertheless, merely a small percentage of the longitudinal modes within the emission range of the gain fiber can survive, owing to the gain competition effect that decreases the oscillating modes and narrows down the laser bandwidth. It is also emphasized that via manipulating the oscillating modes, the fiber lasers could operate at different regimes

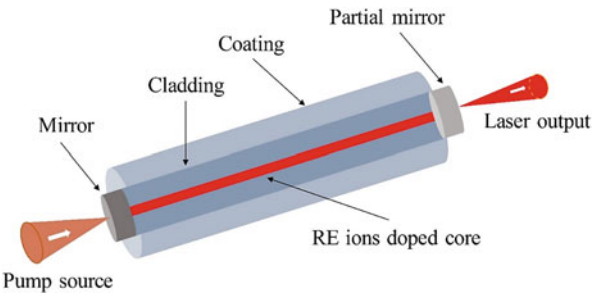

Fig. 1.2 Typical configuration of a linear fiber Fabry-Pérot resonator

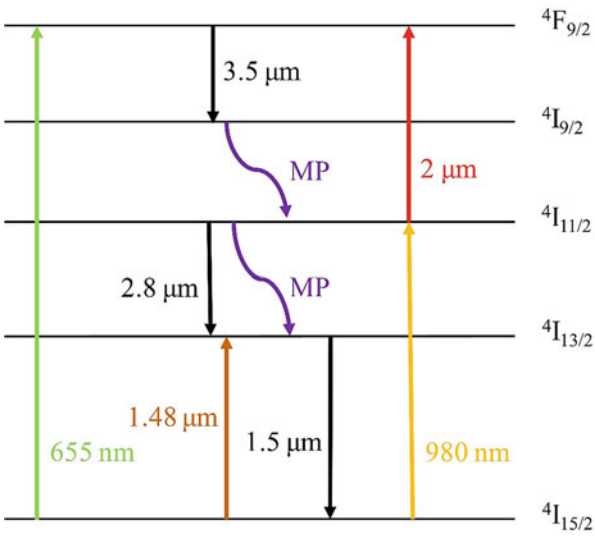

Fig. 1.3 Simplified energy level diagram of Er^{3+} ions, along with corresponding pump and laser transitions denoted by arrows, MP: multiphonon decay

with various spectral and temporal properties. For example, the phase relationship between the longitudinal modes can be fixed through some active or passive mechanisms – indicative of the so-called mode-locked laser which emits ultrashort pulses along with a relatively wide spectrum. Otherwise, when a narrowband filtering effect is added into the cavity, there is opportunity to obtain a single-frequency laser, which is also recognized as the single longitudinal mode laser.

Another indispensable component of a fiber laser is the pump source which excites the RE ions to provide optical gain. Generally, RE ions are comprised of atoms that are made up of nucleus orbited with electrons, which have quantized energy and occupy only certain allowed orbitals with a specific energy, corresponding to different energy levels. These electrons normally sit in the lowest energy level, in other words, the ground state. They will transfer to the excited state – high-energy level when external energy from a pump source is added on – and realize population inversion with respect to the ground state. Under appropriate conditions, photons passing through the excited atoms could stimulate emission of identical photons and thus achieve light amplification by the stimulated emission of radiation (LASER). Figure 1.3 demonstrates the simplified energy level diagram of Er^{3+} ions, along with the corresponding pump and laser transitions that have been exploited in fiber lasers. From the figure, the Er^{3+} ions can be directly excited from the energy level $^4I_{15/2}$ (ground state) to the energy levels $^4I_{13/2}$, $^4I_{11/2}$, and $^4F_{9/2}$ via pump source at 1480 nm, 980 nm, and 655 nm, respectively [20, 21]. Additionally, excited state Er^{3+} ions at the energy level of $^4I_{11/2}$ can regard as a "virtual ground state" and can be further excited to the energy level of $^4F_{9/2}$. With the population accumulation of the excited state, population inversion will take place, and laser emission at the wavelength band of 1.5 μm, 2.8 μm, and 3.5 μm can be achieved. Finally, for some energy levels like $^4I_{11/2}$ and $^4I_{9/2}$ that have a relatively low lifetime,

population inversion is not easy to realize, and the Er^{3+} ions will transfer to lower energy level via multiphonon decay and spontaneous emission.

1.3 Current Development Status of Fiber Lasers

Fiber lasers generally have an all-fiber configuration, where most or all of the laser components are fiber-coupled to one another, and this feature makes the laser system intrinsically compact, free of cumbersome alignment, and capable of outputting laser light with excellent beam quality. The large ratio of surface to volume of fiber facilitates excellent heat dissipation and enables the thermal load formed as a by-product of laser operation to be distributed over a long length. These thermo-optical properties, along with the long gain length that can be exploited in an active fiber, make fiber laser beneficial for high-power/high-energy operation. In 2009, IPG Photonics reported the record continuous-wave (CW) output power of 10 kW from a large mode area (LMA) single-mode ytterbium fiber amplifier [22]. After that, CW output as high as 100 kW in multimode fiber lasers was also achieved by the same company [23]. In the pulsed regime, tens of millijoule energy of single nanosecond pulse as well as millijoule energy and average power approaching 1 kW of femtosecond pulses were also achieved, at a similar rate with that of the CW counterparts [24, 25].

Another distinct feature of optical fiber is its small mode area into which the transmitting laser light is confined. This in turn results in a high intensity per unit area, which, together with the particularly long interaction length in fiber, leads to strong nonlinearity effects such as Kerr effect, Raman scattering, and Brillouin scattering. Usually, these nonlinearities are harmful, especially to high-power fiber lasers and amplifiers. Nevertheless, the fiber nonlinearities can be also very useful in other cases, as they generally involve nonlinear frequency conversion, which can enable laser emission at wavelength regions where RE ions doped fiber cannot cover. Although the frequency conversion via Brillouin scattering actually does not offer such a merit, owing to its trivial frequency shift in the order of 10–20 GHz, it offers an important means to realize highly coherent single-frequency laser sources. Nowadays, fiber nonlinear laser sources such as optical parametric oscillators/amplifiers, stimulated Raman laser, and stimulated Brillouin laser have been recognized as an indispensable part to the fiber laser community [26]. In addition, the nonlinear Kerr effect can be also exploited together with chromatic dispersion in optical fiber to realize mode locking in laser cavity, as well as ultrashort pulses through nonlinear compression. At present, laser pulses with few and even single oscillation periods of the electric field carrier wave have been achieved from optical fiber [27, 28]. As ultrashort pulses intrinsically have a significant high peak power, they would trigger a series of nonlinear effects such as self-phase modulation, four-wave mixing, modulation instability, and stimulated Raman scattering when transmitting in a specific fiber and resulting lasing with broadened spectral width that is many times wider than that of the initial pulse, i.e., supercontinuum generation.

Currently, the widest supercontinuum laser source with three octaves bandwidth spanning from 1.4 μm to 13.3 μm was demonstrated from a specially designed chalcogenide fiber [29].

Contrary to such a wide spectrum, laser sources with quasi-monochromatic spectrum have also been extensively investigated in optical fiber. Here comes to the single-frequency fiber laser (SFFL), which works in the single resonator mode regime and generally has a single transverse mode. To implement this type of laser, an important part is to employ a filterable component that has a bandwidth narrow enough to keep only one longitudinal mode to oscillate in the cavity. In large part, due to the creation of FBG, which can be massively produced with filtering bandwidth as narrow as several tens of pm via transverse holographic writing, SFFLs have been well-developed from near- to mid-IR band. Because of its nature of single longitudinal mode operation, SFFLs generally exhibit narrow linewidth, large coherence length, and low noise. Currently, lots of efforts are focusing on suppressing the linewidth and noise of SFFLs to realize purer and more stable laser sources for high precision applications. Specifically, sub-kHz linewidth and near-shot-noise-limited intensity noise have been achieved directly from the laser output [30, 31]. Other topics concerning SFFLs include high-power output on the basis of heavily RE ions doped multicomponent soft glass fiber and single-frequency lasing at unusual wavelengths by leveraging fiber nonlinear effects. Regarding pulsed operation, the main scheme is intracavity Q-switching or external modulation to render the laser work in the ns/μs regime, as SFFLs are inborn incapable of support ultrashort pulsing output. Finally, amplification of single-frequency laser in optical fiber has also attracted much research attention, and the average power of kW level is now predictable from a single-mode fiber, even though the narrow linewidth of single-frequency laser results in a significant low threshold for the harmful stimulated Brillouin scattering [32].

1.4 The Importance of Single-Frequency Fiber Lasers

Even though being intensively researched for decades, fiber lasers are still at the cutting edge of laser photonics technology and still continuously proceed to trigger the emergence of new technologies and applications. As an important part of fiber lasers, SFFLs have been undergoing prominent advances and finding increasing applications since its creation at 1990s [33]. Figure 1.4 shows a typical optical spectrum of a single-frequency erbium-ytterbium codoped fiber laser at around 1550 nm, and it is noted here that the optical spectrum analyzer (OSA) could not resolve it precisely owing to its ultra-narrow bandwidth. Benefiting from the merit of high purity in optical spectrum, SFFLs have been harnessed in areas such as coherent optical communication, high precision optical sensing, optical metrology, spectroscopy, and interferometry [34–38]. Furthermore, SFFLs can also be utilized to realize tens-kW-level laser via multichannel coherent beam combining, although its single

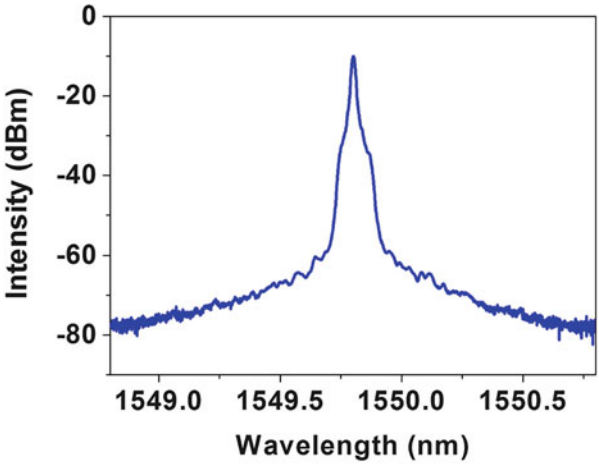

Fig. 1.4 Typical optical spectrum of a single-frequency erbium-ytterbium codoped fiber laser at around 1550 nm

channel amplification is hindered by fiber nonlinear effects and relatively lags behind that of the multi-longitudinal fiber lasers [39].

It should be noted that long before the first demonstration of SFFLs, single-frequency lasing has been achieved from He-Ne gases at the early 1960s [40]. In addition, single-frequency lasers on the basis of bulk glass, crystal, and semiconductor have been reported afterward [41–43]. Along with these pioneer works, researchers have recognized and validated the potentiality of single-frequency lasers for most of the abovementioned applications. For instance, a single-frequency Nd:YAG laser was employed to measure the relative fine-structure cross sections and energy spacing of atomic oxygen [44]. Nevertheless, in the years since the first demonstration of Er-doped distributed Bragg reflector fiber laser by G. A. Ball and coauthors, SFFLs have been continuing to replace its competing laser sources in application occasions and even largely promoting the applying performances. Most bulk solid-state lasers contain free-space components and need careful alignment and separate protection, which make the system fragile and cumbersome. Moreover, its incompatibility with fiber system is also a disadvantage for applications which desire direct fiber delivery. For single-frequency semiconductor laser, it can be easily integrated into a small unit which has a fiber-coupled output. However, its output power is highly limited, and considerable heat would deposit during operation and deteriorate the laser noise as well as broaden the linewidth, leading to compromised spectrum purity of the single-frequency laser. While for SFFL, its virtual alignment-free all-fiber system is inherently compact and rugged, as well as immune to electromagnetic fields and other harsh environments. Other advantages, such as high efficiency, accurate wavelength selection, narrow linewidth, low noise, scalable to high-output power, direct fiber delivery of single mode, and linear polarized laser beam, all render SFFLs attractive for various applications. Additionally, other than providing a high-quality single-frequency laser source, SFFLs can also be mode-hop-free tuned and modulated by lots of external actuation effects and therefore can be measuring or sensing element themselves.

References

1. Maiman TH (1960) Stimulated optical radiation in ruby. Nature 187:493
2. Hecht J (2010) Short history of laser development. Opt Eng 49:91002
3. Svelto O, Hanna DC (2010) Principles of lasers, 5th edn. Springer, New York
4. Snitzer E (1961) Optical maser action of Nd^{+3} in barium crown glass. Phys Rev Lett 7:444
5. Koester CJ, Snitzer E (1964) Amplification in a fiber laser. Appl Opt 3:1182
6. Desurvire E, Simpson JR, Becker PC (1987) High-gain erbium-doped traveling-wave fiber amplifier. Opt Lett 12:888
7. Taga H, Yoshida Y, Edagawa N, Yamamoto S, Wakabayashi H (1990) 459 km, 2.4 Gbit/s four wavelength multiplexing optical fiber transmission experiment using six Er-doped fibre amplifiers. Electron Lett 26:500
8. Buck JA (2004) Fundamentals of optical fibers. Wiley, Hoboken
9. Seddon AB, Tang Z, Furniss D, Sujecki S, Benson TM (2010) Progress in rare-earth-doped mid-infrared fibre lasers. Opt Express 18:26704
10. Jackson SD (2012) Towards high-power mid-infrared emission from a fiber laser. Nature Photon 6:423
11. Funk DS, Carlson JW, Eden JG (1994) Ultraviolet (381 nm), room temperature laser in neodymium-doped fluorozirconate fibre. Electron Lett 30:1859
12. Mizrahi V, DiGiovanni DJ, Atkins RM, Grubb SG, Park Y, Delavaux J (1993) Stable single-mode erbium fiber-grating laser for digital communication. J Lightwave Technol 11:2021
13. Pask HM, Carman RJ, Hanna DC, Tropper AC, Mackechnie CJ, Barber PR, Dawes JM (1995) Ytterbium-doped silica fiber lasers-versatile sources for the 1-1.2 μm region. IEEE J Sel Top Quantum Electron 1:2
14. Hanna DC, Jauncey IM, Percival RM, Perry IR, Smart RG, Suni PJ, Townsend JE, Tropper AC (1988) Continuous-wave oscillation of a monomode thulium-doped fibre laser. Electron Lett 24:1222
15. Dianov EM, Dvoyrin VV, Mashinskii VM, Umnikov AA, Yashkov MV, Guryanov AN (2005) CW bismuth fibre laser. Quantum Electron 35:1083
16. Hanna DC, Percival RM, Smart RG, Townsend JE, Tropper AC (1989) Continuous-wave oscillation of holmium-doped silica fibre laser. Electron Lett 25:593
17. Jackson SD (2003) Continuous wave 2.9 μm dysprosium-doped fluoride fiber laser. Appl Phys Lett 83:1316
18. Baney DM, Rankin G, Chang K (1996) Blue Pr^{3+}-doped ZBLAN fiber upconversion laser. Opt Lett 21:1372
19. Hill KO, Meltz G (1997) Fiber Bragg grating technology fundamentals and overview. J Lightwave Technol 15:1263
20. Giles CR, Desurvire E (1991) Modeling erbium-doped fiber amplifiers. J Lightwave Technol 9:271
21. Henderson-Sapir O, Munch J, Ottaway DJ (2016) New energy-transfer upconversion process in Er^{3+}: ZBLAN mid-infrared fiber lasers. Opt Express 24:6869
22. Stiles E (2009) New developments in IPG fiber laser technology. In: Proceedings of the 5th international workshop on fiber lasers
23. http://www.laserfocusworld.com/articles/print/volume-49/issue-12/world-news/materials-processing-100-kw-fiber-laser-power-meter-serve-industry.html
24. Eidam T, Hanf S, Seise E, Andersen TV, Gabler T, Wirth C, Schreiber T, Limbert J, Tunnermann A (2010) Femtosecond fiber CPA system emitting 830 W average output power. Opt Lett 35:94
25. Stutzki F, Jansen F, Liem A, Jauregui C, Limpert J, Tunnermann A (2012) 26 mJ, 130 W Q-switched fiber laser system with near-diffraction-limited beam quality. Opt Lett 37:1073
26. Agrawal G (2012) Nonlinear fiber optics, Optics and photonics, 5th edn. Academic, Waltham
27. Krauss G, Lohss S, Hanke T, Sell A, Eggert S, Huber R, Leitenstorfer A (2010) Synthesis of a single cycle of light with compact erbium-doped fibre technology. Nat Photon 4:33

28. Gaida C, Gebhardt M, Stutzki F, Jauregui C, Limpert J, Tünnermann A (2015) Self-compression in a solid fiber to 24 MW peak power with few-cycle pulses at 2 μm wavelength. Opt Lett 40:5160
29. Petersen CR, Møller U, Kubat I, Zhou B, Dupont S, Ramsay J, Benson T, Sujecki S, Abdel-Moneim N, Tang Z (2014) Mid-infrared supercontinuum covering the 1.4–13.3 μm molecular fingerprint region using ultra-high NA chalcogenide step-index fibre. Nature Photon 8:830
30. Li C, Xu S, Huang X, Xiao Y, Feng Z, Yang C, Zhou K, Lin W, Gan J, Yang Z (2015) All-optical frequency and intensity noise suppression of single-frequency fiber laser. Opt Lett 40:1964
31. Zhao Q, Xu S, Zhou K, Yang C, Li C, Feng Z, Peng M, Deng H, Yang Z (2016) Broad-bandwidth near-shot-noise-limited intensity noise suppression of a single-frequency fiber laser. Opt Lett 41:1333
32. Ward BG (2015) Maximizing power output from continuous-wave single-frequency fiber amplifiers. Opt Lett 40:542
33. Ball GA, Morey WW, Glenn WH (1991) Standing-wave monomode erbium fiber laser. IEEE Photon Technol Lett 3:613
34. Radic S (2010) Optical communications: coherent regeneration. Nature Photon 4:669
35. Diaz S, Abad S, Lopez-Amo M (2008) Fiber-optic sensor active networking with distributed erbium-doped fiber and Raman amplification. Laser & Photon Rev 2:480
36. Chou CW, Hume DB, Rosenband T, Wineland DJ (2010) Optical clocks and relativity. Science 329:1630
37. Eyler EE (2011) Precision, not power. Science 333:164
38. Adhikari RX (2014) Gravitational radiation detection with laser interferometry. Rev Mod Phys 86:121
39. Liu Z, Zhou P, Wang X, Ma Y, Xu X (2013) Kilowatt coherent beam combining of high-power fiber amplifiers using single-frequency dithering techniques. In: Brignon A (ed) Coherent laser beam combining. Wiley, Weinheim, p 75
40. Massey GA, Oshman MK, Targ R (1965) Generation of single-frequency light using the FM laser. Appl Phys Lett 6:10
41. Zubarev JG, Mulikov VF (1972) Single-frequency Nd: glass laser under non-spiking free oscillation and Q-switched conditions. Sov J Quantum Electron 2:207
42. Owyoung A, Hadley GR, Esherick P, Schmitt RL, Rahn LA (1985) Gain switching of a monolithic single-frequency laser-diode-excited Nd: YAG laser. Opt Lett 10:484
43. Kobayashi K, Mito I (1988) Single-frequency and tunable laser diodes. J Lightwave Tech 6:1623
44. Bamford DJ, Dyer MJ, Bischel WK (1987) Single-frequency laser measurements of two-photon cross sections and Doppler-free spectra for atomic oxygen. Phys Rev A 36:3497

Chapter 2
Fundamental Principle and Enabling Technologies of Single-Frequency Fiber Lasers

In this chapter, we focus on the fundamental principle and enabling technologies of single-frequency fiber lasers. Essentially, the strategy is to implement a narrow band-pass filter to guarantee a single longitudinal mode oscillating in a laser cavity. In this way, the oscillation mode spacing of the cavity should be wide enough to alleviate the requirement on the filter and, more importantly, to realize a more stable single-frequency laser operation. We therefore first introduce the principle of single-frequency lasing and then the important properties of this type of lasers, as well as the corresponding characterizing method. After that, the cavity design of single-frequency fiber lasers is discussed, in terms of representative linear and ring cavity structures and other schemes leveraging different fiber optical filtering effect. Finally, we discuss different cavity designs that enable advanced laser performances such as linearly polarized operation, linewidth and noise suppression, continuous wavelength tuning, and frequency modulation.

2.1 Principle of Single-Frequency Lasing

Considering a typical fiber laser structure shown in Fig. 1.2, the mirrors on both sides of the cavity make sure there are two oppositely propagated plane electromagnetic waves, which interfere with each other and form a standing wave pattern. To maintain this pattern and meet the condition of stable oscillation, the resonator frequencies of the cavity are given by:

$$v = n \cdot \frac{C}{2nl} \tag{2.1}$$

where n is an integral number, C is the speed of light in vacuum, n is the refractive index of fiber, and l is the cavity length. In this way, the frequencies that satisfy

© Springer Nature Singapore Pte Ltd. 2019

Z. Yang et al., *Single-Frequency Fiber Lasers*, Optical and Fiber Communications Reports 8, https://doi.org/10.1007/978-981-13-6080-0_2

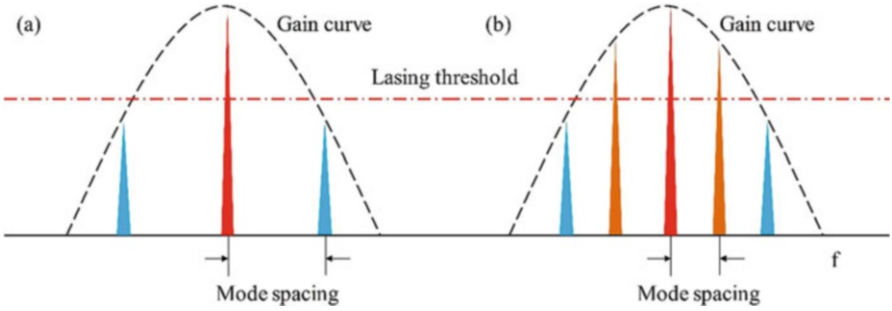

Fig. 2.1 Schematic demonstration of longitudinal modes distribution in a laser cavity: (**a**) only one and (**b**) two or more modes exceed the lasing threshold

Eq. 2.1 all can oscillate in the cavity, corresponding to a series of longitudinal modes with spacing of each other given by:

$$\Delta v = \frac{C}{2nl} \tag{2.2}$$

Therefore, single-frequency operation can be obtained given that the bandwidth of the net gain of the laser is narrower than the frequency spacing of the oscillating modes. However, the mode spacing of fiber lasers is generally in the GHz level or narrower, while the emission bandwidth of RE ions is basically around tens of nanometers owing to the Stark effect induced energy-level splitting. To enable a fiber laser working in the single longitudinal mode regime, a general method is to employ a filtering component in the cavity. Given that the filtering effect is narrow enough, there will be only one longitudinal mode surviving and providing single-frequency lasing.

Under ordinary circumstances, there are still some longitudinal modes presenting inside the bandwidth of the filter, owing to the limited fabrication technique of the filter and the relatively long length of the cavity. Taking into account an RE ions doped silica fiber, a minimum length of several tens millimeters is required to provide enough optical gain for laser operation. In an ideal case, there is only one mode exceeding the lasing threshold and oscillating in the cavity, as shown in Fig. 2.1a. Nevertheless, for a realistic fiber laser, the situation is more likely as shown in Fig. 2.1b; the number of modes over the threshold is two or more. Fortunately, in this case the laser still has the chance to realize single-mode oscillating, thanks to the effect of mode competition generally taking place in condition of identical special intensity distribution of modes in the gain medium. This is attributed to the cross-saturation of the gain when a longitudinal mode acquires the highest optical gain and continuously accumulates intensity, while other modes see a negative net gain and vanish away. However, it is worth noting that in this case, the

laser is susceptive to external perturbations such as temperature change and mechanical vibration, which would cause length drifting of the cavity and thus frequency shifting of the resonator mode. In this way, the phenomena of mode hopping and multimode oscillation would onset and lead to unstable operation of the laser. It is therefore desirable to use a resonator with large mode spacing or free spectral range to maintain a stable laser operation, besides to minimize unwanted perturbations. In addition, a larger mode spacing is more tolerant to frequency change, rendering the laser appealing for applications such as coherent optical sensing [1, 2]. In view of this, a single-frequency fiber laser with ultrashort cavity which is incorporating a high-gain RE ions doped fiber is much advantageous. This will be the main subject of the next chapter.

Additionally, for a linearly configured fiber cavity, the spatial hole burning effect that is caused by the standing wave interference pattern formed by the two counter-propagating light waves should be taken into consideration. As the spatially distributed nodes and antinodes of the pattern would induce a periodical modulation of the local electric field generated by the host glass material that surrounding the doped RE ions, locally varying of energy levels and transition frequencies and strength will be induced. This will result in preferentially saturation of the gain at these antinodes and at the corresponding frequency and accordingly forms a dip in the spectral shape of the gain – spatial hole burning [3]. An intuition consequence of this effect is the inhomogeneous saturation of the gain, and the competing modes would acquire enough gain to lase as they experience weaker saturation than the lasing mode. In this sense, the spatial hole burning is harmful to single-frequency operation and should be got rid of. However, this effect can also be exploited in an unpumped RE ions doped fiber to form an automatic tracking filter, to enable and stabilize single-mode oscillation of a fiber ring cavity [4]. Actually, in a ring laser the light presents as a traveling wave instead of a standing wave pattern, which is then introduced intensively to realize ultra-narrow filtering. Considering the destructive spatial hole burning effect in linear fiber laser, it can be suppressed via manipulating of the polarization states of the intracavity light waves [5]. More details of this technique will be discussed later in this chapter.

2.2 Properties of Single-Frequency Lasers

2.2.1 Single Longitudinal Mode Operation

For a single-frequency laser, a straightforward feature is that it has only one oscillating mode, and other than that there are no any other frequency components presenting both in the cavity and output. To verify this property, a simple method is to launch the laser light into a photodetector (PD) with a response bandwidth larger than the mode spacing of the laser cavity and then examine the resulting electrical

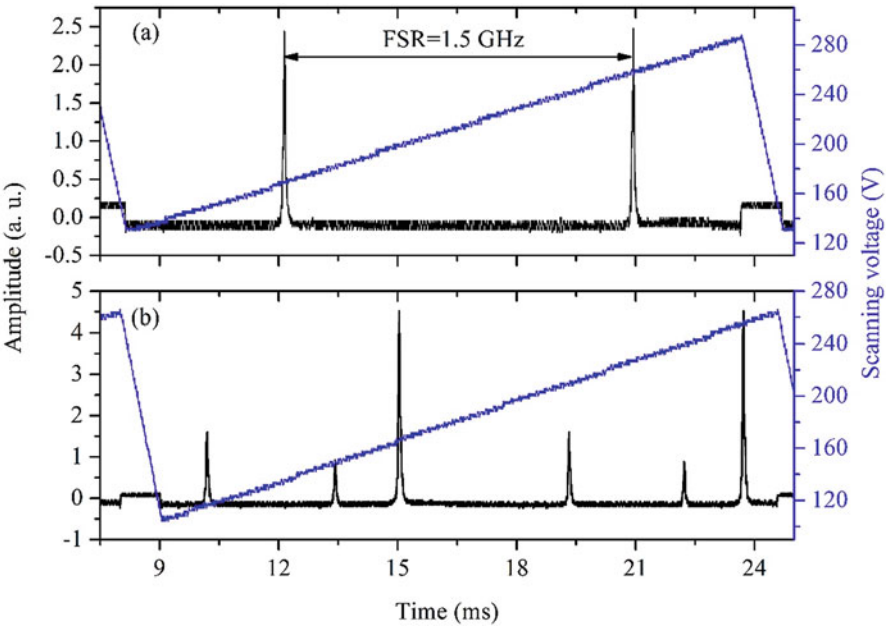

Fig. 2.2 Scanning FP interferometer characterization of a fiber laser working in the single-mode (**a**) and multimode (**b**) regime

signal with an RF spectrum analyzer (SA). In principle, there will be nothing in the spectrum, as any extra parasitic oscillating mode will lead to the generation of a microwave signal owing to the optical heterodyne effect.

Another intuitive method to characterize single longitudinal mode operation is to utilize a scanning Fabry-Perot (FP) interferometer to examine the fine spectral structure of the laser signal. Typically, the FP cavity transmits optical signal at specific frequencies with resolution of several tens MHz. By changing the cavity length periodically with a piezoelectric transducer, the transmitting frequency can be continuously scanned within the free spectral range (FSR) of the cavity. The transmitted signal can then be detected by a photodetector and examined by an oscilloscope. Figure 2.2a, b shows the measurement results of a fiber laser working in the single-mode and multimode regime, respectively.

2.2.2 Intensity Noise

Intensity noise reflects the power fluctuation of laser light, and it can be described by relative intensity noise (RIN), which is defined by [6]:

$$\mathrm{RIN} = \frac{\Delta P^2}{P^2}\,(\mathrm{dB/Hz}) \tag{2.3}$$

where ΔP is the power spectral density of intensity noise in a 1 Hz electrical bandwidth, and P is the average optical intensity. In the electrical spectrum, the intensity noise of single-frequency laser can be categorized as technical noise at low frequency, relaxation oscillation noise at medium frequency, and shot noise at high frequency. In general, technical noise is mainly caused by external disturbances and power fluctuation of pump. In a continuously pumped laser, relaxation oscillation is manifested as a damped oscillation of intensity in the time domain. Its generation mechanism is attributed to the dynamic energy exchange between the gain medium and the photons inside the cavity. For single-frequency fiber lasers, the relaxation oscillation peak generally locates in a frequency range from a few tens of kHz to several MHz [7, 8]. Shot noise is also recognized as quantum noise, which is resulted from the quantum fluctuation when quantizing the laser light into photons. Its power density spectrum is irrelevant to electrical frequency and is demonstrated as the background white noise along the whole spectrum. The calculating formula is:

$$\mathrm{RIN}_{sn} = \frac{2h\nu}{P}\,(\mathrm{dB/Hz}) \tag{2.4}$$

where h is the Planck constant and ν is the optical frequency. It can be seen from Eq. (2.4) that the magnitude of shot noise is inversely proportional to the optical power.

Basically, for SFFLs the intensity noise above the noise limit can be modeled with the help of the simplified rate equation of the laser. Take the case of Er^{3+}-doped SFFL, assuming the gain medium is a homogeneously broadened three-energy model and neglecting the up-conversion process and excited-state absorption; then its rate equation can be written as [6, 8]:

$$\frac{dn_2}{dt} = (1 - n_2)(W_P + W_A) - n_2\left(W_E + \frac{1}{\tau_2}\right) \tag{2.5}$$

$$\frac{dq}{dt} = W_E N_0 n_2 - (1 - n_2) W_A N_0 - \frac{q}{\tau_c} \tag{2.6}$$

where n_2 is the ratio of excited population density ($^4I_{13/2}$, see Fig. 1.3) to the total population density ($^4I_{13/2}$+ $^4I_{15/2}$); q is the photon number density in the laser cavity; W_P, W_A, and W_E are the pump absorption, signal absorption, and signal emission rate, respectively; τ_2 is lifetime of the population at excited state; N_0 is the total ion density; τ_c $\frac{L_0}{\gamma C}$ is the lifetime of photon inside the cavity; L_0 is the optical cavity length; γ is the single-pass loss coefficient; and C is the light velocity in a vacuum. The equations can be solved at the steady state by setting the terms on the left side to

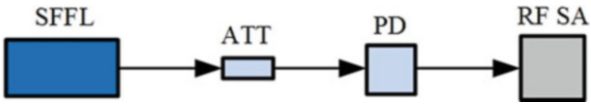

Fig. 2.3 The configuration of RIN measurement that utilizes an RF spectrum analyzer

zero. As the factors that affect the laser intensity are pump rate and loss in the cavity, then when small perturbations are introduced such that $W_P(t) = W_{P0} + \delta W_P(t)$ and $\gamma(t) = \gamma_0 + \delta\gamma(t)$, they will straightly come to the laser intensity and cause noise given by the following formula:

$$\mathrm{RIN}(f) = |H_P(f)|^2 \frac{S_{\delta W_P}}{W_{P0}^2} + |H_L(f)|^2 \frac{S_{\delta\gamma}}{\gamma_0^2} \tag{2.7}$$

in which $\frac{S_{\delta W_P}}{W_{P0}^2}$ and $\frac{S_{\delta\gamma}}{\gamma_0^2}$ are the spectral density functions of the pump rate fluctuation and the cavity loss fluctuation, respectively, while $H_P(f)$ and $H_L(f)$ are the corresponding transfer functions that are deduced from the steady-state solutions via a series of algebraic operations.

The RIN spectrum of single-frequency laser can be experimentally obtained by spectrally analyzing the electrical signal that converted from the optical signal with a fast PD. In general, the spectrum analysis is fulfilled by two methods: directly display on an RF SA and use a data acquisition card to sample the magnitude of laser power and then implement fast Fourier transform. The configuration of RIN measurement that utilizes an RF SA is shown in Fig. 2.3. The output from the SFFL is directed into the PD after being attenuated by an optical attenuator (ATT), and the spectrum of the resulting signal is resolved with the RF SA. It is noted that the ATT should be adjusted to make sure that sufficient laser power is injected into the PD to surpass the intrinsic noise floor of the measurement system while avoiding saturation of the PD. The laser RIN is obtained by normalizing the spectrum acquired from the RF SA with respect to the examining resolution and the mean amplitude of the electrical signal recorded at the output of the PD. Figure 2.4 demonstrates a typical RIN spectrum of SFFL with increasing pump power. It is observed that with the enhancement of the pump power, the relaxation oscillation frequency is gradually approaching a maximum of about 2 MHz, starting at around 1.2 MHz. In the meantime, the amplitude of the RIN is reaching a minimum of about −105 dB/Hz from −91 dB/Hz. Beyond the relaxation oscillation peak, the laser RIN is monotonously decreased to about −142 dB/Hz at 5 MHz. It is noted that the RIN spectrum curve should close to the theoretical shot noise limit at higher RF frequencies, even though it is currently ~10 dB higher than the noise limit, as shown in the figure. The technical noise within several hundreds of kHz is essentially lower than −125 dB/Hz, so the relaxation oscillation peak is the dominating noise component of SFFLs and should be suppressed for the general applications.

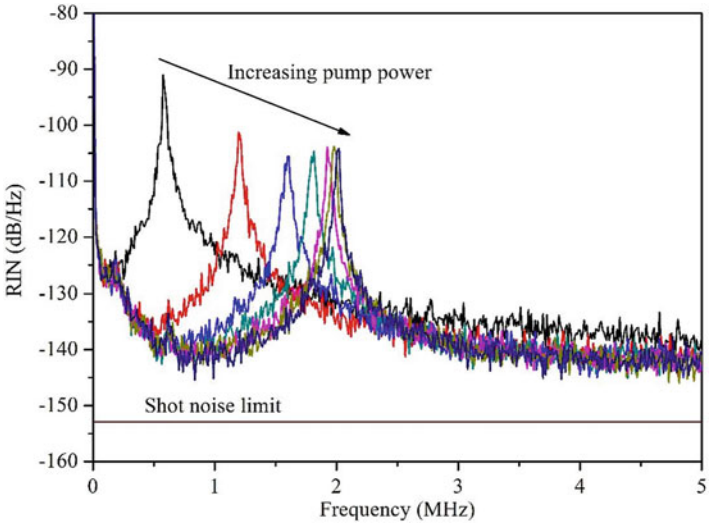

Fig. 2.4 Typical RIN spectrum of SFFL with increasing pump power. The calculated shot noise limit is also shown

2.2.3 Frequency Noise

Frequency noise presents the condition of frequency fluctuation of single-frequency laser, and it is described by the following power spectral density function [9]:

$$S_\nu(f) = \int_{-\infty}^{\infty} C_\nu(\tau) e^{i2\pi f\tau} d\tau \tag{2.8}$$

where $C_\nu(\tau) = \langle \Delta\nu(t)\Delta\nu(t+\tau) \rangle$ is the time domain autocorrelation function of frequency noise, and $\Delta\nu(t)$ is laser frequency change.

In single-frequency laser, the basic frequency noise source comes from the amplified spontaneous emission (ASE), which will add to the existing laser field and appear as a white noise source with spectral power density given by [10, 11]:

$$S_{s-t}(f) = \frac{e_{sp}^2 \delta}{4\pi^2 \tau^2 P} \tag{2.9}$$

in which e_{sp}^2 is the spectral power density of ASE, δ is the single-pass coefficient of transmission loss of the cavity, τ is the photon lifetime inside the laser cavity, and P is the average power. The frequency noise that results from ASE is also regarded as the Schawlow-Townes noise limit. However, in the actual measurement the

frequency noise of single-frequency laser is generally several orders of magnitude higher than this noise limit [12, 13]. According to Eq. (2.1), the laser frequency is also related to the optical path length of the cavity; thus any disturbances such as temperature change and acoustic and mechanical vibration that globally or locally alter the length or refractive index of the gain medium will lead to significant frequency change. Therefore, the laser cavity should be strictly packaged to minimize these disturbances and realize a relatively stable lasing frequency. In view of this, a fiber laser with cavity length in the cm level is advantageous for operating with low-frequency noise, as it can be flexibly encapsulated into a small metal tube [14].

It is noted that even for a fiber laser that is in absolute thermal equilibrium with the surrounding environment, there is still instantaneous temperature fluctuation causing thermal frequency noise. This is owing to the random diffusion of thermal energy deposited inside the gain fiber [15]. Accordingly, the induced laser frequency instability is also called the fundamental thermal noise limit, and the noise spectrum is given by the following formula [16]:

$$S_{th}(f) = q^2\nu^2 T_{th}^2(f) \tag{2.10}$$

$$T_{th}^2(f) = \frac{k_b T^2}{4\pi^2 k_c}\mathrm{Re}\left[e^{ik_1 d^2/2}E_1\left(ik_1 d^2/2\right)\right] \tag{2.11}$$

in which $q = \frac{\delta n}{n\delta T} + \frac{\delta \varepsilon}{\delta T}$ is the thermo-optical coefficient of the gain fiber, ν is the laser frequency, $T_{rms}(f)$ is the power spectral density of the temperature fluctuation, $k_b = 13.81 \times 10^{-24} J/K$ is the Boltzmann constant, T is the equilibrium temperature of the fiber, $k_c = C_V D$ is the thermal conductivity of the fiber, C_V is the heat capacity, D is the thermal diffusion coefficient, $k_1 = \sqrt{fC_V/2k_c}$, d is the mode field diameter corresponding to the boundary that the optical intensity drops to e^{-2} of its maximum, $\mathrm{Re}(\cdot)$ denotes the real part of $(\cdot)$, and E_1 is the standard exponential integral. The fundamental thermal noise sets a floor that is much higher than the Schawlow-Townes noise limit, and it is determined by the basic physical parameters of the fiber laser other than external disturbances or pump instabilities. The theory has already been verified by experimental measuring a single-frequency Er^{3+}-doped silica fiber ring laser [10]. Nevertheless, there are discrepancies between the theoretical predictions and measurements at frequencies lower than ~10 kHz, and this is attributed to another noise component – the so-called $1/f$ noise or pink noise, which has a power spectral density that is inversely proportional to the RF frequency. The origin of this kind of noise has been theoretically and experimentally confirmed to be the diffusion of local entropy fluctuations for RE ions doped fiber lasers [9, 17].

It is worth noting that the fundamental thermal noise was only verified with low-gain fiber laser in the nominal power regime. Actually, researchers have found that with the pump power being enhanced to a specific degree, the laser frequency noise shows an evolution that is not exactly consistent with the theory of the fundamental thermal noise [18, 19]. Further investigations have shown that the self-heating effect in the gain fiber is responsible for this phenomenon. In principle,

owing to the quantum defect between pump and laser photons and the fast non-radiative decay from the excited energy level of RE ions, part of the pump energy will be transferred into heat accumulating inside the laser cavity and thus cause temperature rising. It is therefore intuitive that the pump power instability will induce temperature fluctuation within the cavity and consequently result in another frequency noise component, i.e., self-heating noise. Ref. [20] analyzed this effect thoroughly and gave an analytical expression explaining how the pump intensity noise transfers to the laser frequency fluctuation:

$$S_{s\text{-}h}(f) = q^2\nu^2 T_{s\text{-}h}^2(f) \tag{2.12}$$

$$T_{s-h}^2(f) = P_p^2 \mathrm{RIN}_p(f)|\Theta(f)|^2 \tag{2.13}$$

$$\Theta(f) = \frac{\alpha\bar{n}}{2\kappa_t} E_1\left[ik_1^2a^2/2\right]\exp\left[ik_1^2a^2/2\right] \tag{2.14}$$

where P_p is the pump power, $\mathrm{RIN}_p(f)$ is the relative intensity noise of the pump laser, $\Theta(f)$ is the transfer function from the pump instability to the temperature change, α is the heating coefficient of the gain fiber, $\bar{n}$ is an assumed uniform RE ion density in the fiber, and a is a characteristic radius of the fiber core. In experiment, the authors found that in an Er^{3+}-doped silica fiber laser, the dominating frequency noise component was transferred from the thermal noise at low pump power condition to the self-heating noise at high pump power condition, and the noise spectrum was consistent with the theoretical calculation. However, in this model the authors only considered the situation that the laser is constructed by a low-gain fiber and did not take into account the axial evolution of the heat accumulation. For highly doped fiber lasers, heat accumulation could be significantly varying along the laser cavity due to the high absorption of the pump; thus viewing it as uniform is no longer appropriate. The case of high-gain fiber laser will be further discussed in the next chapter, in which the main topic is about high-power short-cavity SFFLs based on heavily RE ions doped multicomponent soft glass fiber.

Finally, in the experimentally measured frequency noise spectrum of SFFLs, a noise peak can be observed at the laser relaxation oscillation frequency [10]. The origin of this peak is attributed to the correlation between the intensity and frequency fluctuations, caused by the laser intensity modulation of the refractive index in optical fiber. This correlation is related to the linewidth enhancement factor, which is given by [7]:

$$\alpha \cong \frac{2\Delta\nu}{f\mathrm{RIN}} \tag{2.15}$$

It is therefore concluded that the frequency noise spectrum of SFFLs is consisted by thermal noise at low frequencies and RIN-induced noise peak at the relaxation oscillation frequency, where the thermal noise is highly weakened and the intensity fluctuation is significant.

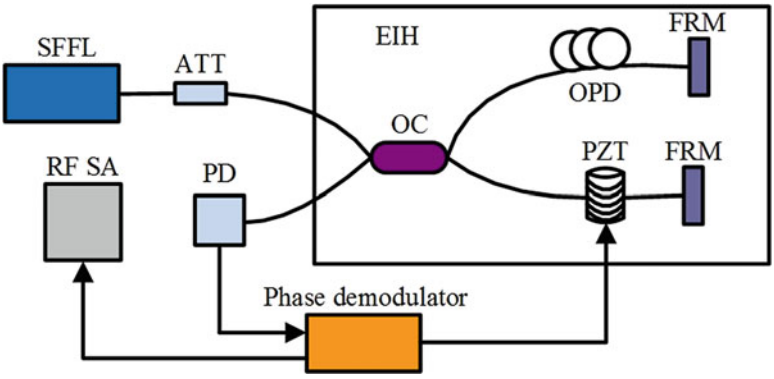

Fig. 2.5 The schematic configuration of the frequency noise measurement system of single-frequency laser

Frequency noise is commonly measured with the help of an unbalanced Michelson interferometer, which will transfer the laser frequency fluctuation to phase fluctuation at the output. Via shielding the laser and the interferometer to minimize the effect of external disturbances, the interferometric phase can be demodulated from the output by implementing the phase-generated carrier (PGC) Scheme [21]. Assume the laser variation to be $\delta\nu$, then the acquired phase noise after the interferometer is written by:

$$\delta\varphi = \frac{2\pi nl}{C}\delta\nu \tag{2.16}$$

in which n is the refractive index of the fiber, l is the optical path difference (OPD) between the two arms of the interferometer, and C is the light velocity in a vacuum. According to the study in Ref. [21], for the measurement of SFFLs, the OPD should be large enough to track the frequency noise components at low RF frequencies; otherwise the system would only reveal white noise of the laser at high frequencies. In addition, a larger OPD results in a higher amplitude of the detecting signal and thus renders the measurement system more robust and immune to environment noises and disturbances.

Figure 2.5 depicts the schematic configuration of the frequency noise measurement system of single-frequency laser. The laser signal is launched into the interferometer after being properly attenuated. A 2×2 optical coupler (OC) is employed to split and combine laser beams. Two Faraday rotating mirrors (FRM) are used to eliminate polarization fading effects of the reflected lights. The OPD between the two arms is chosen to be 100 m, while one of them is partly coiled to a piezoelectric transducer (PZT) which is driven by external modulation signal. The whole interferometer system is shielded by an environmental isolation housing (EIH). The interference signal is then detected by the PD and subsequently demodulated by the phase demodulator, with the final results displaying on the RF SA.

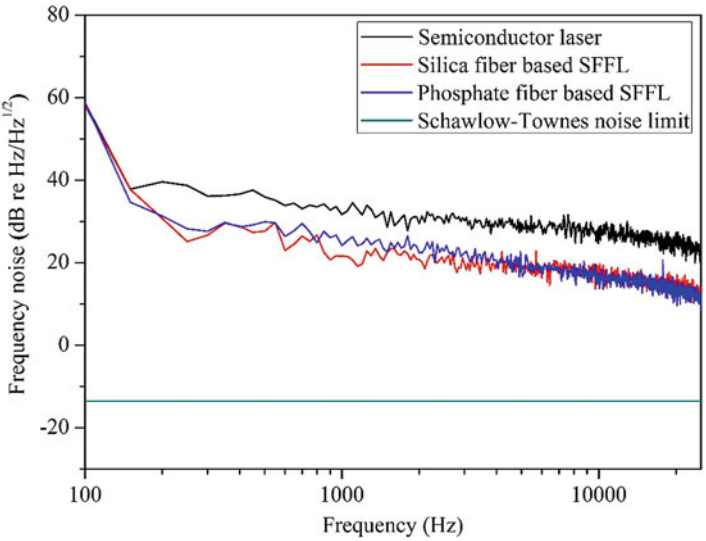

Fig. 2.6 Measured frequency noise spectrum of a single-frequency semiconductor laser, a silica fiber-based SFFL, and a phosphate fiber-based SFFL. The calculated Schawlow-Townes noise limit based on the parameters of the phosphate fiber-based SFFL is also shown for comparison

Figure 2.6 shows the measured frequency noise spectra in the range from 0 to 25 kHz of three types of laser: single-frequency semiconductor laser (Redfern Integrated Optics), silica fiber-based SFFL (NKT Photonics), and phosphate fiber-based SFFL (homemade). It is added that the term "dB re $Hz/Hz^{1/2}$" used in the figure denotes the logarithmic computing of the amplitude of laser frequency noise, with the unit of "$Hz/Hz^{1/2}$." The semiconductor laser demonstrates the highest frequency noise, which is about 10 dB higher than that of the silica and phosphate fiber-based SFFLs. This is attributed to the considerable thermal effects caused by the electrical pump process. The calculated Schawlow-Townes noise limit based on the parameters of the phosphate fiber-based SFFL is also shown in the figure, where one can observe a gap of more than 30 dB between the measured spectra and the noise limit. Therefore the frequency noise of the SFFLs should also be suppressed to facilitate applications such as high precision optical sensing.

2.2.4 Linewidth

The linewidth of single-frequency laser generally refers to the width of the laser power spectral density in terms of frequency. It is described by the full width at half maximum (FWHM) of the laser spectrum. For a single-frequency laser, its linewidth and frequency noise both reflect the optical spectral purity and temporal coherence property. Although the linewidth gives poor information about the laser frequency

fluctuations, which can be completely revealed by the frequency noise spectrum, it offers a simple and straightforward way to compare different laser sources. Theoretically, the laser power spectral density (and thus the linewidth) can be calculated from the frequency noise spectrum, but not vice versa [9, 22]:

$$I_E(\omega) = E_0^2 \int_0^\infty \cos\left[(\omega_0 - \omega)\tau\right] \times \left\{ \exp\left[-4 \int_0^\infty S_\nu(f) \frac{\sin^2(\pi f \tau)}{f^2} df \right] \right\} d\tau \tag{2.17}$$

where $I_E(\omega)$ is the laser power spectral density, $\omega = 2\pi f$ is the optical angular frequency, E_0 is the amplitude of the laser field, and $S_\nu(f)$ is the frequency noise spectrum. In principle, the line shape of single-frequency laser possesses a Voigt profile that can be treated as the convolution of a Lorentzian and Gaussian functions, which, respectively, correspond to the white and $1/f$ noise components in the frequency noise spectrum. Nevertheless, the actual laser frequency noise spectrum is rather complicated, and the integration in Eq. (2.17) cannot be deduced to an analytical function. Numerical calculations are generally utilized to extract the linewidth of a single-frequency laser from its frequency noise spectrum. A relatively simple method was proposed in Ref. [23], where the linewidth is given by:

$$\text{FWHM} = \sqrt{(8 \ln 2) A} \tag{2.18}$$

$$A = \int_{1/T_0}^\infty H\left(S_\nu(f) - \frac{8 \ln 2}{\pi^2} f \right) S_\nu(f) df \tag{2.19}$$

in which $H(x) = 0$ if $x < 0$, $H(x) = 1$ if $x \geq 0$.

Nevertheless, these calculations are rarely used in practical occasions, as the linewidth can be intuitively obtained from the laser spectrum, given that it is acquired with adequate resolution. Since SFFLs generally has a linewidth in the sub-MHz or even sub-kHz level, the conventional devices such as optical spectrum analyzer (resolution >1 GHz) or F–P interferometer (resolution >1 MHz) could not provide an accurate estimate of the laser linewidth. To this end, researchers proposed to shift the laser signal from the optical band to the RF band via optical frequency mixing and then analyze it with an RF SA, i.e., heterodyne or delayed self-heterodyne detection. Direct heterodyne measurement requires another laser source with frequency close to the laser under test and a narrower linewidth, while delayed self-heterodyne measurement can be easily implemented with a Mach-Zehnder interferometer, and thus it is widely used [23]. Figure 2.7 depicts the schematic configuration of the delayed self-heterodyne measurement of laser linewidth. The output power of the SFFL is adjusted by the ATT and then launched into the Mach-Zehnder interferometer that is formed by two 50/50 OCs. In one arm of the interferometer, the laser signal is modulated by a frequency shifter (FS), while in

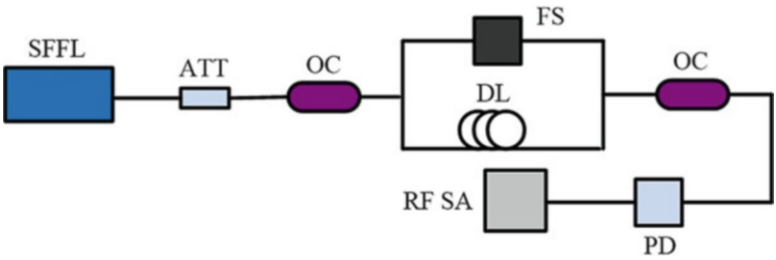

Fig. 2.7 The schematic configuration of the delayed self-heterodyne measurement of laser linewidth

the other arm the signal transmits through a delay line (DL) that is longer than the coherence length of the laser light. In this way, the two signal beams would beat at the PD and result in an RF signal, of which the FWHM is two times the laser linewidth. The measurement resolution of the system is calculated by [24]:

$$\Delta\nu = [-0.4\log(\Delta\nu_B\tau_d) + 0.6]/\tau_d \tag{2.20}$$

in which $\Delta\nu$ denotes the measurement resolution, $\Delta\nu_B$ is the resolution bandwidth of the RF SA, and τ_d is the delay time and satisfies the relationship $\Delta\nu_B\tau_d < 0.3$. Assume the length of the DL is 50 km, which corresponds to a delay time of 243 μs at 1.5 μm, and the resolution bandwidth of the RF SA is 1 kHz, then the system measurement resolution is about 3.5 kHz.

Figure 2.8 shows the typical heterodyne curve of SFFL measured with 40 MHz frequency shift (introduced by an RF signal-driven acoustic optical modulator) and 50 km DL, and Lorentz fitting of the measurement is also shown. It is apparent that the fitting curve is ideally matched with the experimental results, indicating that the $1/f$ or Gaussian frequency noise of the laser has little effect on the measurement. Generally, $1/f$ noise will lead to a Gaussian line shape and cause broadening of the measured linewidth [25]. The minor discrepancy between the fitting and the measurement at the central part of the curve is attributed to the involving of the $1/f$ noise. It is therefore suggesting to read the 20 dB width of the measured curve and then divide it by $2\sqrt{99}$ to obtain the laser linewidth; in this way the effect imposed by the laser $1/f$ noise will be avoided. From Fig. 2.8, the estimated linewidth of the measured laser is about 4 kHz.

It is worth noting that the method of delayed self-heterodyne is mainly employed at the 1.5 μm band, owing to the significant low transmission loss of the DL. When it comes to longer or shorter wavelengths, the transmission loss of the DL would increase and hinder the implementation of this linewidth measurement scheme. For example, the fiber attenuation of single-mode fiber at 1.0 μm band is about ten times higher than that at telecommunication window. As usually tens of kilometers of DL is required to obtain a sufficient resolution for assessing the single-frequency laser, a huge loss would be added to the signal being tested. In addition, the fiber delay line at 1.0 μm is more expensive compared with those in the 1.5 μm band.

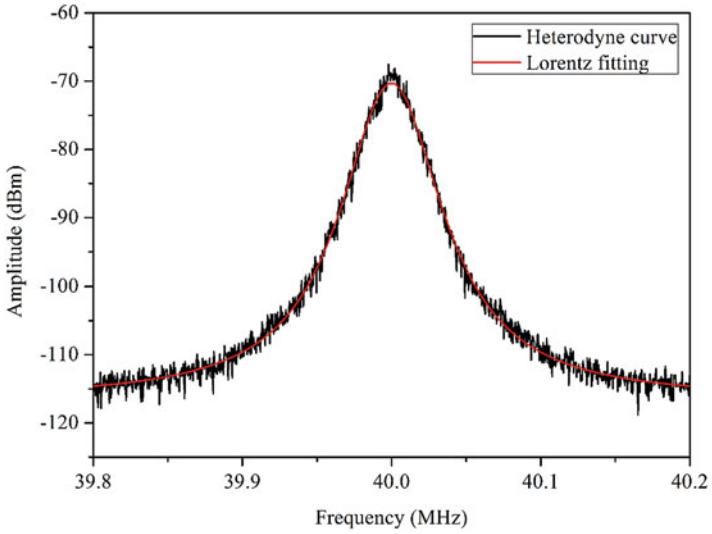

Fig. 2.8 Typical heterodyne curve of SFFL measured with 40 MHz frequency shift and 50 km DL; Lorentz fitting is also shown in the figure

To realize a high-resolution (kHz level) measurement of the linewidth of single-frequency laser at 1.0 μm, Ref. [26] demonstrated a loss-compensated recirculating delayed self-heterodyne (LC-RDSH) method. The experimental setup of the LC-RDSH is shown in Fig. 2.9. A 2 × 2 1/9 fiber OC is employed to construct to a fiber loop. The properly attenuated laser is coupled into the loop via one port of the OC and then successively passed through a fiber isolator (ISO), an FS, a DL, a fiber amplifier, a filter, and a polarization controller (PC). The ISO is employed to ensure unidirectional transmission of the laser light in the loop. The transmission loss of the system is compensated by an in-line fiber amplifier. A band-pass filter is utilized to filter out the unwanted amplified spontaneous emission (ASE) introduced by the amplifier. The PC is introduced to align the state of polarization (SOP) of the laser light to obtain the optimal heterodyne signal, which is extracted through the 10% port of the OC and launched into a PD for the analysis via an RF SA. In principle, every transmission of the laser in the fiber loop will result in a heterodyne beat note in the RF SA, and then a series order of beat notes spaced by the modulation frequency of the FS will be obtained.

Figure 2.10 demonstrates the RF spectrum of the heterodyne signal obtained from the LC-RDSH system. It was measured with the FS formed by two acoustic optical modulators with 80 MHz upshift and 77 MHz downshift, respectively, resulting in a 3 MHz up frequency shifting of the signal. The DL was 6 km single-mode fiber at 1.0 μm with a transmission loss of 1.4 dB km^{-1}. From the figure, over 15 beat notes with harmonic frequency of 3 MHz were realized. The inset of Fig. 2.10 shows the

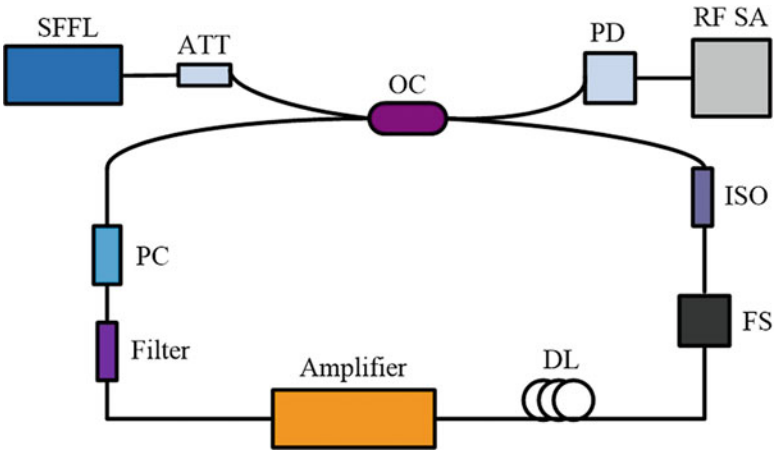

Fig. 2.9 The experimental setup of the LC-RDSH system

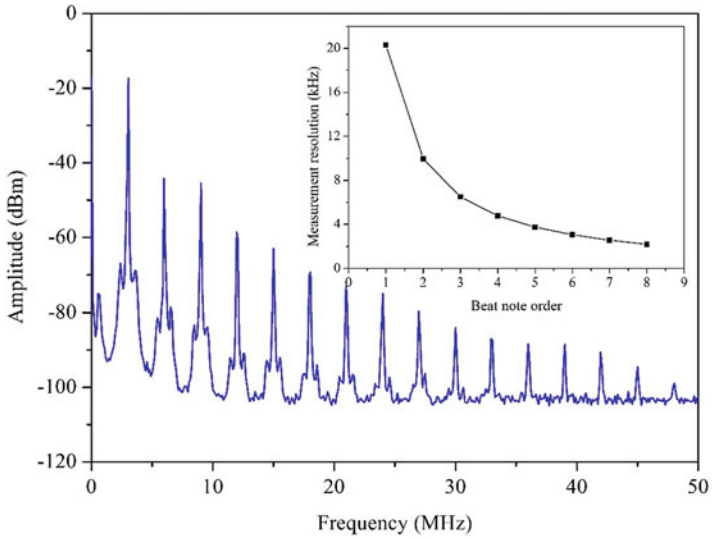

Fig. 2.10 The RF spectrum of the heterodyne signal obtained from the LC-RDSH system. Inset: the calculated measurement resolution of the first eight beat notes

calculated measurement resolution of the first eight beat notes. One can tell that the laser linewidth measurement resolution is monotonously decreasing with the increase of the order of beat notes, i.e., the length of the delay line. The eighth beat note has roughly experienced about 48 km fiber delay and the corresponding linewidth resolution in reaching 2 kHz.

2.3 Cavity Design of Single-Frequency Fiber Lasers

2.3.1 Typical Cavity Structures

As described in Sect. 2.1, the key technology of single-frequency laser is to set up a resonator that can guarantee the light emitted from the RE-doped fiber operating in a single longitudinal mode. Fortunately, FBGs provide the ideal solution by integrating the performances of optical feedback and spectral filtering which make up the fundamental demands of an extremely low loss laser cavity into the fiber core [27, 28]. Figure 2.11 shows a typical structure configuration of a distributed Bragg reflector (DBR) fiber laser, in which the active fiber is fused splicing with one broadband FBG (BB-FBG) and one narrowband FBG (NB-FBG) on each end, respectively. The BB-FBG should be relatively opaque at the signal wavelength while transparent to the pump laser. The NB-FBG serves as the output coupler of the fiber laser; its reflectivity varies on the basis of the specific structure parameters of the fiber laser. As the residual pump power would also pass through the NB-FBG, the output port should adopt a WDM (wavelength division multiplexing) to dump the pump power. Moreover, the reflective spectrum of the NB-FBG is required to be entirely falling into that of the BB-FBG which could be replaced in principle by a dielectric mirror.

The DBR structure enables the realization of a compact and reliable SFFL. The coming problem is the requirement of a considerably short-cavity length to maintain a robust single longitudinal mode operation, which consequently limits the output laser power [29, 30]. Another similar structure configuration is the distributed feedback (DFB) fiber lasers, as shown in Fig. 2.12, where the Bragg grating is directly written into the active fiber, with a π-phase-shifting offset from the center to realize unidirectional light transmission. The relatively long gain fiber can absorb

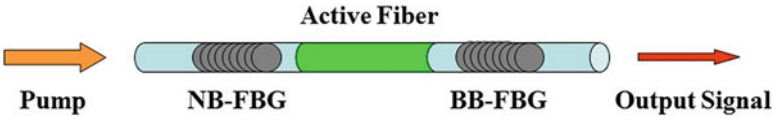

Fig. 2.11 Schematic setup of the DBR fiber laser

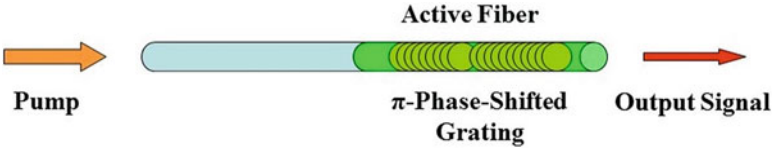

Fig. 2.12 Schematic setup of the DFB fiber laser

more pump power and thus achieve a higher output power than the DBR laser [31–33]. In addition, this laser scheme avoids the splicing procedure between the active fiber and the FBGs, which is difficult to manipulate while maintaining a short-cavity length, as well as the thermal property differences caused optical losses and instabilities at the splicing points. However, as the process of Bragg grating writing requires a highly photosensitive fiber, this laser structure is consequently limited to a few wavebands with special fiber composition and architecture [34–36]. Moreover, the UV exposure of the gain medium during grating fabrication would cause excited-state lifetime quenching and thus the degradation of the laser output performances [37].

Another typical structure of single-frequency fiber laser is the traveling-wave ring or loop cavities, which employs a lengthened cavity, as well as a narrower band-limiting device than FBG [38]. As shown in Fig. 2.13, an extra unpumped active fiber is used as the saturable absorber; when the laser light interferes with the reflected light, the resulted interference pattern would induce standing wave saturation effects and thus a transient band-pass grating filter in the fiber. This self-writing filter generally has a bandwidth of several tens of MHz, and its center frequency tracks the lasing mode and thus guarantees stable single-frequency operation [39, 40]. Moreover, the traveling-wave operation eliminates the spatial hole burning effect that might be serious in the linear DBR and DFB lasers. Owing to the long cavity length, it is convenient to insert a passive tunable filter in the ring cavity to provide coarse wavelength selective and, accordingly, a considerably wide tuning range [41–43]. Despite the notable advantages, the shortcomings of the ring cavity fiber lasers is also apparent, e.g., the laser slope efficiency is rather low due to the large loss introduced by the excessive optical elements, and most importantly, the lasing mode tends to be unstable as a result of the high sensitivity of the ring fiber cavity to the temperature drift and other external disturbances [43].

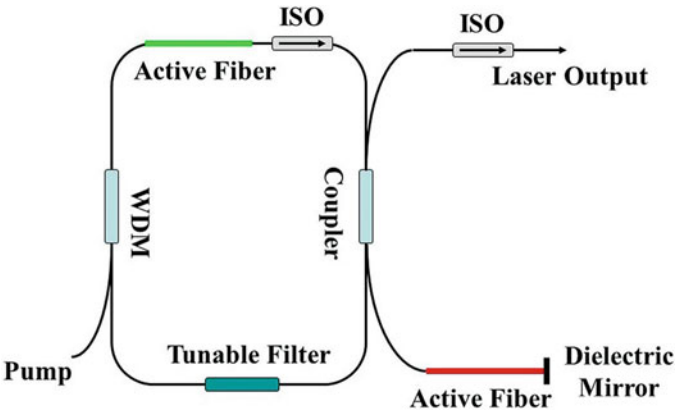

Fig. 2.13 Schematic setup of the typical ring cavity fiber laser

2.3.2 Other Schemes to Achieve Single-Frequency Lasing

Based on the abovementioned typical cavity configurations, there are in fact various practical variants to realize single-frequency laser. The straightforward guideline is to develop filter components as narrow as possible to guarantee only one longitudinal mode to survive, without considering the actual cavity length. A Sagnac loop mirror incorporated with interference-induced saturable-gain or saturable-absorber grating was proven to be an effective substitution to the NB-FBG in DBR cavities [40, 44–46]. A different loop combined with an extremely low reflectivity FBG was demonstrated as a slow-light cavity mirror in Ref. [47], where single longitudinal mode with sub-kilohertz linewidth was achieved. FP filter formed by cascading two NB-FBGs is also a practical candidate for extracting single laser mode [48, 49]. Recently, a novel FP structure built with the splicing point between a hollow-core photonic bandgap fiber (HC-PBF) and a single-mode fiber and a gold-coated end of a microfiber as the two reflection facet was reported to be used as a mode selecting device in a wide wavelength range [50]. To reduce the extra loss that is introduced by the FP cavity, H. Wan et al. demonstrated a tandem Fabry-Pérot architecture, which is constructed by cascading FP micro-cavities formed via making a narrow adjustable air gap between two vertical cleaved fiber ends, to filter out single longitudinal mode [51]. As to the FBGs, endeavors are also dedicated to narrow its bandwidth. Equivalent phase-shifted FBG (EPS-FBG) is such a grating that phase shifting is introduced by only changing several selected sampling periods of a sampled fiber Bragg grating. X. Chen et al. [52] reported an EPS-FBG with an estimated transmission bandwidth of 0.02 pm and obtained single-frequency operation in a fiber ring cavity with the help of this EPS-FBG. A similar configuration was subsequently implemented to realize dual-wavelength single longitudinal mode laser, by fabricating EPS-FBG with dual-transmission bands [53]. Very recently, a polarization-maintaining chirped moiré FBG (CM-FBG) which possesses an ultra-narrow bandwidth of 0.1 pm was utilized to enable a dual-wavelength single-polarization single-frequency ring cavity laser [54]. Followed closely the same research group reported the use of a structured chirped FBG (SC-FBG) to obtain stable single longitudinal mode linear cavity fiber laser [55]. Interestingly, a narrow filter based on two uniform FBGs was demonstrated in [56, 57], where the authors managed to achieve a narrow spectral overlapping between the two FBGs with steep side slopes and realized single-frequency lasing in a DBR and ring cavity structure. At last, in addition to the abovementioned approaches, saturable absorbers based on newly developed materials are also considered by researchers. In 2012, multilayer graphene was reported to be used as saturable absorber in a conventional single-frequency fiber ring laser [58]. Subsequently, a new topological insulator Bi_2Te_3 saturable absorber was also demonstrated to realize a single longitudinal mode fiber ring laser [59].

Another scheme is the compound cavity structure, which is composed of two or more sub-cavities and allows only one laser mode that satisfies the resonate

conditions of all the sub-cavities to oscillate. To this end, the sub-cavities should be asymmetric with each other, that is, configured with different cavity length, and then the effective FSR of the laser would be extended. A representative example is to arrange more than two uniform FBGs with optimized parameters in a linear layout to form sub-cavities with different length [60, 61]. Somewhat different structure has been demonstrated by Y. Zhao et al. in [62], where a π-phase-shifted FBG was inserted into a DBR laser to suppress multi-longitudinal modes. Multi-ring cavity is another common choice; in the last over 10 years, there are many reports on this subject [63–72]. In principle, compound cavity structure can also be a filter element itself; see, for example, recently published works [73]. Actually, compound cavity filtering has also been employed in Brillouin fiber lasers [74, 75], to extract single-frequency component from commercial semiconductor lasers. Details about the principle of Brillouin fiber laser are introduced in Chap. 4. It should be supplemented here that a compound cavity with each sub-cavities working at different wavelengths can also realize single-frequency working, due to the interaction of the laser light from different channels [76–78].

Finally, researchers have found an unusual method to achieve SFFLs based on stimulated Rayleigh scattering (STRS) in recent years. Unlike the Raman and Brillouin scattering, Rayleigh scattering is recognized as an elastic scattering process, which is caused by the random fluctuations of the density in the fiber core [79]. Systematic experimental studies have found that the bandwidth of STRS is about 10 kHz, the threshold power is 6–10 dB lower than that of stimulated Brillouin scattering (SBS), while the Rayleigh gain coefficient is about two orders smaller than that of SBS [80]. Therefore, the STRS effect would be beneficial for achieving narrow linewidth single-frequency fiber laser. Nevertheless, the low-gain coefficient of STRS makes it difficult to be observed, owing to the presence of SBS. However, the solution is actually uncomplicated, that is, changing the shape of the fiber core and cladding and thus destroying the propagation of the acoustic waves which are indispensable for SBS [81–83] or just utilizing a tunable optical band-pass filter with a narrow bandwidth to block the SBS signal [81, 84]. In these works, the STRS is incorporated into the laser cavity via a fiber circulator, and the obtained laser linewidth is kHz or even sub-kHz level.

By and large, there exist various methods or devices to construct SFFLs and would also be emerging more new choices for researchers in this field. It should say that many of the techniques benefit the single longitudinal mode operation in cases where the length of the resonating cavity is too long. However, for the sake of practical applications, most of the proposed schemes are rather complicated and costly and even susceptive to environmental disturbances such as mechanical, thermal, and acoustical fluctuations. It can be concluded that the key factor to realize a simple and compact single-frequency laser with high performance is the development of high-gain active fiber, which could shorten the effective cavity length and thus alleviate the requirement for narrow bandwidth filter. This is the main subject of the next chapter. Additionally, the cavity structures discussed in this section also apply to fiber nonlinear lasers, which are discussed in Chap. 4.

2.4 Single-Frequency Fiber Laser Design with Advanced Performances

Nowadays, there are various methods and techniques to realize single-frequency operation of fiber lasers; however for practical applications many works still need to be done to achieve optimized or customized performances. Here we select some topics from the previous works of our group, to roughly disclose recent progress in this field. These works are all carried out on the basis of short-cavity DBR SFFL, which is recognized as a stable and reliable laser source for various applications.

2.4.1 Linearly Polarized Operation

Generally, the output of an SFFL consists of two orthogonal linearly polarized modes, which can be separated apart from each other when transmitting in a birefringent medium. This would be harmful to applications such as interferometric fiber sensors, as any birefringence effect in the system will induce confusion of the interrogating signal. In addition, applications like nonlinear frequency conversion also require that the pumping lasers are linearly polarized in a stable direction of polarization.

To realize linearly polarized operation of SFFL, different schemes have been proposed, e.g., use an intracavity polarization controller, introduce some pressure or a polarization-dependent phase shift to the laser, and employ particularly designed fibers such as fiber of special geometry [34, 85]. Nevertheless, all of these schemes tend to be inconvenient and difficult to control a stable single-polarization operation. A more desirable method is to make use of the polarization-maintaining fiber Bragg grating (PM-FBG), which is fabricated via writing the grating fringe on a polarization-maintaining single-mode fiber. By intentionally introducing a systematic linear birefringence into the fiber, two orthogonal polarization modes will be induced and propagate along the PM fiber with distinct phase velocities, corresponding to the slow and fast axis. When a linearly polarized light is launched into the PM fiber with its polarization direction aligns with one of the propagation modes, its polarization property will be maintained throughout the transmission. Otherwise, the two propagation modes of the PM fiber will be excited and result in an elliptically polarized light after transmission. Accordingly, the reflectance spectrum of PM-FBG also has two peaks, caused by the two polarization modes. In this way, the PM-FBG can be exploited to construct a linearly polarized SFFL via substituting the NB-FBG in Fig. 2.11. The key requirement is that only one reflectance peak of the PM-FBG is overlapping with that of the BB-FBG, as shown in Fig. 2.14. In this way, there will be only one polarization mode oscillating in the laser cavity. With this configuration, robust single-polarization SFFLs have been demonstrated at both 1.0 μm [86] and 1.5 μm [87] bands.

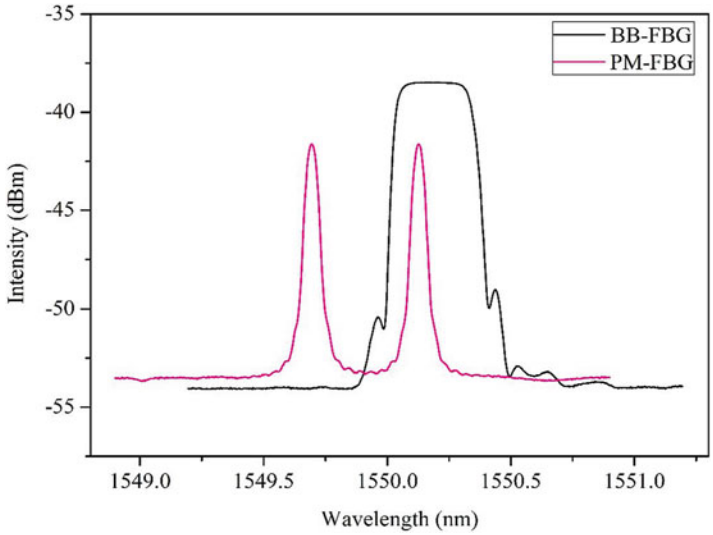

Fig. 2.14 Reflectance spectra of a PM-FBG and a BB-FBG against ASE source

2.4.2 Linewidth Suppression

Generally, the linewidth of a well performed SFFL is about several kHz, and this is actually a major merit that makes this type of laser attractive to applications such as high precision sensing and measurements. Nevertheless, one should keep in mind that a laser source with narrower linewidth will definitely improve the application performances to an unreached level and even find new applications that have never been considered. Although presently researchers can achieve Hz level or even narrower laser spectrum via active feedback control, the system is rather complex and cumbersome [88, 89]. It is then necessary to develop laser linewidth suppression schemes that can maximumly retain the simplicity of SFFLs and is robust and portable for various application needs. In addition, an SFFL with sub-kHz linewidth is also a delightful achievement.

Here we introduce a fiber laser design with a short-linear cavity incorporated with a virtual-folded-ring (VFR) resonator and an FBG Fabry-Perot (FBG-FP) filter, as shown in Fig. 2.15. The laser cavity is pumped by a laser diode (LD) via a polarization-maintained wavelength division multiplexer (PM-WDM), while the laser signal is coupled out through another port of the PM-WDM and a polarization-maintained isolator (PM-ISO). The inset of Fig. 2.15 demonstrates the explosive diagram of the short-linear cavity, which is in fact constructed by inserting the FBG-FP into the VFR resonator. A narrowband PM-FBG (PM-NB-FBG) and a high-reflection PM-FBG (PM-HR-FBG) are fusion spliced with 0° bias angle and used as the output coupler and mode selecting element. The reflectance peak of the fast axis of PM-NB-FBG is configured to coincide with that of the slow axis of

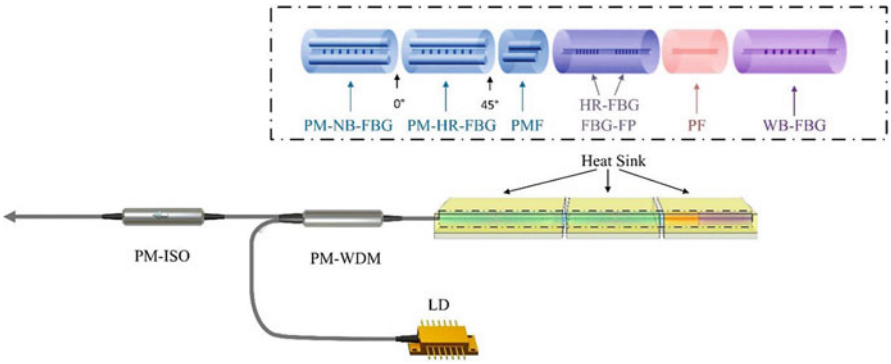

Fig. 2.15 Schematic drawing of the fiber laser design with a short-linear cavity incorporated with a VFR resonator and an FBG-FP filter. Inset: explosive diagram of the short-linear cavity. (Reprinted from Ref. [92], copyright 2014, with permission from OSA Publishing)

PM-HR-FBG. A short piece of PM fiber is fusion spliced to the PM-HR-FBG with a bias angle of ~45° to serve as a fiber-based quarter-wave plate (QWP). Then a segment of active fiber (here it is Er^{3+}/Yb^{3+}-codoped phosphate fiber, PF) and a high-reflection wideband FBG (WB-FBG) are successively connected to the system via fusion splicing, and in this way a VFR resonator is formed.

Without loss of generality, assuming a clockwise circularly polarized wave travels rightward in the PF, it will be changed to anticlockwise circularly polarized wave after being reflected by the WB-FBG, which acts as a half-wave plate. The leftward traveled wave will then become linearly polarized with polarization direction aligning with that of the PM-HR-FBG after passing through the QWP. The readily reflected wave will become anticlockwise circularly polarized wave after passing through the QWP again. Subsequently, it will turn into a clockwise circularly polarized wave after being reflected by the WB-FBG and become linearly polarized with polarization direction aligning with that of the PM-NB-FBG. Finally, the partially reflected wave will be clockwise circularly polarized after experiencing the QWP, and thus a "round trip" in the resonator is finished. Consequently, the effective cavity length of the laser cavity has become twice its physical length. In this way, the rightward and leftward traveled waves in the active fiber have orthotropic polarization directions and avoid the formation of the interference pattern. This will eliminate the harmful spatial hole burning effect in the cavity and suppress the laser linewidth via reducing the frequency noise induced by spatial hole burning. The VFR resonator was explored in Ref. [90], in which sub-kHz laser linewidth was achieved at 1.5 μm.

Considering the FBG-FP filter, it is formed by fusion splicing two highly reflective FBGs (HR-FBGs) with properly designed distance and can be regarded as a slow-light assembly. Owing to the multi-reflect effect, the effective photon lifetime will be extended in the FBG-FP cavity. Therefore, the effective length of a laser cavity will also be lengthened when added with an FBG-FP filter. As the magnitude of the fundamental thermal noise and 1/*f* frequency noise in SFFLs is

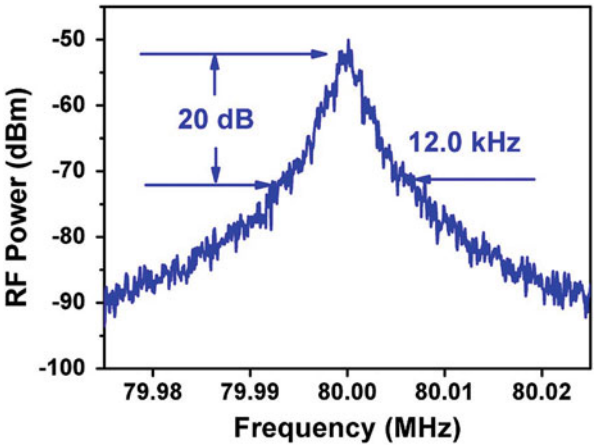

Fig. 2.16 Line shape of the heterodyne signal measured with 97.6 km fiber delay. (Reprinted from Ref. [92], copyright 2014, with permission from OSA Publishing)

inversely proportional to the efficient cavity length, then a slow-light SFFL will principally have reduced frequency noise and corresponding narrower linewidth [16, 17]. Moreover, with increased photon been stored inside the laser cavity, the ASE effect and thus the correspondingly induced linewidth broadening will be weakened. A proof-of-concept demonstration has been carried out in Ref. [91], where a slow-light fiber laser with sub-kHz linewidth was constructed by using an FBG-FP filter as one of the cavity mirrors.

Now it is evidenced that the VFR resonator and the FBG-FP filter are both advantageous to linewidth suppressing of SFFLs. Intuitively, a VFR resonator associated with an FBG-FP filter should be an attractive scheme for single-frequency laser operation with ever narrower linewidth. This was demonstrated in Ref. [92], in which the authors have experimentally verified that the FBG-FP has little effect on the polarization state of the light waves transmitting in the VFR resonator. Figure 2.16 shows the measured heterodyne signal of the laser output with 97.6 km fiber delay, and an estimated laser linewidth of about 600 Hz was achieved.

2.4.3 Frequency and Intensity Noise Suppression

For SFFLs, its noise properties are generally regarded as key performances that determine its applications. In fields such as coherent optical communication, sensing, spectroscopy, and metrology, where the laser noise properties are the most of concern, it is essential that the SFFLs are improved with lower noise. For example, in fiber optical sensing, laser noise would mix with the probe signal and deteriorate the detection resolution and sensitivity. At present, many techniques have been developed to respectively suppress the frequency and intensity noise of single-frequency laser. A common feature of these techniques is that the noise suppression process is realized by implementing an active feedback control. Commonly, the laser

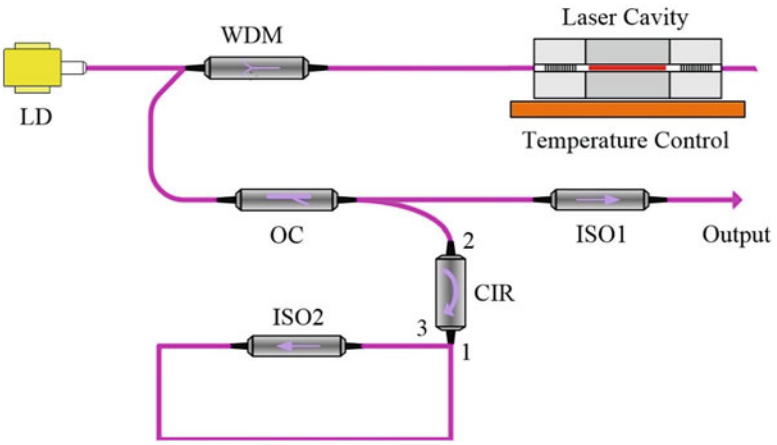

Fig. 2.17 Experimental setup of the self-injection locked SFFL

frequency noise is suppressed via adjusting the laser cavity length with a PZT stretcher driven by error signal that is acquired by comparing the laser frequency with atomic/molecular absorption lines or resonance frequency of a high-stable resonator [93, 94]. While for intensity noise, it can be reduced by changing the current of the pump laser or directly modulating the amplitude of the field of the laser light based on the noise signal detected by a PD [95]. However, the electronic serve system involved in these feedback systems inevitably limits the bandwidth of noise suppression to be less than 1 MHz and even introduces extra electronic noise to the feedback loop.

In this section, we mainly discuss passive noise suppression schemes with the exemption of the electronic part, i.e., all-optical noise suppression. A well-developed frequency noise suppression technique is coherent optical feedback from an external stable high-quality (Q) factor passive resonator to the laser cavity – self-injection locking. The generally employed external resonators are whispering-gallery-mode (WGM) resonators and high-finesse FP cavities [96, 97]. The actual mechanism for the noise suppression is that the self-injection process provides fast optical feedback to the laser cavity. When the optical signal from the external resonator is injected into the laser cavity, the frequency noise of the injecting signal would interfere destructively with the local signal, and in this way the laser frequency noise can be significantly reduced. Nevertheless, the WGM- and FP-based self-injection locking scheme involves complex and vulnerable free-space part and can hardly be widely applied.

For SFFLs, the self-injection locking scheme can be simply implemented in an all-fiber configuration, as shown in Fig. 2.17. The temperature-controlled DBR cavity is constructed by fusion splicing a partially reflective NB-FBG and a highly reflective BB-FBG on both end faces of a segment of RE ions doped fiber, respectively. An LD is used to backward pump the cavity, in which the generated single-frequency laser is coupled out via the NB-FBG and WDM. A small part of the laser

signal is split and launched into a fiber loop formed by connecting the port 1 and port 3 of an optical circulator (CIR) with an optical isolator (ISO2), which is used to guarantee unidirectional transmission of the laser light. The remainder of the laser signal from the OC is then outputted through another isolator (ISO1). It is clear that the split signal is partly injected into the laser cavity via the NB-FBG after transmitting through a cycle that includes the WDM, OC, CIR, and ISO2. In this sense, the CIR loop together with the NB-FBG forms an external resonator to the laser cavity. The Q factor of this external resonator can be estimated based on the following formula:

$$Q = 2\pi\nu\frac{nL}{\delta C} \tag{2.21}$$

where ν is the laser frequency, n is the refractive index of the fiber, L is the fiber path length (FPL), δ is the single-pass loss factor, and C is the speed of light in vacuum.

We have demonstrated a self-injection locked SFFL based on heavily Er^{3+}/Yb^{3+}-codoped fiber at 1.5 μm, with the reflectance coefficient of the employed NB-FBG to be 60% and the splitting ratio of the OC to be 1:9. The total FPL of the external resonator was measured to be 14.5 m, and the single-pass loss factor was estimated to be 0.78 with neglecting of the extra transmission loss in the single-mode optical fiber. According to Eq. (2.21), the calculated value of the Q factor is about 1.1×10^8. We also extended the length of the fiber loop in the CIR by 24 m, for the sake of comparing. Thus the total FPL was increased to 38.5 m, and the corresponding Q factor is calculated to be 2.9×10^8. To examine the self-injection locking performances of the fiber laser, the laser frequency noise spectra under different conditions were measured by an unbalanced Michelson interferometer with 100 m OPD, and a PGC scheme was employed to reduce the random phase shift in the interferometer and demodulate out the frequency noise.

Figure 2.18 demonstrates the measured frequency noise spectra from 0.1 to 25 kHz. The results show that the frequency noise of the fiber laser was reduced by self-injection locking at frequencies higher than 1 kHz, while the reduction at lower frequencies was not obvious. The acoustical noise of environment is considered to be the dominating noise source at frequencies below 1 kHz, and the spectral peaks present at frequencies from 1 to 10 kHz are also attributed to acoustical pickup. The maximum reduction of the frequency noise at around 10 kHz is 12 dB with FPL of 14.5 m and over 20 dB with FPL of 38.5 m. The frequency noise suppression was also verified by separate measurement of the laser linewidth, which was reduced from 1.4 kHz at the free-running condition to 760 Hz when self-injection locked with FPL of 14.5 m and to 690 Hz when self-injection locked with FPL of 38.5 m. Further increasing the FPL will result in a larger Q factor, and consequently lower frequency noise as well as narrower linewidth can be achieved. It should be noted that when using longer FPL, the laser system would be more susceptive to external interferences, as indicated in Fig. 2.18.

It is then necessary to examine the intensity noise properties of the self-injection locked laser. Figure 2.19a shows the RIN spectra recorded from 0 to 4 MHz by an

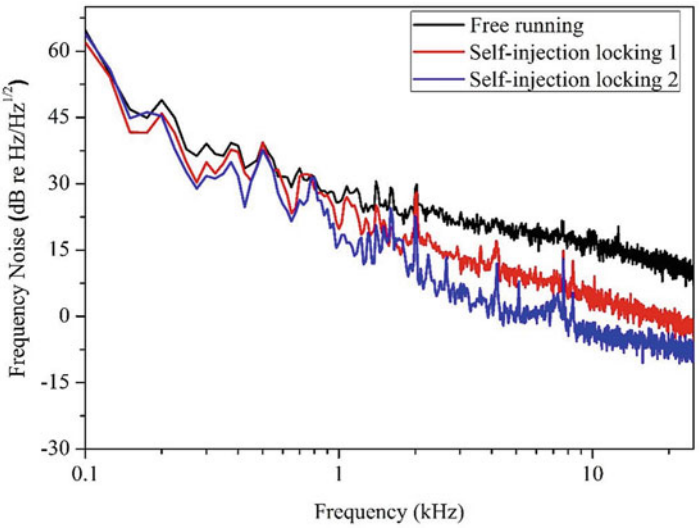

Fig. 2.18 Frequency noise spectra of the free-running and self-injection locked fiber laser: Self-injection locking 1, 14.5 m; self-injection locking 2, 38.5 m

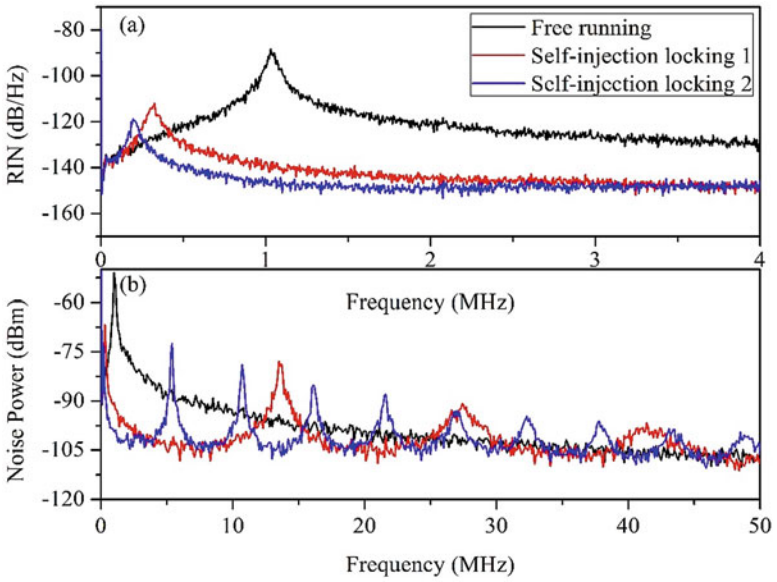

Fig. 2.19 (**a**) RINs of the free-running and self-injection locked fiber laser; (**b**) intensity noise spectra of the free-running and self-injection locked fiber laser from 0 to 50 MHz

RF SA with bandwidth resolution of 1 kHz. It is observed that the relaxation oscillation frequency of the laser shifted from about 1 MHz to 320 kHz and 200 kHz for self-injection locking FPL of 14.5 and 38.5 m, respectively. The corresponding relaxation oscillation peak was reduced from −90 dB/Hz to −113 dB/Hz and − 120 dB/Hz; thus a maximum reduction of 30 dB was achieved. In addition, the amplitude of the RIN was approaching the noise floor of −149 dB/Hz at the frequency of 3 and 1 MHz for the two self-injection cases, respectively. To examine the noise behavior of the laser at higher frequencies, the noise spectra spanning at 0–50 MHz were also measured, as shown in Fig. 2.19b. Interestingly, there arose a series of gradually weakened harmonic peaks in the noise spectra of the two self-injection locked lasers, and the harmonic frequencies were, respectively, 14 and 5.4 MHz, which happen to be the FSR of the 14.5 and 38.5 m long external resonator. However, it is clear that there was only one longitudinal mode in the laser output; thus these harmonic peaks should not be the beating of the multimode laser.

To find out the origin of these harmonic peaks, here we propose a simple recursion model of the intensity noise spectrum to phenomenologically explain the observed phenomena. Without loss of generality, assume the time domain expression of the laser intensity noise to be:

$$f(t) = A^2 e^{-t/10} \tag{2.22}$$

in which A is the amplitude of the intensity noise. Considering the intensity noise is directly weighted superimposing with its delayed replica in the self-injection locking process, and then the final intensity noise should be written as:

$$f_n(t) = 0.99 f_{n-1}(t) + 0.01 f_{n-1}(t - \tau) \tag{2.23}$$

where τ is the time delay of the external resonator. The weight numbers in Eq. (2.23) are selected to facilitate the following simulation. When the FPL of self-injection locking resonator is 38.5 m, i.e., τ is 0.13 μs, $f_n(t)$ is iteratively calculated and Fourier transformed, and the results are shown in Fig. 2.20. Also shown in the figure are the measured intensity noise spectrum of the self-injection locked laser and the initial condition of the simulation, that is, the Fourier transformation of $f_1(t)$. It can be seen that the simulated curve agrees well with the measured results. As the frequency spacing of the noise harmonic peaks is uniquely determined by the fiber delay, say, the FSR of the external resonator, thus the position of the peaks in the simulated and measured curves strictly coincide. Regarding the peak power, it is found that although both the simulated and measured curves manifest the trend of gradual descending, the actual magnitude of the individual peaks is not strictly matched, especially at low frequencies. This is attributed to the imperfection of the initial intensity noise model, as for the sake of simplicity the relaxation oscillation is not reflected. However, it does not affect in obtaining a qualitative understanding of the

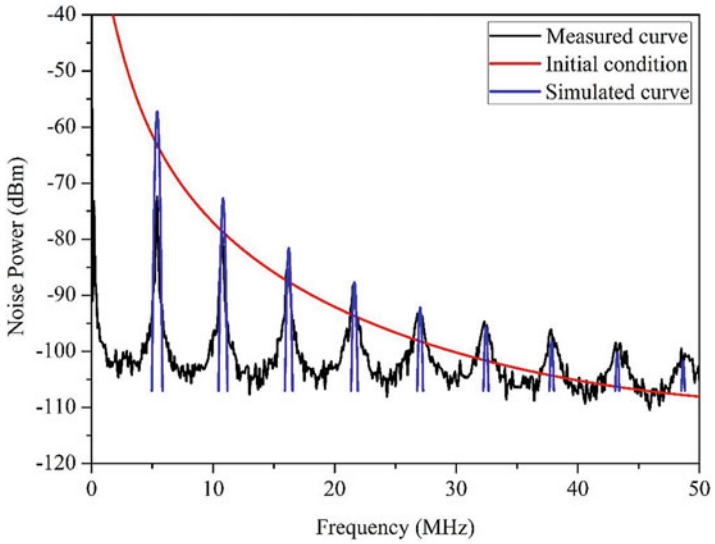

Fig. 2.20 The simulated intensity noise spectrum of the self-injection locked fiber laser with FPL of 38.5 m; also shown are the measured spectrum and the initial condition of the simulation. The intensity noise amplitude A is adjusted to match with the measured results

current issue. In a self-injection locked fiber laser, the injecting signal would interact with the local signal in the laser cavity to produce a new signal, which has an intensity noise that can be regarded as the weighted superimposition of the intensity noise of the two interacting signals. When a stable self-injection locked laser is established, the noise power of the initial laser tends to transfer to a series of harmonic peaks. In this way, in the case of a larger FSR and fewer harmonic numbers, each of the harmonic peaks tends to be wider than that in the case of small FSR and more harmonic number, as indicated in Fig. 2.19b. In addition, it should be noted that the actual signal-to-noise ratio of the simulated harmonic peaks is much larger than the measured results (in order to make the comparison clear, the part of simulation curve below −107 dBm is not shown in Fig. 2.20). This is because there exists a noise floor set by the shot noise in a real fiber laser.

It is concluded that although self-injection locking can significantly suppress the frequency noise of single-frequency laser, it will inevitably introduce harmonic peaks to the intensity noise spectrum and render the laser source disadvantageous for applications. One solution is to increase the FSR of the external resonator and alleviate the effect of the harmonic noise peaks via shifting it to higher frequencies. However, the frequency noise suppression will be compromised as a larger FSR corresponds to a smaller Q factor of the external resonator. It is then desirable to directly suppress the noise peaks of the self-injection locked SFFL. Before that, here we first discuss the all-optical intensity noise suppression scheme for single-frequency laser on the basis of nonlinear amplification of optical amplifiers. When working in the saturation regime, an optical amplifier tends to magnify the

continuous component in a higher rate than that of the temporally varying component, leading to a reduced RIN of the amplified laser. Unfortunately, owing to the long lifetime of the stimulated ions, the general RE ions doped fiber amplifiers can only reduce laser intensity noise at frequencies less than 1 kHz [98]. Another alternative is to utilize the semiconductor optical amplifier (SOA), which has nanosecond level of carrier lifetime, corresponding to a noise reduction bandwidth of up to GHz [99]. Via simply launching the single-frequency laser into a SOA with proper driven current and input power, the RIN of the amplified laser will be reduced (typically within 20 dB). Moreover, theoretical and experimental analyses have shown that SOA only increases the laser frequency noise at high RF frequencies and thus has neglect effects on the linewidth [100]. The main disadvantage of SOA is that it would introduce significant ASE to the laser field and deteriorate the signal-to-noise ratio (SNR) of the laser. Even so, the extra ASE can be easily removed by utilizing band-pass filters such as FBG.

It is worth noting that the intensity noise of single-frequency laser can be successively reduced by passing through cascaded SOAs, thanks to the passive noise suppression mechanism of SOA, i.e., without involving of the noise discrimination and electronical feedback control. In optoelectronic feedback suppression of laser intensity noise, the noise suppression extent is limited by the stability of the electronic serve system. Ref. [101] demonstrated significant intensity noise suppression of a SFFL with the help of two cascaded SOAs, which are commercially available InP/InGaAsP multiple-quantum-well-layer single-pass traveling-wave amplifiers (Thorlabs BOA1004S). The ASE brought in by the SOAs was filtered out by using a CIR associated with a BB-FBG with 3 dB bandwidth of 1 nm. Figure 2.21 shows the intensity noise spectra of the fiber laser before and after the amplification of the cascading SOAs. The input signal power of each SOA was adjusted to 1 mW by using an ATT, respectively. From the figure, the laser intensity noise has been considerably reduced after experiencing each SOA in a frequency bandwidth of 50 MHz, and a total maximum reduction of about 30 dB has been achieved at around the relaxation oscillation peak. Besides the noise peak that was restricted in a considerable narrowband, the laser noise has roughly approached the noise floor of the measurement. One can infer that the remaining noise peak can be further suppressed to the floor by passing through enough SOAs.

Now, it is concluded that besides the traditional electronic feedback control, the frequency and intensity noise of SFFL can be significantly suppressed in an all-optical manner, respectively. Additionally, the noise suppression bandwidth can be extended to a much higher frequency in the all-optical system. Nevertheless, it should be keep in mind that in the self-injection locking of the SFFL, there is compromise to the frequency noise suppression, i.e., the appearance of harmonic noise peaks in the intensity noise. Theoretical analysis has found that these noise peaks are attributed to the iterative interaction of the injecting and the intracavity light, and then it would be helpful to incorporate the SOA into the self-injecting path to suppress the intensity noise peaks. This work was demonstrated in Ref. [102], where a SOA was inserted into the CIR fiber loop of the external resonator in the self-injected laser, as shown in Fig. 2.22. Moreover, another circulator (CIR2)

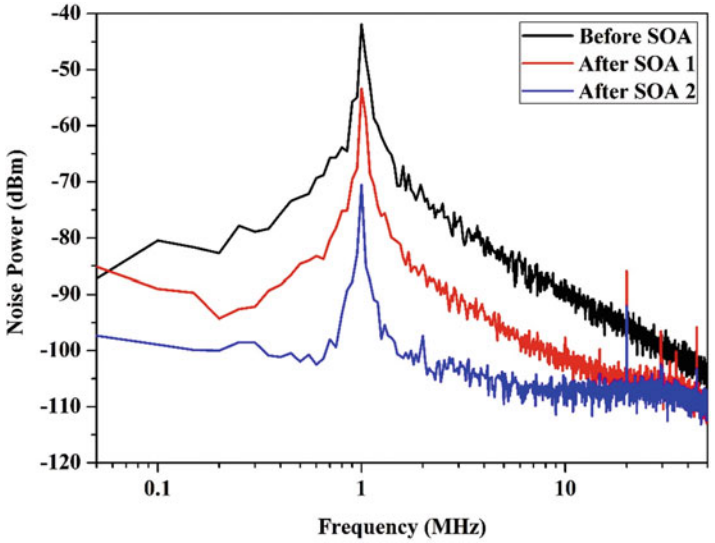

Fig. 2.21 Intensity noise spectra of the fiber laser before and after the amplification of the cascading SOAs. (Reprinted from Ref. [101], copyright 2015, with permission from IOP Publishing)

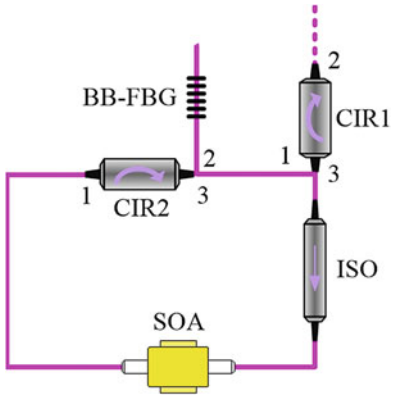

Fig. 2.22 Experimental configuration of incorporating a SOA into the CIR fiber loop of the external resonator in the self-injected laser

together with a BB-FBG (3 dB bandwidth of 1 nm) was also added into the fiber loop to get rid of the unwanted ASE that is generated by the SOA.

By substituting the fiber loop in Fig. 2.22 to that of the self-injection locked laser shown in Fig. 2.17, keeping the FPL of 38.5 m, and changing the splitting ratio of the OC to 1:99, Ref. [102] has achieved simultaneous laser frequency and intensity noise suppression in a remarkably wide frequency range. Figure 2.23 shows the measured

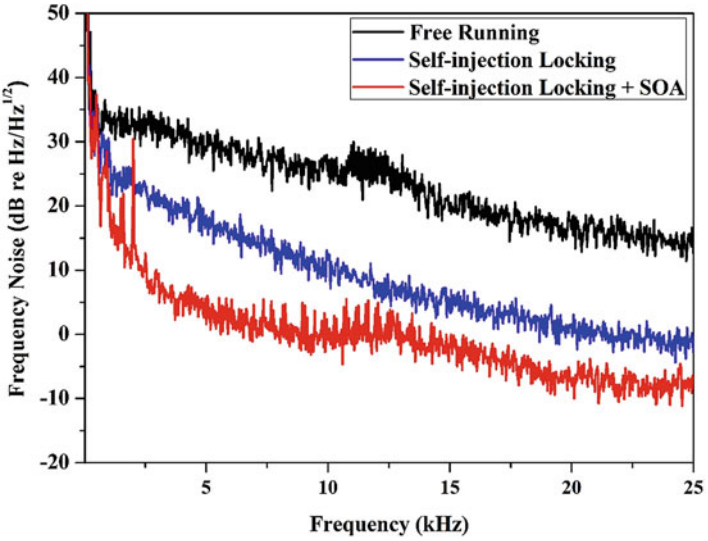

Fig. 2.23 Measured frequency noise spectra of the fiber laser. (Reprinted from Ref. [102], copyright 2015, with permission from OSA Publishing)

laser frequency noise spectra at the condition of free-running, self-injection locking, and self-injection locking associated with SOA, respectively. From the figure, a maximum reduction of about 15 dB to the frequency noise was realized by self-injection locking, and with the incorporating of the SOA, further reduction of 10 dB was achieved. Separate measurements have shown that the laser linewidth has been correspondingly suppressed from 3.5 kHz to 1.1 kHz and 700 Hz. The contribution of SOA to the laser frequency noise and thus linewidth suppression is attributed to its compensation to the transmission loss of the injecting signal. According to Eq. (2.21), a lower single-pass loss factor will result in a higher Q factor of the external resonator.

Regarding the intensity noise, the spectra were also measured under the corresponding conditions, as shown in Fig. 2.24. Also shown in the figure is the noise floor of the measurement system for comparison. It can be seen from the figure that the harmonic noise peaks induced by the recursion dynamics of laser light in the self-injection locking process have all been effectively suppressed. In addition, it is noticed that the harmonic frequency of the residual noise peaks was slightly reduced, and the reason is that the FPL of the self-injecting signal was lengthened by the pigtail of the SOA, CIR2, and BB-FBG. Further examination has shown that the relaxation oscillation peak of the laser was shifted from 1 MHz to 320 kHz and was suppressed by about 35 dB from −90 dB/Hz to −125 dB/Hz with implementation of the SOA-incorporated self-injection locking scheme.

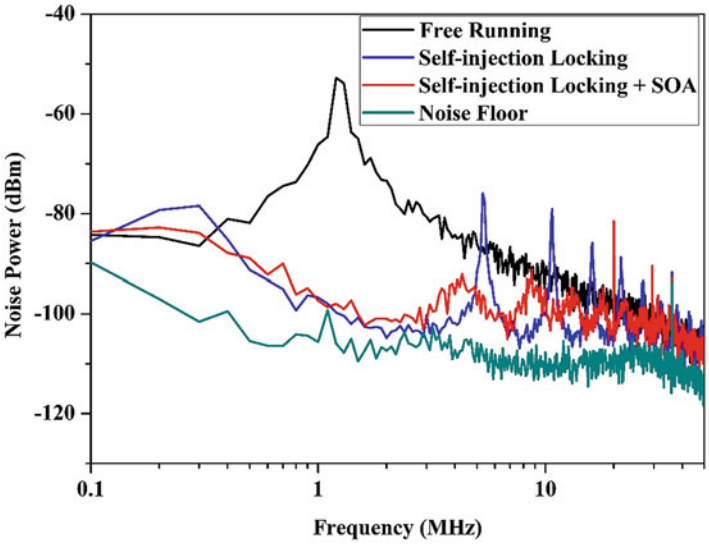

Fig. 2.24 Measured intensity noise spectra of the laser; also shown is the noise floor of the measurement system. (Reprinted from Ref. [102], copyright 2015, with permission from OSA Publishing)

2.4.4 Continuous Wavelength Tuning

Continuous wavelength tuned SFFLs with considerable narrow linewidth and low noise are advantageous for applications such as digital coherent communications and wavelength-division-multiplexing networks [103]. Additionally, SSFLs can be interrogating or sensing element itself in high precision optical sensing, which also require a high-performance tunable laser source. Commonly, the wavelength of a SFFL can be easily changed via imposing mechanical or thermal stress to the cavity. Nevertheless, the wavelength tuning range of SFFL is inherently limited by the narrow mode spacing of the cavity; that is to say, longitudinal mode hopping will inevitably take place in the tuning process. Ref. [104] developed a longitudinal-mode-selection model for short-linear-cavity SFFLs, based on the temperature dependence of the cavity components. According to the model, a short laser cavity length will result in larger longitudinal mode spacing and thus broaden the wavelength tuning range. However, this broadening extent is highly limited, as the laser output power would reduce along with the shortening of the cavity. At least, the cavity length should be long enough to provide enough optical gain to initiate the laser resonating. Then a more feasible method is to make the mode selecting element changing with the laser wavelength in the same pace. Specifically, the center reflectance peak of FBG would also shift under external stress, and it is therefore possible to avoid mode hopping by uniformly stretching or compressing the whole laser cavity. This has been successively demonstrated in Ref. [105], where the

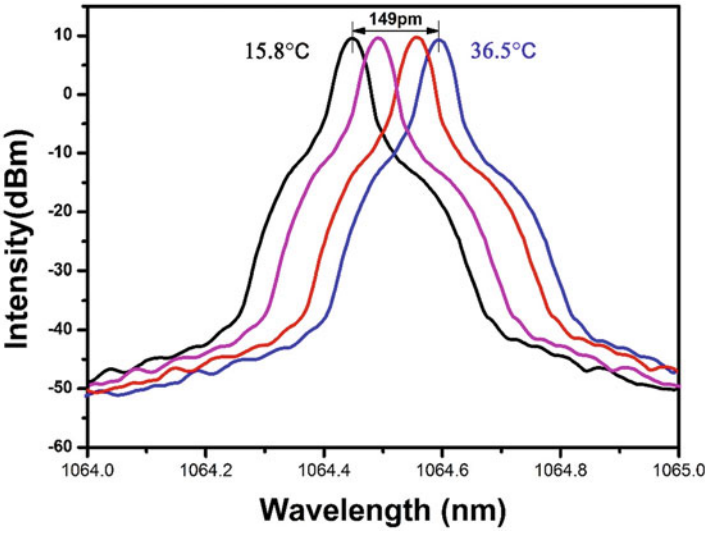

Fig. 2.25 ZC packaged DBR single-frequency fiber laser output spectra at different temperatures. (Reprinted from Ref. [104], copyright 2016, with permission from IEEE)

authors designed a uniform compressing system for a short DBR fiber laser in which the change of the reflectance peak of FBG can track that of the resonating wavelength, and continuous tuning range as larger as 32 nm was achieved. It should be noted that here all the components of the laser were based on silica fiber, which makes it feasible to uniformly stretch or compress the laser cavity. However, it would be not applicable for lasers constructed with active fiber on the basis of multicomponent soft glass fiber, e.g., phosphate fiber, which has entirely different thermal and mechanical properties with that of the silica fiber-based FBG. Then the problem still exists for this type of laser. Ref. [104] proposed to employ different packaging materials for the active fiber and FBG to minimize their thermal difference. Via utilizing zirconia ceramic (ZC) and silica capillary to, respectively, encapsulate the phosphate active fiber and silica FBG, the constructed SFFL can be thermally tuned by over 20 °C, corresponding to a continuous wavelength tuning range of >149 pm, as shown in Fig. 2.25.

Nevertheless, it is apparent that the wavelength tuning range demonstrated in Fig. 2.25 is still far less than that of the silica fiber-based SFFL. Fortunately, the phosphate laser made a comeback soon in Ref. [106], where a tunable SFFL was demonstrated based on self-injection locking, as shown in Fig. 2.26. The active fiber was a 1.5 cm long Er^{3+}/Yb^{3+}-codoped phosphate fiber, to which a high-reflective fiber-chirped grating (HR-FCG) and a low-reflective FCG (LR-FCG) were connected, respectively. The bandwidth of the HR-FCG and the LR-FCG is both 60 nm (from 1515 nm to 1575 nm), while the corresponding reflectivity is 99.9% and 60%, respectively. The DBR cavity was temperature controlled, and pumped by a 980 nm LD via a WDM, which also directed the laser signal to a 1:9 optical coupler.

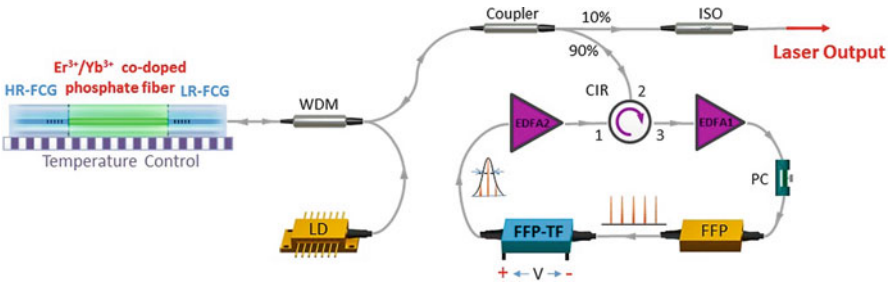

Fig. 2.26 Experimental setup of the self-injection locked tunable single-frequency fiber laser. (Reprinted from Ref. [106], copyright 2016, with permission from OSA Publishing)

Ten percent of the laser was outputted through an ISO, while the remaining 90% was launched into a CIR fiber loop. In the loop, a fiber Fabry-Perot (FFP) interferometer with FSR of 0.2 nm and bandwidth of 5 pm associated with a FFP tunable filter (FFP-TF) with FSR of 88.9 nm and bandwidth of 0.164 nm were utilized to select the resonating mode of the laser, as depicted in the Fig. A PC was inserted into the loop to adjust the polarization state of the self-injecting signal. Moreover, two erbium-doped fiber amplifiers (EDFA1 and EDFA2) were employed to provide optical gain to the fiber loop.

Under a specific pumping power, the lasing wavelength can be continuously tuned from 1527 to 1563 nm (essentially covers the whole C-band) by changing of the driving voltage of the FFP-TF without any spectral distortion, as demonstrated in Fig. 2.27. The wavelength tuning resolution is 0.2 nm, which is determined by the FSR of the FFP. The variation of the SNR of each recorded spectrum is attributed to the uneven gain of the active fiber. Separate examination has shown that the wavelength tuning was linearly related to the changing of the FFP-TF driving voltage, and the stable single longitudinal mode operation has been verified as well. Thanks to the self-injection locking configuration, the laser output manifested superior noise performances.

2.4.5 Fast Frequency Modulation

High-performance SFFLs are ideal sources for application in fiber-optic reflectometry [107] and PGC technique-based interferometric sensing [21], which further require that the laser frequency is linearly modulated. Essentially, the frequency modulation bandwidth and amplitude should be large enough to achieve the desired application performances. In single-frequency semiconductor lasers, this can be easily achieved by modulating the driving current. However, the noise performances of the laser would be significantly deteriorated in the modulating process [108]. For SFFLs, the general method is to utilize a RF signal-driven PZT to modulate its cavity length, which is linearly related to the lasing frequency. Ref. [109] reported a linearly

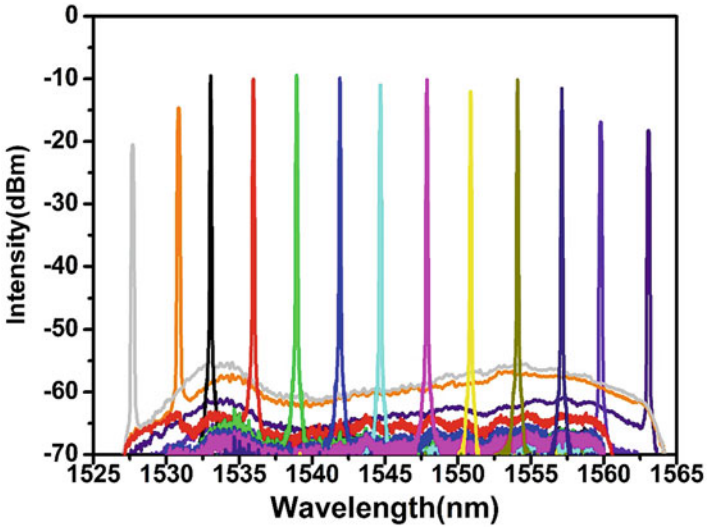

Fig. 2.27 Superimposed spectra of the tunable single-frequency fiber laser at different wavelengths. (Reprinted from Ref. [106], copyright 2016, with permission from OSA Publishing)

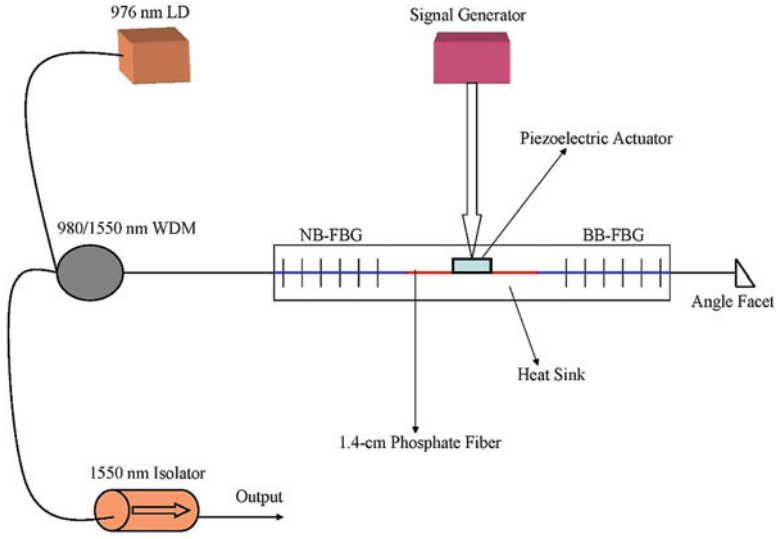

Fig. 2.28 Schematic of the piezoelectrically modulated phosphate fiber laser. (Reprinted from Ref. [109], copyright 2013, with permission from IOP Publishing)

frequency-modulated fiber laser by sticking a PZT onto the short DBR cavity, of which the configuration is demonstrated in Fig. 2.28. The employed active fiber was a segment of 1.4 cm long Er^{3+}/Yb^{3+}-codoped phosphate fiber, while the two cavity

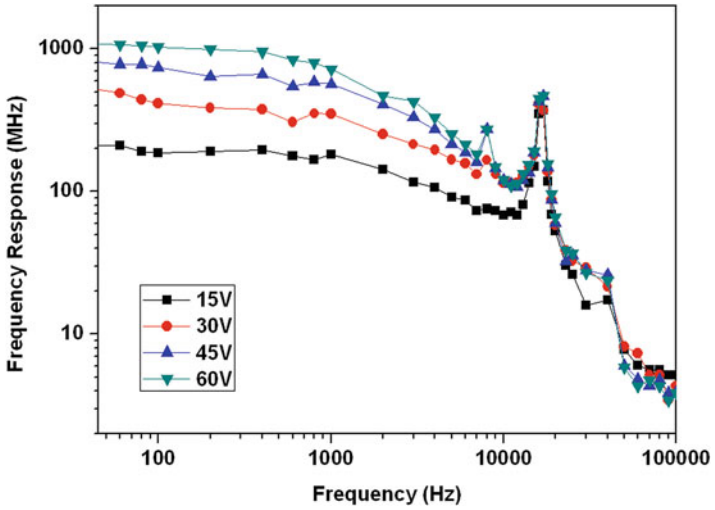

Fig. 2.29 PZT tuning response of the fiber laser as a function of modulation frequency at different applied voltages. (Reprinted from Ref. [109], copyright 2013, with permission from IOP Publishing)

reflectors were a high-reflective BB-FBG and a partial reflective NB-FBG. The idler port of the BB-FBG was ground to an angle facet to avoid reflection from the fiber end. The laser cavity was temperature controlled via embedding into a heat sink and pumped by a 976 nm LD via a WDM. The laser was ultimately outputted from an isolator, which was used to prevent the backscattering light. The frequency modulating was realized by driving a PZT that was adhesively mounted in the middle of the active fiber with a sinusoidal voltage signal provided by a signal generator.

Under a specific output power, the frequency modulating performances were examined with a scanning FP interferometer, as shown in Fig. 2.29. The figure depicts the PZT tuning response of the fiber laser as a function of the modulation frequency at different driven voltages. The frequency response range was roughly flat at modulating frequencies below 1 kHz, beyond which the response range began to decrease owing to the capacitance properties of the PZT. The two peaks at 8 kHz and 16 kHz were attributed to the mechanical resonance of the fiber laser/PZT assembly. It is observed that the laser frequency responded linearly to the modulating frequency at low frequencies until the emerging of the first resonance peak. In addition, the maximum laser frequency modulation range of 700 MHz was measured with 60 V of 1 kHz driven signal. Finally, the single longitudinal mode operation was verified with a scanning FP interferometer across the frequency modulating process. Here the large frequency response was benefited from the considerably short laser cavity, which corresponds to wide longitudinal mode spacing and facilitates the realization of a large axial strain by solely adjusting the active fiber length.

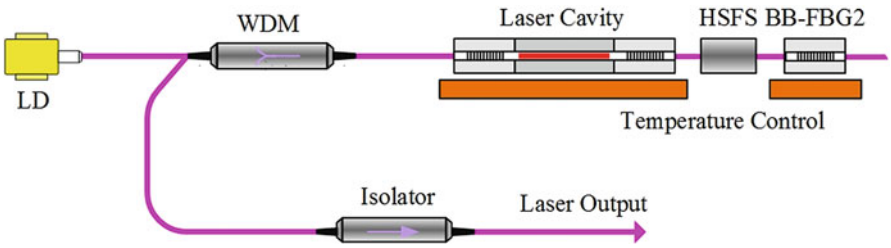

Fig. 2.30 Configuration schematic of the frequency-modulated single-frequency fiber laser. (Reprinted from Ref. [110], copyright 2016, with permission from IEEE)

Now it is clear that a large frequency modulation range of SFFLs can be realized by gluing a RF signal-driven PZT onto the center of the cavity. However, it is also apparent that the modulating frequency is confined to several kHz owing to the weak response of the PZT at higher frequencies. To address this problem, Ref. [110] proposed a novel high-speed frequency modulating scheme based on the self-injection locked SFFL. The experimental setup is shown in Fig. 2.30. The laser cavity and pumping and outputting configuration were similar with that shown in Fig. 2.29, except that the length of the active fiber was 1.5 cm long. The self-injection locking configuration was realized via connecting a BB-FBG2 with the BB-FBG1 employed in the laser cavity. The reflectivity of the BB-FBG1 and the BB-FBG2 at the center wavelength were 99.5% and 99.95%, respectively. In this way, the BB-FBG1 and the BB-FBG2 formed an external resonator to the laser cavity, while the reflectivity difference between the two BB-FBGs enables the resonator to provide optical feedback to the laser. To guarantee stale operation, both the laser cavities and the BB-FBG2 were strictly temperature controlled. Finally, a high-speed fiber stretcher (HSFS, Optiphase PZ1) with effective FPL of about 12.3 m was inserted between the laser cavity and the BB-FBG2 to modulate the laser frequency.

Figure 2.31 demonstrates the frequency modulation range of the laser at different modulating frequencies when the HSFS was driven with a sinusoidal voltage signal with peak to peak amplitude of 120 V. Again, the resonance peak of the HSFS at 58 and 143 kHz was shown up. Other than this, the frequency modulation speed of the laser has reached up to 160 kHz, which is the highest response frequency of the HSFS. Moreover, the frequency response range was verified to be approximately linearly related to the modulating voltage, and a maximum modulation amplitude of over 145 MHz was achieved at the modulation speed of 60 kHz. Finally, the merits of the self-injection locked laser were also preserved, i.e., single longitudinal mode operation, low-frequency noise, as well as narrow linewidth (estimated to be about 800 Hz). The measured intensity noise spectrum showed the same curve with that of the laser before modulation, except a series of gradually weakened harmonic peaks brought in by the modulating process.

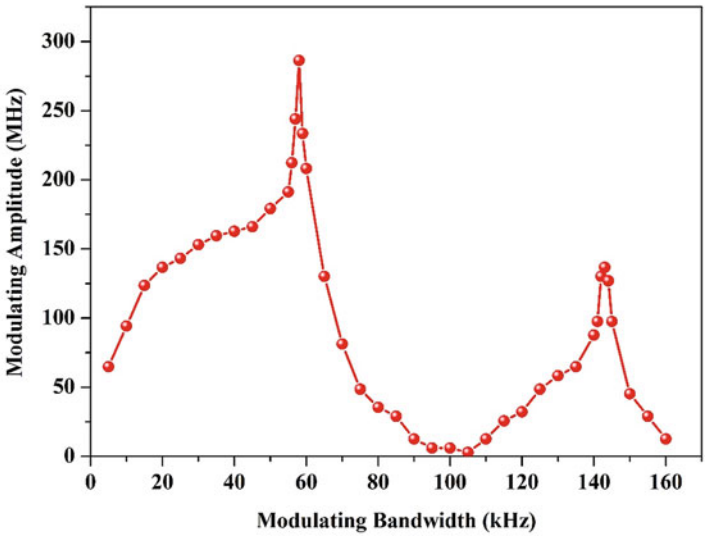

Fig. 2.31 Frequency modulating amplitude of the fiber laser versus modulating frequency with sinusoidal modulating voltage of ±60 V. (Reprinted from Ref. [110], copyright 2016, with permission from IEEE)

References

1. Koo KP, Wanser KH, Kersey AD (1995) Fibre laser sensor with ultrahigh strain resolution using interferometric interrogation. Electron Lett 31:1180
2. Kringlebotn JT, Loh WH, Laming RI (1996) Polarimetric Er^{3+}-doped fiber distributed feedback laser sensor for differential pressure and force measurements. Opt Lett 21:1869
3. Zayhowski JJ (1990) Limits imposed by spatial hole burning on the single-mode operation of standing-wave laser cavities. Opt Lett 15:431
4. Paschotta R, Nilsson J, Reekie L, Trooper AC, Hanna DC (1997) Single-frequency ytterbium-doped fiber laser stabilized by spatial hole burning. Opt Lett 22:40
5. Polynkin P, Polynkin A, Mansuripur M, Moloney J, Peyghambarian N (2005) Single-frequency laser oscillator with watts-level output power at 1.5 μm by use of a twisted-mode technique. Opt Lett 30:2745
6. Taccheo S, Laporta P, Svelto O, De Geronimo G (1998) Theoretical and experimental analysis of intensity noise in a codoped erbium-ytterbium glass laser. Appl Phys B Lasers Opt 66:19
7. Rønnekleiv E (2001) Frequency and intensity noise of single-frequency fiber Bragg grating lasers. Opt Fiber Technol 7:206
8. Cranch GA, Englund MA, Kirkendall CK (2003) Intensity noise characteristics of erbium-doped distributed-feedback fiber lasers. IEEE J Quantum Electron 39:1579
9. Foster S, Cranch GA, Tikhomirov A (2009) Experimental evidence for the thermal origin of 1/f frequency noise in erbium-doped fiber lasers. Phys Rev A 79:53802
10. Cranch GA, Miller GA (2011) Fundamental frequency noise properties of extended cavity erbium fiber lasers. Opt Lett 36:906
11. Schawlow AL, Townes CH (1958) Infrared and optical masers. Phys Rev 112:1940
12. Ball GA, Hull-Allen CG, Livas J (1994) Frequency noise of a Bragg grating fibre laser. Electron Lett 30:1229

13. Babin SA, Dmitriev AK, Dychkov AS, Kablukov SI, Lugovoy AA (2009) Low frequency noise distributed-feedback ytterbium fibre laser. Quantum Electron 39:906
14. Fourcault W, Léger J-M, Costes V, Fratter I, Mondin L (2010) Athermal fiber laser for the swarm absolute scalar magnetometer. In: International conference on Space Optics
15. Wanser KH (1992) Fundamental phase noise limit in optical fibres due to temperature fluctuations. Electron Lett 28:53
16. Foster S, Tikhomirov A, Milnes M (2007) Fundamental thermal noise in distributed feedback fiber lasers. IEEE J Quantum Electron 43:378
17. Foster S (2008) Fundamental limits on 1/f frequency noise in rare-earth-metal-doped fiber lasers due to spontaneous emission. Phys Rev A 78:13820
18. Voo NY, Horak P, Ibsen M, Loh WH (2005) Anomalous linewidth behavior in short-cavity single-frequency fiber lasers. IEEE Photon Technol Lett 17:546
19. Horak P, Voo NY, Ibsen M, Loh WH (2006) Pump-noise-induced linewidth contributions in distributed feedback fiber lasers. IEEE Photon Technol Lett 18:998
20. Foster SB, Tikhomirov AE (2010) Pump-noise contribution to frequency noise and linewidth of distributed-feedback fiber lasers. IEEE J Quantum Electron 46:734
21. Meng Z, Hu Y, Xiong S, Stewart G, Whitenett G, Culshaw B (2005) Phase noise characteristics of a diode-pumped Nd:YAG laser in an unbalanced fiber-optic interferometer. Appl Opt 44:3425
22. Stéphan GM, Tam TT, Blin S, Besnard P, Têtu M (2005) Laser line shape and spectral density of frequency noise. Phys Rev A 71:043809
23. Horak P, Loh WH (2006) On the delayed self-heterodyne interferometric technique for determining the linewidth of fiber lasers. Opt Express 14:3923
24. Tsuchida H (1990) Simple technique for improving the resolution of the delayed self-heterodyne method. Opt Lett 15:640
25. Mercer LB (1991) 1/f frequency noise effects on self-heterodyne linewidth measurements. J Lightwave Technol 9:485
26. Li C, Xu S, Xiao Y, Feng Z, Yang C, Huang X, Zhou K, Yang Z (2015) Experimental investigation on linewidth characteristics of a single-frequency phosphate fiber laser at 1.0 μm. Laser Phys 25:025103
27. Kashyap R, Armitage JR, Wyatt R, Davey ST, Williams DL (1990) All-fibre narrowband reflection gratings at 1500 nm. Electron Lett 26:730
28. Archambault J, Grubb SG (1997) Fiber gratings in lasers and amplifiers. J Lightwave Technol 15:1378
29. Guzmán-Chávez AD, Barmenkov YO, Kir'yanov AV, Mendoza-Santoyo F (2009) A narrow-line Erbium-doped fiber laser and its application for testing fiber Bragg gratings. Opt Commun 282:3775
30. Perez-Herrera RA, Chen S, Zhao W, Sun T, Grattan K, Lopez-Amo M (2010) Stability performance of short cavity Er-doped fiber lasers. Opt Commun 283:1067–1070
31. Kringlebotn JT, Archambault J, Reekie L, Payne DN (1994) Er^{3+}: Yb^{3+}-codoped fiber distributed-feedback laser. Opt Lett 19:2101
32. Nikulin MA, Churin DE, Vlasov AA, Podivilov EV (2010) Distributed feedback ytterbium fiber laser: experiment and analytical model. JOSA B 27:1414
33. Yelen K, Hickey LM, Zervas MN (2004) A new design approach for fiber DFB lasers with improved efficiency. IEEE J Quantum Electron 40:711
34. Dong L, Loh WH, Caplen JE, Minelly JD, Hsu K, Reekie L (1997) Efficient single-frequency fiber lasers with novel photosensitive Er/Yb optical fibers. Opt Lett 22:694
35. Voo NY, Sahu JK, Ibsen M (2005) 345-mW 1836-nm single-frequency DFB fiber laser MOPA. IEEE Photon Technol Lett 17:2550
36. Wong A, Chung WH, Tam HY, Lu C (2011) Ultra-short distributed feedback fiber laser with sub-kilohertz linewidth for sensing applications. Laser Phys 21:163
37. Rønnekleiv E, Hadeler O, Vienne G (1999) Stability of an Er-Yb-doped fiber distributed-feedback laser with external reflections. Opt Lett 24:617

38. Cheng Y, Kringlebotn JT, Loh WH, Laming RI, Payne DN (1995) Stable single-frequency traveling-wave fiber loop laser with integral saturable-absorber-based tracking narrow-band filter. Opt Lett 20:875
39. Xu P, Hu Z, Jiang N, Ma L, Hu Y (2012) Transient reflectance spectra of adaptive filters based on dynamic population gratings. Opt Lett 37:1992
40. Havstad SA, Fischer B, Willner AE, Wickham MG (1999) Loop-mirror filters based on saturable-gain or-absorber gratings. Opt Lett 24:1466
41. Chen H, Babin F, Leblanc M, Schinn GW (2003) Widely tunable single-frequency erbium-doped fiber lasers. IEEE Photon Technol Lett 15:185
42. Zhang K, Kang JU (2008) C-band wavelength-swept single-longitudinal mode erbium-doped fiber ring laser. Opt Express 16:14173
43. Meng Z, Stewart G, Whitenett G (2006) Stable single-mode operation of a narrow-linewidth, linearly polarized, erbium-fiber ring laser using a saturable absorber. J Lightwave Technol 24:2179
44. Yang XX, Zhan L, Shen QS, Xia YX (2008) High-power single-longitudinal-mode fiber laser with a ring Fabry–Perot resonator and a saturable absorber. IEEE Photon Technol Lett 20:879
45. Liaw SK, Wang S, Shin CS, Yu YL, Chen NK, Hsu KC, Manshina A, Tver yanovich Y (2010) Linear-cavity fiber laser using subring-cavity incorporated saturable absorber for single-frequency operation. Laser Phys 20:1744
46. Yin M, Huang S, Lu B, Chen H, Ren Z, Bai J (2013) Slope efficiency over 30% single-frequency ytterbium-doped fiber laser based on Sagnac loop mirror filter. Appl Opt 52:6799
47. Pan Z, Ye Q, Cai H, Qu R (2014) Fiber ring with long delay used as a cavity mirror for narrowing fiber laser linewidth. IEEE Photon Technol Lett 26:1621
48. Chen D, Fu H, Liu W (2007) Single-longitudinal-mode erbium-doped fiber laser based on a fiber Bragg grating Fabry-Perot filter. Laser Phys 17:1246
49. Cheng XP, Shum P, Tse CH, Zhou JL, Tang M, Tan WC, Wu RF, Zhang J (2008) Single-longitudinal-mode erbium-doped fiber ring laser based on high finesse fiber Bragg grating Fabry–Pérot etalon. IEEE Photon Technol Lett 20:976
50. Wang X, Zhu T, Chen L, Bao X (2011) Tunable Fabry-Perot filter using hollow-core photonic bandgap fiber and micro-fiber for a narrow-linewidth laser. Opt Express 19:9617
51. Wan H, Jiang W, Gong Y, Pan C, Sun X (2012) Single-longitudinal-mode fiber ring laser stabilized by tandem all-fiber Fabry-Perot micro-cavities. IEEE Photon Technol Lett 24:404
52. Chen X, Yao J, Zeng F, Deng Z (2005) Single-longitudinal-mode fiber ring laser employing an equivalent phase-shifted fiber Bragg grating. IEEE Photon Technol Lett 17:1390
53. Chen X, Yao J, Deng Z (2005) Ultranarrow dual-transmission-band fiber Bragg grating filter and its application in a dual-wavelength single-longitudinal-mode fiber ring laser. Opt Lett 30:2068
54. Yin B, Feng S, Liu Z, Bai Y, Jian S (2014) Tunable and switchable dual-wavelength single polarization narrow linewidth SLM erbium-doped fiber laser based on a PM-CMFBG filter. Opt Express 22:22528
55. Yin B, Liu Z, Feng S, Bai Y, Li H, Jian S (2015) Stable single-polarization single-longitudinal-mode linear cavity Erbium-doped fiber laser based on structured CFBG. Appl Opt 54:6
56. Rodríguez-Cobo L, Quintela MA, Rota-Rodrigo S, López-Amo M, López-Higuera JM (2013) Single-longitudinal mode laser structure based on a very narrow filtering technique. Opt Express 21:10289
57. Rodriquez-Cobo L, Quintela M, Menezo P, Lopez-Higuera J (2014) Study of fiber Bragg grating spectral overlapping for laser structures. IEEE Photon Technol Lett 26:1108
58. Muhammad FD, Zulkifli MZ, Latif AA, Harun SW, Ahmad H (2012) Graphene-based saturable absorber for single-longitudinal-mode operation of highly doped erbium-doped fiber laser. IEEE J Photon 4:467
59. Chen S, Wang Q, Zhao C, Li Y, Zhang H, Wen S (2014) Stable single-longitudinal-mode fiber ring laser using topological insulator-based saturable absorber. J Lightwave Technol 32:3836

60. Xu O, Lu S, Feng S, Tan Z, Ning T, Jian S (2009) Single-longitudinal-mode erbium-doped fiber laser with the fiber-Bragg-grating-based asymmetric two-cavity structure. Opt Commun 282:962
61. Ting F, Feng-Ping Y, Qi L, Wan-Jing P, Su-Chun F, Si-Yu T, Xiao-Dong W (2013) Stable single longitudinal mode erbium-doped silica fiber laser based on an asymmetric linear three-cavity structure. Chin Phys B 22:14208
62. Zhao Y, Chang J, Wang Q, Ni J, Song Z, Qi H, Wang C, Wang P, Gao L, Sun Z (2013) Research on a novel composite structure Er^{3+}-doped DBR fiber laser with a π-phase shifted FBG. Opt Express 21:22515
63. Zhang J, Yue C, Schinn GG, Clements WR, Lit JW (1996) Stable single-mode compound-ring erbium-doped fiber laser. J Lightwave Technol 14:104
64. Lee C, Chen Y, Liaw S (1998) Single-longitudinal-mode fiber laser with a passive multiple-ring cavity and its application for video transmission. Opt Lett 23:358
65. Lee C, Chi S (2000) Single-longitudinal-mode operation of a grating-based fiber-ring laser using self-injection feedback. Opt Lett 25:1774
66. Zhang X, Zhu NH, Xie L, Feng BX (2007) A stabilized and tunable single-frequency erbium-doped fiber ring laser employing external injection locking. J Lightwave Technol 25:1027
67. Yeh C, Huang TT, Chien H, Ko C, Chi S (2007) Tunable S-band erbium-doped triple-ring laser with single-longitudinal-mode operation. Opt Express 15:382
68. Pan S, Yao J (2010) A wavelength-tunable single-longitudinal-mode fiber ring laser with a large sidemode suppression and improved stability. IEEE Photon Technol Lett 22:413
69. Liaw SK, Wang S, Shin CS, Chen NK, Hsu KC, Manshina A, Tver yanovich Y, Su C, Wang LK (2010) Single-longitudinal-mode linear-cavity fiber laser using multiple subring-cavities. Laser Phys 20:1608
70. Yin F, Yang S, Chen H, Chen M, Xie S (2011) 60-nm-Wide tunable single-longitudinal-mode ytterbium fiber laser with passive multiple-ring cavity. 0IEEE Photon Technol Lett 23:1658
71. Feng S, Mao Q, Tian Y, Ma Y, Li W, Wei L (2013) Widely tunable single longitudinal mode fiber laser with cascaded fiber-ring secondary cavity. IEEE Photon Technol Lett 25:323
72. Salehiomran A, Rochette M (2013) An all-pole-type cavity based on smith predictor to achieve single longitudinal mode fiber lasers. IEEE Photon Technol Lett 25:2141
73. Feng T, Yan F, Peng W, Liu S, Tan S, Liang X, Wen X (2014) A high stability wavelength-tunable narrow-linewidth and single-polarization erbium-doped fiber laser using a compound-cavity structure. Laser Phys Lett 11:045101
74. Pan D, Ke C, Fu S, Liu Y, Liu D, Willner AE (2013) All-optical spectral linewidth reduction of lasers for coherent optical communication. Opt Lett 38:5220
75. Wang T, Yang T, Jia D, Wang Z, Ge C (2014) Multi-wavelength lasers with suppressed spectral linewidth of 10 kHz. Opt Express 22:26862
76. Sun J, Huang L (2007) Single-longitudinal-mode fiber ring laser using internal lasing injection and self-injection feedback. Opt Eng 46:74201
77. Quintela M, Perez-Herrera RA, Canales I, Fernandez-Vallejo M, Lopez-Amo M, Lopez-Higuera JM (2010) Stabilization of dual-wavelength erbium-doped fiber ring lasers by single-mode operation. IEEE Photon Technol Lett 22:368
78. Perez-Herrera RA, Ullan A, Leandro D, Fernandez-Vallejo M, Quintela MA, Loayssa A, Lopez-Higuera JM, Lopez-Amo M (2012) L-band multiwavelength single-longitudinal mode fiber laser for sensing applications. J Lightwave Technol 30:1173
79. Nakazawa M (1983) Rayleigh backscattering theory for single-mode optical fibers. J Opt Soc Am 73:1175
80. Zhu T, Bao X, Chen L, Liang H, Dong Y (2010) Experimental study on stimulated Rayleigh scattering in optical fibers. Opt Express 18:22958
81. Zhu T, Bao X, Chen L (2011) A single longitudinal-mode tunable fiber ring laser based on stimulated rayleigh scattering in a nonuniform optical fiber. J Lightwave Technol 29:1802
82. Zhu T, Chen FY, Huang SH, Bao XY (2013) An ultra-narrow linewidth fiber laser based on Rayleigh backscattering in a tapered optical fiber. Laser Phys Lett 10:055110

83. Zhu T, Huang S (2014) Ultra-narrow linewidth fiber laser with self-injection feedback based on Rayleigh backscattering. In Conference on Lasers and Electro-Optics: Science and Innovations, pp. W1N–W5N
84. Yin G, Saxena B, Bao X (2011) Tunable Er-doped fiber ring laser with single longitudinal mode operation based on Rayleigh backscattering in single mode fiber. Opt Express 19:25981
85. Fu LB, Ibsen M, Turner PW, Richardson DJ, Payne DN (2002) Keyed axis single-polarisation all-fibre DFB laser. Electron Lett 38:1537
86. Feng Z, Mo S, Xu S, Huang X, Zhong Z, Yang C, Li C, Zhang W, Chen D, Yang Z (2013) A compact linearly polarized low-noise single-frequency fiber laser at 1064 nm. Appl Phys Express 6:052701
87. Zhang W, Li C, Mo S, Yang C, Feng Z, Xu S, Xiong S, Peng Y, Zhang Q, Yang Z (2012) A compact low noise single-frequency linearly polarized DBR fiber laser at 1550 nm. Chin Phys Lett 29:084205
88. Kessler T, Hagemann C, Grebing C, Legero T, Sterr U, Riehle F, Martin MJ, Chen L, Ye J (2012) A sub-40-mHz-linewidth laser based on a silicon single-crystal optical cavity. Nature Photon 6:687
89. Vogt S, Lisdat C, Legero T, Sterr U, Ernsting I, Nevsky A, Schiller S (2011) Demonstration of a transportable 1 Hz-linewidth laser. Appl Phys B Lasers Opt 104:741
90. Mo S, Li Z, Huang X, Xu S, Feng Z, Zhang W, Li C, Yang C, Qian Q, Chen D, Yang Z (2014) 820 Hz linewidth short-linear-cavity single-frequency fiber laser at 1.5 μm. Laser Phys Lett 11:035101
91. Mo S, Huang X, Xu S, Feng Z, Li C, Yang C, Yang Z (2015) Compact slow-light single-frequency fiber laser at 1550 nm. Appl Phys Express 8:082703
92. Mo S, Huang X, Xu S, Li C, Yang C, Feng Z, Zhang W, Chen D, Yang Z (2014) 600-Hz linewidth short-linear-cavity fiber laser. Opt Lett 39:5818
93. Kunz PD, Heavner TP, Jefferts SR (2013) Polarization-enhanced absorption spectroscopy for laser stabilization. Appl Opt 52:8048
94. Lee H, Suh M, Chen T, Li J, Diddams SA, Vahala KJ (2013) Spiral resonators for on-chip laser frequency stabilization. Nat Commun 4(2468):2468
95. Kwee P, Willke B, Danzmann K (2009) Shot-noise-limited laser power stabilization with a high-power photodiode array. Opt Lett 34:2912
96. Kieu K, Mansuripur M (2007) Fiber laser using a microsphere resonator as a feedback element. Opt Lett 32:244
97. Zhao Y, Li Y, Wang Q, Meng F, Lin Y, Wang S, Lin B, Cao S, Cao J, Fang Z (2012) 100-Hz linewidth diode laser with external optical feedback. IEEE Photon Technol Lett 24:1795
98. Pan ZQ, Zhou J, Yang F, Ye Q, Cai HW, Qu RH, Fang ZJ (2013) Low-frequency noise suppression of a fiber laser based on a round-trip EDFA power stabilizer. Laser Phys 23:035105
99. Danion G, Bondu F, Loas G, Alouini M (2014) GHz bandwidth noise eater hybrid optical amplifier: design guidelines. Opt Lett 39:4239
100. Yamada M (2012) Analysis of Intensity and Frequency Noises in Semiconductor Optical Amplifier. IEEE J Quantum Electron 48:980
101. Feng ZM, Li C, Xu SH, Huang X, Yang CS, Zhou KJ, Gan JL, Deng HQ, Yang ZM (2015) Significant intensity noise suppression of single-frequency fiber laser via cascading semiconductor optical amplifier. Laser Phys Lett 12:095101
102. Li C, Xu S, Huang X, Xiao Y, Feng Z, Yang C, Zhou K, Lin W, Gan J, Yang Z (2015) All-optical frequency and intensity noise suppression of single-frequency fiber laser. Opt Lett 40:1964
103. Shieh W, Yang Q, Ma Y (2008) 107 Gb/s coherent optical OFDM transmission over 1000-km SSMF fiber using orthogonal band multiplexing. Opt Express 16:6378
104. Zhang Y, Li C, Xu S, Deng H, Feng Z, Yang C, Huang X, Zhang Y, Gan J, Yang Z (2016) A broad continuous temperature tunable DBR single-frequency fiber laser at 1064 nm. IEEE Photon J 8:1501107

105. Ball GA, Morey WW (1994) Compression-tuned single-frequency Bragg grating fiber laser. Opt Lett 19:1979
106. Zhang Y, Zhang Y, Zhao Q, Li C, Yang C, Feng Z, Deng H, Zhou E, Xu X, Wong KKY, Yang Z, Xu S (2016) Ultra-narrow linewidth full C-band tunable single-frequency linear-polarization fiber laser. Opt Express 24:26209
107. Gabai H, Botsev Y, Hahami M, Eyal A (2015) Optical frequency domain reflectometry at maximum update rate using I/Q detection. Opt Lett 40:1725
108. Saliba SD, Scholten RE (2009) Linewidths below 100 kHz with external cavity diode lasers. Appl Opt 48:6961
109. Li C, Xu S, Mo S, Zhan B, Zhang W, Yang C, Feng Z, Yang Z (2013) A linearly frequency modulated narrow linewidth single-frequency fiber laser. Laser Phys Lett 10:075106
110. Li C, Xu S, Huang X, Feng Z, Yang C, Zhou K, Gan J, Yang Z (2016) High-speed frequency modulated low-noise single-frequency fiber laser. IEEE Photon Technol Lett 28:1692

Chapter 3
Single-Frequency Active Fiber Lasers

As discussed in the previous chapter, the cavity length of a single-frequency fiber laser should be short enough (i.e., few centimeters) to realize a wide mode spacing for stable operation. Nevertheless, this in term requires the optical gain of the laser to be significant for high-efficiency operation. Since the doping concentration of rare-earth ions in general silica fiber is limited owing to the unwanted cluster formation phenomena, other glass hosts are required to overcome this limitation. In this chapter, we first introduce the multicomponent glass fiber as the doping host of rare-earth ions, enabling heavy doping concentration and significantly improved optical gain. With the newly developed active fiber, high-power operation of a single-frequency fiber laser is afterward discussed. An inevitable problem risen by high-power lasing is the thermal effect, which is then discussed in the third section. Subsequently, the thermal effect-induced laser noise is also discussed together with the coupling effect between frequency and intensity noise and amplified spontaneous emission noise, which are considerable in a high-gain fiber laser.

3.1 Introduction of Rare-Earth Ions Doped Multicomponent Glass Fiber

Now we have discussed the general performances of SFFLs, including the measurement methods of specific parameters and the corresponding schemes to further optimize or improve these performances to a higher level on the aiding of different application needs. However, the readers may have recognized that another important parameter – the laser output power – has not been considered yet. For many applications, such as laser interferometric gravitational-wave observatory, coherent beam combining, and laser LIDAR, high-power SFFL sources are required [1–3]. Although optical amplifiers can efficiently boost the laser power, it is still preferable to obtain a high-power low-noise lasing directly from a single fiber

© Springer Nature Singapore Pte Ltd. 2019

Z. Yang et al., *Single-Frequency Fiber Lasers*, Optical and Fiber Communications Reports 8, https://doi.org/10.1007/978-981-13-6080-0_3

resonator. It could in some occasions exempt the laser amplification process which would enlarge the laser noise and bring in extra ASE and spurious oscillations [4]. Commonly, increasing the length of active fiber in the laser cavity would accordingly raise the output power; however, there exists a dilemma that a long cavity length would lead to the onset of the mode hopping and the mode competition phenomena. Nevertheless, even in ring cavity lasers that use several meters long active fiber, the highest output power obtained is still several tens of milliwatts [5]. In fact, the main limitation to the operating power of SFFLs is attributed to the low optical gain of the generally utilized RE ions doped silica fiber, e.g., the maximum gain of this type of fiber is about several dB per meter at 1.5 μm band.

Essentially, the dissolution of silica glass to RE ions is less than 1 wt%; otherwise, the undissolved ions would gather together to form clusters in the glass matrix and induce fluorescent quenching [6]. Therefore, alternative (non-silica) glass matrix should be exploited to increase the doping concentration of RE ions while eliminating the ion cluster-induced concentration quenching. In the near-infrared (near-IR) band, the main achievement was the adoption of the multicomponent phosphate glass, thanks to its high solubility and large emission cross sections for many RE ions [7–9], for instance, the gain per unit length of Er^{3+}-doped phosphate glass fiber can be as high as 2.1 dB/cm [10]. Moreover, the relatively good mechanical strength and chemical stability render the phosphate fiber attractive for constructing compact short-cavity SFFLs, especially at the 1.0 μm and 1.5 μm wavelength band. Nevertheless, the operating range of phosphate fiber did not expand to the 2.0 μm band, owing to its large maximum phonon energy (1200 cm^{-1}), which would significantly quench the laser emission via non-radiative decay and even increase the transmission loss of light. Under this condition, other multicomponent glass matrixes such as germanate, silicate, and tellurite glasses were employed to substitute the phosphate glass to fabricate heavily RE ions doped fiber [11]. When going beyond 2.0 μm – the mid-infrared (mid-IR) band – the fundamental challenge caused by the maximum phonon energy becomes even severe, and a multiphonon edge emerges at around 2.2 μm beyond which the general glass matrixes become opaque to light. Fortunately, the fluoride glass-based ZBLAN (ZrF_4-BaF_2-LaF_3-AlF_3-NaF) fiber has been proved to be the most promising alternative for light transmission at the mid-IR band. The considerable low maximum phonon energy of about 565 cm^{-1} of ZBLAN fiber enables optical attenuation of less than 0.2 dB/m at wavelengths up to 4.5 μm [12]. Additionally, ZBLAN glass also exhibits efficient RE ions doping capability, and fiber lasers exploiting transitions from Er^{3+} to Ho^{3+} at around 3 μm have realized encouraging results [13, 14].

Even though RE ions can be highly doped into multicomponent glass fibers, most of them have poor photosensitivity and thus cannot be written into FBG. Now the problem is that, to construct a short-cavity DBR fiber laser, the active fiber and the FBGs are based on different glass matrixes, and it is not easy to splice them as different glass fibers generally possess distinct thermal and mechanical properties such as softening temperature, thermal expansion coefficient, and refractive index. In fact, the commonly used splicing scheme of silica fiber is not applicable to the splicing of heterogeneous fibers. To address this problem, we have proposed an

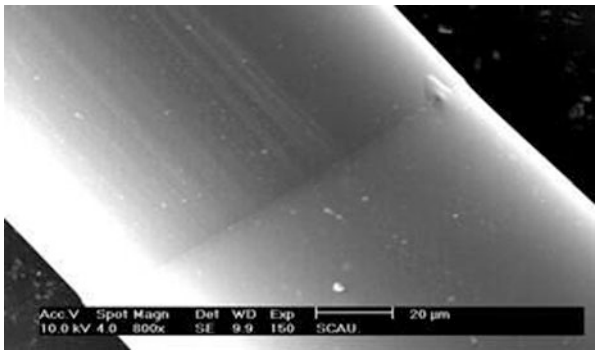

Fig. 3.1 Scanning electron microscope (SEM) image of the splice joint of a homemade phosphate fiber and a commercial silica fiber

asymmetric heating splicing technique based on electric arc splicer to connect a homemade phosphate fiber and a commercial silica fiber. The policy is to locate the heating point of the splicer at the side of the silica fiber instead of the middle of the gap between the two fiber end faces. Via a series of trial and optimization, we have achieved successful fusion splicing of these fibers. The SEM image of the splice joint is shown in Fig. 3.1, from which one can observe a smooth and uniform surface. The estimated splicing loss was about 0.6 dB, and good bending-resist strength between the two splicing fibers was also verified.

3.2 High-Power Operation from Fiber Oscillator

The creation of multicomponent glass fibers has triggered intensive research on high-power SFFLs. On the one hand, the increased doping concentration of RE ions enables the active fiber to provide remarkable gain to the oscillating signal. On the other hand, a high doping concentration also facilitates the advantageous energy transfer between neighboring ions and favors the accumulation of population inversion. For instance, codope with another dopant that has a wider absorption band and a larger absorption cross section as the sensitizer which absorbs the most pump power and then transfers to the lasing ions has been proved to be an efficient way to raise the output power of a single fiber resonator. The typical sensitization pairs are $Yb^{3+} \rightarrow Er^{3+}$ and $Tm^{3+} \rightarrow Ho^{3+}$ [15, 16]. Additionally, in a 790 nm laser pumped Tm^{3+}-doped fiber that operated at around 2 μm, adjacent ions can also be sensitizer of each other owing to the popular cross relaxation phenomenon [17]. Here we briefly introduce the recent progress on high-power SFFLs.

In 2003, C. Spiegelberg et al. reported a short-cavity phosphate fiber single-frequency DBR laser at 1550 nm with output power of more than 200 mW for the first time, while the other characteristics such as the linewidth, mode stability, and noise all show an excellent performance [18]. Subsequently, a 200 mW 1064 nm fiber laser was demonstrated in a highly Yb^{3+}-doped phosphate fiber [19]. It should be noted that the DBR cavity structure is ideal for the phosphate fiber laser, as a short

piece of this highly doped fiber can support a considerable high-power and robust single-frequency operation at the same time. Furthermore, the whole laser structure can be easily packaged into a compact and portable module. Regarding the short DFB cavity, although grating inscribing has been realized in the heavily doped phosphate fiber [20, 21], the high intensity at the center of the phase-shifted grating hampers the ultimate output power of the DFB laser [22, 23]. In addition, the employment of FBGs in a monolithic DBR phosphate fiber laser has shown that the inscribing process would induce considerable scattering loss and thus further affect the laser stability [24].

Since the doping concentration of RE ions has considerably raised, the limitation to further increasing the lasing power then falls on the small core size of the active fiber. To obtain watt-level SFFL source, large mode area phosphate fiber with the cladding-pump scheme was then employed [25–28]. T. Qiu et al. [25] demonstrated a cladding-pumped Er^{3+}/Yb^{3+}-codoped phosphate fiber laser, with the diameters of the cladding and the core of the active fiber to be 125 ± 2 μm and 13.5 ± 0.5 μm, respectively. By using a narrowband FBG as the output coupler, a 1.6 W continuous-wave (CW) single longitudinal mode laser was achieved in a 5.5 cm long fiber. Further increasing the mode area was realized with the air-cladding photonic crystal fiber (PCF), of which the wave guiding is determined by the pattern of an ordered array of microscopic air holes along the fiber length rather than the difference of index in material, and thus rendering the fiber core area can be expanded while maintaining a high numerical aperture (NA) for the pump cladding [29, 30]. Apparently, this new fiber structure exactly meets the requirement of SFFLs with higher output power, that is, a large mode area and high pump absorption while still maintaining single transverse mode confinement. By using the stack-and-draw technique, L. Li et al. [31] fabricated the first highly Er^{3+}/Yb^{3+}-codoped microstructured phosphate glass PCF with the core area of 430 μm^2 and obtained more than 3 W of output power with near single-mode beam quality from 11-cm-long of this type of fiber. After that, by further optimizing the parameters, a maximum output power of 4.7 W was obtained from a 35 mm microstructured glass fiber, corresponding to a power per length ratio of 1.34 W/cm [32].

With the developing of active fibers with ever large mode area for single-mode operation, higher RE ions doping concentration, as well as cladding-pumping by high-power multimode fiber-coupled laser diode, compact watt-level single-frequency lasing can be readily achieved in a single fiber resonator. As the length of the employed fiber can be several centimeters, it is a superiority to suppress the SBS effect which is destructive in the high-power regime. However, it should be noted that the other major properties of SFFLs such as the laser stability and linewidth would be deteriorated to some extent, owing to destructive thermal effects, the poor quality of the pump laser, and the onset of self-pulsing. Apart from high-power operation, a well-performed SFFL should also show excellent behavior in other aspects. In this sense, the scheme of cladding-pumping the heavily doped active fiber with large mode area seems to be questionable, and researchers tend to further optimize the optical gain of the conventional single-mode fiber and consider

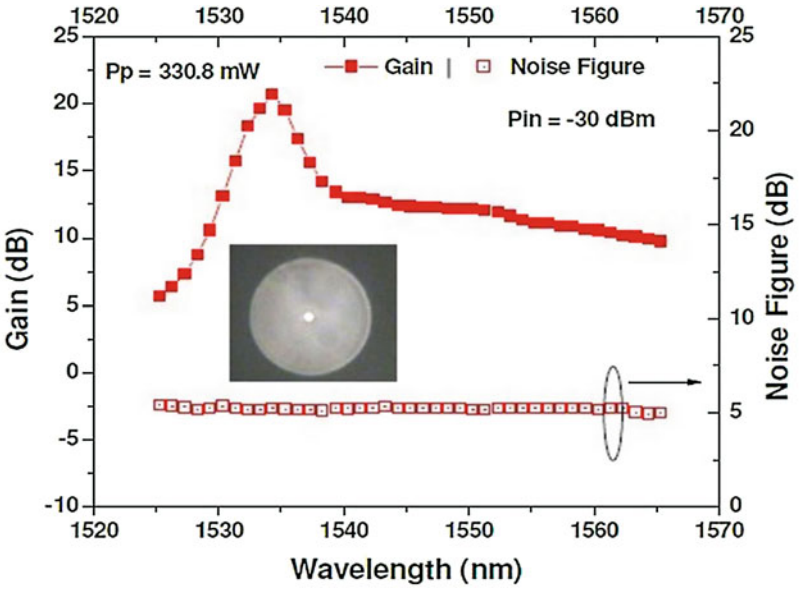

Fig. 3.2 Gain and noise figure characteristics of the Er^{3+}/Yb^{3+}-codoped phosphate glass fiber. Inset: the cross section of the phosphate glass fiber. Pump power $P_P = 330.8$ mW, signal input power $P_{in} = -30$ dBm, fiber length 40 mm. (Reprinted from Ref. [33], copyright 2010, with permission from OSA publishing)

magnifying the single-frequency laser power in an extra amplifier to minimize the tradeoff between the laser power and purity.

In 2010, S. H. Xu et al. [33] reported an over 300 mW low noise narrow-linewidth single-frequency phosphate fiber laser at 1.5 μm with the active fiber length of only 2 cm. The newly developed phosphate fiber codoped with heavily Er^{3+}/Yb^{3+} (3.0 mol% for Er^{3+} and 5.0 mol% for Yb^{3+}) was fabricated in a fiber-drawing tower based on the rod-in-tube technique, and the achieved maximum net gain coefficient is 5.2 dB/cm at 1535 nm, as shown in Fig. 3.2. The figure demonstrates the gain and noise figure characteristics of a 40-mm-long phosphate fiber, of which the cross section captured by an amplified CCD viewer is shown in the inset of Fig. 3.2. At the 1.0 μm band, an Yb^{3+}-doped phosphate fiber with a doping concentration of 15.2 wt% and a net gain coefficient of 5.7 dB/cm was also fabricated by the same group [34]. By using 0.8 cm of this fiber, over 400 mW single-frequency lasing at 1064 nm was obtained, and the main properties of the laser are measured and demonstrated in Fig. 3.3. From the figure, it is observed that the laser was centered at 1063.9 nm with a SNR of more than 72 dB. Stable single-frequency operation was verified by a scanning F-P interferometer. Moreover, the laser slope efficiency was measured to be 72.7%, while the power stability was estimated to be less than 0.25% at 300 mW for an hour. Subsequently, over 164 mW of single-frequency linearly polarized laser at 1014 nm was extracted from only 0.5 cm of this type of fiber [35]. In 2012, P. Hofmann et al. [36] obtained 550 mW of

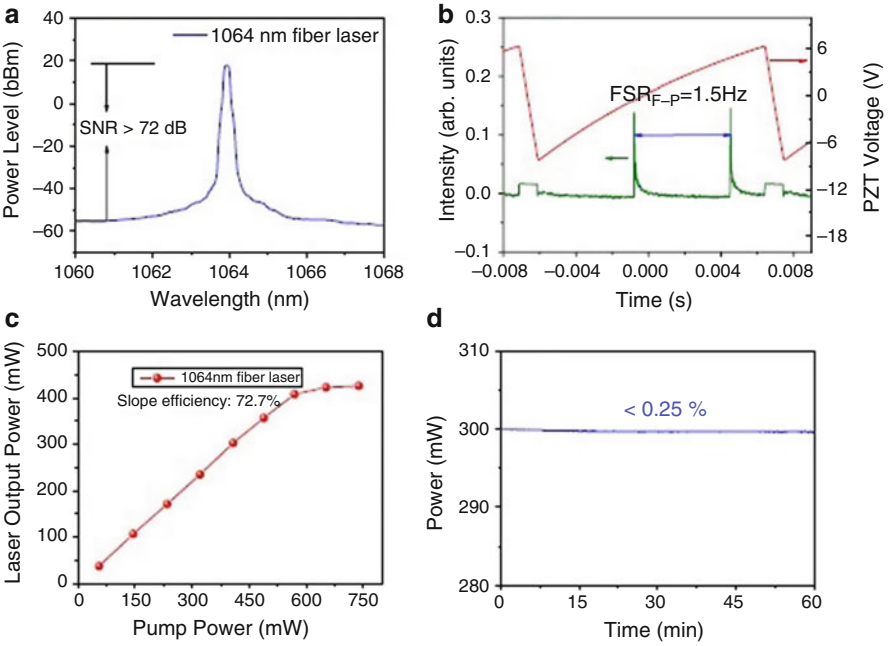

Fig. 3.3 (**a**) Laser spectrum of the Yb^{3+}-doped phosphate fiber laser. (**b**) The longitudinal modes characteristics of the fiber laser measured by the scanning Fabry-Perot interferometer. (**c**) The output power of the fiber laser at 1064 nm versus the pump power. (**d**) The power stabilities of the fiber laser for an hour. (Reprinted from Ref. [34], copyright 2011, with permission from OSA publishing)

output power at 1538.2 nm from an approximately 10-cm-long all-phosphate DBR fiber laser with the FBGs written directly on the active fiber by a Ti:sapphire laser. The corresponding linewidth and the peak amplitude of the RIN spectrum are, respectively, 60 kHz and − 100 dB/Hz, which is about an order of magnitude weaker than that of the precious works. This is attributed to the grating writing process-induced scattering loss and the variation of the FBG parameters caused by the heat accumulation in the active fiber.

Other achievements on phosphate fiber laser were mainly demonstrated in the special wavelengths in the wide florescence spectral range of Yb^{3+} ion, targeting applications such as nonlinear wavelength conversion to generate visible single-frequency sources and high-resolution atomic and molecular spectroscopy. As some required wavelengths unfortunately locate in the margin area of the Yb^{3+} florescence spectra and therefore correspond to a low emission cross section, it is then advantageous for phosphate fiber to provide sufficient optical gain within a short length to realize an efficient single-frequency lasing. In 2012, X. Zhu et al. [37] reported a 976 nm single-frequency laser based on a 2 cm phosphate fiber with output power of more than 100 mW and linewidth of less than 3 kHz. After that, S. Xu et al. [38] realized over 100 mW of output power single-frequency single polarization lasing at

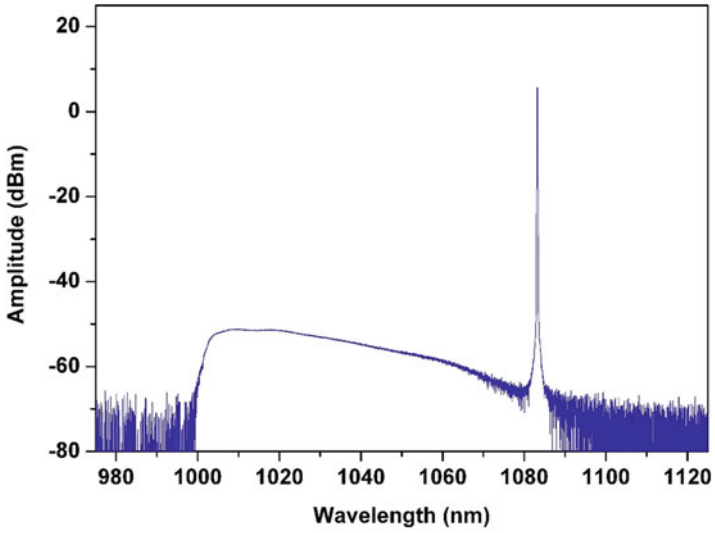

Fig. 3.4 Overall spectrum of an efficient phosphate fiber single-frequency laser with operation wavelength of 1083 nm

1083 nm from only 1.8 cm Yb^{3+}-doped phosphate fiber, and the estimated laser linewidth was less than 2 kHz. Figure 3.4 shows the overall spectrum of a high-power 1083 nm phosphate single-frequency laser. Although significant ASE has risen over several tens of nanometers, the laser can still operate efficiently at the edge of the florescence spectrum. In conclusion, based on the phosphate fiber, Yb^{3+} ion has achieved high-power single-frequency operation at both of its florescence wings. Therefore, it is intuitive to tell that the phosphate glass fiber could facilitate high-power single-frequency oscillation at any wavelength among the spectral range of the doped RE ions given that the corresponding narrow bandpass filtering devices are available.

Regarding the 2.0 μm band, stimulated by its potential applications in, for example, remote sensing, LIDAR, and medicine, intense research works have also been aroused to develop similar laser performances as in the 1.0 and 1.5 μm band [39–41]. Here the main active ions are Tm^{3+} and Ho^{3+}, and the latter has an emission peak wavelength of 0.2 μm longer than that of the Tm^{3+}. Similarly, owing to the limited doping concentration and high maximum phonon energy (1100 cm^{-1}) of the silica glass, the output power of the silica-based fiber laser was restricted to only several milliwatts with a poor efficiency [42]. Germanate glass was then chosen as the host material, thanks to its good doping ability for RE ions and optical and mechanical properties. In 2006, J. Wu et al. [43] reported a 4-cm-long highly Tm^{3+}-doped germanate fiber laser with a measured quantum efficiency of 180%. By further increasing the doping concentration, a maximum output power of 50 mW single-frequency lasing was demonstrated at 1893 nm [44]. Doping with Ho^{3+} was also demonstrated in germanate fiber, and over 50 mW of power at 2053 nm was obtained

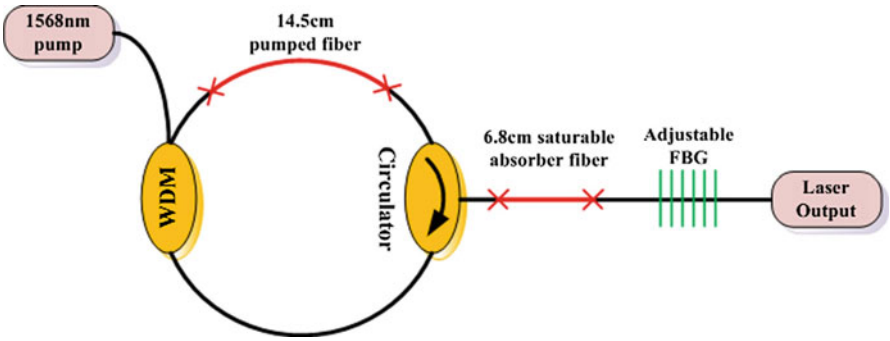

Fig. 3.5 Schematic of the Tm^{3+}-doped narrow-linewidth single-frequency fiber laser. (Reprinted from Ref. [46], copyright 2013, with permission from OSA publishing)

in a short piece of this fiber with the pumping source to be a multimode laser diode-pumped double-cladding Tm^{3+}-doped fiber laser [45]. Even higher laser power was achieved by X. He et al. [46], who developed a heavily Tm^{3+}-doped single-mode germanate glass fiber with the net gain coefficient of 2.3 dB/cm and realized over 200 mW of outputting with estimated linewidth of less than 7 kHz by implementing a single-frequency fiber ring laser, of which the configuration is shown in Fig. 3.5. Here the saturable absorber fiber was a segment of unpumped Tm^{3+}-doped germanate fiber, in which an automatic tracking filter was induced by the spatial hole burning effect that caused by two counter-propagating light waves. It is believed that with this high-gain Tm^{3+}-doped fiber, a short DBR laser should be readily constructed with hundreds of outputting power.

Unlike phosphate glass fiber in the 1.0 and 1.5 μm band, germanate glass fiber is not the only solution in constructing a high-power SFFL near 2.0 μm. Other schemes devoting to improve the laser efficiency have been proposed. Z. Zhang et al. [47, 48] fabricated a Tm-Ge codoped aluminosilicate fiber based on the modified chemical vapor deposition (MCVD) and solution-doping technique. By inscribing Bragg gratings into this type of fiber, both DFB and DBR lasers were demonstrated, with a maximum laser slope efficiency of 27%. J. Geng et al. [49] reported a heavily Tm^{3+}-doped multicomponent silicate glass fiber, in which the doping concentrations of RE ions (Tm^{3+}) could be raised owing to the less-defined glass network. Using 2 cm of this fiber, over 40 mW output power of single-frequency laser was achieved, corresponding to the efficiency greater than 37% relative to the absorbed pump power. Another promising host material system is the tellurite glass, which has a large RE ions solubility and moderate phonon energy (700 cm^{-1}) [50, 51]. In addition, other properties of tellurite glass such as high refractive index, high dielectric constant, as well as good corrosion resistance and thermal and chemical

stability also make it a competitive candidate [52]. In 2008, B. Richards et al. [53] reported the first Tm^{3+}-doped tellurite fiber DBR laser which produced an output power of 280 mW with slope efficiency of 76% in a 32-cm-long fiber. For Ho^{3+}-doped fiber lasers operating near 2.1 μm, although tellurite glass is an ideal host material, the drawback is the lack of commercial high-power laser diodes that can be used as the pump source. The solution is to sensitize the Ho^{3+} ions to diode pumping that is commercially available by codoping with Tm^{3+} or Tm^{3+} and Yb^{3+}, where Yb^{3+} is used as the sensitizer of Tm^{3+} [54]. Y. Tsang et al. [55, 56] demonstrated both the Tm^{3+}/Ho^{3+}-codoped and the $Yb^{3+}/Tm^{3+}/Ho^{3+}$-triply-doped tellurite fiber laser, with the former in-band pumped at 1.6 μm by a Yb^{3+}/Er^{3+}-doped silica fiber laser and realized a maximum slope efficiency of 62%, while the latter in-band pumped by a Yb^{3+}-doped double-cladding silica fiber laser at 1.1 μm and obtained a slope efficiency of 25%. In 2010, K. Li et al. [57] developed a highly Tm^{3+}-doped tungsten tellurite fiber with significantly improved thermal properties which are favorable for solving the heating problems in fiber laser. Subsequently in 2012, Tm^{3+}- and Tm^{3+}/Ho^{3+}-codoped tungsten tellurite glass single-mode fiber laser was demonstrated, and the achieved power was 494 mW at ~1.9 μm and 35 mW at ~2.1 μm, respectively [58].

When going deeper into the mid-infrared region, the relevant technologies are still in its infancy state as compared to their near-IR counterparts. Firstly, the fluoride fiber (active and passive) generally has a poor mechanical strength and is therefore not easy to handle (stripping, cleaving, and connecting). Moreover, the glass constituents of the fiber would react with the ambient water vapor and other contaminants, leading to deterioration of the laser performances [59]. Under these conditions, commercial mid-IR optical fiber components such as WDMs, couplers, and isolators are currently not available. Nevertheless, developing SFFL at the mid-IR band remains very appealing for especially frequency comb laser spectroscopy in the "fingerprint region" [60]. The first effort was demonstrated in Ref. [61], where a SFFL operating at 2914 nm was realized in a DBR configuration with a Ho^{3+}/Pr^{3+}-codoped ZBLAN fiber. The laser cavity was constructed with one end of the active fiber butt-coupled with a dichroic mirror, while the other end written into a FBG by utilizing the femtosecond laser point-by-point technique. Strictly speaking, this laser was not in an "all-fiber" form, as the pumping process was accomplished in a free-space manner. The first fairly "all-fiber" mid-IR SFFL was subsequently reported by M. Bernier et al. [61], who implemented a DFB laser at 2.8 μm with estimated linewidth of less than 20 kHz by inscribing a π-phase-shifted FBG into heavily Ho^{3+}-doped ZBLAN fiber with femtosecond pulses. Although the current maximum power achieved from mid-IR SFFL is about 10 mW, there is no substantial indication that the SFFLs working in the mid-IR band cannot realize hundreds of mW output power.

3.3 Thermal Effects in High-Gain Single-Frequency Fiber Lasers

In the process of seeking high output power from SFFL, we should in the meantime keep in mind to maintain the desirable performances of SFFLs such as narrow linewidth and low noise, as well as the reliable operation of the laser system, for the sake of meeting the requirements of high transmission stability and measuring resolution in most applications. To this aim, an important issue that will be encountered is the thermal effects in the laser. When launched into the cavity, the pump power will be absorbed by the RE ions and partly transferred to the laser signal, while the remains will be dissipated via heat accumulation owing to the quantum defect between pump and laser photons and the non-radiative decay from the excited states [62–64]. Serious heat accumulation in the laser gain medium will lead to broadening of the florescence spectrum, reduced florescence lifetime of the excited states, and even temperature quenching of the RE ions, resulting in lower energy conversion efficiency and higher lasing threshold. Moreover, uneven distribution of the temperature field in the fiber will modify the refractive index and then lead to detrimental thermal effects such as thermal stress fracture, thermal birefringence, and thermal lensing [65].

It is worth noting that in silica fiber lasers, the thermal effects are generally not that serious, owing to the low doping concentration of RE ions. As the pump absorption per unit length of the gain fiber is relatively low, the heat deposited in the fiber is therefore limited and can be easily dissipated into the environment, thanks to the high heat diffusivity of the silica glass. Nevertheless, in heavily doped multicomponent fiber laser, considerable pump power will be absorbed and converted to heat within several cm long of the gain medium; therefore, undesired thermal effect would be taken place and should be carefully managed. We have taken highly Er^{3+}/Yb^{3+}-codoped phosphate fiber short-cavity DBR laser as the representative and carried out a three-dimensional (3D) heat analysis of the gain medium with the consideration of longitudinal heat flow [66]. Figure 3.6 illustrates the simplified configuration of a short-cavity phosphate fiber DBR laser. In the figure, $P_p^{\pm}(z)$ and $P_s^{\pm}(z)$ denote the pump and signal power distribution in the positive and negative axial direction, respectively, while R_1 and R_2 are, respectively, the reflectance and the reflectivity to the laser signal of the two cavity reflectors.

Assuming the gain fiber is adiabatic at the two ends, then thermal exchange only takes place at the boundary between the fiber and the environment air. Regarding the

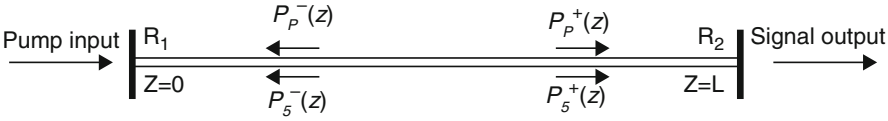

Fig. 3.6 Schematic illustration of phosphate fiber laser. (Reprinted from Ref. [66], copyright 2009, with permission from OSA publishing)

fiber as an isotropic cylinder with radial and axial heat flow, the general steady-state heat equations of the fiber laser can be written by the following Poisson equation and corresponding boundary conditions [67]:

$$\frac{\partial^2 T(z,r)}{\partial r^2}+\frac{1}{r}\frac{\partial T(z,r)}{\partial r}+\frac{\partial^2 T(z,r)}{\partial z^2}=-\frac{Q(z,r)}{k} \qquad 0<r<r_1 \tag{3.1}$$

$$\frac{\partial^2 T(z,r)}{\partial r^2}+\frac{1}{r}\frac{\partial T(z,r)}{\partial r}+\frac{\partial^2 T(z,r)}{\partial z^2}=0 \qquad r_1<r<r_2 \tag{3.2}$$

$$k\partial T/\partial r=h(T_h-T) \qquad r=r_2 \tag{3.3}$$

$$T_1=T_2, \qquad \partial T_1/\partial r=\partial T_2/\partial r \qquad r=r_1 \tag{3.4}$$

$$\partial T/\partial r=0 \qquad r=0 \tag{3.5}$$

$$\partial T/\partial z=0 \qquad z=0,l \tag{3.6}$$

in which r_1 and r_2 are, respectively, the core and cladding radius, $T(r,z)$ is the temperature distribution inside the gain fiber, Q is the heat function that denotes the heat generated at a certain point of the fiber per unit time, k is the fiber thermal conductivity, h is the heat transfer coefficient of air convection, and T_h is the room temperature, while T_1 and T_2 are, respectively, the temperature in fiber core and cladding regions. Considering the fiber laser is pumped by a laser diode, the heat function can be written as [68]:

$$Q(z,r)=\frac{2\left(\alpha_a\eta+\alpha_{ps}\right)\left[P_p^+(z)+P_p^-(z)\right]+2\alpha_s\left[P_s^+(z)+P_s^-(z)\right]}{\pi\omega_p^2}\exp\left(\left.-2r^2\right/\omega_p^2\right) \tag{3.7}$$

where α_a is the pump absorption coefficient; α_{ps} and α_s are, respectively, the scattering loss coefficient of pump and signal light; ω_p is the pump Gaussian radius, and it is approximately equal the core radius given that all of the pump light is coupled into the fiber core; and η is the heat conversion efficiency, and it is given by $\eta = 1$ - λ_p/λ_s if only the quantum defect of the laser is considered.

Set $\theta = T - T_h$, and then partial differential equation Eqs. (3.1), (3.2), (3.3), (3.4), (3.5), (3.6) and (3.7) can be analytically solved to obtain:

$$\begin{aligned}\theta(r,z)&=T-T_0\\&=\sum_{n=1}^{\infty}\frac{1}{lN_n}J_0(\beta_n r)\frac{g_{n0}}{\beta_n^2}+\sum_{n=1}^{\infty}\sum_{m=1}^{\infty}\frac{2}{lN_n}J_0(\beta_n r)\cos(\eta_m z)\frac{g_{nm}}{\beta_n^2+\eta_m^2}\end{aligned} \tag{3.8}$$

where:

$$g_{n0} = \int_0^l \int_0^{r_1} \frac{Q(z,r)}{k} J_0(\beta_n r) r dr dz \tag{3.9}$$

$$g_{nm} = \int_0^l \int_0^{r_1} \frac{Q(z,r)}{k} \cos\left(\frac{m\pi}{L}z\right) J_0(\beta_n r) r dr dz \tag{3.10}$$

$$\eta_m = m\pi/l \qquad N_n = r_2^2\left(k^2\beta_n^2 + h^2\right) J_0^2(\beta_n r_2)/k^2\beta_n^2 \tag{3.11}$$

$$hJ_0(\beta_n r_2) - k\beta_n J_1(\beta_n r_2) = 0 \tag{3.12}$$

in which J_0 and J_1 are, respectively, the zero and first-order Bessel function of the first kind and β_n is the nth order eigenvalue of a typical Bessel equation.

To examine the actual temperature distribution inside the cavity, the heat function of the laser should be resolved first. To this aim, we need to analyze the dynamic operation of the fiber laser based the general rate equations. Figure 3.7 demonstrates the energy diagram of the Er^{3+}/Yb^{3+}-codoped system pumped by a 976 nm laser

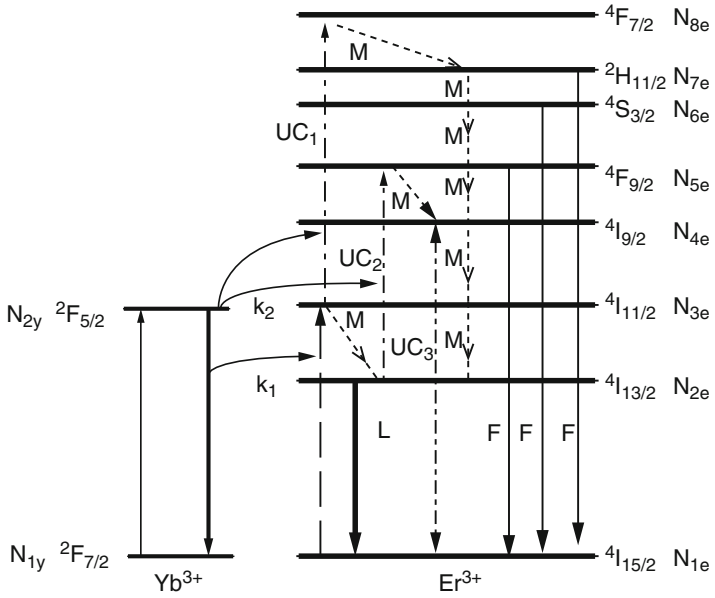

Fig. 3.7 Energy level scheme of the Er^{3+}/Yb^{3+}-codoped system including energy transfer upconversion processes: *UC_1 and UC_2* cumulative upconversion, *UC_3* cooperative upconversion, *M* multiphonon relaxation, *F* fluorescence process, *L* 1535 nm laser emission. (Reprinted from Ref. [66], copyright 2009, with permission from OSA publishing)

diode. From the figure, one can observe three upconversion processes, which are inevitable in highly doped fiber [69–71]:

$$\mathrm{UC}_1 : \mathrm{Yb}^{3+}\left({}^2\mathrm{F}_{5/2}\right) + \mathrm{Er}^{3+}\left({}^4\mathrm{I}_{11/2}\right) \rightarrow \mathrm{Yb}^{3+}\left({}^2\mathrm{F}_{7/2}\right) + \mathrm{Er}^{3+}\left({}^4\mathrm{F}_{7/2}\right)$$

$$\mathrm{UC}_2 : \mathrm{Yb}^{3+}\left({}^2\mathrm{F}_{5/2}\right) + \mathrm{Er}^{3+}\left({}^4\mathrm{I}_{13/2}\right) \rightarrow \mathrm{Yb}^{3+}\left({}^2\mathrm{F}_{7/2}\right) + \mathrm{Er}^{3+}\left({}^4\mathrm{F}_{9/2}\right)$$

$$\mathrm{UC}_3 : \mathrm{Er}^{3+}\left({}^4\mathrm{I}_{13/2}\right) + \mathrm{Er}^{3+}\left({}^4\mathrm{I}_{13/2}\right) \rightarrow \mathrm{Er}^{3+}\left({}^4\mathrm{I}_{15/2}\right) + \mathrm{Er}^{3+}\left({}^4\mathrm{I}_{9/2}\right)$$

These upconversion processes themselves do not cause heating of the fiber; however, the resulting Er^{3+} ions at higher excited states will transfer to the ${}^4I_{13/2}$ energy level through non-radiative multiphonon relaxation process accompanied with heat depositing. In addition, owing to the fast multiphonon relaxation from the ${}^4I_{11/2}$ to ${}^4I_{13/2}$ energy level, the backward energy transition Er^{3+}: ${}^4I_{11/2} \rightarrow Yb^{3+}$: ${}^2F_{7/2}$ and the upconversion process in Er^{3+}: ${}^4I_{11/2}$ can be neglected [72].

Based on the energy level diagram in Fig. 3.7, the rate equations for the Er^{3+} and Yb^{3+} population densities are written as [73]:

$$\frac{\partial N_{2y}}{\partial t} = W_{12y}N_{1y} - W_{21y}N_{2y} - \frac{N_{2y}}{\tau_y} - k_1 N_{2y}N_{1e} - k_2 N_{2y}N_{2e} = 0 \tag{3.13}$$

$$\frac{\partial N_{2e}}{\partial t} = W_{12e}N_{1e} + A_{32e}N_{3e} - W_{21e}N_{2e} - k_2 N_{2e}N_{2y} - \frac{N_{2e}}{\tau_e} - 2C_{up}N_{2e}^2 = 0 \tag{3.14}$$

$$\frac{\partial N_{3e}}{\partial t} = k_1 N_{1e}N_{2y} + A_{43e}N_{4e} - A_{32e}N_{3e} = 0 \tag{3.15}$$

$$\frac{\partial N_{4e}}{\partial t} = C_{up}N_{2e}^2 - A_{43e}N_{4e} = 0 \tag{3.16}$$

$$N_{\mathrm{Er}} = N_{1e} + N_{2e} + N_{3e} + N_{4e} \tag{3.17}$$

$$N_{\mathrm{Yb}} = N_{1y} + N_{2y} \tag{3.18}$$

As the Er^{3+} ions at the excited states of ${}^4F_{7/2}$, ${}^2H_{11/2}$, ${}^4S_{3/2}$, and ${}^4F_{9/2}$ decay rapidly through multiphonon relaxation, they are then neglected in the rate equations. In the equations, A_{ij} is the spontaneous emission probability; τ_e and τ_y are, respectively, the lifetime of the ions at the energy level of ${}^4I_{13/2}$ and ${}^2F_{5/2}$; the energy upconversion from energy level ${}^4I_{13/2}$ to ${}^4I_{15/2}$ and ${}^4I_{9/2}$ is represented by C_{up}; K_1 and K_2 are the transfer coefficient between the Yb^{3+} and Er^{3+} ions; N_{Yb} and N_{Er} are the total doping concentration of Yb^{3+} and Er^{3+} ions, respectively; and W_{ij} denotes the stimulated absorption and emission probability between energy level i and j and are given by:

$$W_{12e}(z,t) = \Gamma_s \sigma_{as}(\nu_s) P_s(z)/h\nu_s A_{core} \tag{3.19}$$

$$W_{21e}(z,t) = \Gamma_s \sigma_{es}(\nu_s) P_s(z)/h\nu_s A_{core} \tag{3.20}$$

$$W_{12y}(z,t) = \Gamma_p \sigma_{ap}(\nu_p) P_p(z)/h\nu_p A_{core} \tag{3.21}$$

$$W_{21y}(z,t) = \Gamma_p \sigma_{ep}(\nu_p) P_p(z)/h\nu_p A_{core} \tag{3.22}$$

in which σ_{as}, σ_{es}, σ_{ap}, σ_{ep} are, respectively, the absorption and emission section of the pump and signal light; ν_s and ν_p are, respectively, the frequency of the signal and pump; A_{core} is the sectional area of the fiber core; and Γ_s and Γ_p are the power filling factors, i.e., the coupling proportion of the pump and signal light in the fiber core, and are written as [74]:

$$\Gamma_{s,p} = 1 - \exp\left(-2r_1^2/\omega_{s,p}^2\right) \tag{3.23}$$

$$\omega_{s,p} = r_1\left(0.616 + 1.660/V^{1.5} + 0.987/V^6\right) \tag{3.24}$$

where $V = 2\pi r_1 NA/\lambda$ is the normalized frequency and NA is the numerical aperture.

To numerically solve the rate equations and obtain the actual distribution of the pump and signal power and the RE ion density along the fiber, the power transmission equations of the laser at the steady state should be accomplished [75, 76]:

$$\pm\frac{dP_p^{\pm}(z)}{dz} = -\Gamma_p\left[\sigma_{ap}N_{1y}(z) - \sigma_{ep}N_{2y}(z)\right]P_p^{\pm}(z) - \sigma_p^{'}P_p^{\pm}(z) \tag{3.25}$$

$$\begin{aligned}\pm\frac{dP_s^{\pm}(z)}{dz} = &-\Gamma_s[\sigma_{es}N_{2e}(z) - \sigma_{as}N_{1e}(z)]P_s^{\pm}(z) \\ &+\Gamma_s\sigma_{es}N_{2e}(z)P_0(\lambda_s) - \sigma_s^{'}P_s^{\pm}(z)\end{aligned} \tag{3.26}$$

in which λ_s is the signal wavelength; $\sigma_p^{'}$ and $\sigma_s^{'}$ are, respectively, the position independent transmission loss coefficient of the pump and signal light in the cavity; and $P_0(\lambda_s) = 2hC^3/\lambda_s^3$ denotes the contribution of spontaneous emission power to the signal power [77]. The boundary conditions of the power transmission equations are defined by:

$$P_s^+(0) = R_1 P_s^-(0) \qquad P_s^-(L) = R_2 P_s^+(L) \qquad P_p^-(L) = R_3 P_p^+(L) \tag{3.27}$$

where R_3 is the reflectance coefficient of the output coupling reflector to the pump light. In this way, the rate equations and power transmission equations can be numerically solved via associating Eq. (3.27). Assuming a 1-cm-long Er^{3+}/Yb^{3+}-codoped phosphate fiber laser with a pump power of 100 mW, the calculated pump and signal power distribution along the fiber length are shown in Fig. 3.8 [66].

It is then clear that the steady-state distribution of the pump and signal power and then the RE ions at different energy levels varies along the gain fiber. Therefore, the heat conversion efficiency η should also be a function of the fiber length. In addition to the quantum defect between the pump and signal photons, the energy upconversion process also contributes considerably to the heat deposition in the

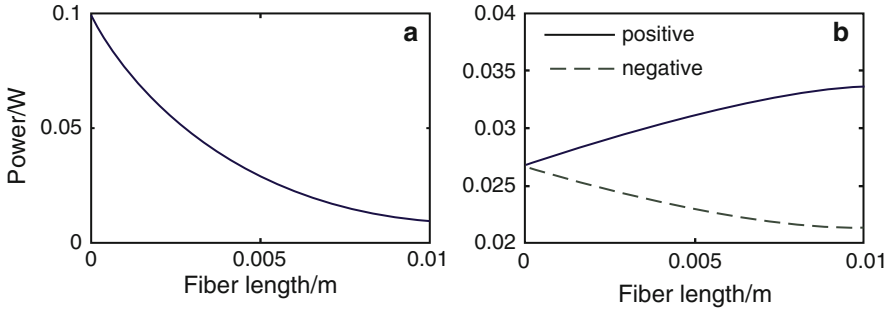

Fig. 3.8 Pump and signal powers as a function of the position along the fiber length: (**a**) pump power along the fiber length; (**b**) signal power in positive and negative directions along the fiber length. (Reprinted from Ref. [66], copyright 2009, with permission from OSA publishing)

Fig. 3.9 The heat conversion efficiency as a function of position along the fiber

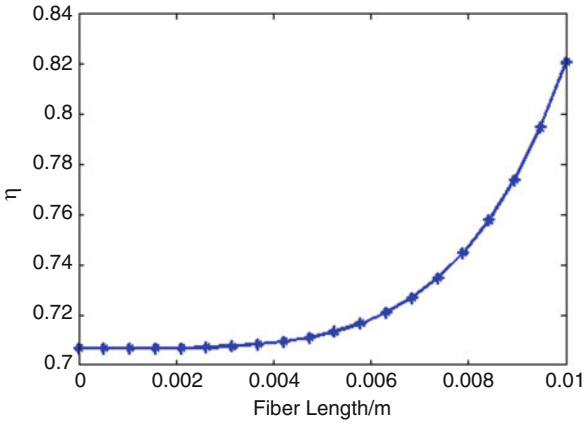

high-gain fiber laser. Denoting the population inversion density between the $^4I_{13/2}$ and $^4I_{15/2}$ energy level without and with upconversion as n^0 and n, then the fractional reduction of the population inversion caused by upconversion is written as [78, 79]:

$$F = \frac{n^0 - n}{n^0} \tag{3.28}$$

Then the position-dependent heat conversion efficiency is given by:

$$\eta(z) = F(z) + [1 - F(z)]\left(1 - \lambda_p/\lambda_s\right) \tag{3.29}$$

It can be readily calculated with the numerical solutions of the rate equations, as shown in Fig. 3.9. It is observed from the figure that fractional thermal loading increases monotonously along the fiber. The reason is that at the start of the fiber, the Er^{3+} ions at the $^4I_{13/2}$ energy level deplete significantly via stimulated emission

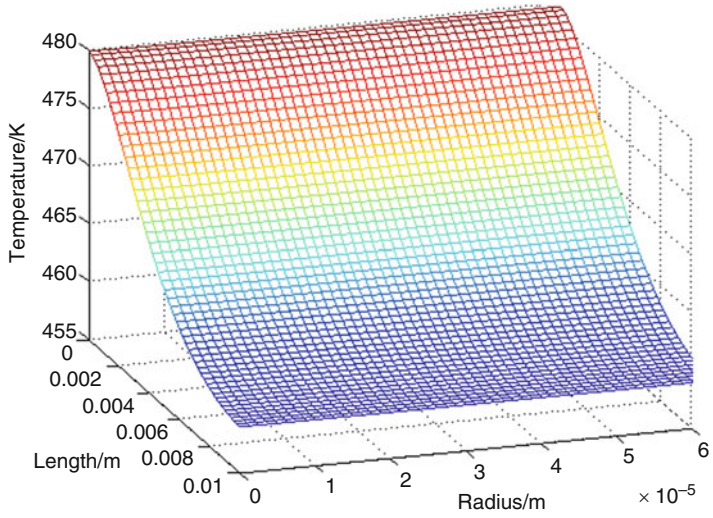

Fig. 3.10 The 3D temperature field distribution in highly Er^{3+}/Yb^{3+}-codoped phosphate fiber

owing to the high pump power. With the gradually weakening of the pump laser, the rate of the stimulated emission decreases, while the value of F increases rapidly.

Based on the above results, the heat function distribution $Q(z, r)$ of the fiber laser can be numerically obtained. Further, the exact 3D temperature field in the gain fiber can be calculated by utilizing Eqs. (3.8), (3.9), (3.10), (3.11) and (3.12), as shown in Fig. 3.10. Other parameters used in the calculations are the fiber thermal conductivity $k = 0.8W \cdot m^{-1}K^{-1}$, the heat transfer coefficient of air convection $h = 10\text{W} \cdot m^{-2} \cdot K^{-1}$, and the room temperature $T_h = 300K$. From the figure, the temperature is substantially unchanged in the radial direction, while it varies from ~480 K to approximately 460 K in the axial direction. The theoretical prediction was verified experimentally through integrating an end-pumped highly Er^{3+}/Yb^{3+}-codoped phosphate DBR laser into a copper tube and measuring its temperature distribution. The results indicate that developing effective cooling system is quite necessary to further produce higher output power of single-frequency laser. Moreover, theoretically acquired temperature field can be utilized to estimate the stress distribution, heat distortion, refractive index change-induced birefringence, and thermal lens effects and provide guidelines for the designing of high-power SFFLs.

3.4 Noise Properties of High-Gain Single-Frequency Fiber Lasers

3.4.1 Self-Heating Noise

In Sect. 2.2.3, we have briefly discussed the self-heating noise in SFFLs. When the pumping power is large enough, the laser frequency noise will be dominated by the self-heating noise that resulted from pump intensity noise-induced temperature fluctuations, other than the fundamental thermal noise. However, related theoretical model only considers the situation of low-gain fiber laser, in which the axial evolution of the heat accumulation can be neglected. For high-gain fiber lasers, our investigations in Sect. 3.3 on the 3D thermal analysis of the cavity have shown that the temperature varies remarkably along the fiber length. In view of this, we have carried out theoretical and experimental study on the self-heating noise of highly Er^{3+}/Yb^{3+}-codoped phosphate fiber laser [80].

Under the condition of a short-cavity DBR laser end-pumped with a 976 nm laser diode, the heat function in the cavity is written by:

$$Q(z,r,t) = \eta(z)\sigma_{ap}P_p(z,r,t) \tag{3.30}$$

where $P_p(z,r,t)$ is the distribution function of the pump field, and it is expressed as:

$$P_p(z,r,t) = P(t)h(z)|e(r)|^2 \tag{3.31}$$

in which $h(z)$ is the axial distribution function of the pump laser, of which the radial distribution function is $|e(r)|^2 = {}^{2}\!/_{\pi\omega_p^2}\exp\left({}^{-2r^2}\!/_{\omega_p^2}\right)$. Here we neglect the scattering loss of the pump and signal light in the fiber and substitute the heat function into the equation of heat conduction:

$$k\nabla^2 T - C_v T' = -Q(z,r,t) = \eta(z)\sigma_{ap}P(t)h(z)|e(r)|^2 \tag{3.32}$$

in which C_v is the specific heat capacity per unit volume.

Through a series of derivation, the transfer from the pump power to the temperature rising in the frequency domain is described by:

$$T(z,f) = \Theta(f)P(f)\eta(z)\sigma_{ap}h(z) \tag{3.33}$$

$$\Theta(f) = \frac{1}{4\pi k}E_1\left({}^{ik_1^2\omega_p^2}\!/_{2}\right)\exp\left({}^{ik_1^2\omega_p^2}\!/_{2}\right) \tag{3.34}$$

$$k_1 = \sqrt{{}^{C_v f}\!/_{2k}} \tag{3.35}$$

where $\Theta(f)$ is the frequency domain transfer function from the pump power change to the temperature fluctuation, and $E_1(\cdot)$ is the standard exponential integral function. Considering the large length to radius ratio of the fiber cavity, here we have neglected the effect of transverse temperature distribution. Based on the above analysis, the pump power fluctuation-induced laser frequency noise, i.e., self-heating noise can be estimated. According to Eq. (2.1), when the temperature change in the laser cavity is ΔT, then the corresponding frequency change satisfies the following equation:

$$\frac{\Delta\nu}{\nu\Delta T} = -\left(\frac{\Delta n}{n\Delta T} + \frac{\Delta l}{l\Delta T}\right) = -q \tag{3.36}$$

in which q is the thermo-optical coefficient of the fiber material. Then the self-heating effect-induced laser frequency change is:

$$\Delta\nu(f) = \nu q \int_0^l \Delta T(z,f)dz = -\nu q\Theta(f)\sigma_{ap}\Delta P(f)\int_0^l \eta(z)h(z)dz \tag{3.37}$$

The corresponding spectral power density of the frequency noise is then written as:

$$S_\nu(f) = \nu^2 q^2[\Theta(f)]^2 RIN_p(f)\sigma_{ap}^2 P_p^2\left[\int_0^l \eta(z)h(z)dz\right]^2 \tag{3.38}$$

where $\sigma_{ap}P_p\int_0^l \eta(z)h(z)dz = \Omega$ is the total heat that transferred from the pump laser in the cavity. It is worth noting that an extra filtering function $T(f)$ should be added into Eq. (3.37), owing to the filtering effects of RE ions themselves and the energy transfer processes between them on the pump power modulation, as well as finite thermal response time of the gain fiber [81]. Equation (3.38) can be directly calculated through numerically resolving the space-dependent rate equations and steady-state power transportation equations of a specific fiber laser, like what we have done in Sect. 3.3. Regarding a high-gain SFFL, its spontaneous emission effect is neglectful when it operates in a relative high-power regime, and then the total deposited heat in the laser cavity can be expressed as:

$$\Omega = P_p(1-\eta_1) \tag{3.39}$$

in which η_1 is the optical-to-optical efficiency of the laser. In this way, the final expression of the spectral power density of the self-heating noise is:

$$S_\nu(f) = \nu^2 q^2[\Theta(f)]^2 P_p^2 RIN_p(f)(1-\eta_1)^2[T(f)]^2 \tag{3.40}$$

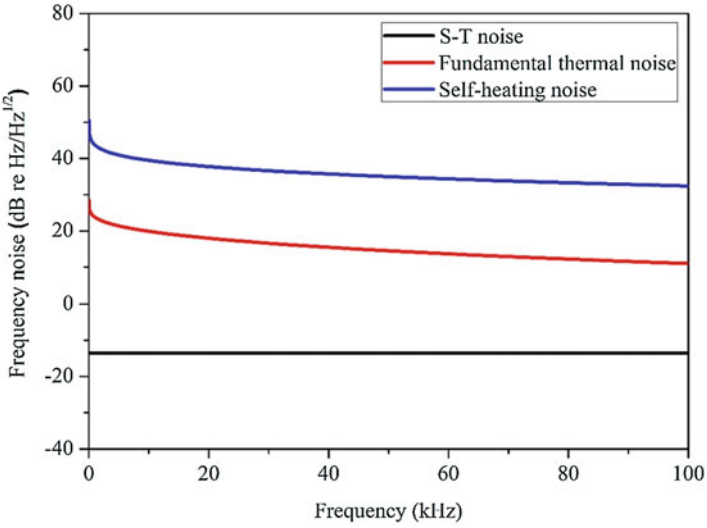

Fig. 3.11 Comparison of the main frequency noise components of high-gain SFFL

To calculate Eq. (3.40), we first measured the thermo-optical coefficient. The scheme is to encapsulate a high-gain phosphate SFFL into a copper tube and change its cavity temperature via a heat sink under the normal operating condition and then record the laser frequency variation with a scanning F-P interferometer. The actual measured thermo-optical coefficient is $q = 6.5 \times 10^{-6} K^{-1}$. It is noted that in the measurement process, the whole laser cavity has experienced the temperature change. In addition to the fiber length, the FBGs on both ends of the laser cavity would also affect the lasing frequency under temperature modulation. Therefore, the measured thermo-optical coefficient should represent the system property of the fiber laser other than the material property of the gain fiber.

Using the same condition and parameters as in Sect. 3.3, we have, respectively, calculated the S-T noise, fundamental thermal noise, and the self-heating noise of a highly Er^{3+}/Yb^{3+}-codoped phosphate SFFL, as shown in Fig. 3.11. It is shown that the self-heating noise overwhelms the other two noise components and should be given priority in optimizing the frequency noise of a high-gain fiber laser. For instance, a pump laser with lower intensity noise would be helpful in reducing the frequency noise of a high-gain SFFL. Moreover, optimizing the laser efficiency to decease the deposited heat in the cavity would be also desirable in suppressing the self-heating noise.

To further verify the theoretical model, we set up a high-gain DBR SFFL based on a segment of homemade heavily Er^{3+}/Yb^{3+}-codoped phosphate fiber. More details of the experiment can refer to Ref. [80]. Figure 3.12 demonstrates the measured and calculated frequency noise spectra of the laser at pump power of 106 mW and 253 mW, with corresponding optical-to-optical efficiency measured to be 35.4% and 42.3%, respectively. With filtering function set to $T(f) = 0.9$, the

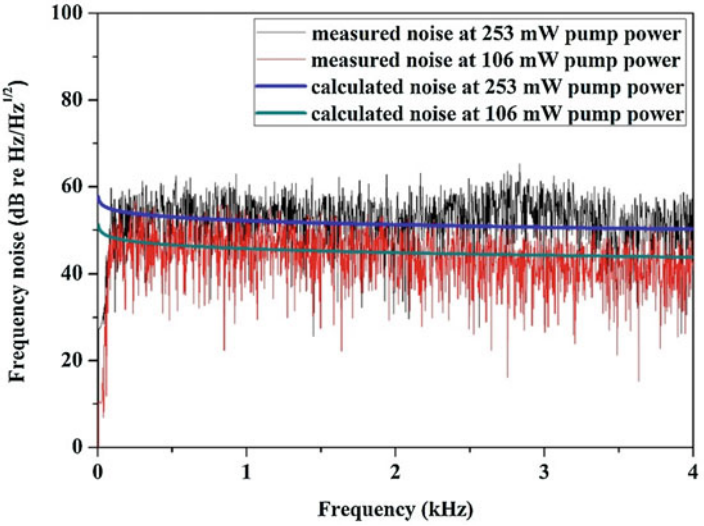

Fig. 3.12 Measured and calculated frequency noise spectra of the phosphate fiber laser at pump powers of 106 and 253 mW. (Reprinted from Ref. [80], copyright 2013, with permission from IOP publishing)

calculation agrees well with the measurement. Separate measurements of the frequency noise under different temperature of the heat sink did not observe any intrinsic thermal noise components, suggesting that the self-heating effect is the dominating noise source.

3.4.2 Coupling Between Frequency and Intensity Noise

According to the analysis of the self-heating effect, the frequency noise of high-gain single-frequency laser is directly related to the pump intensity noise, as indicated by Eq. (3.40). Besides, the pump power fluctuation is also the main component of the low-frequency intensity noise – technical noise of SFFLs. Regarding a well-built SFFL that working in the normal regime, i.e., the output power increases linearly with the enhancement of the pump power, the laser intensity noise is written as [82]:

$$RIN = RIN_p + 20\log\left[P_p/\left(P_p - P_{th}\right)\right] \tag{3.41}$$

in which P_{th} is the threshold pump power of the laser. When the laser has a low threshold and the pump power is large enough, the RIN of the laser is approximately equal to that of the pump source. It is straightforward that the frequency noise and intensity noise of high-gain SFFL are coupled in the low-frequency band through the pump power fluctuations.

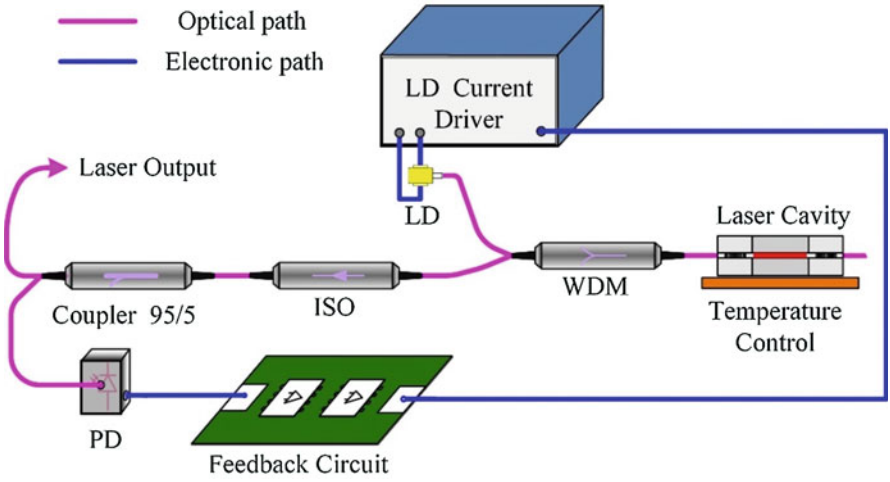

Fig. 3.13 Experimental setup of the single-frequency phosphate fiber laser with the optoelectronic feedback system. (Reprinted from Ref. [83], copyright 2015, with permission from IOP publishing)

To verify this analysis, we have conducted a "noise eater" scheme on a high-gain phosphate SFFL, i.e., detect the laser noise signal and then electronically feedback to the driving current of the pump laser [83]. Figure 3.13 demonstrates the experimental setup of the optoelectronic feedback system. The configuration of the temperature-controlled cavity was quite similar to that in Ref. [80]. The laser cavity was pumped by a 976 nm laser diode (LD) through a WDM, after which a ISO was employed to output the laser signal and block the backscattering light. Subsequently, a 95/5 fiber coupler was utilized to directing 5% of the output to a PD, which translate the optical signal to electronic signal. Then a custom feedback circuit (two-stage lag-lead type RC-filter) was used to compare the signal from the PD with a high precision, low-noise reference voltage to acquire the error signal, which was subsequently low-pass filtered, amplified, phase shifted, and added to the LD current driver to adjust the pump power. By intentionally imposing a modulation signal on the pump power, the transfer function from the pump power to the laser output was measured and was used to determine the parameters of the feedback circuit. The performances of this optoelectronic feedbacked laser were examined at the laser output port.

Figure 3.14 shows the measured intensity noise spectra of the laser with and without noise suppression, as well as the PD and RF SA noise floors. It is observed that the laser intensity noise was substantially suppressed at frequencies lower than 14 kHz, with a maximum noise reduction of over 20 dB from 0.3 to 3 kHz. Here the main limitation of the noise suppression was the noise level of the electronic system. Owing to the combined action of the phase shifting and the gain curves of the feedback loop, extra noise was found to be introduced into the laser, as illustrated by the slight elevation of the noise spectra from 14 to 50 kHz. In addition, further assessing of the laser output power revealed that the low-frequency suppression of

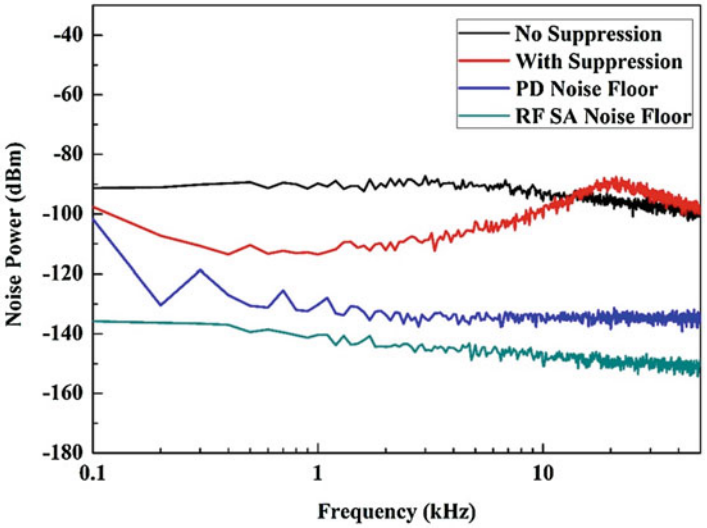

Fig. 3.14 The intensity noise spectra of the fiber laser with and without noise suppression. Also shown are the PD and RF SA noise floors. (Reprinted from Ref. [83], copyright 2015, with permission from IOP publishing)

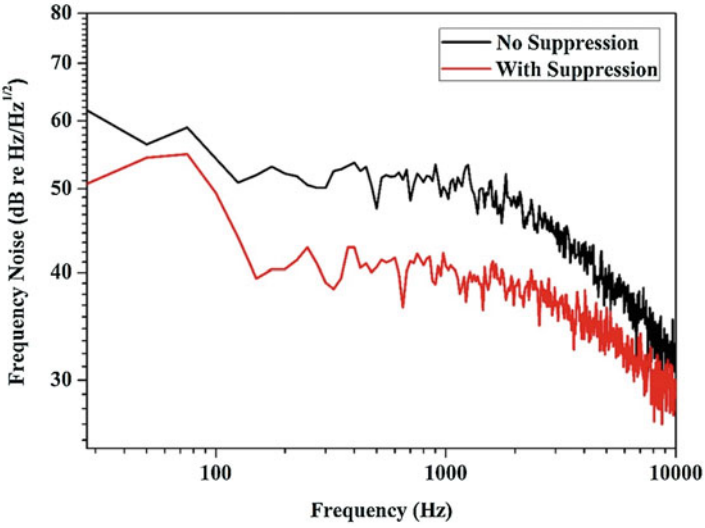

Fig. 3.15 The frequency noise power spectra of the fiber laser with and without noise suppression. (Reprinted from Ref. [83], copyright 2015, with permission from IOP publishing)

the intensity noise has improved the laser instability from ±1.7% to ±0.1% for a period of 2 hours. The frequency noise was also measured with and without the optoelectronic feedback, as shown in Fig. 3.15. From the figure, the noise reduction

range was higher than 10 kHz, while the maximum reduction was about 10 dB at around 1 kHz. The relatively smaller suppression extent of the frequency noise compared with that of the intensity noise might be attributed to the susceptivity of the laser frequency to external disturbances such as the acoustical, mechanical, and thermal perturbations.

It is then concluded that the frequency and intensity noise of a high-gain SFFL are correlated at the low-frequency band through the pump power fluctuation. In the meantime, this correlation can be advantageously exploited to suppress laser frequency and intensity noise simultaneously with a simple "noise eater" scheme. Essentially, the optoelectronic feedback scheme is commonly utilized to suppress the frequency and intensity noise separately, with different noise discrimination and feedback actuation system. Nevertheless, the individual noise suppression setup would more or less affect the performance of its counterpart. Pioneer work was demonstrated in Ref. [84, 85], in which the authors achieved simultaneous noise suppression of a monolithic nonplanar Nd:YAG ring laser by locking it to a frequency reference through feeding back to the pump driving current. In our experiment, the error signal was obtained in an electronic manner, rendering the whole system simple and compact. Although the noise suppression extent and bandwidth of the optoelectronic feedback scheme are substantially less than that of the all optical noise suppression method as discussed in Sect. 3.4.3, it is still desirable in realizing a stable SFFL source with a simple and practicable manner.

3.4.3 Amplified Spontaneous Emission Noise

In general, the ASE noise of SFFLs is negligible and can be hardly observed in experiment. Theoretical analysis has shown that the ASE noise components in both the frequency and intensity noise are frequency independent (white noise) and should be far less than the other noise components. However, in cases such as a high-gain fiber laser at 1083 nm as shown in Fig. 3.4, things might be different as strong ASE raises in a wavelength range wider than 100 nm. Under this condition, the ASE would exchange energy with the laser signal during operation and then deteriorate the noise performances [86, 87]. By employing a band-pass filter (BPF), we have studied the effects of ASE on the noise characteristics of heavily Yb^{3+}-doped phosphate SFFL at 1083 nm [88]. Examination of the optical spectra shows that the BPF have improved the SNR of the laser by about 15 dB.

Figure 3.16 demonstrates the intensity noise spectra of the laser with and without the BPF at different pump powers. It is noted that the laser signal under test was strictly maintained at a constant power by using a variable optical attenuator, to facilitate direct comparing of the results. It can be observed from the figure that beyond the relaxation oscillation peak, the intensity noise before filtering was higher than that after filtering at pump power of 39 mW, with a maximum difference of over 3 dB, while the difference decreased with increasing of the pump power and almost vanished at pump power of 294 mW. It is therefore concluded that the ASE noise in

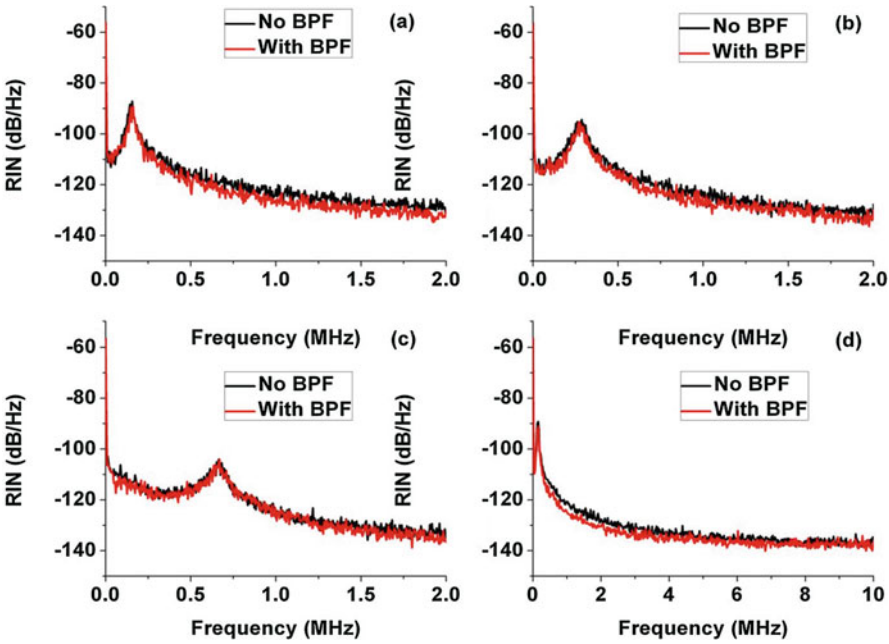

Fig. 3.16 RIN of the fiber laser with and without BPF at different powers of the pump LD: (**a**) 39 mW; (**b**) 68 mW; (**c**) 294 mW; (**d**) 39 mW. (Reprinted from Ref. [88], copyright 2014, with permission from IOP publishing)

the high-gain 1083 nm fiber laser emerges at low operation power, and it can be removed by enhancing the pump power. Figure 3.16(d) shows the noise spectra at 39 mW pump power from 0 to 10 MHz, and it can be seen that the observed ASE noise was mainly distributed in the frequency range of 300 kHz–4 MHz. This makes sense, as at lower frequencies the dominating noise are technical noise and relaxation oscillation, while at higher frequencies, the laser cavity filters all the noise sources, and the noise spectrum approaches the shot noise limit.

The frequency noise of the laser was also measured and compared before and after filtering at pump power of 39 mW and 294 mW, and the results are shown in Fig. 3.17. Similar to the condition of the intensity noise, there was a gap of more than 7 dB between the frequency noise spectra with and without the BPF at pump power of 39 mW. At pump power of 294 mW, the profiles of the two noise spectra coincided with each other. Therefore, the ASE noise also dominates the frequency noise at low operation power condition. Additionally, further examination of the frequency noise after spectrum filtering revealed that its evolution with the pump power aligns with the prediction of Eq. (3.30), indicating that the dominating noise component has transferred from the ASE noise at low-power regime to the self-heating noise at high-power regime. Finally, it is worth noting that to the best of our knowledge, this is the first time that the ASE noise of a SFFL has been experimentally observed in the frequency spectrum.

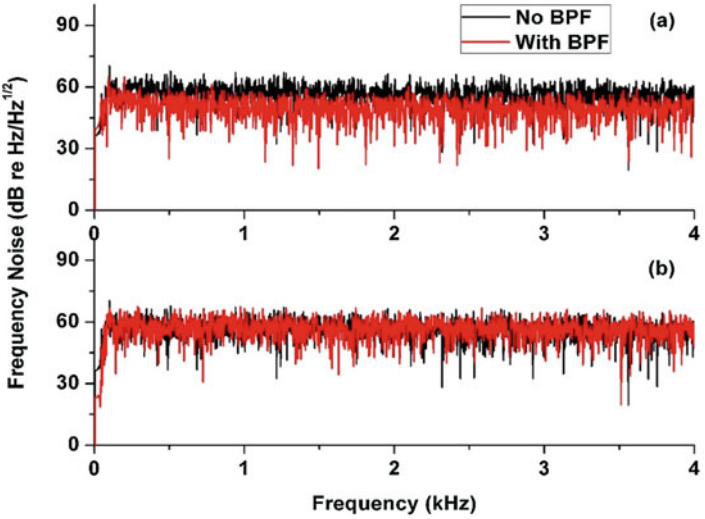

Fig. 3.17 Measured laser frequency noise with and without BPF under different pump powers: (**a**) 39 mW; (**b**) 294 mW. (Reprinted from Ref. [88], copyright 2014, with permission from IOP publishing)

References

1. Willke B (2010) Stabilized lasers for advanced gravitational wave detectors. Laser Photonics Rev 4:780
2. Ma Y, Wang X, Leng J, Xiao H, Dong X, Zhu J, Du W, Zhou P, Xu X, Si L (2011) Coherent beam combination of 1.08 kW fiber amplifier array using single-frequency dithering technique. Opt Lett 36:951
3. Yang F, Ye Q, Pan Z, Chen D, Cai H, Qu R, Yang Z, Zhang Q (2012) 100-mW linear polarization single-frequency all-fiber seed laser for coherent Doppler lidar application. Opt Commun 285:149
4. Xiao H, Zhou P, Wang X, Guo S, Xu X (2012) Experimental investigation on 1018-nm high-power ytterbium-doped fiber amplifier. IEEE Photon Technol Lett 24:1088
5. Chaboyer ZJ, Moore PJ, Das G (2009) Medium power single-mode single-wavelength fiber laser. Opt Commun 282:3100
6. Quimby RS, Miniscalco WJ, Thompson B (1994) Clustering in erbium-doped silica glass fibers analyzed using 980 nm excited-state absorption. J Appl Phys 76:4472
7. Jiang S, Myers M, Peyghambarian N (1998) Er^{3+} doped phosphate glasses and lasers. J Non-Cryst Solids 239:143
8. Jiang C, Liu H, Zeng Q, Tang X, Gan F (2000) Yb: phosphate laser glass with high emission cross-section. J Phys Chem Solids 61:1217
9. Campbell JH, Suratwala TI (2000) Nd-doped phosphate glasses for high-energy/high-peak-power lasers. J Non-Cryst Solids 263:318
10. Hwang BC, Jiang S, Luo T, Watson J, Honkanen S, Hu Y, Smektala F, Lucas J, Peyghambarian N (1999) Erbium-doped phosphate glass fibre amplifiers with gain per unit length of 2.1 dB/cm. Electron Lett 35:1007
11. Tao G, Ebendorff-Heidepriem H, Stolyarov AM, Danto S, Badding JV, Fink Y, Ballato J, Abouraddy AF (2015) Infrared fibers. Adv Opt Photon 7:379

12. Jackson SD (2012) Towards high-power mid-infrared emission from a fibre laser. Nat Photonics 6:423
13. Henderson-Sapir O, Munch J, Ottaway DJ (2014) Mid-infrared fiber lasers at and beyond 3.502 μm using dual-wavelength pumping. Opt Lett 39:493
14. Hudson D, Magi E, Gomes L, Jackson SD (2011) 1 W diode-pumped tunable Ho^{3+}, Pr^{3+}-doped fluoride glass fibre laser. Electron Lett 47:985
15. Veasey DL, Funk DS, Peters PM, Sanford NA, Obarski GE, Fontaine N, Young M, Peskin AP, Liu W, Houde-Walter SN (2000) Yb/Er-codoped and Yb-doped waveguide lasers in phosphate glass. J Non-Cryst Solids 263:369
16. Sakamoto T, Shimizu M, Kanamori T, Terunuma Y, Ohishi Y, Yamada M, Sudo S (1995) 1.4-μm-band gain characteristics of a Tm-Ho-doped ZBLYAN fiber amplifier pumped in the 0.8-μm band. IEEE Photon Technol Lett 7:983
17. Jackson SD, Sabella A, Lancaster DG (2007) Application and development of high-power and highly efficient silica-based Fiber lasers operating at 2 μm. IEEE J Sel Top Quantum Electron 13:567
18. Spiegelberg C, Geng J, Hu Y, Kaneda Y, Jiang S, Peyghambarian N (2004) Low-noise narrow-linewidth fiber laser at 1550 nm (June 2003). J Lightwave Technol 22:57
19. Kaneda Y, Spiegelberg C, Geng J, Hu Y, Luo T, Wang J, Jiang S (2004) 200-mW, narrow-linewidth 1064.2-nm Yb-doped fiber laser. In: Conference on lasers and electro-optics, p CThO3
20. Albert J, Schulzgen A, Temyanko VL, Honkanen S, Peyghambarian N (2006) Strong Bragg gratings in phosphate glass single mode fiber. Appl Phys Lett 89:101127
21. Grobnic D, Mihailov SJ, Walker RB, Smelser CW, Lafond C, Croteau A (2007) Bragg gratings made with a femtosecond laser in heavily doped Er-Yb phosphate glass fiber. IEEE Photon Technol Lett 19:943
22. Loh WH, Samson BN, Dong L, Cowle GJ, Hsu K (1998) High performance single-frequency fiber grating-based erbium: ytterbium-codoped fiber lasers. J Lightwave Technol 16:114
23. Foster S (2004) Spatial mode structure of the distributed feedback fiber laser. IEEE J Quantum Electron 40:884
24. Hofmann P, Pirson-Chavez A, Schülzgen A, Xiong L, Laronche A, Albert J, Peyghambarian N (2011) Low-noise single-frequency all phosphate fiber laser. In: SPIE proceedings, Laser technology for defense and security VII, p 803911
25. Qiu T, Suzuki S, Schülzgen A, Li L, Polynkin A, Temyanko V, Moloney JV, Peyghambarian N (2005) Generation of watt-level single-longitudinal-mode output from cladding-pumped short fiber lasers. Opt Lett 30:2748
26. Qiu T, Li L, Schulzgen A, Temyanko VL, Luo T, Jiang S, Mafi A, Moloney JV, Peyghambarian N (2004) Generation of 9.3-W multimode and 4-W single-mode output from 7-cm short fiber lasers. IEEE Photon Technol Lett 16:2592
27. Li L, Morrell M, Qiu T, Temyanko VL, Schülzgen A, Mafi A, Kouznetsov D, Moloney JV, Luo T, Jiang S (2004) Short cladding-pumped Er/Yb phosphate fiber laser with 1.5 W output power. Appl Phys Lett 85:2721
28. Zhang G, Wang M, Yu C, Zhou Q, Qiu J, Hu L, Chen D (2011) Efficient generation of watt-level output from short-length nd-doped phosphate fiber lasers. IEEE Photon Technol Lett 23:350
29. Wadsworth W, Percival R, Bouwmans G, Knight J, Russell P (2003) High power air-clad photonic crystal fibre laser. Opt Express 11:48
30. Limpert J, Schreiber T, Nolte S, Zellmer H, Tunnermann T, Iliew R, Lederer F, Broeng J, Vienne G, Petersson A (2003) High-power air-clad large-mode-area photonic crystal fiber laser. Opt Express 11:818
31. Li L, Schülzgen A, Temyanko VL, Qiu T, Morrell MM, Wang Q, Mafi A, Moloney JV, Peyghambarian N (2005) Short-length microstructured phosphate glass fiber lasers with large mode areas. Opt Lett 30:1141

32. Li L, Schülzgen A, Temyanko VL, Morrell MM, Sabet S, Li H, Moloney JV, Peyghambarian N (2006) Ultracompact cladding-pumped 35-mm-short fiber laser with 4.7-W single-mode output power. Appl Phys Lett 88:161106
33. Xu SH, Yang ZM, Liu T, Zhang WN, Feng ZM, Zhang QY, Jiang ZH (2010) An efficient compact 300 mW narrow-linewidth single-frequency fiber laser at 1.5 μm. Opt Express 18:1249
34. Xu S, Yang Z, Zhang W, Wei X, Qian Q, Chen D, Zhang Q, Shen S, Peng M, Qiu J (2011) 400 mW ultrashort cavity low-noise single-frequency Yb^{3+}-doped phosphate fiber laser. Opt Lett 36:370
35. Mo S, Xu S, Huang X, Zhang W, Feng Z, Chen D, Yang T, Yang Z (2013) A 1014 nm linearly polarized low noise narrow-linewidth single-frequency fiber laser. Opt Express 21:12419
36. Hofmann P, Voigtlander C, Nolte S, Peyghambarian N, Schülzgen A (2013) 550-mW output power from a narrow linewidth all-phosphate fiber laser. J Lightwave Technol 31:756
37. Zhu X, Shi W, Zong J, Nguyen D, Norwood RA, Chavez-Pirson A, Peyghambarian N (2012) 976 nm single-frequency distributed Bragg reflector fiber laser. Opt Lett 37:4167
38. Xu S, Li C, Zhang W, Mo S, Yang C, Wei X, Feng Z, Qian Q, Shen S, Peng M (2013) Low noise single-frequency single-polarization ytterbium-doped phosphate fiber laser at 1083 nm. Opt Lett 38:501
39. Jackson SD, King T (1998) High-power diode-cladding-pumped tm-doped silica fiber laser. Opt Lett 23:1462
40. Scholle K, Lamrini S, Koopmann P, Fuhrberg P (2010) 2 μm laser sources and their possible applications. In: Frontiers in guided wave optics and optoelectronics. IntechOpen, Bishnu Pal, p 491
41. Walsh BM (2009) Review of tm and Ho materials; spectroscopy and lasers. Laser Phys 19:855
42. Agger S, Povlsen JH, Varming P (2004) Single-frequency thulium-doped distributed-feedback fiber laser. Opt Lett 29:1503
43. Wu J, Jiang S, Luo T, Geng J, Peyghambarian N, Barnes NP (2006) Efficient thulium-doped 2-μm germanate fiber laser. IEEE Photon Technol Lett 18:334
44. Geng J, Wu J, Jiang S, Yu J (2007) Efficient operation of diode-pumped single-frequency thulium-doped fiber lasers near 2 μm. Opt Lett 32:355
45. Wu J, Yao Z, Zong J, Chavez-Pirson A, Peyghambarian N, Yu J (2009) Single-frequency fiber laser at 2.05 μm based on Ho-doped germanate glass fiber. In: SPIE proceedings, Fiber lasers VI: technology, systems, and applications, p 71951K
46. He X, Xu S, Li C, Yang C, Yang Q, Mo S, Chen D, Yang Z (2013) 1.95 μm kHz-linewidth single-frequency fiber laser using self-developed heavily Tm^{3+}-doped germanate glass fiber. Opt Express 21:20800
47. Zhang Z, Shen DY, Boyland AJ, Sahu JK, Clarkson WA, Ibsen M (2008) High-power tm-doped fiber distributed-feedback laser at 1943 nm. Opt Lett 33:2059
48. Zhang Z, Boyland AJ, Sahu JK, Clarkson WA, Ibsen M (2011) High-power single-frequency thulium-doped fiber DBR laser at 1943 nm. IEEE Photon Technol Lett 23:417
49. Geng J, Wang Q, Luo T, Jiang S, Amzajerdian F (2009) Single-frequency narrow-linewidth tm-doped fiber laser using silicate glass fiber. Opt Lett 34:3493
50. Gebavi H, Milanese D, Liao G, Chen Q, Ferraris M, Ivanda M, Gamulin O, Taccheo S (2009) Spectroscopic investigation and optical characterization of novel highly thulium doped tellurite glasses. J Non-Cryst Solids 355:548
51. Richards B, Jha A, Tsang Y, Binks D, Lousteau J, Fusari F, Lagatsky A, Brown C, Sibbett W (2010) Tellurite glass lasers operating close to 2 μm. Laser Phys Lett 7:177
52. Wang M, Wang G, Yi L, Li S, Hu L, Zhang J (2010) 2 μm emission performance of Tm^{3+}-Ho^{3+} co-doped tellurite glasses. Chin Opt Lett 8:78
53. Richards B, Tsang Y, Binks D, Lousteau J, Jha A (2008) Efficient ~2 μm Tm^{3+}-doped tellurite fiber laser. Opt Lett 33:402
54. Richards B, Shen S, Jha A, Tsang Y, Binks D (2007) Infrared emission and energy transfer in Tm^{3+}, Tm^{3+}-Ho^{3+} and Tm^{3+}-Yb^{3+}-doped tellurite fibre. Opt Express 15:6546

55. Tsang Y, Richards B, Binks D, Lousteau J, Jha A (2008) Tm^{3+}/Ho^{3+} codoped tellurite fiber laser. Opt Lett 33:1282
56. Tsang Y, Richards B, Binks D, Lousteau J, Jha A (2008) A $Yb^{3+}/Tm^{3+}/Ho^{3+}$ triply-doped tellurite fibre laser. Opt Express 16:10690
57. Li K, Zhang G, Hu L (2010) Watt-level ~2 μm laser output in Tm^{3+}-doped tungsten tellurite glass double-cladding fiber. Opt Lett 35:4136
58. Li K, Zhang G, Wang X, Hu L, Kuan P, Chen D, Wang M (2012) Tm^{3+} and Tm^{3+}-Ho^{3+} co-doped tungsten tellurite glass single mode fiber laser. Opt Express 20:10115
59. Caron N, Bernier M, Faucher D, Vallée R (2012) Understanding the fiber tip thermal runaway present in 3μm fluoride glass fiber lasers. Opt Express 20:22188
60. Schliesser A, Picque N, Hansch TW (2012) Mid-infrared frequency combs. Nat Photonics 6:440
61. Bernier M, Michaud-Belleau V, Levasseur S, Fortin V, Genest J, Vallée R (2015) All-fiber DFB laser operating at 2.8 μm. Opt Lett 40:81
62. Davis MK, Digonnet M, Pantell RH (1998) Thermal effects in doped fibers. J Lightwave Technol 16:1013
63. Canat G, Mollier J, Jaouën Y, Dussardier B (2005) Evidence of thermal effects in a high-power Er^{3+}-Yb^{3+} fiber laser. Opt Lett 30:3030
64. Feng S, Li S, Chen L, Chen W, Hu L (2010) Thermal loading in laser diode end-pumped Yb^{3+}/Er^{3+} codoped phosphate glass laser. Appl Opt 49:3357
65. Sudesh V, Mccomb T, Chen Y, Bass M, Richardson M, Ballato J, Siegman AE (2008) Diode-pumped 200 μm diameter core, gain-guided, index-antiguided single mode fiber laser. Appl Phys B Lasers Opt 90:369
66. Liu T, Yang ZM, Xu SH (2009) 3-dimensional heat analysis in short-length Er^{3+}/Yb^{3+} co-doped phosphate fiber laser with upconversion. Opt Express 17:235
67. Wang Y, Xu CQ, Po H (2004) Analysis of Raman and thermal effects in kilowatt fiber lasers. Opt Commun 242:487
68. Innocenzi ME, Yura HT, Fincher CL, Fields RA (1990) Thermal modeling of continuous-wave end-pumped solid-state lasers. Appl Phys Lett 56:1831
69. Song F, Liu S, Wu Z, Cai H, Zhang X, Teng L, Tian J (2007) Determination of the thermal loading in laser-diode-pumped erbium-ytterbium-codoped phosphate glass microchip laser. J Opt Soc Am B 24:2327
70. Bjurshagen S, Hellström JE, Pasiskevicius V, Pujol MC, Aguiló M, Díaz F (2006) Fluorescence dynamics and rate equation analysis in Er^{3+} and Yb^{3+} doped double tungstates. Appl Opt 45:4715
71. Song F, Zhang G, Shang M, Tan H, Yang J, Meng F (2001) Three-photon phenomena in the upconversion luminescence of erbirum-ytterbium-codoped phosphate glass. Appl Phys Lett 79:1748
72. Karlsson G, Laurell F, Tellefsen J, Denker B, Galagan B, Osiko V, Sverchkov S (2002) Development and characterization of Yb-Er laser glass for high average power laser diode pumping. Appl Phys B Lasers Opt 75:41
73. Karasek M (1997) Optimum design of Er^{3+}-Yb^{3+} co-doped fibers for large-signal high-pump-power applications. IEEE J Quantum Electron 33:1699
74. Myslinski P, Nguyen D, Chrostowski J (1997) Effects of concentration on the performance of erbium-doped fiber amplifiers. IEEE J Lightwave Technol 15:112
75. Chryssou CE, Di Pasquale F, Pitt CW (2001) Improved gain performance in Yb^{3+}-sensitized Er^{3+}-doped alumina (Al_2O_3) channel optical waveguide amplifiers. J Lightwave Technol 19:345
76. Kelson I, Hardy AA (1998) Strongly pumped fiber lasers. IEEE J Quantum Electron 34:1570
77. Henry C (1986) Theory of spontaneous emission noise in open resonators and its application to lasers and optical amplifiers. J Lightwave Technol 4:288
78. Bjurshagen S, Koch R (2004) Modeling of energy-transfer upconversion and thermal effects in end-pumped quasi-three-level lasers. Appl Opt 43:4753

79. Lan YP, Chen YF, Wang SC (2000) Repetition-rate dependence of thermal loading in diode-end-pumped Q-switched lasers: influence of energy-transfer upconversion. Appl Phys B Lasers Opt 71:27
80. Li C, Xu S, Yang C, Wei X, Yang Z (2013) Frequency noise of high-gain phosphate fiber single-frequency laser. Laser Phys 23:045107
81. Taccheo S, Laporta P, Svelto O, De Geronimo G (1996) Intensity noise reduction in a single-frequency ytterbium-codoped erbium laser. Opt Lett 21:1747
82. Agger SD, Povlsen JH (2006) Dynamical noise in single-mode distributed feedback fiber lasers. IEEE J Quantum Electron 42:433
83. Li C, Xu S, Xiao Y, Feng Z, Yang C, Zhou K, Yang Z (2015) Simultaneously reducing the intensity and frequency noise of single-frequency phosphate fiber laser. J Opt 17:075802
84. Willke B, Brozek S, Danzmann K, Quetschke V, Gossler S (2000) Frequency stabilization of a monolithic Nd:YAG ring laser by controlling the power of the laser-diode pump source. Opt Lett 25:1019
85. Heurs M, Quetschke VM, Willke B, Danzmann K, Freitag I (2004) Simultaneously suppressing frequency and intensity noise in a Nd:YAG nonplanar ring oscillator by means of the current-lock technique. Opt Lett 29:2148
86. Dandridge A, Tveten AB, Miles RO, Jackson DA, Giallorenzi TG (1981) Single-mode diode laser phase noise. Appl Phys Lett 38:77
87. Shtaif M, Eisenstein G (1996) Noise properties of nonlinear semiconductor optical amplifiers. Opt Lett 21:1851
88. Li C, Xu S, Feng Z, Xiao Y, Mo S, Yang C, Zhang W, Chen D, Yang Z (2014) The ASE noise of a Yb^{3+}-doped phosphate fiber single-frequency laser at 1083 nm. Laser Phys Lett 11:025104

Chapter 4
Fiber Nonlinear Single-Frequency Lasers

Other than the rare-earth ions dopants, nonlinear effects can also provide optical gain in a fiber, generally at a detuned wavelength. Since this detuning can be controlled through modifying the parameters of the glass fiber or the pump source, the nonlinear fiber effects (i.e., stimulated Raman scattering and four-wave mixing) can therefore be leveraged to allow for laser operation at spectral bands that cannot be covered by conventional rare-earth ions. However, since the nonlinear effects generally require a long optical path to take place, the resulted narrow mode spacing renders single-mode oscillation difficult to be realized. In this way, relatively complex cavity design such as multi-ring structure is indispensable to achieve fiber nonlinear single-frequency lasers. An exception is the Brillouin fiber laser, which has a very narrow gain bandwidth (several tens of MHz) and can even suppress the linewidth of the pump laser, while its wavelength detuning from the pump is negligible (<0.1 nm). In this chapter, we first introduce the nonlinear effects in optical fibers. Then the Raman and Brillouin fiber lasers are discussed together with the random distributed feedback laser scheme, with the following discussion of fiber optical parametric oscillator.

4.1 Nonlinear Effects in Optical Fibers

Owing to the intensity dependence of the refractive index or the inelastic scattering of the glass medium, nonlinear effects would take place accordingly when a laser light with specific parameters transmits in optical fibers [1, 2]. Essentially, a nonlinear phenomenon means that the process is intensity-dependent. The origin of nonlinear effects in the fiber medium is its third-order susceptibility $\chi^{(3)}$, of which the real part is responsible for the modifying of the refractive index – Kerr effect – while the imaginary part leads to inelastic scattering of the transmitting signal.

Depending on the actual parameters of the optical fiber and the signal, Kerr nonlinearities can cause the occurrence of self-phase modulation (SPM), cross-

© Springer Nature Singapore Pte Ltd. 2019

Z. Yang et al., *Single-Frequency Fiber Lasers*, Optical and Fiber Communications Reports 8, https://doi.org/10.1007/978-981-13-6080-0_4

phase modulation (CPM), and four-wave mixing (FWM). When an optical pulse is propagating in an optical fiber, the SPM effect would induce intensity-dependent phase modulation of the pulse with the association of the spectrum modification. Regarding the CPM effect, it refers to a phenomenon that the nonlinear phase modulation of an optical pulse is caused by the interaction with another co-propagating pulse in the fiber. The FWM effect is described as: if two optical fields with carrier frequencies ω_1 and ω_2 propagate together in an optical fiber, intensity-dependent refractive index modulation at the two different frequencies would create two additional optical fields at $\omega_3 = 2\omega_1 - \omega_2$ and $\omega_4 = 2\omega_2 - \omega_1$. In addition, this process can also take place when two of the four frequencies coincide, resulting in the degenerate FWM.

Considering the inelastic scattering, it would partly shift a high-power optical signal to a new frequency in a stimulated manner. In brief, the scattering process is caused by the vibration of the glass lattice, and optical phonon-associated vibration produces stimulated Raman scattering (SRS), while acoustical phonon-associated phonon yields stimulated Brillouin scattering (SBS). In SRS, a pump photon converts to a Stokes photon and an associated optical phonon according to the law of energy conservation. In addition, a pre-existing phonon can also interact with a pump photon to generate an anti-Stokes photon with wavelength shorter than that of the pump photon. In the process of SBS, a pump photon is converted into a backward scattered Stokes photon and an acoustical phonon through the electrostriction effect. The Brillouin frequency shift can be calculated by $2v_a\nu_p/C$, where v_a is the velocity of sound in the fiber medium, ν_p is the frequency of the pump, and C is the speed of light in the fiber.

It can be concluded that the SPM and CPM only affect the phase of the optical signals, while the FWM, SRS, and SBS process can deplete the energy of the pump and create optical fields at other frequencies. Therefore, these effects that involve the generation of new frequency can be exploited to construct fiber lasers and amplifiers with merits that cannot be provided by the traditional RE ions doped fibers. In the rest of this chapter, we will give the state-of-the-art overview of fiber nonlinear single-frequency lasers by highlighting the most recent progress.

4.2 Raman and Brillouin Fiber Lasers

In principle, the Raman and Brillouin scattering effects inside the optical fiber can both be utilized to achieve single-frequency lasers, given that the nonlinear gain bandwidth or the associated filter bandwidth is narrow enough to support only one longitudinal mode to survive. In this way, the main difference between the nonlinear fiber laser and the RE ions doped fiber laser is the origin of the optical gain, while the configuration of the laser cavity should be similar. By constructing a Raman fiber laser (RFL), one can achieve single-frequency lasing at wavelengths well beyond the gain bandwidth of RE ions, depending only on the availability of appropriate pump sources. However, since the gain provided by the SRS effect is quite small, the

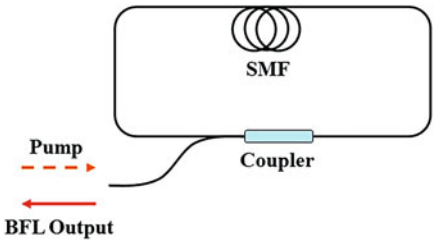

Fig. 4.1 Typical structure of the ring cavity BFL

typical cavity length required for efficient operation of the RFLs is at least 100 m, and it is then difficult to realize single-longitudinal mode oscillation [3, 4]. On the contrary, the SBS gain is much larger than that of the SRS, while the bandwidth of the SBS gain is generally several tens of megahertz and is exceedingly smaller than that of the SRS gain (>10 terahertz). In addition, the dynamic process of the SBS has the advantages of a low-pass filter which can reduce the intensity and frequency noise of the pump laser, for instance, the linewidth of the generated Stokes signal is typically several orders of magnitude narrower than that of the pump source. In view of this, Brillouin fiber laser (BFL) has drawn much attention thanks to its merit of realizing low noise narrow linewidth single-frequency laser sources since its first demonstration [5].

To date, both linear and ring cavity configuration were examined for the BFLs. Generally, the linear BFL employs FBG or optical circulator to make up a F-P cavity which allows the Brillouin to pump light and the SBS light to oscillate inside the resonator. However, it suffers from the problems such as the low output power and the generation of high-order Stokes and anti-Stokes light compared with the ring cavity BFLs, which also shows a comparatively simplicity [6, 7]. Figure 4.1 shows a typical structure of the ring cavity BFL, in which only an optical fiber coupler is used to launch the pump laser and couple a part of the light out of the ring cavity. The lasing mechanism is that the pump light reflects by a co-propagating index grating that induced by the thermally excited acoustic wave in the fiber and the produced counterpropagating Stokes light is correspondingly frequency downshifted according to the Doppler effect.

Practically, to reduce the required fiber length and the lasing threshold, as well as to obtain stable operation of the BFL, the pump laser frequency should be strictly matched to the Brillouin cavity mode, i.e., the pump and the Stokes light should simultaneously resonate inside the cavity [8]. Therefore, a frequency locking process must be implemented as the BFL is extremely sensitive to the frequency detuning between the pump laser and the ring cavity. The common method is to establish an electrically based active frequency locking loop which imposes modulation to adjust the cavity length or tune the pump laser frequency to lock the pump laser to a resonate frequency of the BFL [9, 10]. However, the modulating process would introduce problems such as degrading the noise characteristics of the BFL. Recently, passive frequency locking technique was also proposed, based on the self-injection locking of the semiconductor pump laser [11]. By implementing a fiber-optic F-P interferometer, which acts as not only the BFL cavity but also the frequency-

selective element, self-injection locking of the pump laser to a frequency that tracks the resonance frequency of the ring cavity was then realized. Another method is to utilize the transition population inversion grating induced in a section of unpumped active fiber to select the pump frequency, as demonstrated in Ref. [12].

Nevertheless, the frequency locking scheme is rather complex and susceptive to temperature and mechanical interferences. Another method is to prevent the pump laser from oscillating to guarantee the stable operation of the BFL, by utilizing optical fiber devices such as isolator and circulator. A coming forth advantage is that the operating wavelength of the BFL can be tuned optionally by simply adjusting the wavelength of the pump laser [13]. J. C. Yong et al. [14] demonstrated a novel BFL structure which employs an unbalanced Mach-Zehnder interferometer as the coupling device, which exhibits a frequency-dependent transmission characteristic to make sure that only the Stokes light can oscillate in the Brillouin ring cavity and makes it possible for a stable operating BFL. To compensate for the cavity loss and achieve high output power, besides increasing the length of the nonlinear gain fiber, which inevitably requires an extra extreme narrow bandwidth filter to maintain the single-frequency operation [15], improving the cavity gain is always considered to be more attractive. In recent years, a hybrid BFL which inserts a section of active fiber in the Brillouin ring cavity has been developed to be an effective type of laser structure to produce large output power. By combining the nonlinear gain from the Brillouin scattering with the linear gain from the RE ions, high-power hybrid BFLs have been both achieved at 1.0 μm and 1.5 μm [16–19]. It should be supplemented here that the active fiber can also be used to amplify the pump laser. By implementing a pump preamplification technique in the cavity, the Brillouin laser power was significantly increased in Ref. [20]. Figure 4.2 shows the corresponding experimental setup, in which the pump source from the DFB-LD was first pre-amplified by the 980 nm pumped EDF and then the amplified pump induced backscattering Brillouin signal in the opposite direction. Moreover, the clockwise traveled Brillouin signal can also acquire efficient optical gain from the EDF. The TOF was employed to suppress the ASE noise that resulted from the EDF. With this

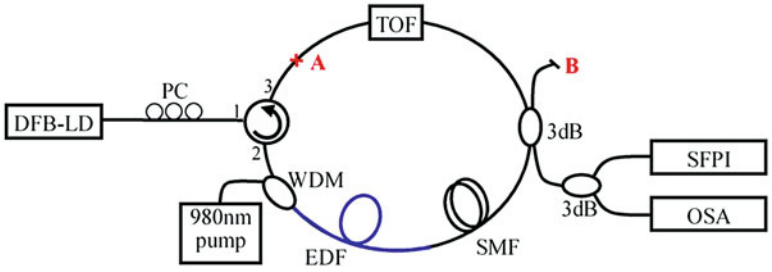

Fig. 4.2 Configuration of the proposed BEFL. DFB-LD, distributed feedback laser diode; WDM, wavelength-division multiplexer; EDF, erbium-doped fiber; SMF, single-mode fiber; PC, polarization controller; TOF, tunable optical filter; SFPI, scanning Fabry-Perot interferometer; OSA, optical spectrum analyzer. (Reprinted from Ref. [20], copyright 2012, with permission from OSA publishing)

laser structure, a low 980 nm pump threshold of about 15 mW and a slope efficiency of 10% were achieved. In a conventional hybrid BFL, the active fiber is generally placed right after the Brillouin fiber to amplify the laser signal.

The shortcoming of the hybrid BFL is mainly the ASE which would deteriorate the laser noise and the linewidth, owing to the presence of the RE ions active fiber. An alternative approach is to use nonlinear fiber with large Brillouin gain coefficient. As_2Se_3 chalcogenide fiber was first verified by K. S. Abedin to have a Brillouin gain coefficient that is about two orders of magnitude larger than that of the silica fiber. By constructing a 2-m-long F-P cavity based on the single mode As_2Se_3 fiber, single longitudinal Brillouin lasing was obtained with an optical conversion efficiency of about 15% [21–23]. Another promising candidate is the tellurite glass, K. S. Abedin [24] also investigated the SBS effect of single-mode tellurite glass fiber, and the Brillouin gain coefficient was measured to be in the range of 1.47×10^{-10}–2.16×10^{-10} m/W, which is over twice larger than that of the silica fiber. Additionally, the background loss of the tellurite fiber can be as low as 0.02 dB/m, which is at least one order of magnitude lower than that of the chalcogenide fiber and makes it ideal in achieving an efficient tellurite-based BFL [25, 26]. As to the chalcogenide fiber, K. H. Tow and coworkers [27] demonstrated a monomodal GeAsSe microstructured fiber and obtained a lowered transmission loss of 0.65 dB/m at 1.55 μm. Recently, to obtain a compact single-frequency BFL, researchers began to use a RE ions doped fiber as both the nonlinear and linear gain media. S. W. Harun et al. [28] demonstrated a BFL by using a 2.15 cm-long bismuth-based Er^{3+}-doped fiber (Bi-EDF) and obtained 2 mW single-frequency lasing. Afterward, M. Chen et al. [29, 30] reported a more compact single-frequency single polarization BFL with nearly 10 mW output power from only 1.5 m long commercialized normal Er^{3+}-doped fiber.

With the intense researches on the BFLs, the only shortage that limits its application fields seems to be the relatively small frequency shift (typically 10 GHz in the 1550 nm region), which is fixed by the pump frequency and the velocity of sound in the fiber. Thanks to the development of the long-length fiber grating techniques, Perlin and Winful [31] proposed and discussed the design of a DFB Raman fiber laser that based on a long length FBG. By conducting a linear analysis, they showed that the threshold power of a 1-m-long DFB RFL could be less than 1 W. Therefore, single-frequency lasing is possible at wavelengths that are out the reach of RE ions doped active fiber-based devices. Inspired by the conventional DFB lasers, Hu and Broderick [32] optimized the DFB RFL structure by introducing a π phase-shift offset from the center of the grating, rendering the laser outputs from one end of the laser cavity with improved efficiency and stability. In addition, theoretical simulations have shown that watt-level threshold could also be achieved in only 20 cm long of this laser structure. In 2011, P. S. Westbrook et al. [33] reported the first DFB RFL at 1.58 μm in a 12.4-cm-long deuterium-loaded germanosilicate fiber. By further lowering the effective area and increasing the index modulation in the fiber, they demonstrated that the threshold power could be reduced from 39 W to 4.3 W. A shortage of this laser is that the measured slope efficiency is less than 2%, which is attributed to the distortion of the grating profile

caused by the thermal variation under the condition of high pump power. J. Shi et al. [34] demonstrated a highly efficiency DFB RFL at 1.1 μm with 30 cm germane-silica fiber, and a threshold power of 1 W together with a measured slope efficiency of 93% against the absorbed pump power was achieved. After that, as the Raman gain is highly polarization dependent, a linear polarized laser was utilized to pump the same laser, and the obtained threshold power was 440 mW, while the measured slope efficiency with respect to the incident pump power was 13.5% [35]. Finally, it should be emphasized that another FBG-based laser structure, i.e., the DBR structure, should be also a probable candidate to realize a single-frequency RFL. A. Siekiera and coworkers [36] reported a linearly polarized laser pumped DBR RFL at 1.1 μm with a 17-cm-long highly nonlinear polarization maintaining Raman fiber, and the Raman lasing threshold was estimated to be 4.1 W, while the measured number of oscillating modes was 24. Therefore, it is evident that single-frequency operation is achievable from a DBR RFL by further reducing the cavity length or optimizing the bandwidth of the filtering elements.

Inspired by the FBG-based short cavity Raman laser, single-frequency Brillouin lasing was also investigated and realized in a DFB cavity by K. S. Abedin et al. [37]. The π-phase-shifted FBG was UV inscribed in a 12.4-cm-long OFS highly nonlinear fiber, and the threshold can be as low as 30 mW. Close behind was a theoretical model that described the dynamics of DFB Brillouin lasers by H. G. Winful et al. [38]. Based on the proposed model, the performances of the before mentioned DFB Brillouin fiber laser were well explained, and sub-milliwatt threshold was found to be achievable in a centimeter-long chalcogenide waveguide-based DFB Brillouin laser.

4.3 Random Distributed Feedback Fiber Lasers

In recent years, the concept of random distributed feedback fiber lasers that exploit the feedback caused by randomly distributed variations of refractive index in the fiber core has attracted much attention [39]. Principally, the scattering of light in submicron-scale nonhomogeneous fiber obeys the Rayleigh law, i.e., the Rayleigh scattering. The linear waveguide configuration of optical fiber captures the backscattered light and forms a so-called open cavity [40, 41]. In primeval works, the Rayleigh scattered light was amplified by the Raman effect. As a result, the laser spectral width was typically 1 nm or wider; even incorporated with narrow band spectral filters such as FBG or F-P filter, the achievable spectral band was still around 0.05 nm [42]. In further works, Brillouin effect-based random fiber laser was demonstrated in Ref. [43], where the laser cavity comprised three different fiber spans, with the middle fiber span the Brillouin gain medium, while the other two fiber spans on the fiber ends were the random feedback unit based on Rayleigh backscattering. When pumping at above threshold, single-frequency lasing with linewidth of 3.4 kHz was achieved. Similar scheme was proposed subsequently; a highly stable pump laser with 3.5 Hz linewidth was employed, and narrow linewidth

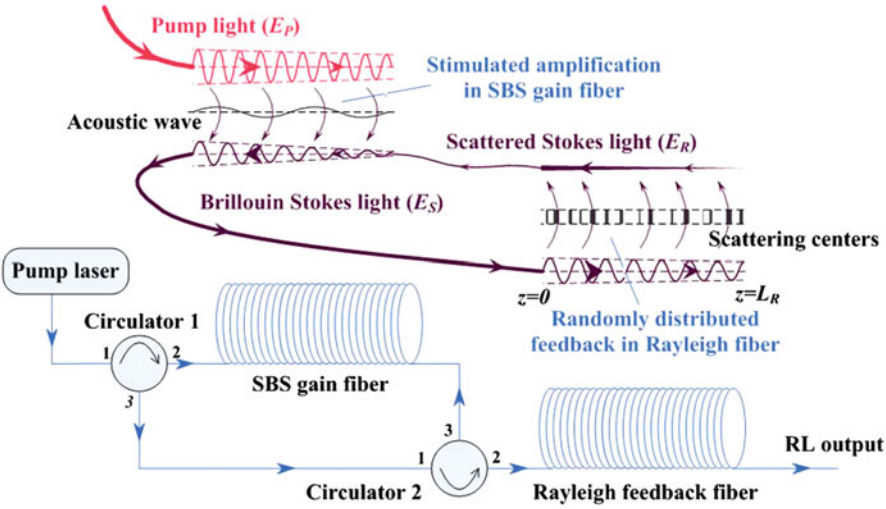

Fig. 4.3 Schematic of the Brillouin random fiber laser. (Reprinted from Ref. [44], copyright 2013, with permission from OSA publishing)

of ~10 Hz was produced [44]. Figure 4.3 shows the corresponding schematic of the experimental setup, in which the laser cavity was constructed by the association of a fiber loop that formed by two circulators and the Rayleigh feedback fiber. In this way, the system can be recognized as an open laser cavity. The initial Brillouin Stokes light induced by the thermally excited acoustic wave transmitted in the anticlockwise direction and was then partially reflected by the feedback fiber through the Rayleigh backscattering effect to seeding the SBS amplification process, while the remaining Stokes light transmitted forward and acted as the laser output. The employed Rayleigh feedback fiber was a 5.4 km long nonuniform fiber with a continuous refractive index changing in the fiber core, and the Rayleigh backscattering coefficient was about −34 dB/km. Based on the setup in Ref. [44], the authors demonstrated the frequency stabilizing by inserting a high finesse narrow band F-P interferometer into the light path to select the lasing frequency, and output laser with linewidth of 20 kHz was obtained when pumped by a laser with linewidth of 500 kHz [45].

Another sort of random distributed feedback fiber laser utilizes the traditional RE ions doped active fiber to providing the optical gain. Ref. [46] demonstrated an Er^{3+}-doped random fiber laser with randomly spaced Bragg grating array inscribed into the fiber to form a complex cavity; however, the laser output showed mode competition. After that, M. Gagné et al. [47] reported a different structure of the Er^{3+}-doped random fiber laser, by replacing the random grating array with a continuous grating with randomly distributed phase errors. This laser achieved a low threshold of ~3 mW and output linewidth of ~0.5 pm but still not the single longitudinal mode operation. Recently, the concept of random spaced index modulation in optical fiber was exploited to suppress longitudinal mode in a tunable Er^{3+}-doped fiber ring laser,

and low noise single-frequency laser with linewidth of 2.4 kHz was realized [48]. In further works, three-dimensional deep refractive index modulation induced by femtosecond laser was demonstrated, and numerous low-finesse spectral filters were formed to ensure single-frequency operation of an Er^{3+}-doped fiber ring laser [49]. Here the achieved laser linewidth was 2.1 kHz.

4.4 Fiber Optical Parametric Oscillator

The parametric gain in optical fiber comes from the FWM effect, a phenomenon induced by the Kerr nonlinearity. Due to the intrinsic nature of the parametric process – the operating wavelength can be arbitrary (depending only on the pump power, fiber nonlinearity, and fiber dispersion); the fiber optical parametric oscillator (FOPO) is recognized as an advantageous complementation of the traditional RE ions based fiber laser [50]. Initial works on the FOPO mainly based on pulsed pumping, as the nonlinearity of the fiber is too low to support continuous-wave (CW) operation in FOPO [51, 52]. The first FOPO that works in the CW regime was demonstrated in Ref. [53], where a 100 m long highly nonlinear fiber together with two FBGs was employed to construct the F-P cavity configuration. In this FOPO, the actual output was the idler channel, while the pump and signal light kept oscillating in the cavity, avoiding the triply resonant condition that is highly phase sensitive. An internal conversion efficiency of 30% between signal and pump was obtained. Recent works devoted by E. A. Zlobina et al. [54] show that pumping with a polarized laser as well as optimizing the pump linewidth could further increase the conversion efficiency of FOPO. As the length of highly nonlinear fiber in FOPO should be relatively long (>100 m) to provide enough parametric gain to enable oscillating, the single-frequency operation of FOPO would be hardly realized.

Until 2010, S. Yang et al. [55] introduced a sub-ring cavity, and a fiber loop mirror together with an unpumped Er^{3+}-doped fiber into a ring cavity configured FOPO and achieved single longitudinal mode output for the first time. The linewidth of this single-frequency FOPO was estimated to be about 1.5 kHz [56]. The corresponding experimental setup is shown in Fig. 4.4, where the cavity was formed by two wavelength-division multiplexing couplers (WDMC1 and WDMC2), while WDMC3 was utilized to dump the idler that generated in the parametric process and facilitate the signal to oscillator inside the laser cavity. A tunable band-pass filter (TBPF2) with bandwidth of 0.35 nm was inserted into the cavity to select the lasing wavelength. A sub-ring cavity constructed by a 50/50 optical coupler and a subsequent loop mirror consisted of a 50/50 optical coupler; an unpumped EDF and a circulator (CIR) were implemented to guarantee single-frequency operation. Then a 10/90 optical coupler was used to couple out 10% signal out of the FOPO. In the cavity, the parametric gain was provided by a 400 m highly nonlinear dispersion-shifted fiber (HNL-DSF). The pump source was a 1556 nm external cavity tunable laser source (TLS), which was first-phase modulated via a phase modulator (PM) with a 10 Gbits/s pseudorandom bit sequence signal to prevent SBS and

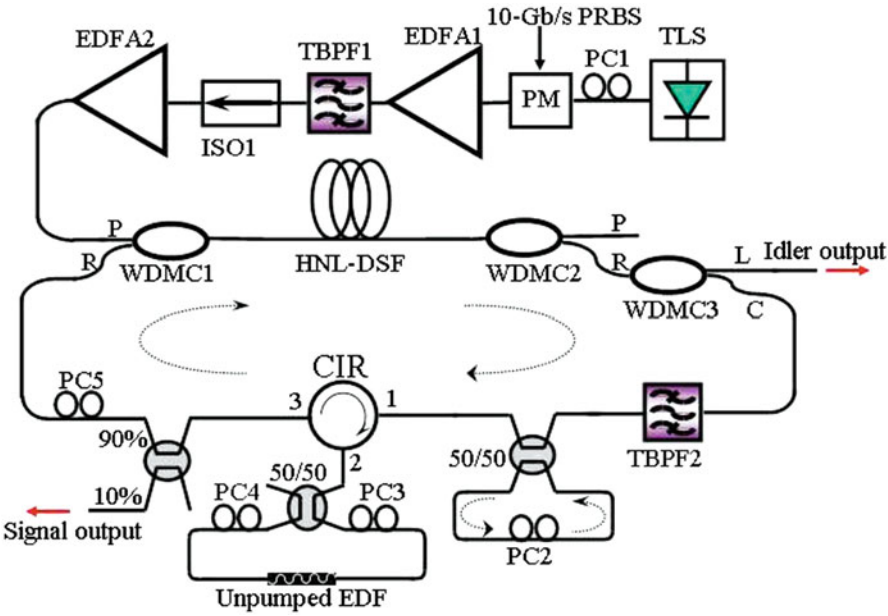

Fig. 4.4 Schematic diagram of the tunable single longitudinal mode FOPO. (Reprinted from Ref. [55], copyright 2010, with permission from OSA publishing)

then was subsequently amplified by two erbium-doped fiber amplifiers (EDFA1 and EDFA2). An isolator (ISO1) was employed to block backscattered light, while another tunable band-pass filter (TBPF1) was used to suppress unwanted ASE from EDFA1. Throughout the system, five polarization controllers (PC1 to PC5) were utilized to optimize the lasing efficiency. Another work was reported in Ref. [57], where two cascaded narrow band filters were used to realize single-frequency operation, and the achieved laser linewidth was less than 400 kHz.

References

1. Singh SP, Singh N (2007) Nonlinear effects in optical fibers: origin, management and applications. PIER 73:249
2. Agrawal GP (2001) Nonlinear fiber optics, 5th edn. Academic, New York
3. Dianov EM, Prokhorov AM (2000) Medium-power CW Raman fiber lasers. IEEE J Sel Top Quantum Electron 6:1022
4. Feng Y, Taylor LR, Calia DB (2009) 150 W highly-efficient Raman fiber laser. Opt Express 17:23678
5. Hill KO, Kawasaki BS, Johnson DC (1976) CW Brillouin laser. Appl Phys Lett 28:608
6. Lecoeuche V, Niay P, Douay M, Bernage P, Randoux S, Zemmouri J (2000) Bragg grating based Brillouin fibre laser. Opt Commun 177:303
7. Shirazi MR, Harun SW, Biglary M, Ahmad H (2008) Linear cavity Brillouin fiber laser with improved characteristics. Opt Lett 33:770

8. Norcia S, Frey R, Tonda-Goldstein S, Dolfi D, Huignard J (2004) High-efficiency single-frequency Brillouin fiber laser with a tunable coupling coefficient. J Opt Soc Am B 21:1424
9. Norcia S, Tonda-Goldstein S, Dolfi D, Huignard J, Frey R (2003) Efficient single-mode Brillouin fiber laser for low-noise optical carrier reduction of microwave signals. Opt Lett 28:1888
10. Geng J, Staines S, Wang Z, Zong J, Blake M, Jiang S (2006) Highly stable low-noise Brillouin fiber laser with ultranarrow spectral linewidth. IEEE Photon Technol Lett 18:1813
11. Spirin VV, Lopez-Mercado CA, Mégret P, Fotiadi AA (2012) Single-mode Brillouin fiber laser passively stabilized at resonance frequency with self-injection locked pump laser. Laser Phys Lett 9:377
12. Spirin VV, López-Mercado CA, Kinet D, Mégret P, Zolotovskiy IO, Fotiadi AA (2013) A single-longitudinal-mode Brillouin fiber laser passively stabilized at the pump resonance frequency with a dynamic population inversion grating. Laser Phys Lett 10:15102
13. Wang G, Zhan L, Liu J, Zhang T, Li J, Zhang L, Peng J, Yi L (2013) Watt-level ultrahigh-optical signal-to-noise ratio single-longitudinal-mode tunable Brillouin fiber laser. Opt Lett 38:19
14. Yong JC, Thévenaz L, Kim BY (2003) Brillouin fiber laser pumped by a DFB laser diode. J Lightwave Technol 21:546
15. Chen X, Xian L, Ogusu K, Li H (2012) Single-longitudinal-mode Brillouin fiber laser incorporating an unpumped erbium-doped fiber loop. Appl Phys B Lasers Opt 107:791
16. Cowle GJ, Stepanov DY (1996) Hybrid Brillouin/erbium fiber laser. Opt Lett 21:1250
17. Cowie GJ, Yu D, Chieng YT (1997) Brillouin/erbium fiber lasers. J Lightwave Technol 15:1198
18. Guan W, Marciante JR (2009) Single-frequency 1 W hybrid Brillouin/ytterbium fiber laser. Opt Lett 34:3131
19. Guan W, Marciante JR (2010) Power scaling of single-frequency hybrid Brillouin/ytterbium fiber lasers. IEEE J Quantum Electron 46:674
20. Zhou H, Sun C, Chen M, Chen W, Meng Z (2012) Characteristics of a Brillouin-erbium fiber laser based on Brillouin pump preamplification. Appl Opt 51:7046
21. Abedin KS (2005) Observation of strong stimulated Brillouin scattering in single-mode As_2Se_3 chalcogenide fiber. Opt Express 13:10266
22. Abedin KS (2006) Brillouin amplification and lasing in a single-mode As_2Se_3 chalcogenide fiber. Opt Lett 31:1615
23. Abedin KS (2006) Single-frequency Brillouin lasing using single-mode As_2Se_3 chalcogenide fiber. Opt Express 14:4037
24. Abedin KS (2006) Stimulated Brillouin scattering in single-mode tellurite glass fiber. Opt Express 14:11766
25. Qin G, Mori A, Ohishi Y (2007) Brillouin lasing in a single-mode tellurite fiber. Opt Lett 32:2179
26. Qin G, Sotobayashi H, Tsuchiya M, Mori A, Suzuki T, Ohishi Y (2008) Stimulated Brillouin scattering in a single-mode tellurite fiber for amplification, lasing, and slow light generation. J Lightwave Technol 26:492
27. Tow KH, Léguillon Y, Fresnel S, Besnard P, Brilland L, Méchin D, Toupin P, Troles J (2013) Towards more coherent sources using a microstructured chalcogenide Brillouin Fiber laser. IEEE Photon Technol Lett 25:238
28. Harun SW, Shahi S, Ahmad H (2009) Compact Brillouin-erbium fiber laser. Opt Lett 34:46
29. Chen M, Meng Z, Tu X, Zhou H (2013) Low-noise, single-frequency, single-polarization Brillouin/erbium fiber laser. Opt Lett 38:2041
30. Chen M, Meng Z, Zhou H (2013) Low-threshold, single-mode, compact Brillouin/erbium fiber ring laser. J Lightwave Technol 31:1980
31. Perlin VE, Winful HG (2001) Distributed feedback fiber Raman laser. IEEE J Quantum Electron 37:38
32. Hu Y, Broderick NG (2009) Improved design of a DFB Raman fibre laser. Opt Commun 282:3356

33. Westbrook PS, Abedin KS, Nicholson JW, Kremp T, Porque J (2011) Raman fiber distributed feedback lasers. Opt Lett 36:2895
34. Shi J, Alam S, Ibsen M (2012) Highly efficient Raman distributed feedback fibre lasers. Opt Express 20:5082
35. Shi J, Alam S, Ibsen M (2012) Sub-watt threshold, kilohertz-linewidth Raman distributed-feedback fiber laser. Opt Lett 37:1544
36. Siekiera A, Engelbrecht R, Nothofer A, Schmauss B (2012) Short 17-cm DBR Raman fiber laser with a narrow spectrum. IEEE Photon Technol Lett 24:107
37. Abedin KS, Westbrook PS, Nicholson JW, Porque J, Kremp T, Liu X (2012) Single-frequency Brillouin distributed feedback fiber laser. Opt Lett 37:605
38. Winful HG, Kabakova IV, Eggleton BJ (2013) Model for distributed feedback Brillouin lasers. Opt Express 21:16191
39. Turitsyn SK, Babin SA, Churkin DV, Vatnik ID, Nikulin M, Podivilov EV (2014) Random distributed feedback fibre lasers. Phys Rep 542:133
40. Turitsyn SK, Babin SA, El-Taher AE, Harper P, Churkin DV, Kablukov SI, Ania-Castaón JD, Karalekas V, Podivilov EV (2010) Random distributed feedback fibre laser. Nat Photonics 4:231
41. Churkin DV, Babin SA, El-Taher AE, Harper P, Kablukov SI, Karalekas V, Ania-Castaón JD, Podivilov EV, Turitsyn SK (2010) Raman fiber lasers with a random distributed feedback based on Rayleigh scattering. Phys Rev A 82:33828
42. Sugavanam S, Tarasov N, Shu X, Churkin DV (2013) Narrow-band generation in random distributed feedback fiber laser. Opt Express 21:16466
43. Pang M, Xie S, Bao X, Zhou D, Lu Y, Chen L (2012) Rayleigh scattering-assisted narrow linewidth Brillouin lasing in cascaded fiber. Opt Lett 37:3129
44. Pang M, Bao X, Chen L (2013) Observation of narrow linewidth spikes in the coherent Brillouin random fiber laser. Opt Lett 38:1866
45. Pang M, Bao X, Chen L, Qin Z, Lu Y, Lu P (2013) Frequency stabilized coherent Brillouin random fiber laser: theory and experiments. Opt Express 21:27155
46. Liz rraga N, Puente NP, Chaikina EI, Leskova TA, Múndez ER (2009) Single-mode Er-doped fiber random laser with distributed Bragg grating feedback. Opt Express 17:395
47. Gagné M, Kashyap R (2009) Demonstration of a 3 mW threshold Er-doped random fiber laser based on a unique fiber Bragg grating. Opt Express 17:19067
48. Li Y, Lu P, Bao X, Ou Z (2014) Random spaced index modulation for a narrow linewidth tunable fiber laser with low intensity noise. Opt Lett 39:2294
49. Li Y, Lu P, Baset F, Ou Z, Song J, Alshehri A, Bhardwaj VR, Bao X (2014) Narrow linewidth low frequency noise Er-doped fiber ring laser based on femtosecond laser induced random feedback. Appl Phys Lett 105:101105
50. Marhic ME, Kagi N, Chiang T, Kazovsky LG (1996) Broadband fiber optical parametric amplifiers. Opt Lett 21:573
51. Serkland DK, Kumar P (1999) Tunable fiber-optic parametric oscillator. Opt Lett 24:92
52. Nowak GA, Kao Y, Xia TJ, Islam MN, Nolan D (1998) Low-power high-efficiency wavelength conversion based on modulational instability in high-nonlinearity fiber. Opt Lett 23:936
53. Marhic ME, Wong K, Kazovsky LG, Tsai T (2002) Continuous-wave fiber optical parametric oscillator. Opt Lett 27:1439
54. Zlobina EA, Kablukov SI, Babin SA (2015) High-efficiency CW all-fiber parametric oscillator tunable in 0.92-1 μm range. Opt Express 23:833
55. Yang S, Cheung KK, Zhou Y, Wong KK (2010) Tunable single-longitudinal-mode fiber optical parametric oscillator. Opt Lett 35:481
56. Zhou Y, Zhang C, Chui PC, Wong KK (2011) A tunable-plus-band continuous-wave single-longitudinal-mode fiber-optical parametric oscillator. IEEE Photon Technol Lett 23:1451
57. Lei GK, Lim LT, Marhic ME (2013) Continuous-wave fiber optical parametric oscillator with sub-MHz linewidth. Opt Commun 306:17

Chapter 5
Single-Frequency Pulsed Fiber Lasers

Pulsed lasing is an important operation regime of single-frequency fiber lasers, owing to its irreplaceable applications in laser ranging, optical fiber sensing, and coherent LIDAR. Considering the single-mode oscillation nature of the single-frequency laser, the straightforward scheme to realize pulse operation is to periodically switch the gain or loss of the cavity. In addition, the pulse width of a single-frequency laser is limited to nanosecond level owing to the Fourier transform limitation. In this chapter, we focus on the scheme of modulating the cavity loss to achieve pulsed output, i.e., Q-switched fiber laser. Although various Q-switching schemes have been proposed previously, only specific schemes can be exploited in a single-frequency laser cavity. Here we first introduce the general principle of Q-switching and then several Q-switching schemes (both active and passive) based on the high-gain short-cavity fiber laser. Finally, other methods for the realization of single-frequency pulsed fiber lasers such as gain switching and extra cavity modulating the laser power are also introduced.

5.1 Principle of Q-Switching

So far, our discussions are mainly focused on SFFLs that are working in the CW regime, i.e., the laser continuously emits light with continuous pumping. To obtain pulsing operation, the common scheme is to implement the Q-switching or the mode-locking technique. A mode-locked laser generally emits pulse with duration in the picosecond or femtosecond level through locking the relative phase of a series of resonating modes in the cavity to realize coherent output. Essentially, it cannot be applied to a SFFL which has only one longitudinal mode resonating in the cavity. While for the Q-switching technique, it is in principle applicative to both the multi- and single longitudinal mode laser.

The mechanism of Q-switched laser is to periodically modulate the Q factor of the cavity to generate energetic short pulse. According to Eq. (2.21), a cavity's Q factor

© Springer Nature Singapore Pte Ltd. 2019

Z. Yang et al., *Single-Frequency Fiber Lasers*, Optical and Fiber Communications Reports 8, https://doi.org/10.1007/978-981-13-6080-0_5

is inversely proportional to the single-pass loss factor of the laser light, and then the Q-switching process can be realized through adjusting the cavity loss. Considering a laser that is under pumping, the population at the upper laser level will accumulate when the cavity loss is initially kept at a high level. In this way, the energy that continuously comes from the pump is stored in the cavity as lasing won't onset given that the cavity loss is high enough. Nevertheless, it is noted that the spontaneous emission process would still deplete the energy reserve no matter how large the cavity loss is. In this sense, the Q-factor can be also given by:

$$Q = 2\pi\nu\frac{W}{W'} \tag{5.1}$$

in which W is stored energy, while W' is the single-pass energy dissipation. Therefore, an upper laser level with long lifetime is advantageous for Q-switching as the probability of spontaneous emission is the inverse of the level lifetime. In addition, a high saturation energy of the gain medium enables more pump energy to be stored and is thus more suitable for Q-switching. At a specific point, the loss is suddenly reduced to a small value, then the laser oscillation builds up quickly from the spontaneous emission, and the accumulated energy via population inversion is highly consumed and transferred to a giant pulse output. After that, the cavity loss is reset to a high level again, and the Q-switching enters the next cycle. Generally, the duration of the pulse ranges from nanosecond to microsecond level and is basically larger than the resonator round-trip time. Moreover, the peak power of the pulse can be orders of magnitude improved compared with the power of a CW laser. Regarding the repetition rate, it is essentially determined by the repetitive Q-switching process and is generally less than 1 MHz.

Commonly, the Q-switching process can be classified into the active and passive types, depending on the modulating mechanism. In principle, the cavity loss is modulated by an active controlled element for active Q-switching, while for passive Q-switching, the loss is automatically modulated by a real or artificial saturable absorber. Active Q-switching allows externally controllable modulation of the cavity loss, and in this way, the pulsing parameters such as the repetition frequency can be adjusted independently. Otherwise, the loss modulation in passive Q-switching is internally triggered by intensity-dependent loss unit in the laser cavity; thus the pulsing parameters are generally fixed. Nowadays, there are numerous Q-switching schemes for fiber lasers, to name a few: active Q-switching such as intracavity modulating with an acousto-optic modulator (AOM) or an electro-optic modulator (EOM) [1–4], imposing the gain fiber with a lateral stress induced by a PZT to change the loss of transverse mode [5] or polarization mode [6], modulating the FBG to introduce transient phase shift with magnetostrictive material [7, 8] or acoustic waves [9–11], polarization switching within electrically controlled microstructured fiber [12], and employing ultrafast in-line variable optical attenuator [13], passive Q-switching exploiting the nonlinear effects such as Raman and Brillouin scattering in optical fiber [14–17], various saturable absorber materials [18–22], as well as the nonlinear polarization evolution (NPE) technique [23].

5.2 Q-Switched Single-Frequency Fiber Lasers

As single-frequency pulsed laser sources are widely required in the fields of fiber-based sensing, coherent LIDAR, spectroscopy, and nonlinear frequency generation, many research groups have been devoting on realizing pulsed SFFLs. Based on the abovementioned Q-switching techniques, another key factor is to construct a laser cavity that satisfies the condition of single longitudinal mode operation, that is, Q-switching of single-frequency laser cavity. Primary work utilized volume diffraction grating in the laser cavity to filter the optical spectrum and obtained nanosecond pulses with linewidth of 0.04 nm [24]. However, the involvement of free-space components discards the merit of all-fiber laser structure and renders the system fragile and cumbersome. A significant work was carried out in Ref. [25], where a high-Q microsphere resonator was taper-coupled into the laser cavity, while the Q-switching was realized by modulating the distance between the microsphere and the taper. As the microsphere resonator has a narrow transmission band (several tens MHz), pulse narrow bandwidth lasing with duration of 160 ns was achieved. In 2008, C. Cuadrado-Laborde et al. [26] demonstrated a transform-limited pulsing laser through inducing dynamic phase shift in a FBG to form a DFB structure with an in-line acoustic pulse generator and achieved pulses with 6 MHz linewidth, 10 kHz repetition rate, 80 ns temporal width, and 60 mW peak power.

Injection seeding a CW signal into a resonator which subjects to loss modulating is another efficient way. In 2004, P. D. Dragic et al. [27] demonstrated a narrow linewidth pulsing laser by injection seeding the output from an external cavity diode laser (ECDL) to an EDFA-based fiber ring cavity, which was modulated by an AOM. Later in 2012, R. Zhou et al. [28] reported a transform-limited single-frequency pulsed laser, by injection seeding a CW signal to an AOM-modulated ring cavity into which a section of Er-doped fiber was incorporated to provide gain. Moreover, a theoretical model was developed to study the laser characteristics of this kind of configuration. Subsequently, a similar work was carried out in Ref. [29], where the Q-switching was realized by controlling the coupling ratio of a variable optical coupler inside the ring cavity and nanosecond lasing with 3 dB linewidth of 7 kHz and peak power of 40 W was achieved. In addition, as in this scheme the Q-switching process is outside of the laser cavity, Ref. [30] has demonstrated an externally Q-switched single-frequency laser that was frequency modulated with an intracavity PZT and achieved a pulsed SFFL with linearly frequency modulating at the same time.

Finally, it is worth noting that the recent development of heavily RE ions doped multicomponent soft glass fiber has provided a favorable way to realize compact single-frequency Q-switched laser with high average or peak power. The general scheme is to utilize a PZT to side press the fiber and induce a polarization-related loss modulation in a short linear polarized DBR laser cavity, and compact high-power single-frequency pulsed lasing with repetition rate up to hundreds of kilohertz was achieved at the 1.0, 1.5, and 2.0 μm wavelength bands [31–34]. Figure 5.1 demonstrates the experimental setup of a 1950 nm Q-switched single-frequency

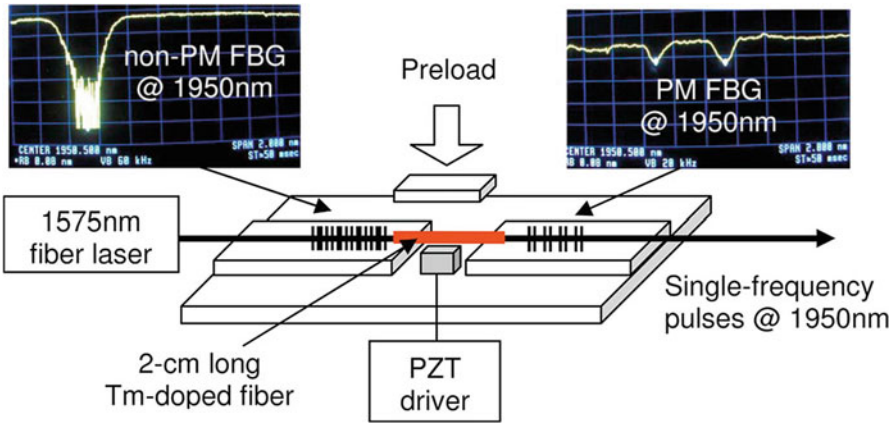

Fig. 5.1 Diagram of the experimental setup. A Tm^{3+}-doped DBR fiber cavity was formed by two FBGs. Preload force and PZT-induced stress are applied to a small section of the active fiber for polarization modulation. Inset, transmission spectra of the two FBGs measured with an in-house 2 μm broadband fiber source. (Reprinted from Ref. [34], copyright 2009, with permission from OSA publishing)

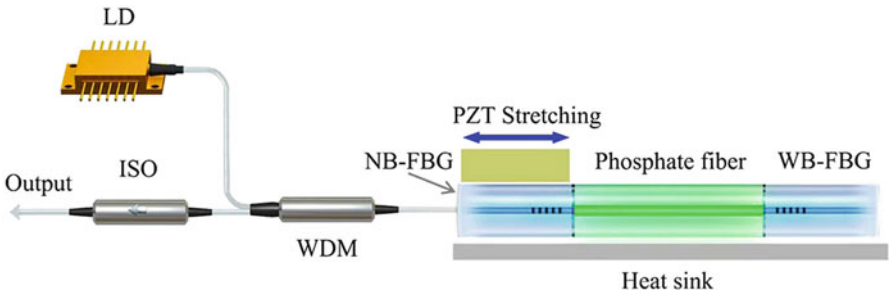

Fig. 5.2 Schematic configuration of the actively PZT Q-switched compact DBR single-frequency laser. (Reprinted from Ref. [35], copyright 2015, with permission from IOP publishing)

laser cavity, of which the configuration is a general linearly polarized SFFL as discussed in Sect. 2.4.1. The cavity was core-pumped with a 1575 nm fiber laser seeded erbium-doped fiber amplifier. Specifically, the 2-cm-long Tm^{3+}-doped fiber was preloaded with appropriate amount of stress at an arbitrary location, to induce birefringence effect and then increase the loss of the orthogonal polarizing modes. Active Q-switching was realized by driving a PZT that was attached to the Tm^{3+}-doped fiber. When appropriate driving signal was applied, the PZT can quickly release the preloaded stress periodically, leading to desired single-frequency Q-switching operation.

Another active Q-switching mechanism based on PZT was demonstrated in Ref. [35], in which the cavity loss was controlled by using the PZT to periodically modulate the center wavelength of a FBG. Figure 5.2 shows the corresponding

schematic of the experimental setup. The gain fiber was a segment of 12-mm-long Yb^{3+}-doped phosphate fiber, while the cavity reflector was a NB-FBG and a WB-FBG with 3-dB bandwidth/center reflectivity are, respectively, 0.05 nm/60% and 0.3 nm/99.9%. The reflectance peak of the two FBGs was slightly staggered from each other. A PZT driven by an external RF signal was glued onto the NB-FBG to dynamically modulate its reflectance peak (Bragg wavelength λ_B) through the following equation:

$$\Delta\lambda_B = \lambda_B(1-\rho)\Delta\varepsilon \tag{5.2}$$

where $\Delta\lambda_B$ is the change of the Bragg wavelength of the NB-FBG, ρ is the photoelastic coefficient of the fiber, and $\Delta\varepsilon$ is the strain induced by the PZT. In this way, the reflectance peak of the two FBGs can be periodically overlapped, enabling active Q-switching of the laser cavity. Moreover, the whole laser cavity was temperature controlled to guarantee its operation stability. The pumping and the outputting configuration were similar with that of the short-cavity DBR laser discussed before. With this design, Q-switched pulsing with repetition rate ranging from 10 to 240 kHz and maximum peak power of 6.93 W at the repetition rate of 10 kHz were achieved.

Besides the active PZT modulation scheme, passive Q-switching was also demonstrated in a compact short-cavity SFFL with a saturable absorber, which has a certain optical loss that will be reduced at high optical intensities. In Ref. [36], the authors utilized a semiconductor saturable absorber mirror (SESAM) to switch the cavity loss, as shown in Fig. 5.3. The gain fiber was a 17-mm-long Er^{3+}/Yb^{3+} codoped phosphate fiber (EYDPF), while the two reflectors of the cavity were, respectively, a butt-coupled SESAM and a fusion spliced PM-FBG. The SESAM

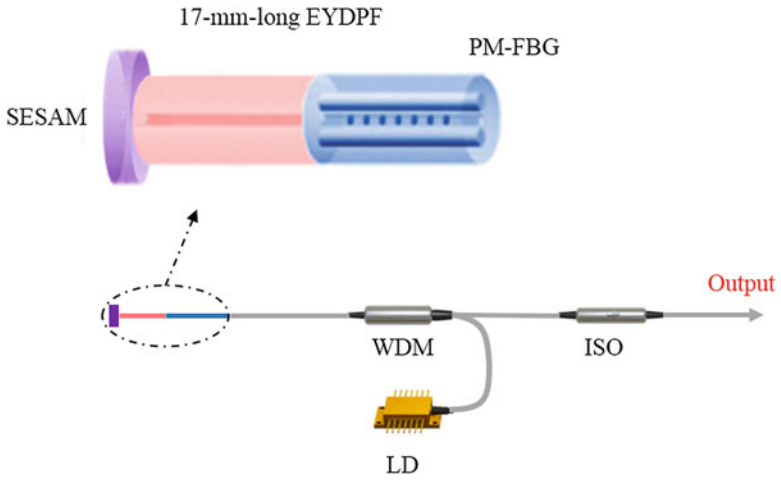

Fig. 5.3 Schematic configuration of the passively Q-switched compact DBR single-frequency laser. (Reprinted from Ref. [36], copyright 2016, with permission from OSA publishing)

has an absorbance of 4% at around 1540 nm and a modulation depth of 2.4%, while the PM-FBG has a 3-dB bandwidth of 0.05 nm and a reflectivity of 50% at 1540 nm. Other than that, the rest of the laser configuration was quite similar to that of a standard short-cavity DBR laser. Dual-wavelength Q-switching operation was achieved with maximum pulse energy of more than 34.5 nJ and minimum pulse duration of 110.5 ns.

5.3 Other Single-Frequency Pulsed Fiber Lasers

It should be noted that except Q-switching, there are other schemes that can realize pulsed operation of a single-frequency laser cavity. A straightforward one is to pump the cavity with a pulsed laser source, i.e., modulating the optical gain in the cavity. For instance, single-frequency pulsed laser with optical bandwidth of about 500 kHz has been realized in a fiber DBR configuration in Ref. [37], where the pulsing operation was realized via modulating the pump laser with a sinusoidal signal. Similar work was carried out in Ref. [38], where the authors in band pumped a Ho^{3+}-doped DBR fiber laser with a Q-switched Tm-doped laser at 1.95 μm and obtained single-frequency lasing at 2.05 μm. Moreover, the nonlinear SBS effect-induced weak feedback in the cavity can also cause a pulsed operation of the laser [39, 40]. Recently, a SBS-based Tm^{3+}-doped fiber laser was demonstrated in Ref. [41], in which the effect of nonlinear polarization rotation (NPR) and active phase modulation (APM) was exploited to improve the pulsing operation. In this system, single-frequency pulsed laser with linewidth of about 6 MHz, repetition rate of ~310 kHz, and a pulse width of ~200 ns were achieved.

Further, directly modulating the intensity of a CW single-frequency laser outside of the cavity with an external AOM or EOM is a convenient and simple method to obtain pulsed source [33, 42]. As the pulsing parameters can be controlled by just adjusting the modulating conditions, nanosecond pulses with repetition rate up to megahertz can be realized. However, the shortcomings are the remarkable transmission loss and high damage threshold of the external modulator, and thus the achievable average or peak power of the pulsed laser is highly limited. Actually, this external modulation scheme is generally associated with an amplifier to magnify the laser power to the desired level, as will be discussed in the next chapter.

References

1. Chen ZJ, Grudinin AB, Porta J, Minelly JD (1998) Enhanced Q switching in double-clad fiber lasers. Opt Lett 23:454
2. Michaille L, Taylor DM, Bennett CR, Shepherd TJ, Ward BG (2008) Characteristics of a Q-switched multicore photonic crystal fiber laser with a very large mode field area. Opt Lett 33:71

3. El-Sherif AF, King TA (2003) High-energy, high-brightness Q-switched Tm^{3+}-doped fiber laser using an electro-optic modulator. Opt Commun 218:337
4. Wang J, Cui S, Si L, Chen J, Feng Y (2013) All-fiber single-mode actively Q-switched laser at 1120 nm. Opt Express 21:289
5. Saez-Rodriguez D, Cruz JL, Diez A, Barmenkov YO, Andres MV (2013) Q-switch all-fiber laser pulsed by high order modes. IEEE Photon Technol Lett 25:1058
6. Fraser A, Bernier M, Deschênes J, Weynant E, Genest J, Vallée R (2010) Polarization-switchable Q-switched DFB fiber laser. Opt Lett 35:1046
7. Pérez-Millán P, Díez A, Andrés M, Zalvidea D, Duchowicz R (2005) Q-switched all-fiber laser based on magnetostriction modulation of a Bragg grating. Opt Express 13:5046
8. Pérez-Millán P, Cruz JL, Andrés MV (2005) Active Q-switched distributed feedback erbium-doped fiber lasers. Appl Phys Lett 87:11104
9. Delgado-Pinar M, Díez A, Cruz JL, Andrés MV (2007) Single-frequency active Q-switched distributed fiber laser using acoustic waves. Appl Phys Lett 90:171110
10. Delgado-Pinar M, Diez A, Cruz JL, Andres MV (2009) Enhanced Q-switched distributed feedback fiber laser based on acoustic pulses. Laser Phys Lett 6:139
11. Delgado-Pinar M, Zalvidea D, Diez A, Perez-Millan P, Andres M (2006) Q-switching of an all-fiber laser by acousto-optic modulation of a fiber Bragg grating. Opt Express 14:1106
12. Yu Z, Malmström M, Tarasenko O, Margulis W, Laurell F (2010) Actively Q-switched all-fiber laser with an electrically controlled microstructured fiber. Opt Express 18:11052
13. Chang YM, Lee J, Jhon YM, Lee JH (2011) Active Q-switching in an erbium-doped fiber laser using an ultrafast silicon-based variable optical attenuator. Opt Express 19:26911
14. Chernikov SV, Zhu Y, Taylor JR, Gapontsev VP (1997) Supercontinuum self-Q-switched ytterbium fiber laser. Opt Lett 22:298
15. Fotiadi AA, Mégret P, Blondel M (2004) Dynamics of a self-Q-switched fiber laser with a Rayleigh-stimulated Brillouin scattering ring mirror. Opt Lett 29:1078
16. Zhao Y, Jackson SD (2006) Passively Q-switched fiber laser that uses saturable Raman gain. Opt Lett 31:751
17. Kir yanov AV, Barmenkov YO, Andres MV (2013) An experimental analysis of self-Q-switching via stimulated Brillouin scattering in an ytterbium doped fiber laser. Laser Phys Lett 10:55112
18. Liu J, Wu S, Yang Q, Wang P (2011) Stable nanosecond pulse generation from a graphene-based passively Q-switched Yb-doped fiber laser. Opt Lett 36:4008
19. Yang W, Hou J, Zhang B, Song R, Liu Z (2012) Semiconductor saturable absorber mirror passively Q-switched fiber laser near 2 μm. Appl Opt 51:5664
20. Luo Z, Huang Y, Zhong M, Li Y, Wu J, Xu B, Xu H, Cai Z, Peng J, Weng J (2014) 1-, 1.5-, and 2-μm fiber lasers Q-switched by a broadband few-layer MoS_2 saturable absorber. J Lightwave Technol 32:4077
21. Luo Z, Liu C, Huang Y, Wu D, Wu J, Xu H, Cai Z, Lin Z, Sun L, Weng J (2014) Topological-insulator passively Q-switched double-clad fiber laser at 2 μm wavelength. IEEE J Sel Top Quantum Electron 20:902708
22. Liu S, Zhu X, Zhu G, Balakrishnan K, Zong J, Wiersma K, Chavez-Pirson A, Norwood RA, Peyghambarian N (2015) Graphene Q-switched Ho^{3+}-doped ZBLAN fiber laser at 1190 nm. Opt Lett 40:147
23. He X, Luo A, Lin W, Yang Q, Yang T, Yuan X, Xu S, Xu W, Luo Z, Yang Z (2014) A stable 2 μm passively Q-switched fiber laser based on nonlinear polarization evolution. Laser Phys 24:85102
24. Fan Y, Lu F, Hu S, Lu K, Wang H, Zhang G, Dong X (2003) Narrow-linewidth widely tunable hybrid Q-switched double-clad fiber laser. Opt Lett 28:537
25. Kieu K, Mansuripur M (2006) Active Q switching of a fiber laser with a microsphere resonator. Opt Lett 31:3568

26. Cuadrado-Laborde C, Pérez-Millán P, Andrés MV, Díez A, Cruz JL, Barmenkov YO (2008) Transform-limited pulses generated by an actively Q-switched distributed fiber laser. Opt Lett 33:2590
27. Dragic PD (2004) Injection-seeded Q-switched fiber ring laser. IEEE Photon Technol Lett 16:1822
28. Zhou R, Shi W, Petersen E, Chavez-Pirson A, Stephen M, Peyghambarian N (2012) Transform-limited, injection seeded, Q-switched, ring cavity fiber laser. J Lightwave Technol 30:2589
29. Wan H, Wu Z, Sun X (2013) A pulsed single-longitudinal-mode fiber laser based on gain control of pulse-injection-locked cavity. Opt Laser Technol 48:167
30. Zhang Y, Yang C, Li C, Feng Z, Xu S, Deng H, Yang Z (2016) Linearly frequency-modulated pulsed single-frequency fiber laser at 1083 nm. Opt Express 24:3162
31. Leigh M, Shi W, Zong J, Wang J, Jiang S, Peyghambarian N (2007) Compact, single-frequency all-fiber Q-switched laser at 1 μm. Opt Lett 32:897
32. Fang Q, Shi W, Peyghambarian N (2014) 978 nm single-frequency actively Q-switched all fiber laser. IEEE Photon Technol Lett 26:874
33. Shi W, Leigh MA, Zong J, Yao Z, Nguyen DT, Chavez-Pirson A, Peyghambarian N (2009) High-power all-fiber-based narrow-linewidth single-mode fiber laser pulses in the C-band and frequency conversion to THz generation. IEEE J Sel Top Quantum Electron 15:377
34. Geng J, Wang Q, Smith J, Luo T, Amzajerdian F, Jiang S (2009) All-fiber Q-switched single-frequency tm-doped laser near 2 μm. Opt Lett 34:3713
35. Zhang Y, Feng Z, Xu S, Mo S, Yang C, Li C, Gan J, Chen D, Yang Z (2015) Compact frequency-modulation Q-switched single-frequency fiber laser at 1083 nm. J Opt 17:125705
36. Zhang Y, Yang C, Feng Z, Deng H, Peng M, Yang Z, Xu S (2016) Dual-wavelength passively q-switched single-frequency fiber laser. Opt Express 24:16149
37. Barmenkov YO, Kir'yanov AV, Mora J, Cruz JL, Andrés MV (2005) Continuous-wave and giant-pulse operations of a single-frequency erbium-doped fiber laser. IEEE Photon Technol Lett 17:28
38. Geng J, Wang Q, Luo T, Case B, Jiang S, Amzajerdian F, Yu J (2012) Single-frequency gain-switched ho-doped fiber laser. Opt Lett 37:3795
39. Montes C, Bahloul D, Bongrand I, Botineau J, Cheval G, Mamhoud A, Picholle E, Picozzi A (1999) Self-pulsing and dynamic bistability in cw-pumped Brillouin fiber ring lasers. J Opt Soc Am B 16:932
40. Kir'yanov AV, Barmenkov YO, Andres MV (2013) An experimental analysis of self-Q-switching via stimulated Brillouin scattering in an ytterbium doped fiber laser. Laser Phys Lett 055112:10
41. Wang X, Lv H, Zhou P, Wu W, Wang X, Xiao H, Liu Z (2014) Single-frequency pulsed Brillouin-thulium fiber laser at 2 μm with nonlinear polarization rotation and active phase modulation. Appl Phys Express 7:102701
42. Fang Q, Shi W, Kieu K, Petersen E, Chavez-Pirson A, Peyghambarian N (2012) High power and high energy monolithic single-frequency 2 μm nanosecond pulsed fiber laser by using large core tm-doped germanate fibers: experiment and modeling. Opt Express 20:16410

Chapter 6
Amplification Technologies of Single-Frequency Lasers

Up to now, we have already discussed the technologies concerning the single-frequency fiber cavity, which can be engineered to realize various performance targeting a vast number of applications. Nevertheless, one of the most important performance, i.e., the output power, is yet to be scaled for many applying occasions, even though heavily doped active fiber can enable watt-level output power from a single resonator. Therefore, extra amplification of the single-frequency laser is indispensable to further booster its power. To this end, a common method is to implement the double-clad fiber-based master oscillation power amplifier, which has a similar pumping scheme with that of the fiber oscillator while without the cavity design. In this chapter, we first discuss the significance of amplifying single-frequency lasers and then introduce the principle of the amplifier scheme. After that, the structure of a general fiber amplifier is introduced in terms of the double-clad fiber technology and the cladding pump-coupled technology. Finally, the limitation factors of amplifying single-frequency lasers in optical fiber are discussed.

6.1 The Significance of Amplifying Single-Frequency Lasers

It is usually demanded for high-power/high-energy output of single-frequency laser in many applications, such as nonlinear frequency conversion, coherent beam combining, and laser radar. Especially, in general occasions [1, 2], it is also requested for the control of other output performances of the laser, such as operation wavelength, polarization state, laser linewidth, beam quality, and CW/pulsed condition. Up to now, stable single-frequency fiber lasers operating at 1.0, 1.5, and 2.0 μm regions can be achieved through either DBR or DFB short cavity with a single fiber oscillator (or laser resonator). However, owing to the single-mode core-pumping method used in such configuration, the output power is limited to hundred

© Springer Nature Singapore Pte Ltd. 2019

Z. Yang et al., *Single-Frequency Fiber Lasers*, Optical and Fiber Communications Reports 8, https://doi.org/10.1007/978-981-13-6080-0_6

milliwatts caused by the low pump power and internal thermal effect of short cavity [3, 4].

In order to obtain higher output power, a low-power single-frequency laser can be utilized as a seed source for power amplification through a master oscillation power amplifier (MOPA) configuration. At present, semiconductor laser (LD) or nonplanar ring oscillator (NPRO) are generally used as the seed laser for high-power single-frequency fiber amplifier, by using the bulk free-space components [5–7] and rare-earth-ions doped silica fiber as the gain medium. Since the seed laser has low output power (generally a few milliwatts) and poor signal-to-noise ratio, it often requires multistages fiber amplifiers. In addition, the free-space components would introduce significant insertion loss to the system and are prone to be disturbed by the environment, leading to a non-all-fiber configuration that is more complex, poor controllability, and low conversion efficiency [3, 4, 8]. Moreover, the output laser performances such as linewidth, noise, and power stability are greatly restricted by the seed laser itself. Therefore, all-fiber MOPA technology employing optimized seed lasers is a good choice for realizing the high-performance single-frequency laser output.

6.2 Basic Principles of MOPA Fiber Laser

The MOPA scheme has been regarded as an ideal approach to achieve high-power single-frequency fiber lasers [9–11]. Its advantage is that the spectral characteristics, operating wavelength, polarization state, and laser linewidth of the laser system are determined by the seed laser, while the beam quality and the power/energy scaling depend on the fiber amplifier configuration [12–15]. All-fiber high-power single-frequency MOPA laser generally uses multistage fiber amplifier design, including several pre-amplifier stages (preamplifier) and one power amplifier stage (power amplifier), as shown in Fig. 6.1.

As the core part of the MOPA system, the power amplifier stage usually consists of several pump sources, a segment of active fiber, a coupling component (i.e.,

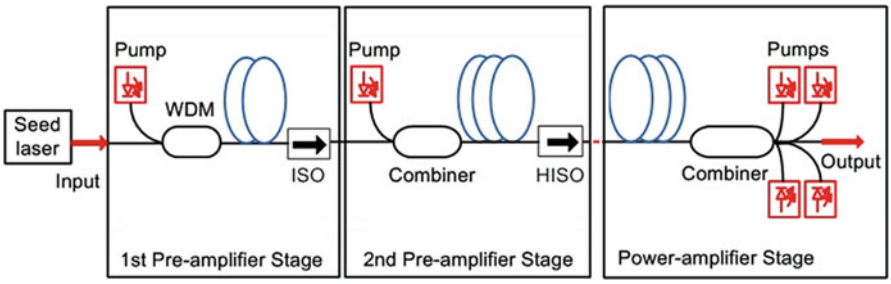

Fig. 6.1 Schematic configuration of a typical MOPA. *WDM* wavelength division multiplexing, *ISO* isolator, *HISO* high-power isolator

pump/signal combiner), and an isolator (ISO), which directly determines the beam quality and the output power scaling. An indispensable part of power amplifier is the multimode cladding-pumping method, namely, the pump light is launched into the inner cladding of the double-clad active fiber and then effectively absorbed by the rare-earth ions doped in the core of the fiber, providing efficient optical gain for laser amplification. The signal light is injected into the fiber core and amplified while transmitting through the gain fiber. Since there is no resonating design in a fiber amplifier, the laser power can be greatly enhanced through a one-trip traveling while almost preserving the properties of a high-performance single-frequency fiber laser.

6.3 Structure of MOPA Fiber Laser

6.3.1 Double-Clad Fiber Technology

In 1988, Snitzer first proposed the concept of double-clad fiber and multimode cladding pumping scheme. Up to now, many new types of double-clad fiber have been developed and underpin the continuous increasement of the output power from a single fiber [16, 17]. Double-clad active fiber overcomes the disadvantages of the single-clad active fiber and single-mode core pumping structure and greatly enhances the output power scaling of MOPA laser (CW single-transverse mode output power more than 10 kW). In addition, compared with other solid gain mediums, the double-clad active fiber has obvious advantages such as high damage threshold and large surface/volume ratio (excellent heat dissipation).

Double-clad active fiber is composed of doped fiber core (glass), inner cladding (glass), outer cladding (fluorinated polymer), and coating (acrylate polymer). The key difference between double-clad fiber and the traditional single-clad active fiber is that an extra inner cladding is added on the outside of the fiber core to transmit the multi-mode pump lights. On the one hand, the relative small size of the fiber core is used as the waveguide to amplify and transmit the laser signal, guaranteeing the single-transverse-mode output. On the other hand, the large cross section of the inner cladding facilitates the process of coupling and transmitting the multimode pump lights. It is worth noting that the inner cladding consists of glass with larger transverse dimensions (with diameter larger than 125 μm and even up to 400 μm) and numerical aperture (NA) as well as smaller refractive index. Such a structure greatly reduces the requirement of the pump beam quality and improves the available pump power.

In order to effectively improve the absorption efficiency of the pump light, researchers have been working on optimizing the design of the inner cladding. The convention cross section of the inner cladding is a symmetrical circle, which induces a spiral transmission of the pump light along the inner cladding while cannot be absorbed effectively. To address this problem, researchers have designed different cross sections of the inner cladding such as D-type, rectangle, plum-flower shape, star shape, and hexagonal structure [18–20], as shown in Fig. 6.2. As such the

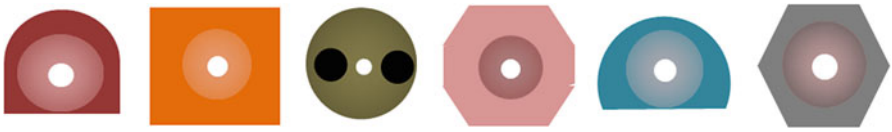

Fig. 6.2 Various cross sections of double-clad fiber

noncircular inner clad structure can significantly improve the absorption efficiency of the pump light, which is much higher than that of the circular one. For example, the theoretical pump absorption efficiency of a double-clad fiber with a rectangle inner clad that can reach to be 100%.

6.3.2 Cladding Pump Coupling Technology

Over the last 30 years, the pump methods of fiber laser and amplifier have been well-developed. Based on the traditional end pump technology, many new pump coupling technologies have proposed. Here are several typical cladding pump coupling schemes.

6.3.2.1 End-Face Coupling via Lens Group

This is a basic and now matured pump coupling method. The principle is that the pump light is calibrated by a collimating lens group and then focused onto the end face of the double-cladding fiber. This method is widely used with a free-space coupling manner by using bulk optical components. However, its disadvantage is needed to occupy the fiber end face. In addition, the system is cumbersome and prone to be disturbed by the environment while compared with the all-fiber structure.

6.3.2.2 V-Groove Side-Pump Coupling

This pump coupling method was proposed by Ripin and Goldberg et al. in 1995 [21]. Through taking off a piece of fiber coating and fabricating a V-groove on one side of the inner cladding, the pump light can enter the inner cladding by leveraging the total internal reflection by focusing on the ramp of the V-groove via a focusing lens from the other side of the inner cladding. With this method, the coupling efficiency can reach 89%. However, the fabricating technology of the V-groove is very difficult, and the employed lens has limitations on the pump coupling efficiency.

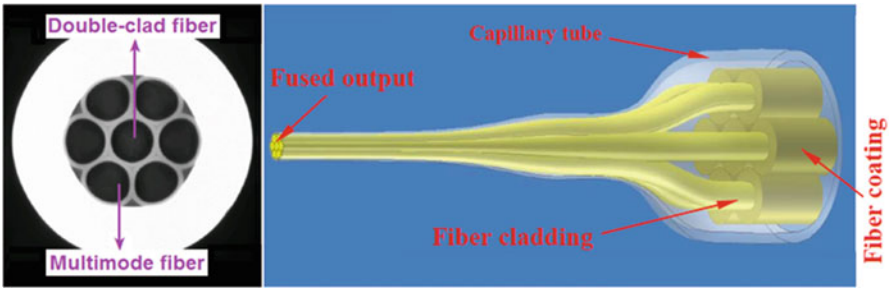

Fig. 6.3 End-view image and schematic diagram of a fused 7 × 1 fiber combiner. (Reprinted from Ref. [24], copyright 2009, with permission from SPIE Digital Library)

6.3.2.3 Embedded Prism Side-Pump Coupling

In fact, this is an advanced version of the V-groove side-pump coupling [22]. Unlike the former, in this scheme a microprism is embedded into a slot that is carved on the inner cladding of the fiber. The pump is injected into the inner surface of the ipsilateral through a prism and then coupled into the inner cladding. The main improvement is that the pump is coupled into the inner cladding through the reflection of a microprism, instead of being focused by a micro-lens. Hence, the sensitivity of coupling efficiency on the position of pump source can be greatly reduced.

6.3.2.4 Fused Fiber Bundle Coupler

In this scheme, the coating of several multimode fibers are stripped off and then entangled with each other, melted with heat, and pulled into a taper shape. Hence, the pump can be directly coupled into the double-cladding fiber through multimode fibers. This technology was proposed by Giovanni and Stentz et al. in 1999. Figure 6.3 shows a typical 7 × 1 multimode pump combiner [23]. In the cone area, the coating and outer cladding of the multimode fiber are removed to the fiber core so that the double-cladding fibers can be fused together. Its production process is becoming mature nowadays, since it has been recognized as one of the key components to realize the all-fiber MOPA laser structure.

6.4 Limitation Factors of High-Power Single-Frequency MOPA Laser

With the development of the application prospects of single-frequency laser systems in industrial processing and military fields, the requirements on output power scaling are getting higher and higher [25–27]. Up to now, the maximum continuous wave

(CW) laser output power from a single double-clad fiber has reached tens of kW. In addition, the output power of single-frequency fiber laser based on the MOPA structure has also approached to kilowatts level. Nevertheless, the continuous improvement of the power scaling of all-fiber single-frequency lasers is still limited by the fiber nonlinear effects and other accompanying effects.

6.4.1 Nonlinear Effects

In high-power MOPA laser system, due to the relatively small core size of the double-clad fiber and long transmission length of the amplified narrow linewidth laser signal, unwanted fiber nonlinear effects can easily arise and hamper the amplification process. Regarding CW single-frequency lasers, the main detrimental nonlinear effects are stimulated Brillouin scattering (SBS) [28, 29], stimulated Raman scattering (SRS), and optical Kerr effect.

Both SBS and SRS are caused by molecular vibrational modulation when the pump light passes through the fiber and both have a gain characteristic, which reduces the conversion efficiency and brightness of the output laser. The frequency shift of SBS is about 11 GHz (at ~1550 nm in silica fiber), which is three orders of magnitude smaller than that of SRS. The SBS threshold is highly depended on the spectral linewidth of the signal laser [30]. It is found that both of these effects have a certain threshold, and the threshold of SBS is lower than that of SRS. The two effects can be, respectively, expressed as [31, 32].

$$P_{\text{th}}^{\text{SBS}} = \frac{21}{g_B} \times \frac{\Delta\nu_B}{\Delta\nu_B + \Delta\nu_S} \times \frac{A_{\text{eff}}}{L_{\text{eff}}} \tag{6.1}$$

$$P_{\text{th}}^{\text{SRS}} = \frac{16}{g_R} \times \frac{A_{\text{eff}}}{L_{\text{eff}}} \tag{6.2}$$

in which g_B and g_R are the gain factors of SBS and SRS, respectively. A_{eff} is the effective mode area of the fiber core. L_{eff} is the effective length of the fiber. $\Delta\nu_B$ is the Brillouin gain bandwidth. $\Delta\nu_S$ is the spectral linewidth of the signal laser. It can be seen that the SBS threshold is related to the spectral linewidth of signal laser, and in this way, its effect on the amplification of narrow-linewidth single-frequency laser is more significant [33]. When the laser linewidth is wider than 0.5 GHz, the SRS becomes the most concern since the SBS threshold increases. In addition, the threshold of both SBS and SRS effects increases with the increasement of $A_{\text{eff}}/L_{\text{eff}}$; therefore a straightforward way to suppress the SBS and SRS effects is to increase the effective mode area of the active fiber and reduce the fiber length at the same time.

6.4.2 Thermal Lens Effect

Although fiber laser has a high surface/volume ratio and good heat dissipation, the temperature difference between the fiber surface and the core is still considerable due to quantum defect and non-radiative relaxation when operating in a high-power regime [34–37]. Under this condition, the refractive index of the fiber material will change accordingly, resulting in the onset of the thermal lens effect. This detrimental effect would affect the pump efficiency and the laser conversion efficiency and also degrade the laser beam quality.

6.4.3 Fiber End-Face Damage

Owing to the small mode field diameter (~10 μm) of single-mode fiber, fiber laser has a large optical power density at the output end face. Despite the pure bulk, silica material has a high damage threshold; its density and homogeneity will change when doped with rare-earth ions, and then the damage threshold of the fiber end face is significantly reduced in the double-clad active fiber. Especially, the estimated damage threshold is less than 25 W/μm^2 in high-power CW fiber laser [38, 39]. Figure 6.4 shows the limiting factors of power scaling in an Yb^{3+}-doped double-clad fiber laser with core diameter of 35 μm [40]. The calculated damage threshold of

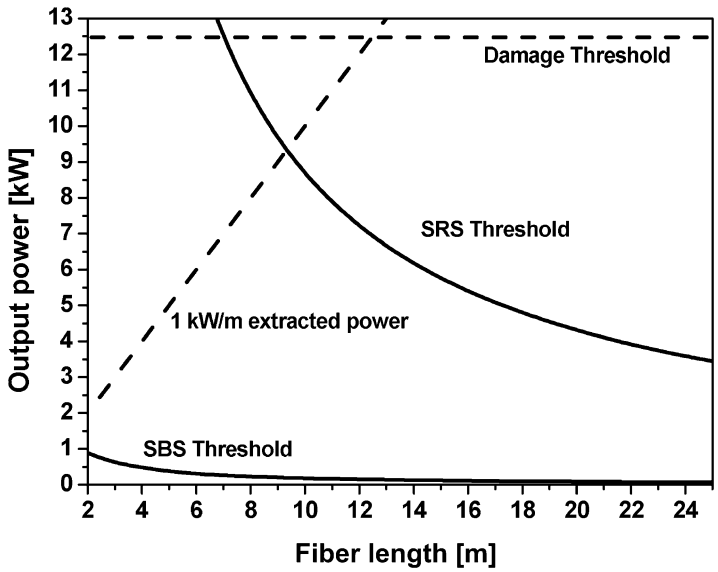

Fig. 6.4 Limiting factors of power scaling in Yb^{3+}-doped double-clad fiber laser. (Reprinted from Ref. [40], copyright 2007, with permission from IEEE)

about 12.5 kW is only slightly higher than the maximum power level achieved by current single-mode MOPA fiber lasers.

6.4.4 Pump Coupling Method

Pumping power and coupling efficiency are the basic factors that determine the output power of single-frequency MOPA laser. Free space coupling system based on discrete lens group is capable of withstanding high temperatures, but the stability and coupling efficiency under high-power operating condition are compensated. All-fiber (N + 1) × 1 multimode pump combiner has lower insertion loss and higher pump efficiency but has poor temperature resistance. This will also be a limiting factor for increasing the output power of all-fiber single-frequency MOPA laser.

Therefore, the power scaling of narrow-linewidth single-frequency MOPA laser is mainly limited by the SBS effect. Currently, the key issue to improve the output power is how to suppress the SBS effect in the MOPA system. The main methods are:

1. Increasing the mode field area and pump absorption coefficient of double-clad active fiber (large mode area fiber, LMAF) to reduce the laser power density and the length of the gain fiber (typically 1~3 m).
2. Applying temperature or stress gradient distribution along the axial direction of the double-clad active fiber to reduce the effective gain coefficient of SBS.
3. Using a narrow-linewidth or multiwavelength seed source. The signal power is distributed over several frequency components, reducing spectral power density of each frequency component.
4. Using special structure of active fiber to suppress SBS.

References

1. Lienhart F, Boussen S, Carat O, Zahzam N, Bidel Y, Bresson A (2007) Compact and robust laser system for rubidium laser cooling based on the frequency doubling of a fiber bench at 1560 nm. Appl Phys B Lasers Opt 89:177
2. Mugnier A, Jacquemet M, Mercier EL, Lebref R, Pureur D (2012) High power single-frequency 780 nm fiber laser source for Rb trapping and cooling applications. Proc SPIE 8237:82371F–1
3. Ball GA, Holton CE, Hull-Allen G, Morey WW (1994) 60 mW 1.5 μm single-frequency low-noise fiber laser MOPA. IEEE Photon Technol Lett 6:192
4. Pan JJ, Shi Y (1999) 166-mW single-frequency output power interactive fiber lasers with low noise. IEEE Photon Technol Lett 11:36
5. Alegria C, Jeong Y, Codemard C, Sahu JK, Alvarez-Chavez JA, Fu L, Ibsen M, Nilsson J (2004) 83-W single-frequency narrow-linewidth MOPA using large-core erbium-ytterbium co-doped fiber. IEEE Photon Technol Lett 16:1825
6. Li L, Schülzgen A, Temyanko VL, Morrell MM, Sabet S (2006) Ultracompact cladding-pumped 35-mm-short fiber laser with 4.7-W single-mode output power. Appl Phys Lett 88:161106

7. Qiu T, Li L, Schülzgen A, Temyanko VL, Luo T, Jiang S, Mafi A, Moloney JV, Peyghambarian N (2004) Generation of 9.3-W multimode and 4-W single-mode output from 7-cm short fiber lasers. IEEE Photon Technol Lett 16:2592
8. Höfer S, Liem A, Limpert J, Zellmer H, Tünnermann A, Unger S, Jetschke S, Müller HR, Freitag I (2001) Single-frequency master-oscillator fiber power amplifier system emitting 20 W of power. Opt Lett 26:1326
9. Yarnall TM, Ulmer TG, Spellmeyer NW, Caplan DO (2009) Single-polarization cladding-pumped optical amplifier without polarization-maintaining gain fiber. IEEE Photon Technol Lett 21:1326
10. Wysocki P, Wood T, Grant A, Holcomb D, Chang K, Santo M, Braun L, Johnson G (2006) High reliability 49 dB gain 13 W PM fiber amplifier at 1550 nm with 30 dB PER and record efficiency. OFC. Postdeadline Session II, PDP17
11. Jeong Y, Nilsson J, Sahu J, Soh D, Alegria C, Dupriez P, Codemard C, Payne D, Horley R, Hickey L, Wanczyk L, Chryssou C, Alvarez-Chavez J, Turner P (2004) Single-frequency polarized Ytterbium-doped fiber MOPA source with 264 W output power. Conference on Lasers electro-optics postdeadline papers CPDD1
12. Vu KT, Malinowski A, Richardson DJ, Ghiringhelli F, Hickey LMB, Zervas MN (2006) Adaptive pulse shape control in a diode-seeded nanosecond fiber MOPA system. Opt Express 14:10996
13. Schimpf DN, Ruchert C, Nodop D, Limpert J, Tünnermann A, Salin F (2008) Compensation of pulse distortion in saturated laser amplifiers. Opt Express 16:17637
14. He F, Price JH, Vu KT, Malinowski A, Sahu JK, Richardson DJ (2006) Optimisation of cascaded Yb fiber amplifier chains using numerical-modelling. Opt Express 14:12846
15. Morasse B, Chatigny S, Desrosiers C, Gagnon É, Lapointe M, Sandro J (2009) Simple design for single mode high power CW fiber laser using multimode high NA fiber. Proc SPIE 7195:7195
16. Karasek M (1997) Optimum design of Er^{3+}-Yb^{3+} codoped fibers for large-signal high-pump-power applications. IEEE J Quantum Elect 33:1769
17. Chryssou CE, Pasquale FD, Pitt CW (2001) Improved gain performance in Yb^{3+} sensitized Er^{3+} doped alumina (Al_2O_3) channel optical waveguide amplifiers. IEEE J Lightwave Technol 19:343
18. Liu AP, Ueda K (1996) The absorption characteristics of circular offset and rectangular double-clad fibers. Opt Commun 132:511
19. Muendel MH (1996) Optimal inner cladding shapes for double-clad fiber lasers. Lasers and electro-optics conference (CLEO 96), 209
20. Liu AP, Ueda K (1996) Propagation losses of pump light in rectangular double-clad fibers. Opt Eng 35:3130
21. Goldberg L, Koplow J (1999) "High power side-pumped Er/Yb doped fiber amplifier," OFC/IOOC'99. Technical Digest 2:21
22. Koplow JP, Moore SW, Kliner DAV (2003) A new method for side pumping of double-clad fiber sources. IEEE J Quantum Elect 39:529
23. http://www.itflabs.com
24. Wang B, Mies E (2009) Review of fabrication techniques for fused fiber components for fiber lasers. SPIE photonic West 09, Fiber lasers VI: technology, systems, and applications
25. Farrow RL, Kliner DAV, Schrader PE, Hoops AA, Moore SW, Hadley GR, Schmitt RL (2006) High-peak-power (>1.2 MW) pulsed fiber amplifier. SPIE Photonics West paper 6102–22
26. Teodoro FD, Brooks CD (2005) 1.1 MW peak-power, 7 W average-power, high spectral brightness, diffraction-limited pulses from a photonic crystal fiber amplifier. Opt Lett 30:2694
27. Zheng Y, Yang Y, Wang J, Hu M, Liu G, Zhao X, Chen X, Liu K, Zhao C, He B, Zhou J (2016) 10.8 kW spectral beam combination of eight all-fiber superfluorescent sources and their dispersion compensation. Opt Express 24:12063
28. Shiraki K, Ohashi M (1996) SBS threshold of a fiber with a Brillouin frequency shift distribution. J Lightwave Technol 14:50

29. Liu AP (2006) Novel SBS suppression scheme for high power fiber amplifiers. Proc SPIE 6102:1
30. Wang Y (2004) Heat dissipation in kilowatt fiber power amplifiers. IEEE J Quantum Elect 40:731
31. Jäger M, Caplette S, Verville P, Villeneuve A (2005) Fiber lasers and amplifiers with reduced optical nonlinearities employing large mode area fibers. Proc SPIE 5971:59710N-1
32. Payne DN, Jeong Y, Nilsson J, Sahu JK, Soh DBS, Alegria C, Dupriez P, Codemard CA, Philippov VN, Hernandez V, Horley R, Hickey L, Wanzcyk L, Chryssou CE, Alvarez-Chavez JA, Turner PW (2005) Kilowatt class single-frequency fiber sources (invited paper). Proc SPIE 5709:133
33. Agrawal GP (1989) Nonlinear fiber optics. Academic Press, San Diego
34. Brown DC, Hoffman HJ (2001) Thermal stress and thermo optic effects in high average power double-clad silica fiber lasers. IEEE J Quantum Elect 37(183):207–217
35. Li J, Duan K, Wang Y, Cao X, Zhao W, Guo Y, Lin X (2008) Theoretical analysis of the heat dissipation mechanism in Yb^{3+}-doped double-clad fiber lasers. J Mod Opt 55:459
36. Yan P, Xu A, Gong M (2006) Numerical analysis of temperature distributions in Yb doped double-clad fiber lasers with consideration of radiative heat transfer. Opt Eng 45:124201–124201
37. Guillaume CG, Mollier J-C (2005) Evidence of thermal effects in a high-power Er^{3+}-Yb^{3+} fiber laser. Opt Lett 30:3030
38. Smith AV, Do BT, Soderlund M (2007) Deterministic nanosecond laser-induced breakdown thresholds in pure and Yb^{3+} doped fused silica. Proc SPIE 6453:645317–645311
39. Smith AV, Hadley GR, Farrow RL, Do BT (2008) Nonlinear optical limits to power in fiber amplifiers. OSA/CLEO/QELS, CFR2
40. Limpert J, Roser F, Klingebiel S, Schreiber T, Wirth C, Peschel T, Eberhardt R, Tunnermann A (2007) The rising power of fiber lasers and amplifiers. IEEE J Sel Top Quant Electron 13:537

Chapter 7
Amplification of CW Single-Frequency Lasers

In this chapter, we focus on the amplification of continuous-wave single-frequency lasers. In this case, the single-frequency power scaling is mainly limited by the stimulated Brillouin scattering and thermal effects in the amplifying fiber. To address these problems, different schemes have been proposed to suppress the fiber nonlinear and thermal effects, a most popular one is using large mode area active fiber to decrease the laser intensity and thermal energy per unit area. The layout trifurcates into three sections concerning the laser amplification in the 1.0 μm, 1.5 μm, and 2.0 μm regions, which corresponds to the well-known dopants (i.e., erbium, ytterbium, and thulium ions) in optical fiber. In each section, the emission characteristics such as the spectral features of the corresponding rare-earth dopants are first introduced. Then a theoretical mode is established for the analysis of the fiber amplifiers in the three wavelength bands. Finally, experimental progress on single-frequency fiber amplification is introduced and discussed in each section.

7.1 Amplification of CW Single-Frequency Lasers at the 1.0 μm Region

Continuous-wave (CW) single-frequency lasers at the 1.0 μm region have important applications in industrial, military, and scientific research. Especially, single-frequency lasers in the wavelength range of 1010–1025 nm can be used in optical lattice clock (OLC), deep space detection, quantum computing, and fundamental physics [1–4]. The OLC based on the $^1S_0 \leftrightarrow {}^3P_2$ transition of Yb atoms and the $^1S_0 \leftrightarrow {}^3P_1$ transition of Hg atoms can achieve ultra-precision time and frequency metrology with a fractional uncertainty, much more accurate than the microwave atomic clocks. In addition, the single-frequency laser at 1083 nm can be used for nonlinear frequency conversion and atomic and molecular spectroscopy [5–7]. As

© Springer Nature Singapore Pte Ltd. 2019

Z. Yang et al., *Single-Frequency Fiber Lasers*, Optical and Fiber Communications Reports 8, https://doi.org/10.1007/978-981-13-6080-0_7

for high-power single-frequency laser at 1064 nm, it can be used for coherent beam combining, nonlinear frequency conversion, gravitational wave detection, and laser radar [8–12].

However, these applications typically require the 1.0 μm single-frequency laser equipped with excellent characteristics of all-fiber design, low noise, kHz linewidth, linearly polarized, and high-output power. To this end, the MOPA technology must be employed to realize significant power amplification of CW single-frequency seed laser.

7.1.1 Spectral Features of Yb^{3+} Emission

The absorption cross section and emission cross section of Yb^{3+} in the matrix material directly determine the fluorescence output of the Yb^{3+}-doped fiber amplifier and laser. Figure 7.1a shows the absorption and emission cross sections of Yb^{3+}-doped silica glass. It can be seen that the absorption spectrum of Yb^{3+} has two strong absorption peaks at 915 and 976 nm, respectively. In addition, there are also two strong emission peaks at 975 and 1036 nm, which, respectively, correspond to a three-level transition system and a four-level transition system.

The absorption and emission cross sections of Yb^{3+} strongly depend on the host material or the glass components. For example, the fluorescence lifetime would become shorter, and the amplitude of the absorption and emission cross sections increases when changing the content of germanium in the silica fiber. Therefore, the actual emission spectrum changes significantly in the 950–1050 nm band. Figure 7.1b shows the absorption and emission cross sections of Yb^{3+}-doped phosphate glass. It can be seen from the figure that in this case the spectral shape of the Yb^{3+} emission changes significantly compared to that of the Yb^{3+}-doped silica glass, and the corresponding amplitude of the absorption and emission cross sections becomes larger.

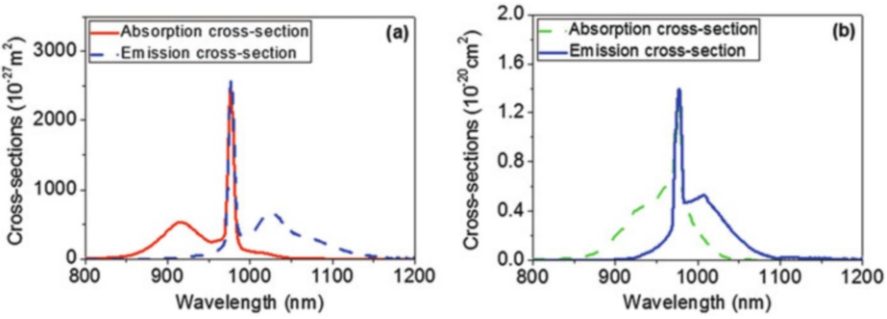

Fig. 7.1 Absorption and emission cross sections of the Yb^{3+} ions in different host materials. (**a**) Silica glass, (**b**) phosphate glass

7.1.2 Theoretical Model of Yb^{3+}-Doped Fiber Amplifier

In a Yb^{3+}-doped fiber amplifier, the spontaneous emission is also amplified at the same time other than the laser signal, deteriorating the output performances of the amplified signal laser. The simplified two-level steady-state rate equations of the Yb^{3+}-doped fiber amplifier can be expressed as follows [13]:

$$\begin{aligned}\frac{dN_2(z,t)}{dt} = & \frac{\Gamma_p\lambda_p}{hcA}\left[\sigma_a(\lambda_p)N_1(z,t) - \sigma_e(\lambda_p)N_2(z,t)\right]\left[P_p^+(z,t) + P_p^-(z,t)\right] - \frac{N_2(z,t)}{\tau} \\ & + \frac{\Gamma}{hcA}\sum_{k=1}^{K}\lambda_k\left[\sigma_a(\lambda_k)N_1(z,t) - \sigma_e(\lambda_k)N_2(z,t)\right]\left[P_s^+(z,t,\lambda_k) + P_s^-(z,t,\lambda_k)\right]\end{aligned} \tag{7.1}$$

$$N = N_1(z,t) + N_2(z,t) \tag{7.2}$$

Due to the wide emission cross section of the Yb^{3+}-doped fiber, it is impossible to accurately calculate the equations using the emission cross section of a fixed wavelength. A compromised method is to divide the spectrum of amplified spontaneous emission (ASE) into multiple K channels, of which the corresponding center wavelength and bandwidth can be recorded as λ_k ($k = 1, 2, \cdots, K$) and $\Delta\lambda$, respectively. In this way, the signal and ASE light can share the same power propagation equations, which can be expressed as follows:

$$\begin{aligned}\pm\frac{\partial P_p^{\pm}(z,t)}{\partial z} + \frac{1}{\nu_p}\frac{\partial P_p^{\pm}(z,t)}{\partial t} = & -\Gamma_p\left[\sigma_a(\lambda_p)N_1(z,t) - \sigma_e(\lambda_p)N_2(z,t)\right]P_p^{\pm}(z,t) \\ & -\alpha(\lambda_p)P_p^{\pm}(z,t)\end{aligned} \tag{7.3}$$

$$\begin{aligned}\pm\frac{\partial P_s^{\pm}(z,t,\lambda_k)}{\partial z} + \frac{1}{\nu_k}\frac{\partial P_s^{\pm}(z,t,\lambda_k)}{\partial t} = & \Gamma_s\left[\sigma_e(\lambda_k)N_2(z,t) - \sigma_a(\lambda_k)N_1(z,t)\right]P_s^{\pm}(z,t,\lambda_k) \\ & -\alpha(\lambda_k)P_s^{\pm}(z,t,\lambda_k) + 2\sigma_e(\lambda_k)N_2(z,t)\frac{hc^2}{\lambda_k^3}\Delta\lambda \\ & +S_R(\lambda_k)P_s^{\pm}(z,t,\lambda_k), k = 1,2,\ldots K\end{aligned} \tag{7.4}$$

where N is the dopant concentration of Yb ions and assumed to be uniform along the fiber. z is the positional coordinate along the axial direction of the fiber ($z \in [0, L]$). L is the fiber length. N_1 (z, t) and N_2 (z, t) are, respectively, the population of Yb^{3+} ions at the ground and upper level. $P_p^{\pm}(z,t)$ is the forward and backward pump power. $P_s^{\pm}(z,t,\lambda_k)$ is the forward and backward signal power at the center wavelength of λ_k. Γ_p and Γ_s are, respectively, the overlap factors of the pump light and the signal light with respect to the fiber core. $\sigma_a(\lambda_p)$ and $\sigma_e(\lambda_p)$ are the absorption and emission cross section of the pump light, respectively. $\sigma_a(\lambda_k)$ and $\sigma_e(\lambda_k)$ are the absorption and emission cross section of the signal light at the wavelength of λ_k, respectively. V_p and V_k are the group velocity of pump light and signal light,

respectively. h is the Planck's constant. c is the light velocity in the vacuum. A is the effective mode area of the fiber. τ is the upper state lifetime of the Yb ions. S_R is the Rayleigh scattering coefficient. $\alpha(\lambda_p)$ and $\alpha(\lambda_k)$ are the propagation loss of the pump light and the signal light, respectively.

To solve the above equations, the initial boundary conditions of the equations are also needed to be given.

Considering the forward pumping configuration, it satisfies the following initial boundary conditions:

$$P_p^+(0) = P_p^{in}, P_p^-(L) = 0, P_s^+(0,\lambda_s) = P_s^{in}, P_s^+(0,\lambda_k) = 0, P_s^-(L,\lambda_k) = 0 \quad (7.5)$$

As to the backward pumping configuration, it satisfies the following initial boundary conditions:

$$P_p^-(L) = P_p^{in}, P_p^+(0) = 0, P_s^+(0,\lambda_s) = P_s^{in}, P_s^+(0,\lambda_k) = 0, P_s^-(L,\lambda_k) = 0 \quad (7.6)$$

While for the bidirectional pumping configuration, it satisfies the following initial boundary conditions:

$$P_p^-(L) = P_p^{in1}, P_p^+(0) = P_p^{in2}, P_s^+(0,\lambda_s) = P_s^{in}, P_s^+(0,\lambda_k) = 0, P_s^-(L,\lambda_k) = 0 \quad (7.7)$$

where P_p^{in} is the injected pump power and P_s^{in} is the injected signal power. P_p^{in1} and P_p^{in2} are, respectively, the forward and backward launched pump power in the condition of bidirectionally pumping.

7.1.3 Experimental Study of Single-Frequency MOPA Laser Below 1030 nm

Laser sources in the blue to deep ultraviolet (UV) regions have potential applications in Raman spectroscopy, industrial micromachining, laser cooling and capturing, optical data storage, underwater communication, and medical diagnostics. Although semiconductor lasers can work in the blue to deep UV region, its low output power, poor beam quality, and wide spectral linewidth limit their application level. Another alternative is to realize high-performance blue to deep UV lasers through double or quadruple frequency conversion of high-power linearly polarized single-frequency lasers with an operating wavelength below 1030 nm.

In 2013, Zhu et al. demonstrated a power amplification of a 976 nm single-frequency fiber laser by using a segment of several centimeter-long polarization-maintaining highly Yb^{3+}-doped (6 wt%) phosphate fiber (YPF) [14]. The experimental setup of the 976 nm single-frequency MOPA laser is shown in Fig. 7.2. It consists of a 976 nm single-polarization single-frequency seed laser and a

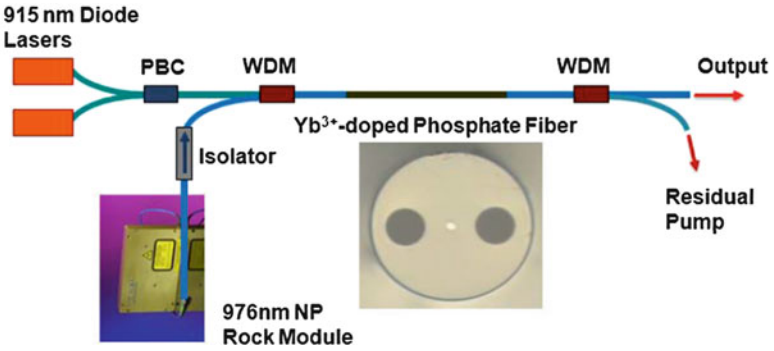

Fig. 7.2 Experimental setup of the 976 nm single-frequency MOPA laser. (Reprinted from Ref. [14], copyright 2013, with permission from IEEE)

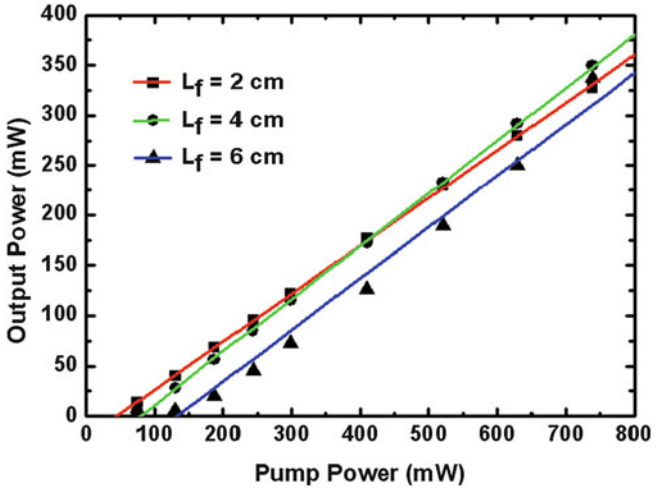

Fig. 7.3 Relationship between the output power and pump power with different YPF lengths. (Reprinted from Ref. [14], copyright 2013, with permission from IEEE)

polarization-maintaining short-length YPF amplifier. Yb^{3+}-doped phosphate fibers with lengths of 2, 4, and 6 cm were used in the experiment to optimize the system performance. The output port of the seed source is connected to the signal port of a polarization-maintaining wavelength division multiplexer (WDM) and then the polarization-maintaining YPF. Another polarization-maintaining WDM is connected to the spare end the YPF to separate the amplified laser signal and residual pump light.

Figure 7.3 shows the relationship between the output power of the MOPA laser and the pump power with different YPF lengths. It can be seen that the MOPA laser with 2 cm length YPF has the lowest threshold, while that with 6 cm length has the highest threshold, indicating that higher pump power is required to achieve efficient

population inversion for longer active fiber. At a signal power of 10 mW, the slope efficiencies of the MOPA laser with the length of 2, 4, and 6 cm were 47.5%, 52.5%, and 51.2%, respectively. At a pump power of 739 mW, the system with the 4 cm length YPF obtained a maximum output power of 350 mW. The measured signal-to-noise ratio (SNR) of the MOPA laser was greater than 50 dB. The obtained polarization extinction ratio (PER) was greater than 20 dB, indicating that the output laser was linearly polarized. In addition, a delayed self-heterodyne method was used to measure the output laser linewidth. The measured linewidth of the MOPA laser was about 3 kHz, which was basically the same as that of the seed laser.

In order to study the process of atomic transitions in the visible and ultraviolet (UV) bands, a kHz-linewidth, low-noise, and high-power (watt-level) 1014 nm single-frequency laser is required. To leverage the single-frequency MOPA laser system at the short wavelength side (i.e., <1030 nm) of the Yb^{3+} emission, a problem that need to be addressed is the strong reabsorption at the laser wavelength and amplified spontaneous emission (ASE) at longer wavelength. Through cooling the Yb^{3+}-doped silica fiber with liquid nitrogen, several groups have demonstrated 1014 nm single-frequency MOPA lasers by employing bulk free-space components and external cavity diode laser as the seed signal [18~20]. However, in these works, the conversion efficiency (typical values of 20–40%) and the OSNR (typical values of <30 dB) of the laser system are still needed to be further improved.

In 2014, Yang et al. [15] reported a high-efficiency single-frequency MOPA laser at 1014 nm based on core pumping a Yb^{3+}-doped phosphate fiber amplifier with 4.0-cm-long fiber gain fiber. Up to 1.06 W stable laser output was demonstrated with one-stage amplification. The experimental setup of the single-frequency MOPA laser is depicted in Fig. 7.4. It comprised a 1014 nm single-frequency seed laser and a one-stage short YPF amplifier. The seed laser was based on a short-cavity DBR structure consisting of a 1.4-cm-long YPF with a maximum output power of 40 mW. Regarding the amplifier, YPF with lengths of 2.1, 4.0, and 6.2 cm was used to optimize the laser performances. Both end faces of the YPF were, respectively, fusion spliced with the common port of two wavelength division multiplexers

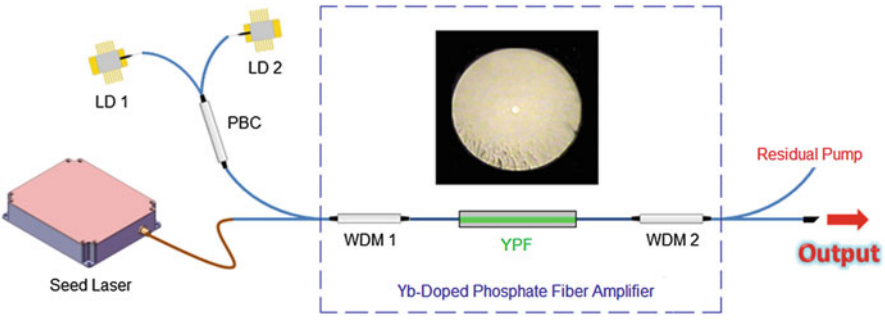

Fig. 7.4 Experiment setup of the 1014 nm MOPA laser. Inset: cross section of the YPF. (Reprinted from Ref. [15], copyright 2014, with permission from IOP Publishing)

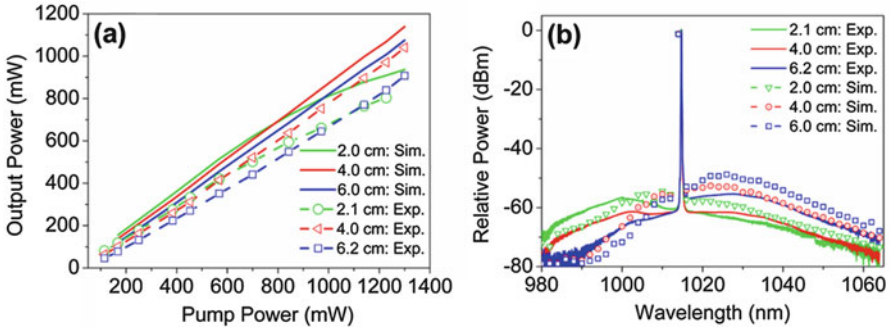

Fig. 7.5 (**a**) Simulated (solid curves) and measured (dotted curves) output power versus pump power of the MOPA lasers with an input power of 21.4 mW. (**b**) Corresponding output optical spectra under a pumping power of 1140 mW. (Reprinted from Ref. [15], copyright 2014, with permission from IOP Publishing)

(WDM1, WDM2), and the WDM2 was used to separate the amplified signal laser and residual pump.

Based on the theoretical model of Yb^{3+}-doped fiber amplifier [16, 17] and the specific optical parameters of the employed YPF, the length of the gain fiber in the 1014 nm MOPA laser system was theoretically and experimentally optimized. Figure 7.5a illustrates the simulated and measured output powers versus the pump power with different length of the gain fiber. The calculated slope efficiencies of the 2.0-, 4.0-, and 6.0-cm-long MOPA were, respectively, 66.7%, 88.5%, and 84.5%, while the corresponding measured values with an input signal power of 21.4 mW were 67.6%, 81.1%, and 71.6%, respectively. The experimental results were in very good agreement with the simulation results, that is, the optimized gain fiber length is 4.0 cm in terms of efficiency.

Under a pump power of 1140 mW, the optical spectra of the MOPA with different fiber lengths were measured by an OSA with a spectrum resolution of 0.1 nm. Figure 7.5b shows the measured and simulated spectra of the MOPA lasers with an input power of 21.4 mW. The simulated results were in good agreement with the measurement, and a highest OSNR was obtained from the MOPA with 4.0-cm-long YPF.

The MOPA with 4.0-cm-long YPF was characterized by measuring the output powers with different input powers, as shown in Fig. 7.6. With an input power of 38.8 mW and launched pump power of 1300 mW, the MOPA laser realized a highest output power of 1059 mW and a highest optical-to-optical conversion efficiency of 81.4%.

In addition, the linewidths of the seed laser and the MOPA laser were measured with the self-heterodyne method by using an acousto-optic modulator with a driving frequency of 80 MHz and a 10-km-long fiber-delay line. The measured result of ~2 kHz for both the seed laser and the MOPA output indicates that the linewidth broadening effect was negligible during the amplification.

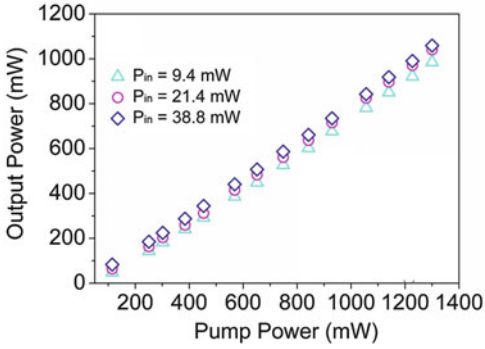

Fig. 7.6 Measured output powers versus pump power of the MOPA with 4.0-cm-long YPF at different input powers. (Reprinted from Ref. [15], copyright 2014, with permission from IOP Publishing)

In 2014, Hu et al. also demonstrated a 1014.8 nm single-frequency MOPA laser [18]. The laser system was consisted of an external cavity single-frequency semiconductor laser (seed laser) and a two-stage polarization-maintaining fiber amplifier. The active fiber used for the power amplifier was a 1.4-m-long polarization-maintaining Yb^{3+}-doped double-clad silica fiber, of which the core/inner cladding diameter was 10/125 μm. With a signal power of 3.1 W, a linearly polarized single-frequency laser with a maximum power of 19.3 W and a conversion efficiency of 33.5% was obtained. Further increasing the output power was limited by the onset of SBS effect. The linewidth of the MOPA laser was measured to be approximately 24 kHz by using the self-heterodyne method, and no significant linewidth broadening was observed during the amplification.

7.1.4 Experimental Study of Single-Frequency MOPA Laser at 1064 Nm

The 1064 nm high-power single-frequency fiber laser has a very wide range of applications, such as laser ranging, coherence and spectral beam combining, gravitational wave detection, and laser lidar [9, 10, 19]. In particular, in some applications such as nonlinear frequency conversion, optical parametric oscillation, and optical parametric amplification, the single-frequency lasers are often required with an all-fiber design, kHz linewidth, linear-polarization, low noise, and high-output power [8, 20–22].

Due to the strong limitation of SBS effect, the output power of a single-frequency MOPA fiber laser at 1064 nm has remained at the power level of 500 W for many years [23, 24]. Furthermore, most of the previous works use bulk optical components. The free-space structure renders the laser system to be bulky, heavy, and sensitive to the environmental vibration. Considering the all-fiber MOPA single-frequency laser, 194 W and 310 W laser outputs were achieved by using multistage amplifier configuration with Yb^{3+}-doped large mode area fibers (LMAFs) [9, 25]. However, with a further increasement of the output power, the laser

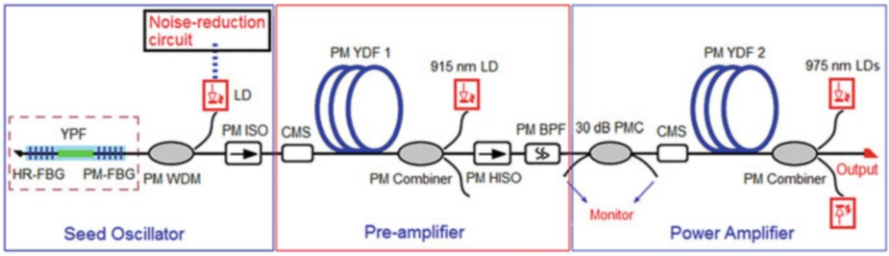

Fig. 7.7 Schematic setup of the LP-MOPA laser. PM WDM, 980/1064 nm PM wavelength division multiplexer and PM ISO, 1064 nm PM isolator. (Reprinted from Ref. [11], copyright 2016, with permission from IOP Publishing)

characteristics (e.g., laser linewidth, noise, polarization state, beam quality, etc.) will be deteriorated mainly due to the onset of nonlinear effects, amplified spontaneous emission (ASE), noise accumulation, and thermal effects.

In order to suppress the SBS, a straightforward method is to modulate the phase of the single-frequency seed laser to broaden its linewidth. Besides, the introduction of temperature gradient and stress gradient along the fiber can also effectively increase the SBS threshold; however, it would cause instabilities in polarization-maintaining MOPA systems. So, a simplest and most effective method is to directly use a short-length, large-core, highly Yb^{3+}-doped active fiber.

In 2016, Yang et al. developed an all-fiber kHz-linewidth linearly polarized single-frequency MOPA laser at 1064 nm with a stable CW output power of >52 W [11]. Figure 7.7 shows the experimental setup of the MOPA laser, which consists of a single-frequency seed laser and a two-stage polarization-maintaining Yb^{3+}-doped double-clad fiber amplifier. The seed oscillator was based on a DBR short cavity that constructed with a segment of Yb^{3+}-doped phosphate fiber and two fiber Bragg gratings. It produced an output power of >53 mW with a polarization extinction ratio (PER) of >30 dB. In addition, a tailored optoelectronic feedback circuit acting on the pump current was integrated into the LD driver module for the suppression of intensity noise generated by the resonant relaxation oscillation of the laser.

The output power of the seed laser was amplified to 4.2 W by a preamplifier with a 5-m-long polarization-maintaining Yb^{3+}-doped double-clad fiber. The power amplifier was mainly composed of a 2.5-m-long polarization-maintaining Yb^{3+}-doped double-clad fiber with a 12 μm/0.10 NA core and a 125 μm/0.45 NA cladding. The cladding absorption of the fiber was 12 dB/m at 975 nm.

To realize a narrower linewidth of the LP-MOPA laser, the relative intensity noise (RIN) of the seed oscillator was suppressed before amplified. Using a 20-km-long delay fiber, the laser linewidth before and after noise suppression was measured with the delayed self-heterodyne method, and the results are shown in Fig. 7.8a. It is seen that the noise suppression has negligible influence on the seed laser linewidth, which was less than 2 kHz (full width half width, FWHM). After noise suppression, the laser linewidth of the LP-MOPA was basically the same as that of the seed oscillator.

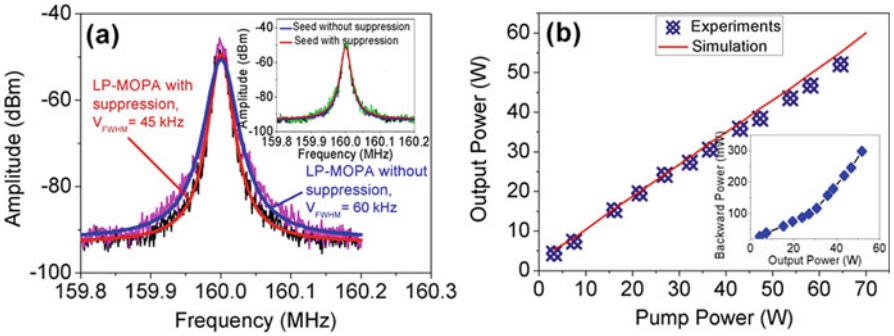

Fig. 7.8 (**a**) Measured self-heterodyne signals of the LP-MOPA laser. Inset: measured self-heterodyne signals of the seed oscillator with and without noise reduction. (**b**) Experiment (dotted curve) and simulation (solid curve) of output power versus pump power of the LP-MOPA laser. Inset: the backscattered power versus laser output power. (Reprinted from Ref. [11], copyright 2016, with permission from IOP Publishing)

While without suppression, the laser linewidth of the LP-MOPA was slightly broadened to 3 kHz due to the self-phase modulation caused by the relaxation oscillation-induced intensity fluctuations in the amplification [26]. In addition, the relative intensity noise (RIN) of the seed oscillator before and after noise suppression was characterized using an InGaAs photodetector and an electrical spectrum analyzer with a bandwidth resolution of 1 kHz. The dominating peak of the laser relaxation oscillation at 1.1 MHz was reduced by approximately 15 dB (from −110 to −125 dB/Hz). At the highest output power, the RIN of the LP-MOPA laser was less than −130 dB/Hz at frequency higher than 2 MHz. There was no obvious degradation of the RIN after power amplification.

Figure 7.8b shows the experimental and simulated results of the output power versus the pump power of the LP-MOPA laser. When the pump power was 64.5 W, the output power reached 52.1 W without any rollover, and the optical-to-optical (O-O) efficiency was approximately 81%. The calculated output power and O-O efficiency were 60 W and 86%, respectively. The inset of Fig. 7.8b shows the backward propagating power versus the laser output power. The power level in the backward direction enhanced gradually without any sudden increasement, indicating that no SBS occurred. The SBS threshold was calculated to be approximately 45 W, which was slightly lower than the value in the experiment.

In addition, the phase noise of the fiber laser was tested by an unbalanced Michelson interferometer, which was constructed with 100 m optical path difference. Figure 7.9 shows the measured phase-noises of the seed oscillator and LP-MOPA laser with an output power of 52 W. At frequencies in the 100 Hz–1 kHz range, the phase-noises were at the same level mainly caused by the ambient acoustics and vibration. However, in the frequency region of >1 kHz, the phase-noise of the LP-MOPA laser was <5 urad/$Hz^{1/2}$, slightly higher than that of the seed oscillator, owing to the small fluctuations of the pump power and the thermal effect generated in the process of amplification.

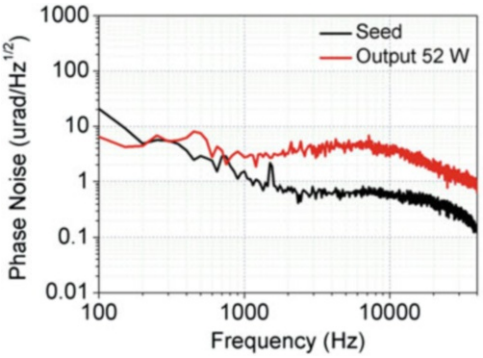

Fig. 7.9 Measured phase-noise spectra of the seed oscillator and LP-MOPA laser. (Reprinted from Ref. [11], copyright 2016, with permission from IOP Publishing)

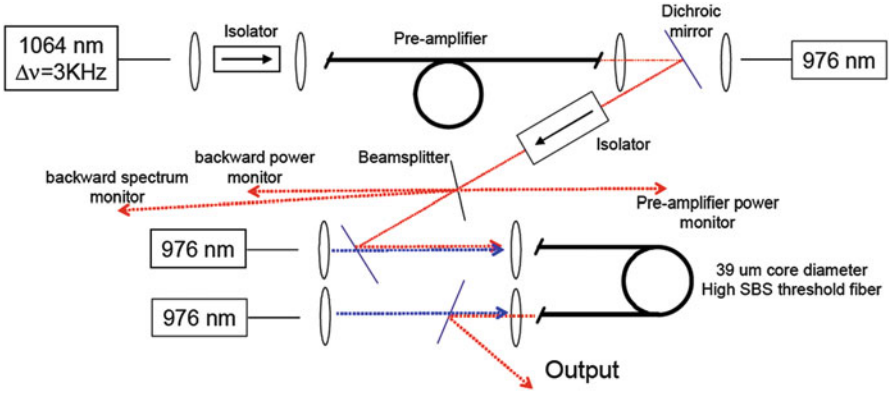

Fig. 7.10 The schematic of two-stage amplifier system with a high SBS threshold fiber. (Reprinted from Ref. [8], copyright 2007, with permission from OSA Publishing)

For the 1064 nm CW single-frequency MOPA laser, another representative research work was carried out by Gray et al., who demonstrated an over 500 W single-frequency laser at 1064 nm based on bulk optical components and large-core double-clad active fiber [8]. The amplification part adopted a two-stage Yb^{3+}-doped fiber amplifier structure. A 1064 nm fiber laser with a power of 100 mW and a laser linewidth of less than 3 kHz was used as a seed source. The preamplifier used a 4-m-long Yb^{3+}-doped polarization-maintaining double-clad fiber with 20 μm core diameter to raise the signal power to 5 W. The gain fiber was bent to a diameter of about 70 mm to control the mode quality, which was measured to be 1.06 in pre-amplifier stage. The power amplifier consisted of a 8.5-m-long Yb^{3+}-doped polarization-maintaining double-clad fiber with a core/cladding diameter of 39 μm/420 μm and a numerical aperture (NA) of 0.05. The pump absorption coefficient of the active fiber was 3.2 dB/m at 976 nm. The schematic of the MOPA laser is shown in Fig. 7.10.

The power amplifier achieved a maximum output power of 502 W at a pump power of 800 W. The beam quality factor of the output laser was measured to be 1.4 by using a beam quality analyzer, indicating that the output beam had a good mode

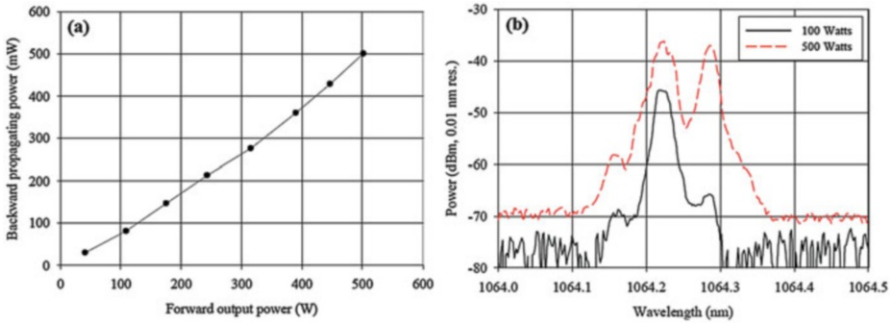

Fig. 7.11 (**a**) Backward propagating power measured as a function of forward output power. (**b**) Spectra of backward propagating light for 100 W and 500 W output powers. (Reprinted from Ref. [8], copyright 2007, with permission from OSA Publishing)

quality. Figure 7.11a shows the relationship between the backward propagating power and the laser output power. The power level in the backward direction did not exhibit any sudden increase that is caused by SBS effect.

The spectrum of the backward propagating light was also recorded and is plotted in Fig. 7.11b for the cases of 100 and 500 W of forward output power. With only 100 W of output power, the backward spectrum was dominated by the Rayleigh scattering of the injected signal. The two subsidiary peaks, more than 20 dB below the main peak, were caused by the Stokes and anti-Stokes Brillouin scattering within the fiber. At 500 W of output power, the Stokes peak was almost equal in magnitude to the Rayleigh scattered peak, indicating a significant increase in the relative level of the Brillouin scattered light and showing that although the output power was approaching the SBS threshold, it is still pump limited. Furthermore, based on the Brillouin gain coefficient value of 0.9×10^{-11} m/W, the SBS threshold of the MOPA laser system was calculated to be about 542 W, which was slightly higher than the actual value.

7.1.5 Experimental Study of CW Single-Frequency MOPA Laser at 1083 Nm

Narrow-linewidth single-frequency lasers at 1083 nm can be applied to nonlinear frequency conversion and atomic and molecular spectroscopy [5–7, 27, 28]. A representative example is to use the 1083 nm single-frequency laser to study the multiplet of the helium (He) atom to improve the measurement precision of the constant of the fine structure [29, 30]. In addition, using this naturally occurring metastable state of He, the upper neutral atmosphere from 300 to 1000 km can be actively probed with a resonance fluorescence Doppler wind/temperature lidar operating at 1083 nm [31, 32]. Thus, the narrow-linewidth, low-noise, watt-level,

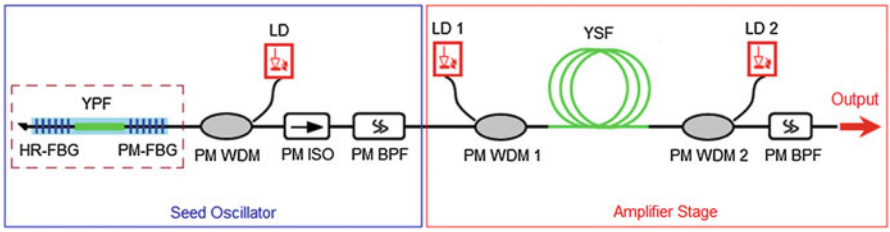

Fig. 7.12 Experiment setup of the single-frequency 1083 nm PM-MOPA laser. (Reprinted from Ref. [38], copyright 2014, with permission from OSA Publishing)

and polarization-maintained (PM) lasers of radiation at 1083 nm are required for many of these applications.

There are several ways to obtain a single-frequency 1083 nm laser source. Flash-pumped LNA solid-state laser can deliver several watts power with a 2 GHz bandwidth [33]. Distributed Bragg reflector (DBR) diode laser offers several milliwatts output with a few hundred kHz linewidth [34, 35]. Yb-doped fiber laser operating at 1083 nm can realize a few milliwatts output with linewidth of about several MHz [36] and even several kHz linewidth [37]. Usually, in order to further increase the output power of the single-frequency 1083 nm laser, a MOPA configuration must be used.

Though the output power of diode laser and fiber oscillator could be boosted to a few hundred milliwatts, further amplifying to tens of watts based on the Yb^{3+}-doped fiber amplifier would produce a wide linewidth and a low optical signal-to-noise ratio (OSNR) due to the ASE noise and even unstable operation at a certain longitudinal mode. It is worth noting that the operating wavelength of 1083 nm is almost approaching the edge of the gain spectrum and the available gain is usually limited to below 14 dB, thus it is difficult to efficiently amplify a 1083 nm seed laser if no ASE filtering or suppression schemes are used.

In 2014, Yang et al. presented a high OSNR watt-level single-frequency PM-MOPA laser, which amplified the output of a 1083 nm laser oscillator using a single-mode core-pumped Yb^{3+}-doped PM fiber amplifier [38]. Figure 7.12 shows the 1083 nm PM-MOPA laser configuration, including a single-frequency linearly polarized seed oscillator and a one-stage single-clad PM fiber amplifier. The seed oscillator has a maximum power of 110 mW, a laser linewidth of ? 3 kHz, and a polarization extinction ratio (PER) of 30 dB. A 2.5-m-long highly Yb^{3+}-doped PM single-clad fiber was employed as the laser gain medium in the amplifier stage. The fiber had a 6.0 μm mode field diameter at 1064 nm, a 0.14 numerical aperture (NA), and a 125 μm cladding. The amplifier was bidirectionally pumped by two single-mode fiber-coupled LDs centered at 976 nm (provide a total pump power of 1500 mW).

Generally, the primary limitation on the output power or the gain achievable at 1083 nm from a Yb^{3+}-doped fiber amplifier is the generation of ASE at around 1030 nm, which could significantly deplete the pump power. To address this problem, a polarization-preserving band-pass filter (PM BPF) with an operating

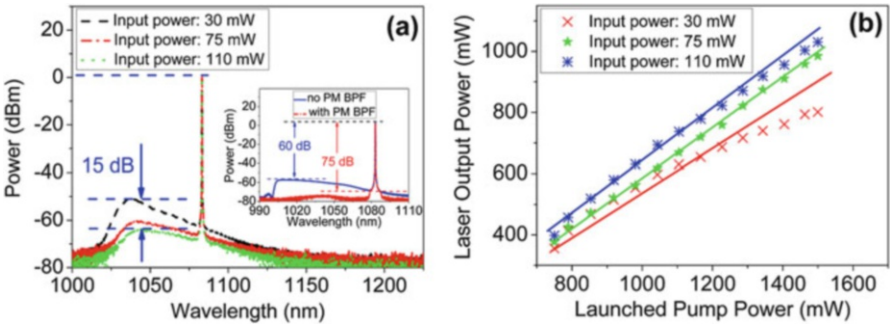

Fig. 7.13 (**a**) Output spectra of the fiber laser with different input powers of the seed oscillator. Inset: output spectra of the seed oscillator with PM BPF and without PM BPF. (**b**) Measured laser output power versus the launched pump power for different input powers of the seed oscillator. (Reprinted from Ref. [38], copyright 2014, with permission from OSA Publishing)

wavelength of 1083 ± 3 nm was used to directly filter out the ASE light from the seed oscillator, increasing its signal-to-noise ratio from 60 dB to 75 dB, as plotted in the inset of Fig. 7.13a. Then, the signal power of the seed oscillator was increased from 30 to 110 mW, and the output spectrum of the MOPA laser at the pump power of 1300 mW was measured with an optical spectrum analyzer (OSA), as shown in Fig. 7.13a. It can be seen that the whole ASE power level was suppressed successfully by more than 15 dB.

Figure 7.13b shows the output power of the PM-MOPA laser versus the launched pump power for different input powers of the seed oscillator. With the maximal input power (110 mW) and pump power (1500 mW), the 1083 nm laser was amplified up to the highest value of 1.03 W with a typical gain of 9.7 dB, and the highest optical-to-optical conversion efficiency (the output power versus the launched pump power) was about 68.7%.

In addition, the laser linewidth was measured by the self-heterodyne method using a 20-km-long fiber delay. The heterodyne signal was fit with a Lorentzian profile to estimate the spectral linewidth. The FWHM (full width at half maximum) linewidth was measured to be less than 3.5 kHz, which was the same as that of the seed oscillator. Thanks to the effective ASE suppression and low relative intensity noise of the seed laser, there was no obvious linewidth broadening effect.

To further demonstrate the output power scaling of CW single-frequency laser at 1083 nm, Xu et al. developed a 90.4 W single-frequency MOPA laser based on multistage fiber amplifier structure in 2012 [36]. The signal was a homemade 1083 nm single-frequency seed laser (based on ring cavity) with a power of 2.8 mW and a laser linewidth of 12 MHz, followed by four fiber amplifiers for power amplification. A maximum power of 90.4 W with a conversion efficiency of 72.5% and a polarization extinction ratio of 13 dB were obtained from the MOPA

laser. In terms of power scaling, this work pushed the output power of 1083 nm single-frequency MOPA laser to a higher level.

7.2 Amplification of CW Single-Frequency Lasers at 1.5 μm Regions

High-power single-frequency fiber lasers at 1.5 μm are attractive for many potential applications, such as Doppler *lidar*, coherent and spectrum beam combining, atom clock, and atom cooling and trapping. As discussed previously, single-frequency fiber lasers based on a single fiber oscillator can obtain a laser output power of up to several hundred milliwatts [39, 40]. However, due to the limitations on cavity length and thermal effects, it is difficult to further realize output power scaling. In order to obtain higher power output at 1.5 μm regions, the MOPA scheme must be used. In other words, a fiber amplifier that is constructed by a segment of Er^{3+}-doped or Er^{3+}/Yb^{3+}-codoped active fiber is needed to amplify the 1.5 μm single-frequency seed laser.

7.2.1 Characteristics of Er^{3+}/Yb^{3+}-Codoped Fiber

In Er^{3+}-doped laser system, on the one hand, the pure Er^{3+}-doped fiber is not enough to provide sufficient pump absorption, so that its output power and slope efficiency are highly limited. On the other hand, the intrinsic concentration quenching effect of Er^{3+} ions in heavily doped fiber not only reduces the quantum efficiency but also easily causes the self-pulse effect. Another alternative is the Er^{3+}/Yb^{3+}-codoped fiber, which is an ideal solution for improving pump absorption and obtaining high-output power. The Er^{3+}/Yb^{3+}-codoped fiber contains the sensitization Yb^{3+} ion, which has a wide absorption band and has some strong absorption peaks within the range of 800~1080 nm, covering several wavelength regions of pump source [13]. The absorption and emission spectra of Er^{3+}/Yb^{3+}-codoped fiber in the range of 500~1700 nm are shown in Fig. 7.14.

In Er^{3+}/Yb^{3+}-codoped fiber, Yb^{3+} ions are used as the tool to transfer energy by means of cross relaxation process to the Er^{3+} ions. In this way, it makes the population inversion of the Er^{3+} ions increased dramatically. In addition, the Er^{3+} and Yb^{3+} ions should reach a certain doping concentration in order to achieve the efficient laser amplification. Meanwhile, there is an optimal ratio of the doping concentration of the Er^{3+} and Yb^{3+} ions for uniformly surrounding the Er^{3+} ions with Yb^{3+} ions to form Er^{3+}/Yb^{3+} ion pairs and effective energy transferring via the ion pairs.

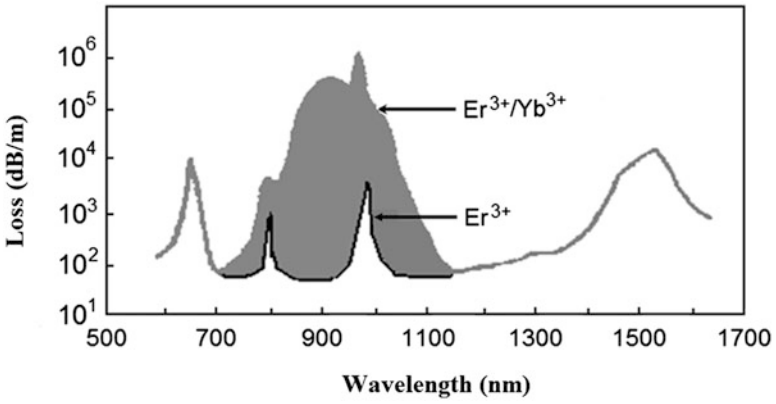

Fig. 7.14 Absorption and emission spectra of Er^{3+}/Yb^{3+}-codoped fiber

7.2.2 *Theoretical Model of Er^{3+}/Yb^{3+}-Codoped Fiber Amplifier*

In general, the rate equations describe the transition between energy levels of active ions, and the power propagation equation describes the evolution of optical field in the gain medium. A theoretical model of Er^{3+}/Yb^{3+}-codoped fiber amplifier can be established based on the above equations. It can be leveraged to analyze different parameters such as active fiber length, signal power, signal wavelength, pump power, pump wavelength, and so on and the specific influences on the characteristics of the laser output.

It is assumed that the Er^{3+} and Yb^{3+} ions are uniformly distributed in the fiber core, and the population densities are N_{Er} and N_{Yb}, respectively. The quantities $N_1(z, t)$, $N_2(z, t)$, $N_3(z, t)$, and $N_4(z, t)$ denote the Er^{3+} population density of the $^4I_{15/2}$, $^4I_{13/2}$, $^4I_{11/2}$, and $^4I_{9/2}$ levels, respectively. The quantities $N_5(z, t)$ and $N_6(z, t)$ are the Yb^{3+} population density of $^2F_{7/2}$ and $^2F_{5/2}$ levels, respectively. Therefore, the rate equations concerning the Er^{3+} and Yb^{3+} population densities can be written as [41, 42]:

$$\frac{\partial N_1}{\partial t} = -W_{12}N_1 - W_{13}N_1 + \frac{N_2}{\tau_{Er}} + W_{21}N_2 + C_{up}{N_2}^2 - C_{14}N_1N_4 + C_{up}{N_3}^2 - C_{cr}N_1N_6 \tag{7.8}$$

$$\frac{\partial N_2}{\partial t} = W_{12}N_1 - W_{21}N_2 - \frac{N_2}{\tau_{Er}} + A_{32}N_3 - 2C_{up}{N_2}^2 + 2C_{14}N_1N_4 \tag{7.9}$$

$$\frac{\partial N_3}{\partial t} = W_{13}N_1 - A_{32}N_3 + A_{43}N_4 - 2C_{up}{N_3}^2 + C_{cr}N_1N_6 \tag{7.10}$$

$$\frac{\partial N_4}{\partial t} = C_{up}N_2^2 - C_{14}N_1N_4 - A_{43}N_4 + C_{up}N_3^2 \tag{7.11}$$

$$\frac{\partial N_6}{\partial t} = W_{56}N_5 - \frac{N_6}{\tau_{Yb}} - W_{65}N_6 - C_{cr}N_1N_6 \tag{7.12}$$

in which W_{12}, W_{13}, W_{21}, W_{56}, and W_{65} are, respectively, the excited absorption transition rate between the $^4I_{15/2}$ and $^4I_{13/2}$ energy level, the excited absorption transition rate between the $^4I_{15/2}$ and $^4I_{11/2}$ level, the stimulated emission transition rate between the $^4I_{13/2}$ and $^4I_{15/2}$ level, the excited absorption transition rate between the $^4F_{7/2}$ and $^4F_{5/2}$ level, and the stimulated emission transition rate between the $^4F_{5/2}$ and $^4F_{7/2}$ level. τ_{Er} and τ_{Yb} are the spontaneous emission lifetime of the $^4I_{13/2}$ and $^2F_{5/2}$ level, respectively. A_{32} is the non-radiative transition rate between the $^4I_{11/2}$ and $^4I_{13/2}$ level. A_{43} is the non-radiative transition rate between the $^4I_{9/2}$ and $^4I_{11/2}$ level. C_{up} is the upconversion coefficient from the $^4I_{13/2}$ to $^4I_{11/2}$ level. C_{14} is the cross relaxation coefficient from the $^4I_{15/2}$ and $^4I_{9/2}$ to $^4I_{13/2}$ level. C_{cr} is the energy transfer coefficient between the $^2F_{5/2}$ and $^4I_{15/2}$ level.

The excited absorption transition rate and the stimulated emission transition rate (W_{ij}) of signal and pump light can be expressed as:

$$W_{12} = \frac{\Gamma_s\sigma_{12}(\lambda_s)\lambda_s}{hcA_{core}}P_s(z,\lambda_s) + \frac{\Gamma_s}{hcA_{core}}\int \sigma_{12}(\lambda)\left[P_{ASE}^{+}(z,\lambda_s) + P_{ASE}^{-}(z,\lambda_s)\right] * \lambda d\lambda \tag{7.13}$$

$$W_{21} = \frac{\Gamma_s\sigma_{21}(\lambda_s)\lambda_s}{hcA_{core}}P_s(z,\lambda_s) + \frac{\Gamma_s}{hcA_{core}}\int \sigma_{21}(\lambda)\left[P_{ASE}^{+}(z,\lambda_s) + P_{ASE}^{-}(z,\lambda_s)\right] * \lambda d\lambda \tag{7.14}$$

$$W_{13} = \frac{\Gamma_p\sigma_{13}(\lambda_p)\lambda_p}{hcA_{core}}P_p(z,\lambda_p) \tag{7.15}$$

$$W_{56} = \frac{\Gamma_p\sigma_{56}(\lambda_p)\lambda_p}{hcA_{core}}P_p(z,\lambda_p) \tag{7.16}$$

$$W_{65} = \frac{\Gamma_p\sigma_{65}(\lambda_p)\lambda_p}{hcA_{core}}P_p(z,\lambda_p) \tag{7.17}$$

in which $\sigma_{56}(\lambda)$ and $\sigma_{65}(\lambda)$ are the absorption and emission cross section of Yb^{3+} ions at the pump wavelength. $\sigma_{13}(\lambda)$ is the absorption cross section of Er^{3+} ions at the pump wavelength. The quantities $\sigma_{12}(\lambda)$ and $\sigma_{21}(\lambda)$ are, respectively, the absorption and emission cross section of Er^{3+} ions at the signal wavelength. h is Planck's constant; c is the light velocity in vacuum; and A_{core} is the effective mode area of the fiber. $P_p(z,\lambda_p)$ is the pump power; $P_s(z,\lambda_s)$ is the input signal power; and $P_{ASE}{}^{\pm}(z,\lambda_k)$ is the ASE power of each channel ($\pm$ corresponds to the forward and backward

propagations, respectively). The ASE spectrum is divided into K channels with central wavelengths of λ_k, $k = 1, \ldots K$ and with an even spacing of $\Delta\lambda$. λ_s and λ_p are the signal and pump wavelength, respectively.

Due to the number of Yb^{3+} ions in the metastable level is relatively small compared with that in the ground level, the 1.0 μm band ASE from the Yb^{3+} ions can be ignored. Γ_p and Γ_s are the spatial overlap factor between the pump/signal light and the fiber core. For double-cladding fiber, Γ_p can be approximately estimated with the ratio of the core area to the inner cladding area, while for Γ_s, it can be calculated by the following formula:

$$\Gamma_s = 1 - \exp\left(-2a^2/\omega_s^2\right) \tag{7.18}$$

where a is the core radius of the double-cladding fiber and ω_s is the module radius of the signal field.

Assuming that the doping concentration of Er^{3+} and Yb^{3+} ions remains unchanged in the fiber core and along the direction of the fiber length, the Er^{3+} and Yb^{3+} population densities (N_{Er}^t and N_{Yb}^t) can, respectively, be given by:

$$N_{\mathrm{Er}}^t = N_1(r,z) + N_2(r,z) + N_3(r,z) + N_4(r,z) \tag{7.19}$$

$$N_{\mathrm{Yb}}^t = N_5(r,z) + N_6(r,z) \tag{7.20}$$

To solve the above equations, the energy distribution of the optical light along the fiber axial is needed. The propagation equations of the pump/signal light and spontaneous emission (ASE) along the fiber can be expressed as:

$$\begin{aligned}\pm\frac{dP_p^{\pm}(z,\lambda_p)}{dz} &= \mp\Gamma_p(\lambda_p)\left[\sigma_{56}(\lambda_p)N_5(r,z) + \sigma_{13}(\lambda_p)N_1(r,z)\right.\\ &\left.-\sigma_{65}(\lambda_p)N_6(r,z)\right]P_p^{\pm}(z) \mp \alpha(\lambda_p)P_p^{\pm}(z,\lambda_p)\end{aligned} \tag{7.21}$$

$$\begin{aligned}\pm\frac{dP_s^{\pm}(z,\lambda_s)}{dz} &= \pm\Gamma_s(\lambda_s)[\sigma_{21}N_2(r,z) - \sigma_{12}N_1(r,z)]P_s^{\pm}(z,\lambda_s)\\ &\mp \alpha(\lambda_s)P_s^{\pm}(z,\lambda_s)\end{aligned} \tag{7.22}$$

$$\begin{aligned}\pm\frac{dP_{ASE}^{\pm}(z,\lambda_k)}{dz} &= \pm\Gamma_s(\lambda_k)[\sigma_{21}N_2(r,z) - \sigma_{21}N_1(r,z)]P_{ASE}^{\pm}(z,\lambda_k)\\ &\mp \alpha(\lambda_k)P_{ASE}^{\pm}(z,\lambda_k)\end{aligned} \tag{7.23}$$

in which $P_p^+(z,\lambda_p)$ and $P_p^-(z,\lambda_p)$ are the power distribution functions of the forward- and backward-propagated pump laser, respectively. $P_s^+(z,\lambda_s)$ and $P_s^-(z,\lambda_s)$ are the signal power distribution functions at the forward and backward directions, respectively. $\alpha(\lambda_p)$ and $\alpha(\lambda_s)$ are the propagation loss of the pump and signal light, respectively.

Since it is difficult to directly measure the upconversion coefficient (C_{up}) and the energy transfer coefficient (C_{cr}), they are generally estimated by comparing the functional relationship between the optical gain and the concentration of the relevant ions. According to the dipole interaction hypothesis, the following equations can be given:

$$C_{up} = \frac{4\pi}{3}\frac{R_0^6}{R_{\mathrm{Er/Er}}^3 \tau_{21}} \tag{7.24}$$

$$C_{cr} = \frac{4\pi}{3}\frac{R_0^6}{R_{\mathrm{Er/Yb}}^3 \tau_{65}} \tag{7.25}$$

where $R_{\mathrm{Er/Yb}}$ is the average distance between the uniformly distributed Er^{3+} and Yb^{3+} ions. $R_{\mathrm{Er/Er}}$ is the average distance between the uniformly distributed Er^{3+} ions. R_0^6 is the critical interaction distance. As the average distance between ions under different concentrations is difficult to measure, empirical values are usually employed to obtain the following formula:

$$C_{up} = 3.5 \times 10^{-24} + \left(N_{\mathrm{Er}} - 4.4 \times 10^{25}\right) \times 2.4107 \times 10^{-49} \tag{7.26}$$

$$C_{\mathrm{cr}} = 1.0 \times 10^{-22} + \left(N_{\mathrm{Yb}} - 1.0 \times 10^{25}\right) \times 4.0000 \times 10^{-49} \tag{7.27}$$

To solve these equations, the initial boundary conditions associated with the above ordinary differential equations are written as:

$$P_p^+(0) = P_p^{in}, P_p^-(L) = 0, P_s^+(0) = P_s^{in}, P_s^-(L) = P_s^{out} \tag{7.28}$$

$$P_p^-(L) = P_p^{in}, P_p^+(0) = 0, P_s^+(0) = P_s^{in}, P_s^-(L) = P_s^{out} \tag{7.29}$$

$$P_p^-(L) = P_p^{in1}, P_p^+(0) = P_p^{in2}, P_s^+(0) = P_s^{in}, P_s^-(L) = P_s^{out} \tag{7.30}$$

where L is the length of the active fiber. P_p^{in} and P_s^{in} are the pump and signal power, respectively. P_p^{in1} and P_p^{in2} are the pump power at the forward and backward directions, respectively.

7.2.3 *Experimental Study of Core-Pumped 1.5 μm Single-Frequency MOPA Laser*

Single-frequency fiber lasers around 1.5 μm regions have attracted extensive research interests for applications in coherent telecommunication, high-resolution sensing, optical frequency-domain reflectometry, and *lidar* [43–46]. However, the linear DFB or DBR cavity configuration using a few centimeters of Er^{3+}-doped silica

fiber limits the output power of single-frequency laser to milliwatt levels. Up to now, several research groups have reported the single-frequency phosphate fiber lasers with the output power approaching 300 mW at 1.5 μm [39, 40]. Nevertheless, a MOPA structure is still needed to further increase the output power.

For single-frequency MOPA laser, a single-mode core pumping method is usually used by early researchers. In the 1990s, a single-frequency laser with an output power of 60 mW and a relative intensity noise (RIN) of less than −110 dB/Hz was firstly demonstrated by Ball et al. based on the core pumping configuration [47]. Afterward, Pan et al. achieved single-frequency laser output with a power of 166 mW and a side-mode suppression ratio of more than 52 dB [48]. The laser power scaling to watt levels based on multimode cladding-pumped large mode area phosphate fiber and phosphate microstructure fiber was demonstrated [49–51]. However, such configurations are quite complex and typically require several amplifier stages with isolators to suppress the ASE or optical reflection. The free-space components used in these configurations would cause considerable ASE noise, low slope efficiency (a typical value of 20~29% with multimode output), and instability of the laser power due to the reflection of residual cladding pump light between discrete components.

Compared with the traditional core-pumped EDFA, the bidirectionally pumped Er^{3+}/Yb^{3+}-codoped phosphate fiber amplifier (Bi-EYPFA) is ultracompact and more flexible, offering a more promising and economical solution to high-power laser output. In 2013, Yang et al. have studied a bidirectionally core-pumped single-frequency MOPA laser at 1535 nm [52]. It mainly comprised a 1535 nm DBR single-frequency seed laser and a one-stage bidirectionally core-pumped EYPF amplifier. A 4-cm-long EYPF was used as the laser gain medium. Both fiber ends of the EYPF were fused with a 2.5-cm-long mini-size 980/1550 nm WDM, respectively. The effective length of the whole Bi-EYPFA assembly is only 12 cm.

Figure 7.15a shows the output power from the Bi-EYPFA as a function of the launched pump power at different input power of the seed laser. An output power of 611 mW was obtained when the input power of seed laser was up to 14.7 dBm and

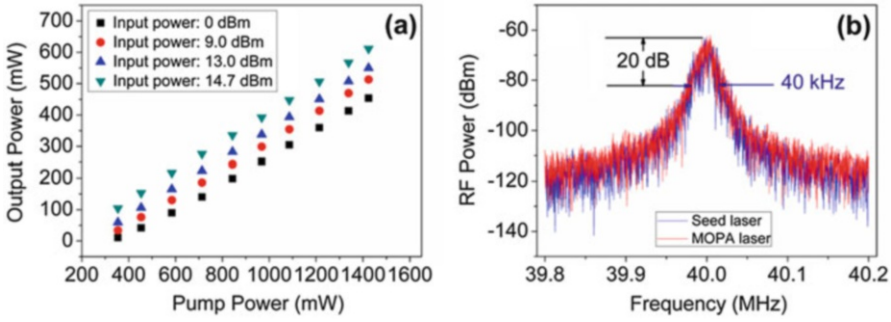

Fig. 7.15 (**a**) Measured MOPA laser output power as a function of the launched pump power at different input powers of the seed laser. (**b**) Linewidth measurements of the seed and MOPA laser. (Reprinted from Ref. [52], copyright 2013, with permission from IOP Publishing)

the total launched maximum pump power was 1420 mW. The optical-to-optical conversion efficiency and the per unit fiber length generated laser power reached 42.9% and 150 mW/cm, respectively.

Figure 7.15b shows the linewidth measurements of the seed and MOPA laser, by using a self-heterodyne method with a 50 km fiber delay. Both of the measured values are about 40 kHz at the intensity dropping 20 dB down from the peak, indicating that the full linewidth at half maximum of the laser is less than 2 kHz. Therefore, the Bi-EYPFA system did not broaden the laser linewidth. Furthermore, the output spectra of the seed and MOPA laser were measured by an optical spectrum analyzer (OSA) with a spectrum resolution bandwidth of 0.1 nm. The signal-to-noise ratio (SNR) of the single-frequency seed laser was more than 70 dB and that of the MOPA laser with an output power of 611 mW was slightly deteriorated to 65 dB due to the ASE noise.

7.2.4 *Experimental Study of Cladding-Pumped 1.5 μm Single-Frequency MOPA Laser*

High-power single-frequency fiber lasers at 1.5 μm are attractive for some potential applications, such as Doppler *lidar*, coherent and spectrum beam combining, atom clock, and atom cooling and trapping [53, 54]. Especially, the fiber laser at 1560 nm can be used to generate frequency-doubled (-harmonic generation) laser source at around 780 nm, which is the transition wavelength of the D_2 line of rubidium (Rb) atom used in the atom clock. In order to obtain high performances and high-frequency conversion efficiencies, watt-level and linearly polarized (LP) laser output is particularly desirable [54, 55]. With the continuous development of multimode semiconductor laser and double-cladding active fiber fabrication technology, most of the reported high-power single-frequency LP lasers use either free-space linear cavity with bulk optical-polarizing components or complex multistage master-oscillator power amplifier (MOPA) Schemes [56–59].

As early as 2003, Alam et al. used a two-stage amplifier to obtain 1549 nm CW single-frequency laser output with a power of 14 W and laser linewidth of less than 30 kHz [60]. After that, a DFB laser diode with the power of 10 mW and laser linewidth of 13 kHz was employed by Alegria et al., who achieved an 83 W single-frequency power at 1552 nm from 3.5 m Er^{3+}/Yb^{3+}-codoped D-shaped LMA fiber with a three-stage amplifier Scheme [49]. However, in a real laser system, the MOPA configuration with less stage of fiber amplifier and simple all-fiber design is more desirable. Meanwhile, to remove the limitation on the power scaling of MOPA laser, it is essential to suppress the stimulated Brillouin scattering (SBS) effect [61, 62], thermal effect, ASE noise, as well as parasitic lasing.

In 2013, Yang et al. have studied an all-fiber 10.9 W single-frequency one-stage linearly polarized MOPA laser at 1560 nm [63]. Figure 7.16 shows the experimental setup of a linearly polarized MOPA laser system. It consists of a homemade 1560 nm

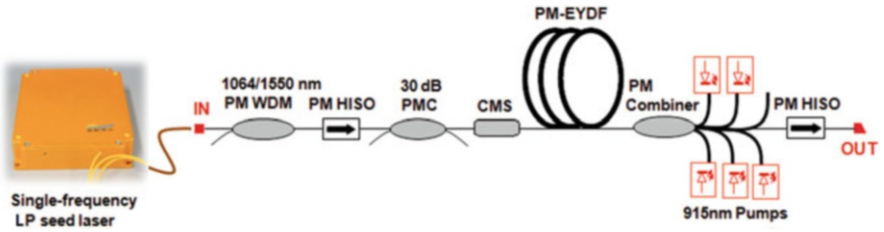

Fig. 7.16 Experimental setup of the linearly polarized MOPA laser. PM HISO-polarization-maintaining high-power isolator. (Reprinted from Ref. [63], copyright 2013, with permission from OSA Publishing)

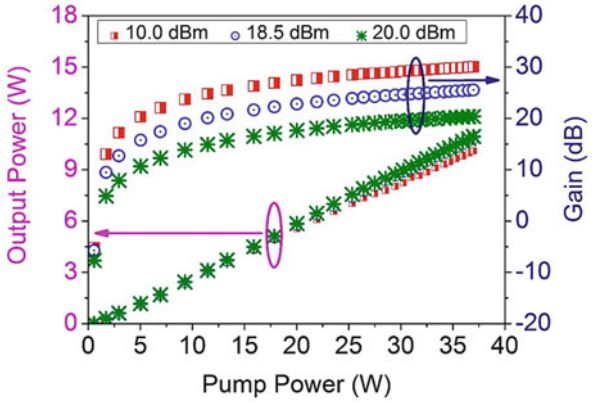

Fig. 7.17 Output power and gain as a function of the launched pump power with different input power. (Reprinted from Ref. [63], copyright 2013, with permission from OSA Publishing)

single-frequency LP seed laser and an all-fiber one-stage power amplifier. The linewidth of the seed laser was narrower than 2.0 kHz, the PER was 26 dB, the signal-to-noise ratio (SNR) was more than 75 dB, and its output power can be adjusted from 0 to 20 dBm. The gain fiber was a 7-m-long PM Er^{3+}/Yb^{3+}-codoped double-cladding fiber (PM-EYDF), and it was pumped by five 915 nm pump diodes through a $(6 + 1) \times 1$ PM fiber combiner. The fiber had a 10 μm diameter core and a 128 μm diameter inner cladding, and the cladding absorption was 2.1 dB/m at 915 nm.

Figure 7.17 shows the laser output power and the gain as a function of the pump power with different input power of the seed laser. When the input power was 10.0 dBm and the pump power was 37 W, the gain could reach the maximum value of 30.0 dB. However, the corresponding laser output power and optical-to-optical conversion efficiency (CE) were only 10.0 W and 27.3%, respectively. When the input power was increased to 20.0 dBm, the gain dropped off dramatically to ~ 20.5 dB. Nevertheless, a highest output power of 10.9 W and a maximum CE of 29.5% were achieved. It should be noted that the maximum output power was limited by the available pump power without any rollover. As mentioned before, the primary limitation on the output power from the LP-MOPA laser is the onset of SBS. The temperature gradient along the PM-EYDF leads to an effective thermal

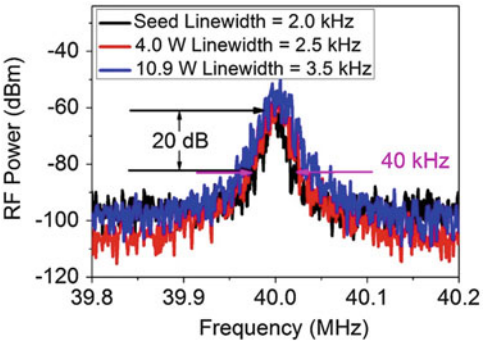

Fig. 7.18 Measured linewidth of the seed laser and LP-MOPA output under different power levels. (Reprinted from Ref. [63], copyright 2013, with permission from OSA Publishing)

Brillouin gain broadening and reduction of the effective Brillouin gain, resulting in a significant suppression of the SBS [61, 62]. With the value of the Brillouin gain coefficient (0.9×10^{-11} m/W), the estimated SBS threshold was increased from 5 to 26 W.

The single-frequency nature of the LP-MOPA laser was verified by a scanning Fabry-Pérot interferometer with a resolution of 7.5 MHz and a free spectral range of 1.5 GHz. Figure 7.18 shows the linewidth measurements of the two lasers, which were obtained with a self-heterodyne method using a 50-km-long fiber delay. The linewidth of the seed laser was approximately 2.0 kHz FWHM (full width at half maximum). However, the linewidth of the fiber laser with an output power of 10.9 W was 3.5 kHz, indicating that the laser linewidth was broadened slightly, owing to the self-phase modulation caused by the laser intensity relaxation oscillation fluctuations [26].

In 2015, Bai et al. reported an all-fiber single-frequency MOPA laser at 1550 nm with wavelength-stabilized 976 nm LDs [64]. A pump-limited maximum continuous-wave output power of 56.4 W with a laser linewidth of 4.21 kHz was achieved under the pump power of 150 W, corresponding to a slope efficiency of 37.0%. High-power single-frequency MOPA lasers in the 1.5 μm spectral region have not scaled as rapidly as Yb^{3+}- or Tm^{3+}-doped fibers. Most reported works of power scaling are limited to below 100 W due to the relatively low gain of the Er^{3+} ions. Besides, the Er^{3+}/Yb^{3+}-codoped fiber amplifiers typically suffer from severe 1.0 μm band ASE or even parasitic lasing and consequently a reduced efficiency for the 1.5 μm laser.

Recently, Creeden et al. demonstrated a single-frequency amplification (540 Hz linewidth) at 1560 nm and achieved 207 W average output power with an Er^{3+}/Yb^{3+}-codoped LMA fiber [65]. The achieved slope efficiency of 50.5% is the highest reported efficiency from a high-power 9 × ×nm pumped Er^{3+}/Yb^{3+}-codoped fiber amplifier. The power amplifier adopted pump diodes with wavelength of 940 nm instead of 976 nm. By pumping off-peak at 940 nm, the population inversion of Yb^{3+} ions versus length was accordingly decreased, and the 1.0 μm ASE/lasing under high pump power level was accordingly suppressed, leading to the improvement of the conversion efficiency in the 1.5 μm region.

The schematic of the high-power single-frequency Er^{3+}/Yb^{3+}-codoped fiber laser was based on a MOPA configuration. A single-frequency DFB fiber laser with a central wavelength of 1560 nm and a linewidth of 540 Hz was used as the seed laser. The signal light was boosted to ~10 W via a preamplifier and then launched into the power amplifier. In the power amplifier, a 5-m-long PM DCF with the core/inner cladding diameter of 25/300 μm was counter-pumped with 940 nm diodes through a conventional (6 + 1) × 1 fiber combiner. Under the pumping of six 65 W 940 nm laser diodes, a record highest efficiency and output power was demonstrated for a high-power single-frequency Er^{3+}/Yb^{3+}-codoped fiber MOPA. Besides, the beam quality (M^2) of the MOPA laser at 200 W power level was measured to be 1.05, indicating a good mode quality of the output beam.

7.3 Amplification of CW Single-Frequency Lasers at 2.0 μm Regions

High-power single-frequency fiber lasers (SFFLs) operating in the eye-safe wavelength regime around 2 μm have numerous applications, including high-resolution spectroscopy, laser surgery, coherent beam combination, and the nonlinear frequency conversion [66–72]. In addition, the nonlinear effect threshold of a 2.0 μm single-frequency fiber laser is higher than that in the 1.0 μm band, leading to advantages in terms of narrow-linewidth and high-power/high-energy output [73, 74].

Most of the current research reported about 2.0 μm single-frequency fiber lasers are mainly using Tm^{3+}-doped silica fiber as the gain medium [39, 75–80]. Stable single longitudinal mode operation can be achieved based on a DBR or DFB short-linear-cavity structure, but the output power is usually only a few milliwatts, and the conversion efficiency is limited [81–84]. In addition, the use of highly Tm^{3+}-doped germanate glass fiber can reduce the length of the gain medium in the traditional linear cavity to centimeter level, and the interval between adjacent longitudinal modes in the cavity can reach several GHz. More importantly, the use of high-gain active fiber can realize 100 mW single-frequency laser output directly from a single cavity [85, 86].

Single-frequency laser based on a single fiber oscillator or resonant cavity has already well met the practical application requirements. However, in some specific applications, such as laser radar, laser surgery, and material processing, higher output power with narrow linewidth and low noise is still required. To further improve the power scaling of 2.0 μm single-frequency lasers, a MOPA scheme is generally adopted [8, 87–90]. Multistage Tm^{3+}-doped fiber amplifier structure can be used to obtain single-frequency laser with hundred watts or even up to thousand kilowatts of output [73, 74].

7.3.1 Theoretical Model of Tm^{3+}-Doped Fiber Amplifier

To describe the physical process of optical amplification in Tm^{3+}-doped fiber amplifier, the theoretical model generally composes of rate equations and power propagation equations [89, 90]. Taking the in-band pumping at 1.6 μm as an example, the laser system can be simply treated as a two-level system, and the corresponding rate equations reflecting the changes in the energy state of Tm^{3+} ions can be given by:

$$\frac{dn_1}{dt} = -(R_{12} + W_{12})n_1 + (W_{21} + A_{21})n_2 \tag{7.31}$$

$$n_1 + n_2 = n \tag{7.32}$$

in which n_1 and n_2 are, respectively, the lower-level and upper-level populations. n is the dopant concentration of Tm^{3+} ions in the optical fiber. W_{12} is the excited absorption transition rate, W_{21} is the stimulated emission transition rate, and R_{12} is the pumping rate of the Tm^{3+} ions from the lower level to the upper level.

The change of optical power in the fiber along the axial direction can be expressed by the following formula:

$$\frac{dP}{dz} = \int_0^{2\pi} \int_0^{\infty} \frac{dI(r,\theta,z)}{dz} r dr d\theta \tag{7.33}$$

in which P is optical power, I is optical intensity, r is the radial coordinate of the fiber core on the transverse section of the fiber, θ is the angular coordinate, and z is the axis coordinate of the fiber. According to the definition of optical power:

$$g = \frac{dI(r,\theta,z)}{I(r,\theta,z)dz} \tag{7.34}$$

$$\frac{dP}{dz} = \int_0^{2\pi} \int_0^{\infty} g \cdot I(r,\theta,z) r dr d\theta \tag{7.35}$$

$$g = \sigma_e n_2(r,\theta,z) - \sigma_a n_1(r,\theta,z) \tag{7.36}$$

where σ_a and σ_e are the absorption and emission cross sections of Tm^{3+} ions. Then:

$$\frac{dP}{dz} = \int_0^{2\pi} \int_0^{b} [\sigma_e n_2(r,\theta,z) - \sigma_a n_1(r,\theta,z)] I(r,\theta,z) r dr d\theta \tag{7.37}$$

Since the Tm^{3+}-doped ions are confined to the fiber core, the radius b is smaller than or equal to the core radius a. That is, when $r > b$, $n_1 = n_2 = 0$. If the rare-earth ions are uniformly distributed in the core, n_1 and n_2 are independent of the coordinate r and θ. Therefore:

$$\begin{aligned}\frac{dP}{dz} &= [\sigma_e n_2(z) - \sigma_a n_1(z)] \int_0^{2\pi} \int_0^b I(r,\theta,z) r dr d\theta \\ &= [\sigma_e n_2(z) - \sigma_a n_1(z)] \cdot P \cdot \frac{1}{P} \int_0^{2\pi} \int_0^b I(r,\theta,z) r dr d\theta \\ &= [\sigma_e n_2(z) - \sigma_a n_1(z)] \cdot P \cdot \frac{\int_0^{2\pi} \int_0^b I(r,\theta,z) r dr d\theta}{\int_0^{2\pi} \int_0^{\infty} I(r,\theta,z) r dr d\theta} \\ &= [\sigma_e n_2(z) - \sigma_a n_1(z)] \cdot P \cdot \Gamma\end{aligned} \tag{7.38}$$

$$\Gamma = \frac{\int_0^{2\pi} \int_0^b I(r,\theta,z) r dr d\theta}{\int_0^{2\pi} \int_0^{\infty} I(r,\theta,z) r dr d\theta} \tag{7.39}$$

where Γ is the overlap factor of the light field and rare-earth ion doping area. Taking into account the transmission loss in the fiber, eventually one can obtain:

$$\frac{dP}{dz} = [\sigma_e n_2(z) - \sigma_a n_1(z)] \cdot P \cdot \Gamma - \alpha \cdot P \tag{7.40}$$

$$W_{12} = \frac{\sigma_{as} P_s}{h\nu_s A_{eff}} \tag{7.41}$$

$$W_{21} = \frac{\sigma_{es} P_s}{h\nu_s A_{eff}} \tag{7.42}$$

$$R_{12} = \frac{\sigma_{ap} P_p}{h\nu_p A_{eff}} \tag{7.43}$$

in which σ_{as} and σ_{ap} are the absorption cross sections at the signal and pump wavelength, respectively. σ_{es} is the emission cross section at the signal light. ν_s and ν_p are, respectively, the frequency of signal and pump light. A_{eff} is the effective mode area of the fiber, and h is the Planck constant.

7.3.2 Experimental Study of 2.0 μm Single-Frequency MOPA Laser

In 2007, Gapontsev et al. demonstrated a single-frequency MOPA laser based on a DFB 1932 nm single-frequency seed laser [80]. The amplification section was a

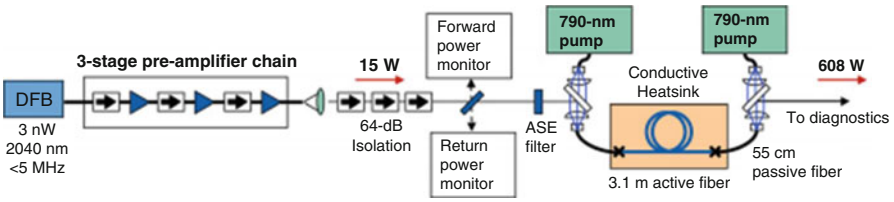

Fig. 7.19 Layout of the four-stage Tm^{3+}-doped fiber amplifier. (Reprinted from Ref. [74], copyright 2009, with permission from OSA Publishing)

two-stage Tm^{3+}-doped fiber amplifier, which was pumped by a 1567 nm fiber laser at each stage. A laser output of 20 W single-frequency was achieved from a 2-m-long Tm^{3+}-doped silica fiber. Further improvement in the power scaling was only limited by the available pump power.

In recent years, a representative research work was presented by Goodno et al. in 2009 [74]. A record maximum power of 608 W at 2.0 μm was achieved with a multi-amplifier MOPA structure. The amplification part used a four-stage Tm^{3+}-doped fiber amplifier in a cascading configuration. A 2040 nm DFB single-frequency semiconductor laser with a power of 3 mW and a linewidth of <5 MHz was used as a seed source, while three all-fiber polarization-maintaining preamplifiers were used to amplify the signal up to 16 W. The power amplifier consisted of a 3.1-m-long non-polarization-maintaining double-clad Tm^{3+}-doped silica fiber with a core diameter/cladding diameter of 25 μm/400 μm. The experimental setup is shown in Fig. 7.19. As shown in the experiment, the high-order mode was filtered by coiling the active fiber to a diameter of about 10 cm, and in this way the beam quality factor of the output laser was measured to be 1.05 ± 0.03.

Regarding all-fiber design, Wang et al. demonstrated an single-frequency Tm^{3+}-doped MOPA laser in 2013 [91]. The laser system adopted the MOPA structure and used a short-cavity 1.97 μm single-frequency fiber laser with a power of 40 mW and a linewidth of 100 kHz as the seed laser, and a three-stage Tm^{3+}-doped fiber amplifier was used for power amplification. With a 220 W pump power, a single-frequency laser with a maximum output power of 102 W was obtained with a slope efficiency of 50%. The estimated SBS threshold of the laser system was 460 W, which was much higher than the experimental value.

In 2014, Liu et al. also presented an all-fiber single-frequency single-polarization Tm^{3+}-doped MOPA laser and realized a linearly polarized 210 W laser output at 2000.9 nm [73]. The MOPA laser was composed of a 3.5 mW DFB single-frequency semiconductor laser and a four-stage Tm^{3+}-doped polarization-maintaining fiber amplifier. The signal power was amplified to 75 W by the three fiber preamplifiers. The active fiber used in the power amplifier stage was a polarization-maintaining double-clad Tm^{3+}-doped silica fiber with a core diameter/cladding diameter of 25 μm/400 μm. The experimental setup is shown in Fig. 7.20. The beam quality factor measured in the experiment was 1.6, and the polarization extinction ratio was higher than 17 dB.

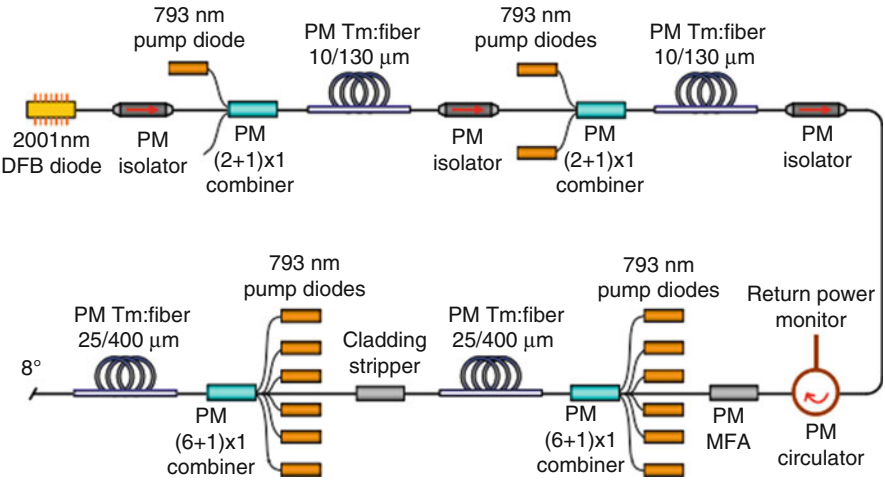

Fig. 7.20 Schematic setup of the high-power single-frequency single-polarization Tm^{3+}-doped all-fiber MOPA. (Reprinted from Ref. [73], copyright 2014, with permission from OSA Publishing)

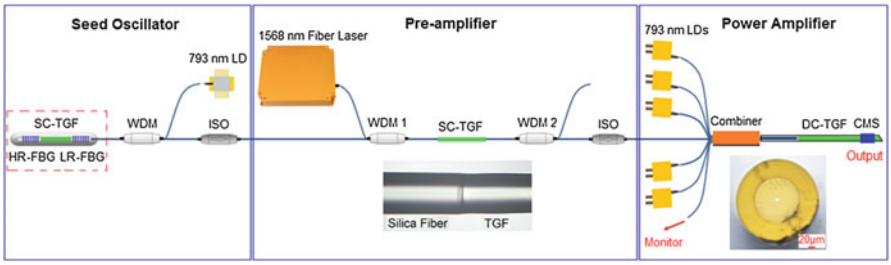

Fig. 7.21 Experimental setup of a short all-TGF single-frequency MOPA laser. Inset (central): photograph of the splice joint between the TGF and the silica fiber. Inset (right): cross section of the DC-TGF. (Reprinted from Ref. [93], copyright 2016, with permission from OSA Publishing)

Compared to the traditional Tm^{3+}-doped silica active fiber in MOPA structure, the high-gain coefficient and short length of Tm^{3+}-doped germanate glass fiber (TGF) can significantly reduce the nonlinear effect during the amplification process [92–94], providing a potential solution for high-power single-frequency MOPA lasers. In 2016, Yang et al. reported a short all-TGF single-frequency MOPA laser. As high as 11.7 W of 1.95 μm low-noise single-frequency laser output was obtained in a homemade 31-cm-long double-cladding single-mode TGF [93]. The experimental setup is shown in Fig. 7.21. The MOPA laser consisted of a homemade 1950 nm DBR short-cavity single-frequency fiber laser (seed laser) and a two-stage Tm^{3+}-doped germanate glass fiber amplifier. The length of the active fiber (31 cm) in the power amplifier stage was optimized through simulation and experiment. The signal and pump light were launched into the DC-TGF through a commercial (6 + 1) × 1 combiner with a 8 μm/0.14 NA core and a 125 μm/0.45 NA cladding.

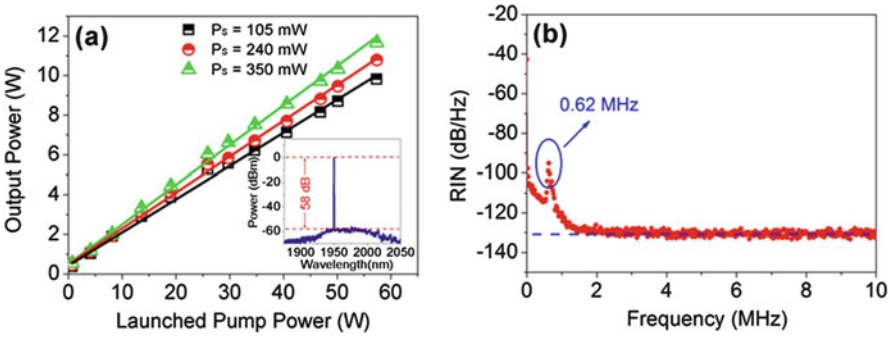

Fig. 7.22 (**a**) Output powers versus pump power of the 31-cm-long DC-TGF at different input power. Inset: output spectrum of the TGF-MOPA laser. (**b**) Measured RIN of the TGF-MOPA laser. (Reprinted from Ref. [93], copyright 2016, with permission from OSA Publishing)

The output powers versus the launched pump powers at different input signal power (105, 240, and 350 mW) are shown in Fig. 7.22a. When the input power was 105 mW and the launched pump power was 57.4 W, the output power of the MOPA laser was only 9.8 W. When the input power was increased to 350 mW, the maximum output power of >11.7 W and corresponding O-O conversion efficiency of about 20.4% were obtained. Based on the theoretical formula of the SBS effect, the SBS threshold of the power amplifier was estimated to be about 980 W, which was much higher than the output power value. Therefore, the output power of the single-frequency fiber laser can be further increased as long as sufficient pump power is provided and the thermal effect in the MOPA laser system is removed. The relative intensity noise (RIN) of the TGF-MOPA laser was measured using an electrical spectrum analyzer with a bandwidth resolution of 1 kHz, as shown in Fig. 7.22b. A measured relative intensity noise of < -130 dB/Hz at frequencies above 2 MHz were achieved in this MOPA system.

References

1. Harber DM, Romalis MV (2000) Measurement of the scalar Stark shift of the $6^1S_0 \rightarrow 6^3P_1$ transition in Hg. Phys Rev A 63:13402–13401
2. Scheid M, Markert F, Walz J, Wang J, Kirchner M, Hänsch TW (2007) 750 mW continuous-wave solid-state deep ultraviolet laser source at the 253.7 nm transition in mercury. Opt Lett 32:955
3. Yamaguchi A, Uetake S, Takahashi Y (2008) A diode laser system for spectroscopy of the ultranarrow transition in ytterbium atoms. Appl Phys B Lasers Opt 91:57
4. Paul J, Kaneda Y, Wang TL, Lytle C, Moloney JV, Jones RJ (2011) Doppler-free spectroscopy of mercury at 253.7 nm using a high-power frequency-quadrupled optically pumped external-cavity semiconductor laser. Opt Lett 36:61
5. Bohler CL, Marton BI (1994) Helium spectroscopy using an InGaAs laser diode. Opt Lett 19:1346

6. Arie A, Pastor PC, Pavone FS, Massimo I (1995) Diode laser sub-Doppler spectroscopy of $^{133}Cs_2$ around the 1083 nm ^{4}He transitions. Opt Commun 117:78
7. Wu T, Peng X, Gong W, Zhan Y, Lin Z, Luo B, Guo H (2013) Observation and optimization of ^{4}He atomic polarization spectroscopy. Opt Lett 38:986
8. Gray S, Liu A, Walton DT, Wang J, Li M, Chen X, Ruffin AB, DeMeritt JA, Zenteno LA (2007) 502 Watt single transverse mode narrow linewidth bidirectionally pumped Yb-doped fiber amplifier. Opt Express 15:17044
9. Zhou P, Ma YX, Wang XL, Ma HT, Xu XJ, Liu ZJ (2009) Coherent beam combination of three two-tone fiber amplifiers using stochastic parallel gradient descent algorithm. Opt Lett 34:2939
10. Advanced LIGO homepage: http://www.ligo.caltech.edu/advLIGO
11. Yang CS, Xu SH, Chen D, Zhang YF, Zhao QL, Li C, Zhou KJ, Feng ZM, Gan JL, Yang ZM (2016) 52 W kHz-linewidth low-noise linearly polarized all-fiber single-frequency MOPA laser. J Opt 18:055801
12. Yang CS (2015) Study on high-performance high-power kHz linewidth single-frequency fiber laser and its application in frequency doubling. Ph. D. thesis of South China University of Technology, Guangzhou
13. Guo YB, Huo JY (2008) Fiber laser and its application. Beijing Science Press, Beijing, p 124
14. Zhu XS, Zhu GW, Shi W, Zong J, Wiersma K, Nguyen D, Norwood RA, Pirson AC, Peyghambarian N (2013) 976 nm single-polarization single-frequency Ytterbium-doped phosphate fiber amplifiers. IEEE Photon Technol Lett 25:1365
15. Yang CS, Xu SH, Yang Q, Lin W, Mo SP, Li C, Feng ZM, Chen DD, Yang ZM, Jiang ZH (2014) High-efficiency watt-level 1014 nm single-frequency laser based on short Yb-doped phosphate fiber amplifiers. Appl Phys Express 7:062702
16. Giles CR, Desurvire E (1991) Modeling erbium-doped fiber amplifier. J Lightwave Technol 9:271
17. Wang Y, Po H (2003) Dynamic characteristics of double-clad fiber amplifiers for high-power pulse amplification. J Lightwave Technol 21:2262
18. Hu JM, Zhang L, Liu HL, Liu KK, Xu Z, Feng Y (2014) High power single-frequency 1014.8 nm Yb-doped fiber amplifier working at room temperature. Appl Opt 53:4972
19. Paschotta R, Nilsson J, Tropper AC, Hanna DC (1997) Ytterbium-doped fiber amplifiers. IEEE J Quantum Electron 33:1049
20. Kontur FJ, Dajani I, Lu Y, Knize RJ (2007) Frequency-doubling of a CW fiber laser using PPKTP, PPMgSLT and PPMgLN. Opt Express 15:12882
21. Kumar SC, Samanta GK, Devi K, Ebrahim-Zadeh M (2011) High-efficiency multicrystal single-pass continuous-wave second harmonic generation. Opt Express 19:11152
22. Samanta GK, Fayaz GR, Ebrahim-Zadeh M (2007) 1.59 W single-frequency continuous-wave optical parametric oscillator based on MgO:sPPLT. Opt Lett 32:2623
23. Zhang L, Cui SZ, Liu C, Zhou J, Feng Y (2013) 170 W single-frequency single-mode linearly-polarized Yb-doped all-fiber amplifier. Opt Express 21:5456
24. Liu C, Qi YF, Ding YQ, Zhou J, Dong JX, Wei YR, Lou QH (2011) All-fiber high power single-frequency linearly polarized ytterbium-doped fiber amplifier. Chin Opt Lett 9:031402–031401
25. Mermelstein MD, Brar K, Andrejco MJ, Yablon AJ, Fishteyn M, Headley C, DiGiovanni DJ (2008) All-fiber 194 W single-frequency single-mode Yb-doped master-oscillator power-amplifier. Proc SPIE 6873:68730L-1
26. Höfer S, Liem A, Limpert J, Zellmer H, Tünnermann A, Unger S, Jetschke S, Müller HR, Freitag I (2001) Single-frequency master-oscillator fiber power amplifier system emitting 20 W of power. Opt Lett 26:1326
27. Knight DJE, Minardi F, Natale PD, Laporta P (1998) Frequency doubling of a fibre-amplified 1083 nm DBR laser. Eur Phys J D 3:211
28. Hong FL, Inaba H, Hosaka K, Yasuda M, Onae A (2009) Doppler-free spectroscopy of molecular iodine using a frequency-stable light source at 578 nm. Opt Express 17:1652

29. Minardi F, Bianchini G, Pastor PC, Giusfredi G, Pavone FS, Inguscio M (1999) Measurement of the Helium $2^3P_0 - 2^3P_1$ fine structure interval. Phys Rev Lett 82:1112
30. Pastor PC, Natale PD, Giusfredi G, Pavone FS, Inguscio M (2001) High precision measurements on helium at 1083 nm. Lect Notes Phys 570:314
31. Carlson CG, Dragic PD, Graf BW, Price RK, Coleman JJ, Awenson GR (2008) High power Yb-doped fiber laser-based LIDAR for space weather. Proc SPIE 6873:68730K-1
32. Carlson CG, Dragic PD, Price RK, Coleman JJ, Awenson GR (2009) A narrow-linewidth Yb fiber-amplifier-based upper atmospheric Doppler temperature lidar. IEEE J Sel Top Quant Electron 15:451
33. Daniels JM, Schearer LD, Leduc M, Nacher PJ (1987) Polarizing ^{3}He nuclei with neodymium La_{1-x} $Nd_xMgAl_{11}O_{19}$ lasers. J Opt Soc Am B 2:1133
34. Prevedelli M, Cancio P, Giusfredi G, Pavone FS, Inguscio M (1996) Frequency control of DBR diode lasers at 1.08 micrometer and precision spectroscopy of helium. Opt Commun 125:231
35. Paschotta R, Hanna DC, Natale PD, Modugno G, Inguscio M, Laporta P (1997) Power amplifier for 1083 nm using ytterbium doped fibre. Opt Commun 136:243
36. Xu JM, Su RT, Xiao H, Zhou P, Hou J (2012) 90.4-W all-fiber single-frequency polarization-maintained 1083-nm MOPA laser employing ring-cavity single-frequency seed oscillator. Chin Opt Lett 10:031402–031401
37. Huang S, Feng Y, Dong J, Shirakawa A, Musha M, Ueda K (2005) 1083 nm single-frequency ytterbium doped fiber laser. Laser Phys Lett 2:498
38. Yang CS, Xu SH, Yang Q, Mo SP, Li C, He X, Feng ZM, Yang ZM, Jiang ZH (2014) High OSNR watt-level single-frequency one stage PM-MOPA fiber laser at 1083 nm. Opt Express 22:1181
39. Spiegelberg C, Geng J, Hu Y, Kaneda Y, Jiang SB, Peyghambarian N (2004) Low-noise narrow-linewidth fiber laser at 1550 nm. J Lightwave Technol 22:57
40. Xu SH, Yang ZM, Liu T, Zhang WN, Feng ZM, Zhang QY, Jiang ZH (2010) An efficient compact 300 mW narrow-linewidth single-frequency fiber laser at 1.5 μm. Opt Express 18:1249
41. Barnard C, Myslinski P, Chrostowski J, Kavehrad M (1994) Analytical model for rare-earth-doped fiber amplifiers and lasers. IEEE J Quantum Electron 30:1817
42. Wang Q, Dutta NK (2003) Er-Yb doped double clad fiber amplifier. Proc SPIE 5246:208
43. Psaltis D (2002) Coherent optical information systems. Science 298:1359
44. Williams JG, Turyshev SG, Boggs DH (2004) Progress in lunar laser ranging tests of relativistic gravity. Phys Rev Lett 93:261101
45. Geng JH, Spiegelberg C, Jiang SB (2005) Narrow linewidth fiber laser for 100-km optical frequency domain reflectometry. IEEE Photon Technol Lett 17:1827
46. Ma YX, Wang XL, Leng JY, Xiao H, Dong XL, Zhu JJ, Du WB, Zhou P, Xu XJ, Si L, Liu ZJ, Zhao YJ (2011) Coherent beam combination of 1.08 kW fiber amplifier array using single-frequency dithering technique. Opt Lett 36:951
47. Ball GA, Holton CE, Hull-Allen G, Morey WW (1994) 60 mW 1.5 μm single-frequency low-noise fiber laser MOPA. IEEE Photon Technol Lett 6:192
48. Pan JJ, Shi Y (1999) 166-mW single-frequency output power interactive fiber lasers with low noise. IEEE Photon Technol Lett 11:36
49. Alegria C, Jeong Y, Codemard C, Sahu JK, Alvarez-Chavez JA, Fu L, Ibsen M, Nilsson J (2004) 83-W single-frequency narrow-linewidth MOPA using large-core erbium-ytterbium co-doped fiber. IEEE Photon Technol Lett 16:1825
50. Li L, Schülzgen A, Temyanko VL, Morrell MM, Sabet S (2006) Ultracompact cladding-pumped 35-mm-short fiber laser with 4.7-W single-mode output power. Appl Phys Lett 88:161106
51. Qiu T, Li L, Schülzgen A, Temyanko VL, Luo T, Jiang S, Mafi A, Moloney JV, Peyghambarian N (2004) Generation of 9.3-W multimode and 4-W single-mode output from 7-cm short fiber lasers. IEEE Photon Technol Lett 16:2592

52. Yang CS, Xu SH, Li C, Mo SP, Feng ZM, Yang ZM, Jiang ZH (2013) Ultra compact kilohertz-linewidth high-power single-frequency laser based on Er^{3+}/Yb^{3+}-codoped phosphate fiber amplifier. Appl Phys Express 6:022703
53. Leng JY, Wang XL, Xiao H, Zhou P, Ma YX, Guo SF, Xu XJ (2012) Suppressing the stimulated Brillouin scattering in high power fiber amplifiers by dual-single-frequency amplification. Laser Phys Lett 9:532
54. Sané SS, Bennetts S, Debs JE, Kuhn CCN, McDonald GD, Altin PA, Close JD, Robins NP (2012) 11 W narrow linewidth laser source at 780 nm for laser cooling and manipulation of rubidium. Opt Express 20:8915
55. Vyatkin MY, Dronov AG, Chernikov MA, Gapontsev DV, Gapontsev VP (2005) High power 780 nm single-frequency linearly-polarized laser. Proc SPIE 5709:125
56. Yusim A, Barsalou J, Gapontsev D, Platonov NS, Shkurikhin O, Gapontsev VP, Barannikov YA, Shcherbina FV (2005) 100 Watt single-mode CW linearly polarized all-fiber format 1.56 μm laser with suppression of parasitic lasing effects. Proc SPIE 5709:69
57. Liem A, Limpert J, Schreiber T, Reich M, Zellmer H, Tünnermann A, Carter A, Tankala K (2004) High power linearly polarized fiber laser. In Lasers Electro-Optics proceedings CMS4 Conference, San-Francisco, CA, USA
58. Sobon G, Kaczmarek P, Antonczak A, Sotor J, Waz A, Dudzik G, Krzempek K, Abramski KM (2012) 3-stage all-in-fiber MOPA source operating at 1550 nm with 20 W output power. Proc SPIE 8237:82372R
59. Khitrov V, Samson B, Manyam U, Tankala K, Machewirth D, Heinemann S, Galvanauskas A (2005) Linearly polarized high power fiber lasers with monolithic PM-LMA-fiber and LMA-grating based cavities and their use for nonlinear wavelength conversion. Proc SPIE 5709:53
60. Alam SU, Wixey R, Hickey L, Yla-Jarkko K, Zervas M (2004) High power single-mode single-frequency DFB fibre laser at 1550 nm in MOPA configuration. In Lasers and Electro-Optics (CLEO) Conference, San Francisco, 1
61. Imai Y, Shimada N (1993) Dependence of stimulated Brillouin scattering on temperature distribution in polarization-maintaining fibers. IEEE Photon Technol Lett 5:1335
62. Hansryd J, Dross F, Westlund M, Andrekson PA, Knudsen SN (2001) Increase of the SBS threshold in a short highly nonlinear fiber by applying a temperature distribution. J Lightwave Technol 19:1691
63. Yang CS, Xu SH, Mo SP, Li C, Feng ZM, Chen DD, Yang ZM, Jiang ZH (2013) 10.9 W kHz-linewidth one-stage all-fiber linearly-polarized MOPA laser at 1560 nm. Opt Express 21:12546
64. Bai XL, Sheng Q, Zhang HW, Zhang SJ, Shi W, Yao JQ (2015) High-power all-fiber single-frequency erbium-ytterbium co-doped fiber master oscillator power amplifier. IEEE Photonics J 7:7103106
65. Creeden D, Pretorius H, Limongelli J, Setzler SD (2016) Single-frequency 1560 nm Er: Yb fiber amplifier with 207 W output power and 50.5% slope efficiency. Proc SPIE 9728:97282L-1
66. Fortin V, Bernier M, Bah ST, Vallée R (2015) 30 W fluoride glass all-fiber laser at 2.94 μm. Opt Lett 40:2882
67. Percival RM, Szebesta D, Seltzer CP, Perin SD, Davey ST, Louka M (1995) A 1.6-μm pumped 1.9-μm thulium-doped fluoride fiber laser and amplifier of very high efficiency. IEEE J Quantum Electron 31:489
68. Clément Q, Melkonian JM, Barrientos-Barria J, Dherbecourt JB, Raybaut M, Godard A (2013) Tunable optical parametric amplification of a single-frequency quantum cascade laser around 8 μm in $ZnGeP_2$. Opt Lett 38:4046
69. Stutzki F, Gaida C, Gebhardt M, Jansen F, Wienke A, Zeitner U, Fuchs F, Jauregui C, Wandt D, Kracht D, Limpert J, Tünnermann A (2014) 152 W average power Tm-doped fiber CPA system. Opt Lett 39:4671
70. Wang X, Zhou P, Zhang HW, Wang XL, Xiao H, Liu ZJ (2014) 100 W-level Tm-doped fiber laser pumped by 1173 nm Raman fiber lasers. Opt Lett 39:4329

71. Hutcheon RJ, Perrett BJ, Mason PD (2004) Modeling of thermal effects within a 2 μm pumped ZGP optical parametric oscillator operating in the mid-infrared. Proc SPIE 5620:264
72. Lippert E, Rustad G, Nicolas S, Arisholm G, Stenersen K (2004) Fibre laser pumped mid-infrared source. Proc SPIE 5620:56
73. Liu J, Shi HX, Liu K, Hou YB, Wang P (2014) 210 W single-frequency, single-polarization, thulium-doped all-fiber MOPA. Opt Express 22:13572
74. Goodno GD, Book LD, Rothenberg JE (2009) Low-phase-noise, single-frequency, single-mode 608 W thulium fiber amplifier. Opt Lett 34:1204
75. Xu SH, Yang ZM, Zhang WN, Wei XM, Qian Q, Chen DD, Zhang QY, Shen SX, Peng MY, Qiu JR (2011) 400 mW ultrashort cavity low-noise single-frequency Yb^{3+}-doped phosphate fiber laser. Opt Lett 36:3708
76. Babin SA, Churkin DV, Kablukov SI, Nikulin MA (2007) Single-frequency linearly polarized DFB fiber laser source. Proc SPIE 6727:672716–672711
77. Agger S, Povlsen JH, Varming P (2004) Single-frequency thulium-doped distributed-feedback fiber laser. Opt Lett 29:1503
78. Geng JH, Wang Q, Luo T, Jiang SB, Amzajerdian F (2009) Single-frequency narrow-linewidth Tm-doped fiber laser using silicate glass fiber. Opt Lett 34:3493
79. Voo NY, Sahu JK, Ibsen M (2005) 345-mW 1836-nm single-frequency DFB fiber laser MOPA. IEEE Photonic Tech L 17:2550
80. Gapontsev D, Platonov N, Meleshkevich M, Mishechkin O, Shkurikhin O, Agger S, Varming P, Povlsen JH (2007) 20 W single-frequency fiber laser operating at 1.93 μm. In Conference on Lasers and Electro-Optics
81. Shen DY, Zhang Z, Boyland AJ, Sahu JK, Clarkson WA, Ibsen M (2007) Thulium-doped distributed-feedback fiber laser with >0.3 W output at 1935 nm. In Bragg Gratings, Photosensitivity, and Poling in Glass Waveguides
82. Zhang Z, Shen DY, Boyland AJ, Sahu JK, Clarkson WA, Ibsen M (2008) High-power tm-doped fiber distributed-feedback laser at 1943 nm. Opt Lett 33:2059
83. Zhang Z, Boyland AJ, Sahu JK, Ibsen M, Clarkson WA (2008) Single-frequency Tm-doped fiber master-oscillator power-amplifier with 10 W linearly polarized output at 1943 nm. In Lasers and Electro-Optics Conference
84. Pearson L, Kim JW, Zhang Z, Ibsen M, Sahu JK, Clarkson WA (2010) High-power linearly-polarized single-frequency thulium-doped fiber master-oscillator power-amplifier. Opt Express 18:1607
85. Geng J, Wu J, Jiang SB, Yu JR (2007) Efficient operation of diode-pumped single-frequency thulium-doped fiber lasers near 2 μm. Opt Lett 32:355
86. Yang Q, Xu SH, Li C, Yang CS, Feng ZM, Xiao Y, Huang X, Yang ZM (2015) A single-frequency linearly polarized fiber laser using a newly developed heavily Tm^{3+}-doped germanate glass fiber at 1.95 μm. Chin Phys Lett 32:094206
87. Wang X, Zhou P, Xiao H, Ma YX, Xu XJ, Liu ZJ (2012) 310 W single-frequency all-fiber laser in master oscillator power amplification configuration. Laser Phys Lett 9:591
88. Yin K, Zhu RZ, Zhang B, Liu GC, Zhou P, Hou J (2016) 300 W-level, wavelength-widely-tunable, all-fiber integrated thulium-doped fiber laser. Opt Express 24:11085
89. Jackson SD, King TA (1999) Theoretical modeling of Tm-doped silica fiber lasers. J Lightwave Technol 17:948
90. Jackson SD, King TA (1999) Dynamics of the output of heavily Tm-doped double-clad silica fiber lasers. J Opt Soc Am B 16:2178
91. Wang X, Zhou P, Wang XL, Xiao H, Si L (2013) 102 W monolithic single-frequency tm-doped fiber MOPA. Opt Express 21:32386
92. Wu JF, Yao ZD, Zong J, Jiang SB (2007) Highly efficient high-power thulium-doped germanate glass fiber laser. Opt Lett 32:638

93. Yang CS, Chen D, Xu SH, Deng HQ, Lin W, Zhao QL, Zhang YF, Zhou KJ, Feng ZM, Qian Q, Yang ZM (2016) Short all tm-doped germanate glass fiber MOPA single-frequency laser at 1.95 μm. Opt Express 24:10956
94. Barnes NP, Walsh BM, Reichle DJ, DeYoung RJ, Jiang SB (2007) Tm: germanate fiber laser: tuning and Q-switching. Appl Phys B Lasers Opt 89:299

Chapter 8
Amplification of Pulsed Single-Frequency Lasers

Regarding the amplification of pulsed single-frequency laser, the seed laser is generally obtained by modulating the output of a CW single-frequency laser with an electro-optic modulator (EOM) or acousto-optic modulator (AOM). As we discussed in Sect. 5.3, besides the disadvantage of compromised power, externally modulating CW laser could flexibly adjust the pulsing parameters such as pulse width and repetition rate. Therefore, the configuration of external modulation combines with MOPA that is beneficial for achieving high average/peak power single-frequency pulsing laser with adjustable parameters. Meanwhile, although it is feasible to realize relatively high average/peak power from a single Q-switched fiber resonator, by exploiting the high gain of heavily RE ion-doped multicomponent fiber, stable pulses are rather difficult to maintain in the high-power regime. Therefore, stable laser pulses from a Q-switched cavity also need to be externally amplified to higher power levels.

Finally, single-frequency pulsed amplifiers also suffer from limitation caused by the SBS effect, especially in case of narrow laser linewidth. When the pulsing duration is relatively short, the interaction time between the laser and the acoustical phonon would also be short, resulting in a high SBS threshold. However, in this case another nonlinear effect in optical fiber – the SRS effect would onset and distorts the pulsed laser performances as well as reduces the amplification efficiency. Additionally, in case of high peak power of the pulse laser, other detrimental nonlinear effects such as SPM and FWM would also take place. Following this section, the recent progress in single-frequency pulsed fiber amplifier at the 1.0 μm, 1.5 μm, and 2.0 μm band will be, respectively, reviewed.

© Springer Nature Singapore Pte Ltd. 2019

Z. Yang et al., *Single-Frequency Fiber Lasers*, Optical and Fiber Communications Reports 8, https://doi.org/10.1007/978-981-13-6080-0_8

8.1 Amplification of Pulsed Single-Frequency Lasers in 1.0 μm Regions

Single-frequency nanosecond pulsed fiber laser has extremely narrow spectral linewidth and can be widely used in nonlinear frequency conversion, laser radar, laser ranging, and coherent beam combining [1–4]. Especially, 1.0 μm single-frequency nanosecond pulse laser can produce green light output through frequency doubling. High-energy single-frequency nanosecond pulse green light can be used as the light source of laser radar, which can provide the long distance and high precision measurement in many occasions, such as measuring the water temperature and water flow speed.

All-fiber pulse laser based on MOPA structure has the advantages of compact design and stable operation. Usually, the generation of pulsed seed laser is realized by means of direct signal modulation or Q modulation of a cavity, and the output power is limited to milliwatt level. At present, the average output power of nanosecond single-frequency pulse laser is achieved at the 100 W level [5, 6]. Further increasing the power is mainly limited by the nonlinear effects (SBS, SRS, self-focusing effect, etc.) owing to the high peak power, thermal effect, and optical damage.

In 2011, Zhu et al. [7] demonstrated an all-fiber MOPA system with a NPRO CW single-frequency laser with kHz-linewidth as the seed source, which was externally modulated (via an AOM) into a pulse train with a repetition rate of 10 kHz. The laser system consisted of a single-frequency pulse seed laser, a three-stage preamplifier, and a power amplifier. Another AOM was inserted between the second and third amplifier stage to further reduce the repetition frequency to 100 Hz. A 1.8-m-long double-cladding Yb^{3+}-doped fiber with a core/inner cladding diameter of 25/250 μm was employed in the power amplifier. A 1064 nm single-frequency pulsed MOPA laser was achieved with a repetition frequency of 100 Hz, pulse width of 500 ns, single pulse energy of 100 μJ, and beam quality $M^2 = 1.1$ (near the diffraction limit). No SBS effect was observed during the power amplification process.

In 2012, Su et al. studied a single-frequency pulsed fiber laser with a modulation pulse width of about 10 ns [8]. The laser system consisted of the single-frequency pulsed seed laser, three preamplifiers, and a power amplifier, as shown in Fig. 8.1. A 1064 nm short-linear-cavity CW single-frequency laser with a linewidth of 20 kHz and a power of 50 mW was used as the seed source. The CW seed laser was externally modulated by an EOM with a pulse width of 8 ns. The power amplifier stage adopted 5-m-long large mode area double-cladding Yb^{3+}-doped fiber with a core/inner cladding diameter of 30/250 μm.

As shown in Fig. 8.2, a single-frequency pulsed laser output with an average power of 139.3 W and peak power of 1.07 kW was achieved under the repetition frequency of 10 MHz, while under the repetition frequency of 20 MHz, these values changed to 153.1 W and 668 W. The linewidth of the finally amplified laser was estimated to 50 ~ 70 MHz.

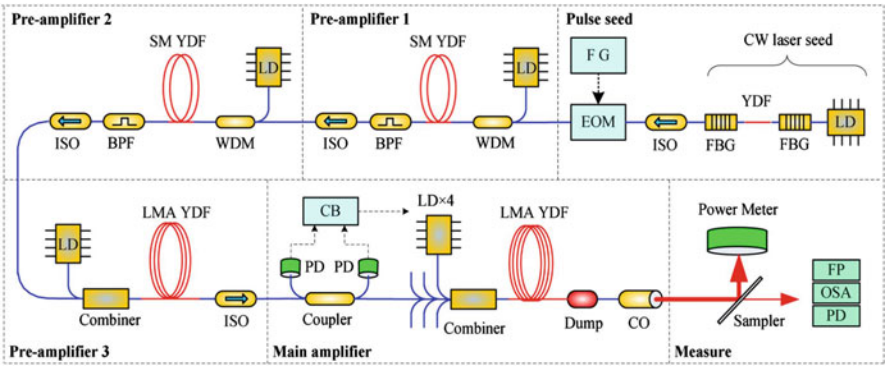

Fig. 8.1 Schematic of the single-frequency, all-fiber pulsed MOPA system: *CW laser* continuous wave laser, *FBG* fiber Bragg grating, *LD* laser diode, *FG* function generator, *EOM* electro-optic modulator, *WDM* wavelength division multiplexing, *ISO* isolator, *BPF* bandpass filter, *SM YDF* single-mode Yb^{3+}-doped fiber, *LMA YDF* large mode area Yb^{3+}-doped fiber, *PD* photodetector, *CB* circuit board, *CO* collimator, *FP* Fabry-Perot interferometer, *OSA* optical spectrum analyzer. (Reprinted from Ref. [8], copyright 2012, with permission from OSA Publishing)

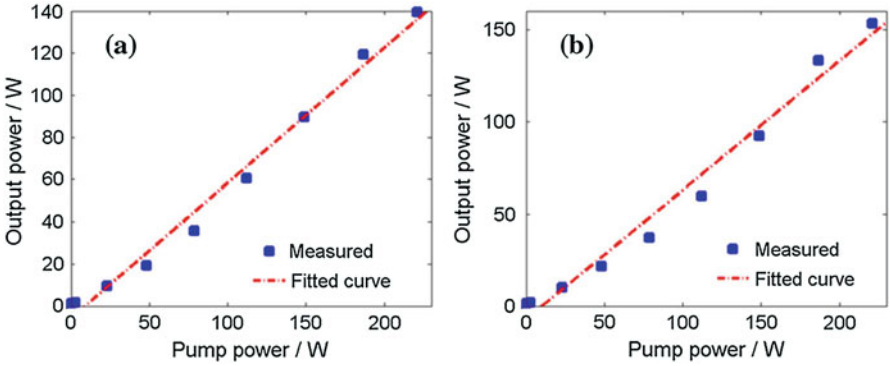

Fig. 8.2 Output power of the main amplifier as a function of the absorbed pump power with repetition rate of (**a**) 10 MHz and (**b**) 20 MHz. (Reprinted from Ref. [8], copyright 2012, with permission from OSA Publishing)

In 2013, Wang et al. have utilized a 1064 nm linearly polarized single-frequency laser with a linewidth of 200 kHz and a power of 45 mW as the seed laser for MOPA system [9]. The CW seed laser was externally modulated by an EOM with the pulse width of 6 ns and repetition frequency of 10 MHz. The laser system was composed of a single-frequency pulsed seed laser, a two-stage preamplifier, and a power amplifier. The experimental setup of the all-fiber MOPA structure is shown in Fig. 8.3.

In the power amplifier stage, a 3-m-long large mode area dual-cladding Yb^{3+}-doped fiber with a core/inner cladding diameter of 30/250 μm was adopted. An average power of 280 W and a peak power of 4.6 kW were obtained. The large mode

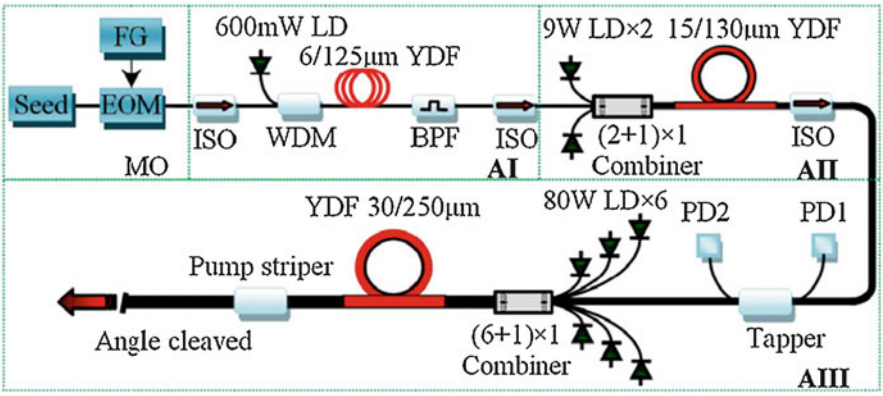

Fig. 8.3 Experimental setup of the single-frequency all-fiber pulsed MOPA. *EOM* electro-optic modulator, *FG* function generator, *ISO* isolator, *LD* laser diode, *WDM* wavelength division multiplexing, *YDF* Yb^{3+}-doped fiber, *BPF* band pass filters, *PD1, PD2* photodetectors, *AI, AII, AIII* amplifiers in different stages. (Reprinted from Ref. [9], copyright 2013, with permission from IOP Publishing)

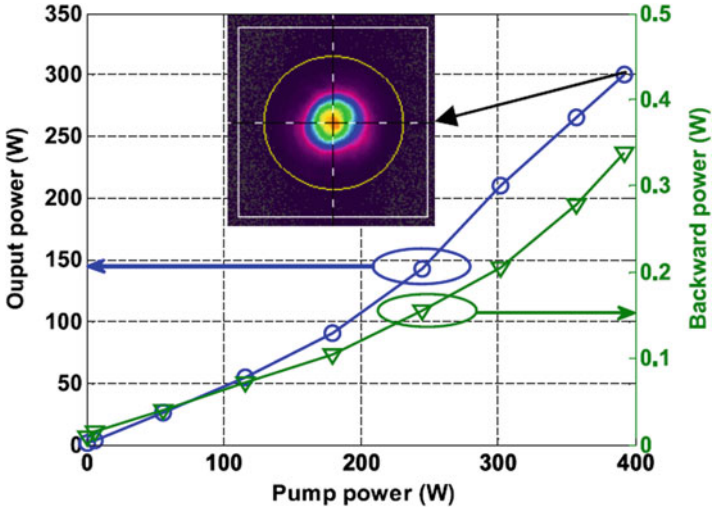

Fig. 8.4 Output power and backward power versus pump power. Inset: two-dimensional beam profile measurement of the laser. (Reprinted from Ref. [9], copyright 2013, with permission from IOP Publishing)

area Yb^{3+}-doped fiber was coiled with a diameter of less than 10 cm. A pump striper was used to filter out the high-order-mode light and the residual pump in inner cladding. The power amplifier was working in the single transverse mode regime, and a final single-frequency pulsed laser output was achieved with the M^2 of 1.3, as shown in the inset of Fig. 8.4.

8.2 Amplification of Pulsed Single-Frequency Lasers in 1.5 μm Regions

With the development of laser technology and coherent detection technology, narrow linewidth and high-power/energy single-frequency lasers have become a hot research topic. It has wide applications in, for example, laser radar, laser hydrophone, and optical fiber gyroscope. Laser sources at the 1.5 μm region are relatively safe for human eyes, rendering it more suitable for practical application requirements.

In 2011, Liu et al. [10] studied an all-fiber 1533 nm single-frequency pulsed fiber laser with a MOPA configuration. A short-cavity CW single-frequency Er^{3+}-doped phosphate fiber laser with a linewidth of 5 kHz and a power of 40 mW was used as the seed source. An AOM was employed to produce the pulse laser with a pulse width of 500 ns and repetition frequency of 10 kHz. Then the seed pulse was injected into a three-stage amplifier structure for power amplification. The experiment setup is shown in Fig. 8.5.

A 6-m-long large mode field erbium ytterbium co-doped double-clad fiber with a core/inner cladding diameter of 25/300 μm was employed in the power amplifier stage. Under the pump power of 8.4 W, a single-frequency laser pulse output with an average power of 1.16 W and single pulse energy of 116 uJ were obtained, as shown in Fig. 8.6.

In addition, the linewidth of the output pulsed laser from the power amplifier stage was measured by the self-heterodyne method with 30 km optical fiber delay, and the result of beat frequency signal is shown in Fig. 8.7. It can be seen from the figure that the linewidth of the amplified pulsed laser was slightly broadened from 800 kHz (pulsed seed laser) to 1.1 MHz.

As mentioned earlier, SBS effect is one of the main limiting factors for power scaling of pulsed single-frequency MOPA laser. The general solution is to use the large mode area double-cladding silica fiber for power amplification. Another

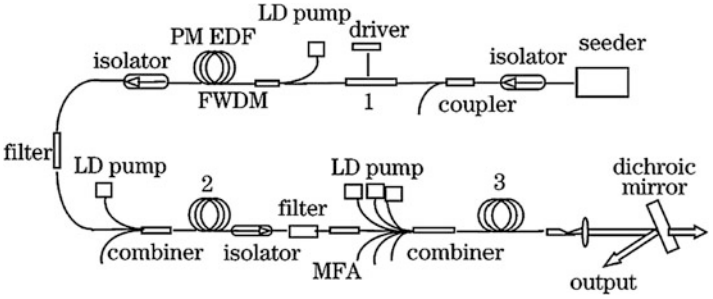

Fig. 8.5 Experimental setup of the MOPA fiber laser system. *LD* laser diode, *MFA* mode field adaptor; 1, acousto-optic modulator (AOM); 2, PM double-clad EYDF; 3, LMA PM double-clad EYDF. (Reprinted from Ref. [10], copyright 2011, with permission from OSA Publishing)

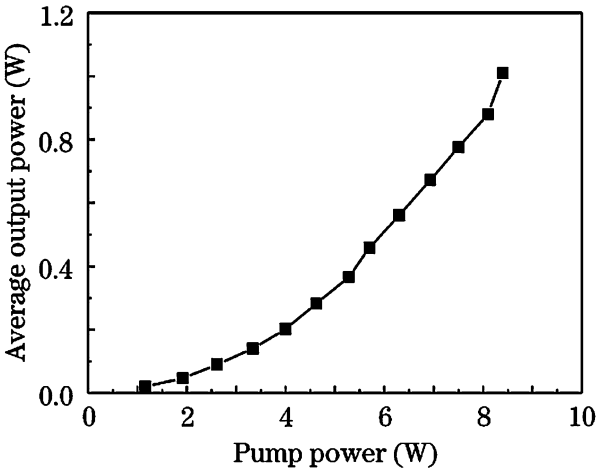

Fig. 8.6 Average output power of the power amplifier stage at 1533 nm versus the pumping power at 976 nm. (Reprinted from Ref. [10], copyright 2011, with permission from OSA Publishing)

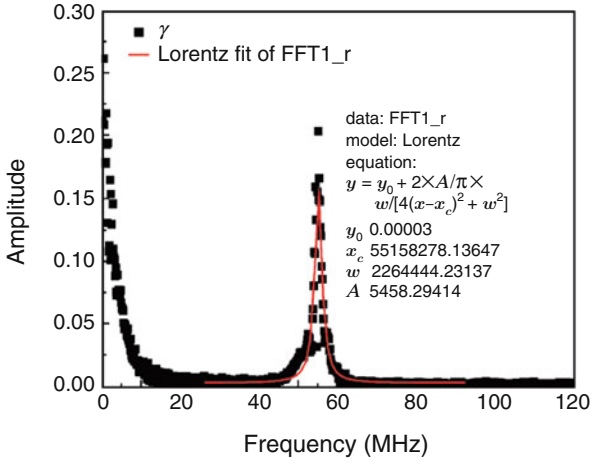

Fig. 8.7 Linewidth measurement of the third-stage amplifier. (Reprinted from Ref. [10], copyright 2011, with permission from OSA Publishing)

alternative is the high-gain multicomponent glass fibers (phosphate, germanate, tellurite glass, etc.) that can greatly shorten the length of fiber amplifier (i.e., increase the SBS threshold) while guaranteeing enough optical gain.

In 2009, Shi et al. [11] demonstrated a 1538 nm Q-switched DBR single-frequency fiber laser through employing a PZT to generate pressure-induced birefringence in the short cavity. A pulse width of 160 ns and a repetition frequency of 20 kHz were achieved from this laser cavity. A MOPA structure that includes two polarization-maintaining preamplifiers and a polarization-maintaining power amplifier was used to boost the laser pulse. Especially, a 12-cm-long erbium ytterbium co-doped phosphate polarization-maintaining fiber with a core/inner cladding diameter of 15/125 μm was employed in the power amplifier stage. The experimental setup is shown in Fig. 8.8. The calculated SBS threshold was 2.8 ~ 5.6 kW.

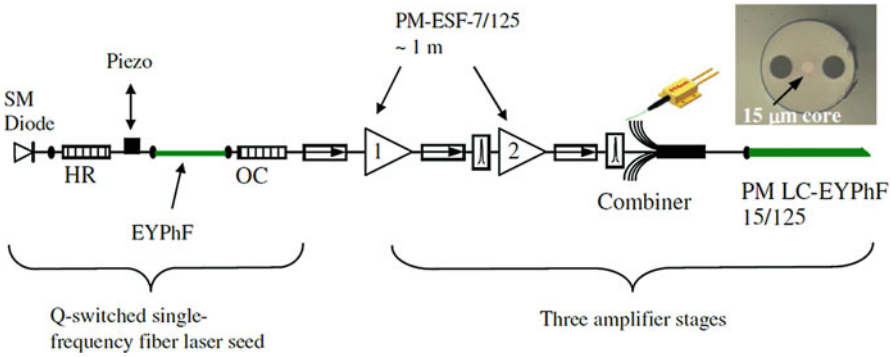

Fig. 8.8 Schematic of the SM single-frequency Q-switched fiber laser with a MOPA system. (Reprinted from Ref. [11], copyright 2009, with permission from OSA Publishing)

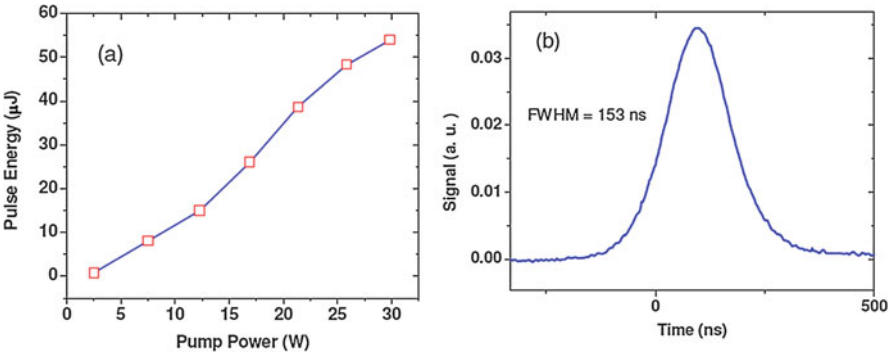

Fig. 8.9 (**a**) Pulse energy versus pump power of the MOPA system. (**b**) Typical pulse shape of the amplified pulse with energy of 54 μJ. (Reprinted from Ref. [11], copyright 2009, with permission from OSA Publishing)

Finally, a polarization-maintaining single-frequency pulsed laser output with pulse width of 153 ns, repetition frequency of 20 kHz, single pulse energy of 54 μJ, and peak power of 332 W was realized. The experiment results are shown in Fig. 8.9.

In 2012, Petersen et al. [12] developed a monolithic high-power pulsed fiber laser with a MOPA configuration, which can reach 0.38 mJ pulse energy and 128 kW peak power for a 3 ns pulse at 1550 nm while maintaining transform-limited linewidth. The pulse seed laser with a repetition frequency of 10 kHz and a pulse width of 12 ns was achieved by directly modulating a CW single-frequency fiber laser using an EOM. An arbitrary waveform generator (AWG) was used to preshape the laser pulses before amplification to avoid pulse steepening and dynamic gain saturation. Single-mode, polarization-maintaining highly Er^{3+}/Yb^{3+} co-doped large core phosphate fiber was used in the power amplifier to scale the transform-limited laser pulses, while avoiding any unwanted nonlinearity. The experimental setup is shown in Fig. 8.10.

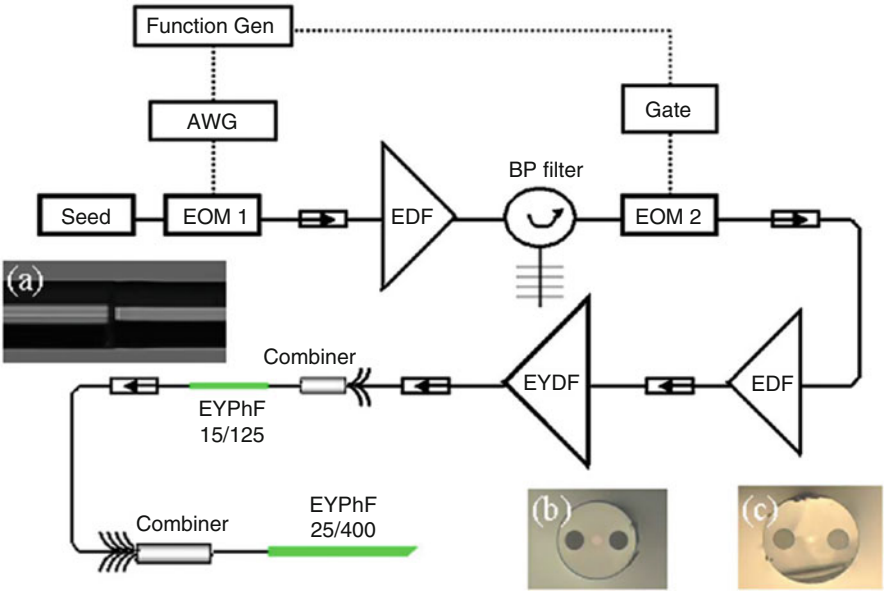

Fig. 8.10 Monolithic MOPA-based high-power pulsed fiber laser system. *AWG* arbitrary waveform generator, *EDF* Er^{3+}-doped fiber amplifiers, *EYDF* Er^{3+}/Yb^{3+} co-doped double-cladding fiber amplifier, *BP filter* band-pass filter, *EOM* electro-optic modulator. Insets: (**a**) silica to EYPhF 25/400 fusion splice; (**b**) and (**c**)15 μm and 25 μm cleaved fiber faces, respectively. (Reprinted from Ref. [12], copyright 2012, with permission from OSA Publishing)

Figure 8.11 shows the measured output pulse energy after the second power amplifier stage versus the pump power at 10 kHz repetition rate. One can see that the highest pulse energy can reach 0.384 mJ, corresponding to an average power of 3.84 W. The calculated highest peak power was ~128 kW based on the measured pulse energy. The inset of Fig. 8.11 shows the spectrum of the fiber laser with ~0.3 mJ pulse energy measured by an OSA with 2 nm resolution. The signal was ~22 dB above any ASE. It is worth noting that the two-stage fiber amplifier used highly 12-cm-long Er^{3+}/Yb^{3+} co-doped polarization-maintaining phosphate fiber, whose core/inner cladding diameter were 15/125 μm and 25/400 μm for the first and second stage.

Although large mode area fiber (LMAF) is an effective solution for solving the problem induced by nonlinear effects (stimulated Brillouin scattering, stimulated Raman scattering, self-phase modulation, etc.), it allows high-order transversal-mode transmission and reduces the output beam quality. So the key problem is to try to allow only fundamental mode oscillations in LMAFs. Therefore, the nonlinear effects can be removed by designing the new structure fiber, such as increasing the mode field effective area of the short-rod-type fiber, chirally coupled fibers, leakage channel fibers, and helically coiled cores [13–16]. Another method of increasing the mode field effective area is based on the mode conversion mechanism, for example, using the combining of a long-period fiber grating and a high-order-mode fiber (HOF)

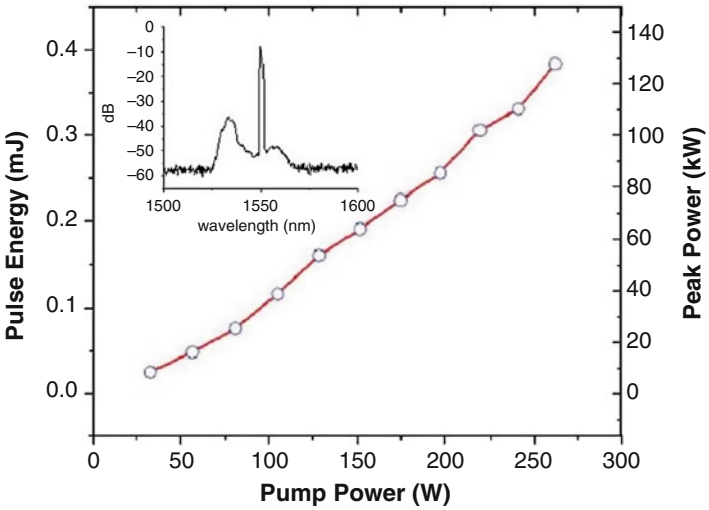

Fig. 8.11 Pulse energy and peak power versus pump power of the final EYPF amplifier. Inset: the spectrum at the highest pulse energy. (Reprinted from Ref. [12], copyright 2012, with permission from OSA Publishing)

to implement the conversion between high order and low order modes. It makes the light field mainly exists in the high order mode, demonstrating the large mode field area [17].

In 2013, Nicholson et al. [18] studied pulse amplification in a high-order-mode (HOM) amplifier for the first time. An external cavity 1560 nm semiconductor laser with a linewidth of 400 kHz was modulated into a pulsed laser. The pulsed signal and a high-power 1480 nm Raman fiber laser (pump source) were coupled into the amplifier through a 1480/1550 nm WDM. Two long-period fiber gratings (LPGs) together with a 4.5-m-long high-order-mode fiber were employed to complete the mode conversion.

The HOF has an effective area mode field of 6000 μm^2 to amplify the laser pulse. A peak power of 820 W and single pulse energy of 82 μJ were obtained from this laser system. Meanwhile, the output spectrum of the single-frequency pulsed laser was also tested. The experimental results show that the high-order-mode fiber (HOF) can effectively amplify the 1.5 μm single-frequency laser pulse.

In order to evaluate the SBS effect in the high-order-mode (HOM) amplifier, the SBS threshold can be calculated based on the formula: $P_{\text{th}} = 21 * A_{\text{eff}}/(g_B L) * (1 + \Delta\nu_S/\Delta\nu_B)$, in which g_B is the SBS gain factor ($g_B = 4 \times 10^{-11}$m/W) and $\Delta\nu_B$ is the Brillouin gain bandwidth ($\Delta\nu_B = 20$MHz). For the effective area mode field of 6000 μm^2, the SBS threshold of the 4.5-m-long HOF amplifier was calculated to be 700 W. When the laser linewidth of the seed source was extended to 1.8 GHz, the SBS threshold was accordingly increased to 64 kW. Although the SBS effect was no longer a limiting factor, along with the further increase of the peak power and pulse energy, other restrictive factors (energy saturation, phase modulation, optical damage, etc.) will occur.

8.3 Amplification of Pulsed Single-Frequency Lasers in 2.0 μm Regions

Pulsed single-frequency fiber lasers in the human eye safety wavelength band (2.0 μm) have many practical applications, such as laser radar, laser medical treatment, pollution control, and infrared supercontinuum generation, all of which need a high-power output. In 2011, Geng et al. [19] used the MOPA technology to study an all-fiber 1950 nm single-frequency pulsed fiber laser. The experimental structure is shown in Fig. 8.12. A single-mode Tm^{3+}-doped fiber amplifier was employed to amplify the single-frequency pulsed signal. A 1.55 μm Er^{3+}-doped fiber laser was used as the pump source. A 20-cm-long highly Tm^{3+}-doped single-mode non-polarized-maintaining silica fiber (core diameter of 7.8 μm and NA of 0.153) was used as a gain medium.

A peak power of up to kilowatt level with a repetition frequency of 10 kHz and 50 kHz was obtained. When the repetition frequency was 50 kHz, the average power of about 240 mW was generated with a pulse width of 7 ns. The corresponding experimental results are shown in Fig. 8.13. The SBS effect was effectively suppressed thanks to the short-length active fiber in the amplifier stage and the short pulse width.

In 2012, Fang et al. [20] studied a high-power and high-energy all-fiber single-frequency nanosecond pulsed laser based on the MOPA technology. The experimental setup is shown in Fig. 8.14. Through an arbitrary waveform generator (AWG)-driven fast EOM, a 1918.4 nm CW linearly polarized single-frequency fiber laser was externally modulated into a pulse train with arbitrarily controlled repetition frequency and pulse width. In addition, a single-mode large-core-diameter (30 μm) Tm^{3+}-doped germanate glass fiber (LC-TGF) was used as the gain medium.

A near-transform-limited single-frequency pulsed output with a pulse width of about 2 ns and an average power of 16.01 W at a repetition rate of 500 kHz was achieved. The maximum peak power of 78.1 kW was obtained at the repetition

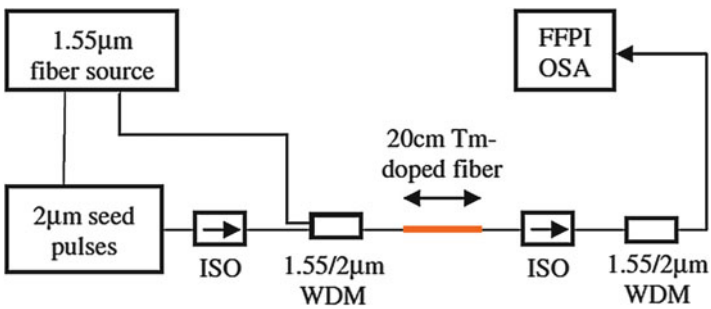

Fig. 8.12 Schematic of a single-frequency pulsed Tm^{3+}-doped fiber MOPA system: *ISO* isolator, *WDM* wavelength division multiplexing, *FFPI* fiber Fabry-Perot interferometer, *OSA* optical spectrum analyzer. (Reprinted from Ref. [19], copyright 2011, with permission from OSA Publishing)

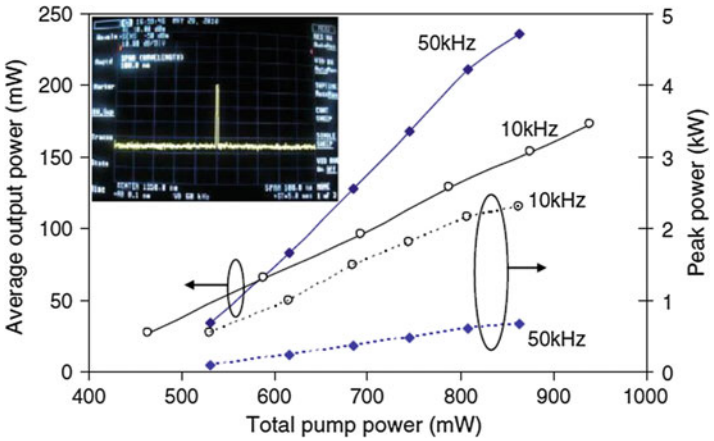

Fig. 8.13 Average output power (solid curve) and its corresponding peak power (dotted curve) of the amplified laser pulses as a function of pump power. Inset, optical spectrum of the amplified pulses. (Reprinted from Ref. [19], copyright 2011, with permission from OSA Publishing)

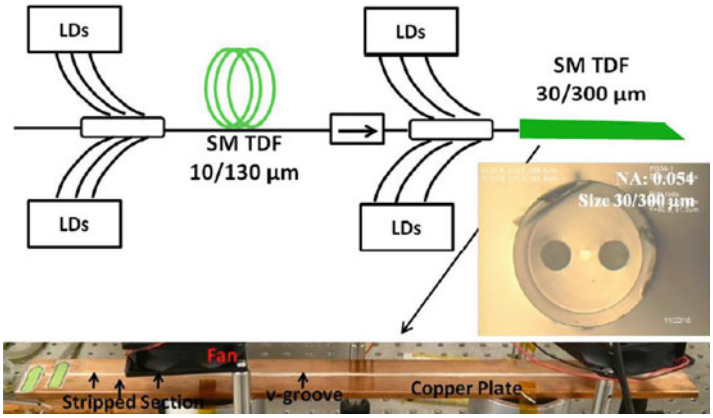

Fig. 8.14 Diagram of the two-stage power amplifier. The inset is the cross section of the gain fiber placed in a v-groove in a copper plate. *SM* single mode, *TDF* thulium-doped fiber, *LDs* laser diodes. (Reprinted from Ref. [20], copyright 2012, with permission from OSA Publishing)

frequency of 100 kHz. Moreover, when the repetition frequency was 1 kHz and the pulse width was about 15 ns, an output pulse energy of near mJ was obtained. The experimental results are shown in Fig. 8.15.

In 2015, Wang et al. [21] studied a 2 μm single-frequency pulsed fiber laser based on a MOPA configuration. The experimental setup is shown in Fig. 8.16. A short-cavity single-frequency fiber laser with a central wavelength of 1971 nm, a linewidth of less than 100 kHz, and a power of 40 mW was used as the seed source. Firstly, the linewidth of the seed source was broadened to suppress the SBS effect via an electro-optic phase modulator (PM). Then an acousto-optic modulator (AOM) was used to

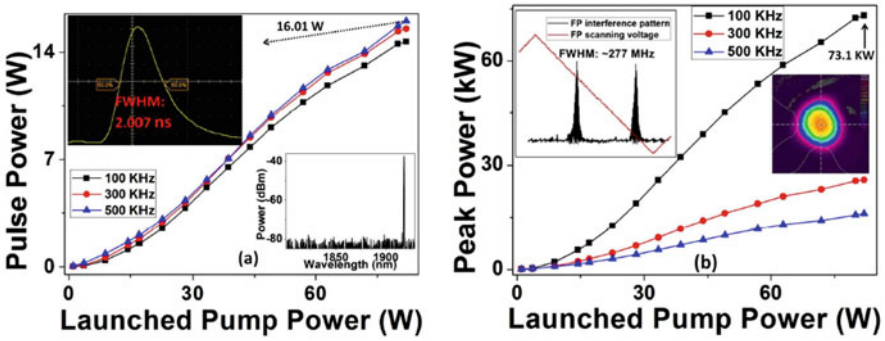

Fig. 8.15 (**a**) Average power of the amplified pulse under different pump level. Inset: pulse shape and spectrum when the pump power was ~16.01 W. (**b**) Peak power of the amplified pulse under different pump level. Inset: Fabry-Perot scanning spectrum and the beam profile of the amplified pulse with 2 ns pulse width (over 10 W average power). (Reprinted from Ref. [20], copyright 2012, with permission from OSA Publishing)

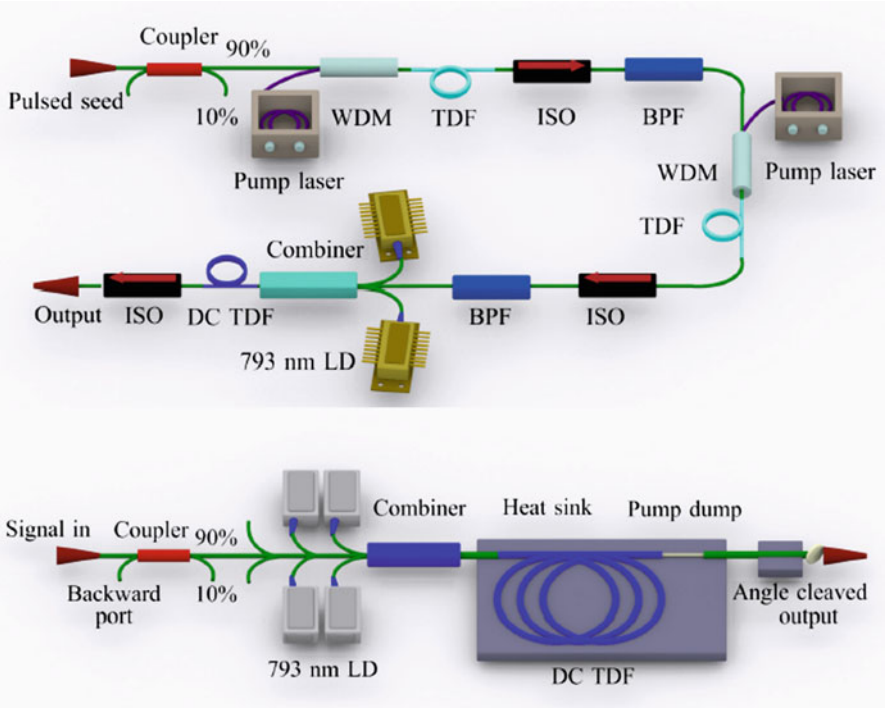

Fig. 8.16 Schematic sketch of the preamplifier and the main amplifier. (Reprinted from Ref. [21], copyright 2015, with permission from OSA Publishing)

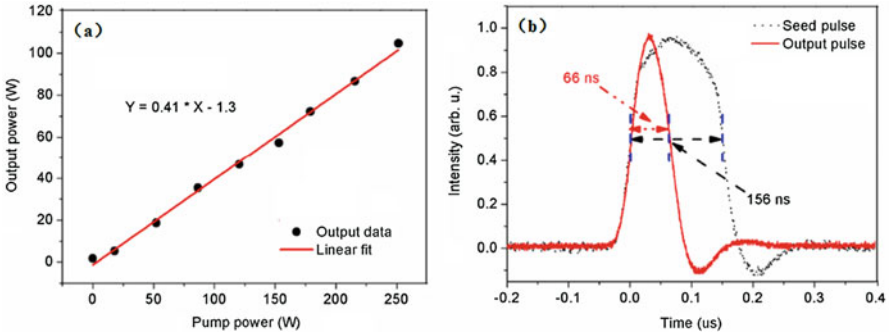

Fig. 8.17 (**a**) Output power of the ultra-narrowband pulsed MOPA. (**b**) Pulse shapes of the ultra-narrowband pulsed MOPA. (Reprinted from Ref. [21], copyright 2015, with permission from OSA Publishing)

modulate the laser intensity into a pulse train. Finally, a single-frequency pulsed signal output with a repetition frequency of 1 MHz and a pulse width of 156 ns were produced. In the power amplifier stage, a 2.9-m-long Tm^{3+}-doped double-cladding fiber with a core diameter of 25 μm was used as the gain medium.

The pulsed seed laser was amplified by a monolithic Tm^{3+}-doped fiber MOPA. The average output power reached 105 W with a slope efficiency of 41%. The output pulse train has a repetition rate of 1 MHz and a pulse width of 66 ns. The experimental results are shown in Fig. 8.17. The output power was limited by the onset of SBS effect. Higher output power can be achieved by further broadening the linewidth or narrowing the pulse width to several nanoseconds.

References

1. Jiang PP, Yang DZ, Wang YX, Chen T, Wu B, Shen YH (2009) All-fiberized MOPA structured single-mode pulse Yb-fiber laser with a linearly polarized output power of 30 W. Laser Phys Lett 6:384
2. Su RT, Zhou P, Xiao H, Wang XL, Xu XJ (2011) MOPA structured single-frequency nanosecond pulsed laser in all fiber format. Chin J Lasers 38:1102013
3. Zhang YF, Feng ZM, Xu SH, Mo SP, Yang CS, Li C, Gan JL, Chen DD, Yang ZM (2015) Compact frequency-modulation Q-switched single-frequency fiber laser at 1083 nm. J Opt 17:125705
4. Su RT, Zhou P, Xiao H, Wang XL, Xu XJ (2012) 96.2 W all-fiberized nanosecond single-frequency fiber MOPA. Laser Phys 22:248
5. Su RT, Zhou P, Wang XL, Ma YX, Xu XJ (2012) Active coherent beam combination of two high-power single-frequency nanosecond fiber amplifiers. Opt Lett 37:497
6. Stutzki F, Jansen F, Liem A, Jauregui C, Limpert J, Tünnermann A (2012) 26 mJ 130 W Q-switched fiber-laser system with near-diffraction-limited beam quality. Opt Lett 37:1073
7. Zhu R, Zhou J, Liu J, Chen WB (2011) High energy, narrow-linewidth, ytterbium-doped pulsed fiber amplifier. SPIE 8192:81922S
8. Su R, Zhou P, Xiao H, Wang XL, Xu XJ (2012) 150 W high-average-power, single-frequency nanosecond fiber laser in strictly all-fiber format. Appl Opt 51:3655

9. Wang XL, Zhou P, Su RT, Xiao H, Xu XJ, Liu ZJ (2013) A 280 W high average power, single-frequency all-fiber nanosecond pulsed laser. Laser Phys 23:015101
10. Liu Y, Liu J, Chen W (2011) Eye-safe, single-frequency pulsed all-fiber laser for Doppler wind lidar. Chin Opt Lett 9:090604
11. Shi W, Petersen EB, Leigh M, Zong J, Yao ZD, Chavez-Pirson A, Peyghambarian N (2009) High SBS-threshold single-mode single-frequency monolithic pulsed fiber laser in the C-band. Opt Express 17:8237
12. Petersen E, Shi W, Chavez-Pirson A, Peyghambarian N (2012) High peak-power single-frequency pulses using multiple stage, large core phosphate fibers and preshaped pulses. Appl Opt 51:531
13. Limpert J, Deguil-Robin N, Manek-Hönninger I, Salin F, Röser F, Liem A, Schreiber T, Nolte S, Zellmer H, Tünnermann A, Broeng J, Petersson A, Jakobsen C (2005) High-power rod-type photonic crystal fiber laser. Opt Express 13:1055
14. Liu CH, Chang G, Litchinitser N, Guertin D, Jacobsen N, Tankala K, Galvanauskas A (2007) Chirally coupled core fibers at 1550-nm and 1064-nm for effectively single-mode core size scaling. CLEO, CtuBB3
15. Wong WS, Peng X, Mclaughlin JM, Dong L (2005) Breaking the limit of maximum effective area for robust single-mode propagation in optical fibers. Opt Lett 30:2855
16. Jiang Z, Marciante JR (2005) Mode-area scaling of helical-core dual-clad fiber lasers and amplifiers. CLEO 3:1849
17. Ramachandran S, Nicholson JW, Ghalmi S, Yan MF, Wisk P, Monberg E, Dimarcello FV (2006) Light propagation with ultra-large modal areas in optical fibers. Opt Lett 31:1797
18. Nicholson JW, Fini JM, Liu X, DeSantolo AM, Westbrook PS, Windeler RS, Monberg E, DiMarcello F, Headley C, DiGiovanni DJ (2013) Single-frequency pulse amplification in a higher-order mode fiber amplifier with fundamental-mode output. CLEO, CW3M.3
19. Geng JH, Wang Q, Jiang Z, Luo T, Jiang SB, Czarnecki G (2011) Kilowatt-peak-power, single-frequency, pulsed fiber laser near 2 μm. Opt Lett 36:2293
20. Fang Q, Shi W, Kieu K, Petersen E, Chavez-Pirson A, Peyghambarian N (2012) High power and high energy monolithic single-frequency 2 μm nanosecond pulsed fiber laser by using large core Tm-doped germanate fibers: experiment and modeling. Opt Express 20:16410
21. Wang X, Jin X, Zhou P, Wang XL, Xiao H, Liu ZJ (2015) 105 W ultra-narrowband nanosecond pulsed laser at 2 μm based on monolithic Tm-doped fiber MOPA. Opt Express 23:4233

Chapter 9
Representative Applications of Single-Frequency Fiber Lasers

Along with the continuous development of single-frequency fiber laser technologies, numerous research works concerning the actual application of single-frequency laser sources have been carrying out. In this chapter, we will briefly introduce the current developing status of representative applications of single-frequency fiber laser in the following three aspects: next-generation optical communication, high precision optical sensing, and laser coherent beam combining.

9.1 Next-Generation Optical Communication

Laser sources are ideal carriers of information in optical communication systems, thanks to its high coherence, flexibility and stability, and potential to realize high capacity information transmission in long haul optical fiber system [1]. Over the past two decades, the development of erbium-doped fiber amplifier and wavelength division multiplexer has facilitated the prominent growth in high capacity optical communication. At present, many research interests have been attracted to exploiting the single-frequency laser light to enhance the spectral efficiency of fiber-optic communication [2–4]. Through exploring advanced modulation format for the emitting laser and corresponding detection technology, significant high transmission capacity could be realized within a narrow optical bandwidth, and in this way, the system is more tolerant to chromatic dispersion and polarization-mode dispersion, which are the main obstacles in traditional optical communication system [5]. Especially, with the development of coherent detection technology and related digital signal processing (DSP) technology, coherent optical communication has been recognized as the next-generation optical communication due to its merit of high sensitivity and capability of realizing high message capacity [6, 7].

In coherent optical communication system, decoding information from carriers is conducted by mixing the signal with a local oscillator to acquire the message encoded in the amplitude, frequency, phase, or polarization of laser light [5]. Reliable

© Springer Nature Singapore Pte Ltd. 2019

Z. Yang et al., *Single-Frequency Fiber Lasers*, Optical and Fiber Communications Reports 8, https://doi.org/10.1007/978-981-13-6080-0_9

information decoding requires the phase as well as the polarization of the local laser to be locked to the transmitting laser. Therefore, both the employed lasers should be featured with low noise and high stability; otherwise the system would be on penalty of high bit error ratio (BER) [8, 9]. Owing to the advantages of convenient current modulation and commercial available, single-frequency semiconductor lasers are widely applied in coherent communication, despite its inherent high phase noise [10, 11]. However, higher-speed network communication requires higher-order modulation format and lower noise and narrower linewidth of the carrier laser [12]. In recent years, numerous works have been dedicated to suppression of the phase noise and linewidth of semiconductor lasers, and desired low noise output with kHz has been achieved [13, 14]. Nevertheless, for low noise semiconductor laser, the scheme of current modulation would deteriorate its intensity noise and thus affect the quality of communication [15]. Other schemes are based on quadrature amplitude modulation (QAM) and orthogonal frequency-division multiplexing (OFDM), which modulate the laser signal outside the cavity [6, 16]. In this way, single-frequency fiber lasers are more competitive and promising than its semiconductor counterparts, in view of its intrinsic low noise and narrow linewidth. In 2013, T. Omiya et al. [17] demonstrated a 400 Gbit/s 256 QAM-OFDM transmission over 720 km by using single-frequency fiber laser and achieved a record spectral efficiency of 14 bit/s/Hz. Subsequently, this record was updated with spectral efficiency of 15.3 bit/s/Hz by the same group, which carried out a 2048 QAM single-carrier coherent optical transmission over 150 km based on single-frequency fiber laser [18].

9.2 High Precision Optical Sensing

Single-frequency fiber lasers are versatile tools that facilitate measuring of various physical parameters such as strain, temperature, pressure, and acoustic/ultrasonic signal based on coherent optical sensing, given that appropriate transducer design as well as demodulation scheme are implemented. In addition to the merits of high precision and high-resolution measurement, the long-range interrogation ability and the exemption of electronic part in the sensing region render the optical fiber sensing system immune to electromagnetic interference (EMI) and advantageous for operating in the harsh environments [19, 20]. Moreover, the fiber laser sensor possesses a favorable multiplexing capability which enables monitoring of multiparameters or multi-positions in the form of sensor array or networks [21–23]. In general, the sensor element can be unbalanced Michelson/Mach-Zehnder interferometer [24, 25], FBG [26, 27], FBG-based Fabry-Perot cavity [28], or the fiber laser itself [29, 30]. Under these circumstances, the intended measurand would induce phase or frequency change proportionally in the sensor element, while these changes can be demodulated out by employing phase-generated carrier (PGC) technique on the unbalanced interferometer [31, 32] or locking the laser frequency with the Pound-Drever-Hall (PDH) technique to the sensor element or other frequency reference in

case of the sensor element is the laser itself [27, 33]. Besides, linearly modulating the laser frequency with external PZT actuator can be utilized in coherent optical frequency domain reflectometry (OFDR), which facilitates fault locating in optical fiber with self-heterodyne detection [34–36]. Actually, frequency-modulated laser sources can also be utilized in PGC technique-based interferometric sensing [37]. In recent years, with the development of stable short-cavity single-frequency fiber lasers, polarimetric heterodyning sensors with this type of laser to be the interrogating element have been attracting intense interests [38, 39]. The strategy is to convert the measurand into the change of the beat frequency between the two orthogonal polarization modes in the laser, via modulating the fiber birefringence. At present, polarimetric heterodyning fiber laser sensors have been demonstrated in measuring of current [40], bending [41], strain [42], temperature [43], acceleration [39], hydrostatic pressure [44], magnetic field [45], and acoustic signal [46].

9.3 Laser Coherent Beam Combining

As mentioned in Chap. 6, scaling the power of single-frequency laser via fiber amplifier would be limited to several hundreds of watts owing to the undesirable nonlinear and thermal effects, while higher power is obtainable by coherently combining the outputs from multiple fiber amplifiers. Actually, as an effective scheme to realize high-power laser, coherent beam combining also calls for single-frequency laser sources [47–49]. In brief, by tiling multiple MOPA lasers that have the same spectrum into an array and loop controlling the phase of each array element to the same pace, the beamlets would interfere constructively at the far-field and realize laser power that increases proportionally with the scale of the array [50]. Currently, coherent beam combining has been successfully applied to boost the power of both CW and pulsed single-frequency fiber laser at 1.0, 1.5, and 2.0 μm band, and laser power in the kW level was realized [51–55].

References

1. Psaltis D, Al E, Psaltis D (2009) Coherent optical information systems. Science 298:1359
2. Tokle T, Davidson CR, Nissov M, Cai JX, Foursa D, Pilipetskii A (2004) 6500 km transmission of RZ-DQPSK WDM signals. Electron Lett 40:444
3. Hmood JK, Harun SW, Emami SD, Khodaei A, Noordin KA, Ahmad H, Shalaby HM (2015) Performance analysis of an all-optical OFDM system in presence of non-linear phase noise. Opt Express 23:3886
4. Lin C, Djordjevic IB, Zou D (2015) Achievable information rates calculation for optical OFDM few-mode fiber long-haul transmission systems. Opt Express 23:16846
5. Li G (2009) Recent advances in coherent optical communication. Adv Opt Photon 1:279
6. Shieh W, Yi X, Ma Y, Yang Q (2008) Coherent optical OFDM: has its time come [Invited]. J Opt Netw 7:234

7. Ly-Gagnon DS, Tsukamoto S, Katoh K, Kikuchi K (2006) Coherent detection of optical quadrature phase-shift keying signals with carrier phase estimation. J Lightwave Technol 24:12
8. Li J, Li L, Tao Z, Hoshida T, Rasmussen JC (2011) Laser-linewidth-tolerant feed-forward carrier phase estimator with reduced complexity for QAM. J Lightwave Technol 29:2358
9. Cheng J, Tang M, Fu S, Shum PP, Liu D, Xiang M, Feng Z, Yu D (2014) Relative phase noise estimation and mitigation in Raman amplified coherent optical communication system. Opt Express 22:1257
10. Olsson N, Van Der Ziel J (1987) Performance characteristics of 1.5-μm external cavity semiconductor lasers for coherent optical communication. J Lightwave Technol 5:510
11. Wong Y, Hsu C, Yang CC (1999) Characteristics of a dual-wavelength semiconductor laser near 1550 nm. IEEE Photon Technol Lett 11:173
12. Chandrasekhar S, Liu X (2011) Enabling components for future high-speed coherent communication systems. In: Optical fiber communication conference, p U5
13. Zhang D, Zhao J, Yang Q, Liu W, Fu Y, Li C, Luo M, Hu S, Hu Q, Wang L (2012) Compact MEMS external cavity tunable laser with ultra-narrow linewidth for coherent detection. Opt Express 20:19670
14. Bennetts S, McDonald GD, Hardman KS, Debs JE, Kuhn CC, Close JD, Robins NP (2014) External cavity diode lasers with 5 kHz linewidth and 200nm tuning range at 1.55 μm and methods for linewidth measurement. Opt Express 22:10642
15. Saliba SD, Scholten RE (2009) Linewidths below 100 kHz with external cavity diode lasers. Appl Opt 48:6961
16. Schmogrow R, Hillerkuss D, Wolf S, uerle BB, Winter M, Kleinow P, Nebendahl B, Dippon T, Schindler PC, Koos C (2012) 512 QAM Nyquist sinc-pulse transmission at 54 Gbit/s in an optical bandwidth of 3 GHz. Opt Express 20:6439
17. Omiya T, Yoshida M, Nakazawa M (2013) 400 Gbit/s 256 QAM-OFDM transmission over 720 km with a 14 bit/s/Hz spectral efficiency by using high-resolution FDE. Opt Express 21:2632
18. Beppu S, Kasai K, Yoshida M, Nakazawa M (2015) 2048 QAM (66 Gbit/s) single-carrier coherent optical transmission over 150 km with a potential SE of 15.3 bit/s/Hz. Opt Express 23:4960
19. Culshaw B, Kersey A (2008) Fiber-optic sensing: a historical perspective. J Lightwave Technol 26:1064
20. Liu Y, Zhang W, Xu T, He J, Zhang F, Li F (2011) Fiber laser sensing system and its applications. Photon Sensors 1:43
21. Zhu J, Yang K, Yin H, Wang H, Yu B (2013) Proposal for eliminating the external disturbance via digital PGC technique in a multiplexed fiber interferometer measurement system. Opt Commun 295:53
22. Wang P, Chang J, Zhu C, Sun B, Lv G, Zhang S, Zhao Y, Sun Z, Zhang X, Peng G (2014) A four-element sensor array consisting of asymmetric distributed-feedback fiber lasers. Photon Sensors 4:180
23. Yu K, Wu C, Mao Y, Wang Z, Lu C, Tam H, Zhao Y (2014) Distributed Bragg reflector fibre laser-based sensor array for multi-parameter detection. Electron Lett 50:1301
24. Lam TT, Chow JH, Mow-Lowry CM, McClelland DE, Littler I (2009) A stabilized fiber laser for high-resolution low-frequency strain sensing. IEEE Sensors J 9:983
25. Hu X, Chen W, Fan L, Meng Z, Chen M (2014) An optical modulation method to suppress stimulated Brillouin scattering and the phase noise in a remote interferometric fiber sensing system. Opt Fiber Technol 20:547
26. Wen H, Skolianos G, Fan S, Bernier M, Vallée R, Digonnet MJ (2013) Slow-light fiber-Bragg-grating strain sensor with a 280-femtostrain/$\sqrt{\text{Hz}}$ resolution. J Lightwave Technol 31:1804
27. Guo J, Yang C (2015) Highly stabilized phase-shifted fiber bragg grating sensing system for ultrasonic detection. IEEE Photon Technol Lett 27:848
28. Liu Q, Tokunaga T, He Z (2012) Sub-nano resolution fiber-optic static strain sensor using a sideband interrogation technique. Opt Lett 37:434

29. Zhang F, Zhang W, Li F, Liu Y (2011) DFB fiber laser hydrophone with band-pass response. Opt Lett 36:4320
30. Lv C, Guo X, Gao J, Liu Y, Li B, Wu C, Ge C (2015) Design evaluation of DBR fiber laser sensor for directional lateral force monitoring. IEEE Photon Technol Lett 27:1515
31. Liu Y, Wang L, Tian C, Zhang M, Liao Y (2008) Analysis and optimization of the PGC method in all digital demodulation systems. J Lightwave Technol 26:3225
32. Fang G, Xu T, Li F (2013) 16-channel fiber laser sensing system based on phase generated carrier algorithm. IEEE Photon Technol Lett 25:2185
33. Lam TT, Chow JH, Shaddock DA, Littler I, Gagliardi G, Gray MB, McClelland DE (2010) High-resolution absolute frequency referenced fiber optic sensor for quasi-static strain sensing. Appl Opt 49:4029
34. Geng J, Spiegelberg C, Jiang S (2005) Narrow linewidth fiber laser for 100-km optical frequency domain reflectometry. IEEE Photon Technol Lett 17:1827
35. Li C, Xu S, Mo S, Zhan B, Zhang W, Yang C, Feng Z, Yang Z (2013) A linearly frequency modulated narrow linewidth single-frequency fiber laser. Laser Phys Lett 10:75106
36. Chen M, Meng Z, Tu X, Zhang Y (2014) Fast-tuning, low-noise, compact Brillouin/erbium fiber laser. Opt Lett 39:689
37. Meng Z, Hu Y, Xiong S, Stewart G, Whitenett G, Culshaw B (2005) Phase noise characteristics of a diode-pumped Nd: YAG laser in an unbalanced fiber-optic interferometer. Appl Opt 44:3425
38. Zhang Y, Guan B, Tam H (2009) Ultra-short distributed Bragg reflector fiber laser for sensing applications. Opt Express 17:10050
39. Guan B, Jin L, Zhang Y, Tam H (2012) Polarimetric heterodyning fiber grating laser sensors. J Lightwave Technol 30:1097
40. Guan B, Wang S (2010) Fiber grating laser current sensor based on magnetic force. IEEE Photon Technol Lett 22:230
41. Liu W, Guo T, Wong AC, Tam H, He S (2010) Highly sensitive bending sensor based on Er^{3+}-doped DBR fiber laser. Opt Express 18:17834
42. Wo J, Jiang M, Malnou M, Sun Q, Zhang J, Shum PP, Liu D (2012) Twist sensor based on axial strain insensitive distributed Bragg reflector fiber laser. Opt Express 20:2844
43. Jin L, Tan Y, Quan Z, Li M, Guan B (2012) Strain-insensitive temperature sensing with a dual polarization fiber grating laser. Opt Express 20:6021
44. Jin L, Quan Z, Cheng L, Guan B (2013) Hydrostatic pressure measurement with heterodyning fiber grating lasers: mechanism and sensitivity enhancement. J Lightwave Technol 31:1488
45. Cheng L, Han J, Guo Z, Jin L, Guan B (2013) Faraday-rotation-based miniature magnetic field sensor using polarimetric heterodyning fiber grating laser. Opt Lett 38:688
46. Lyu C, Wu C, Tam H, Lu C, Ma J (2013) Polarimetric heterodyning fiber laser sensor for directional acoustic signal measurement. Opt Express 21:18273
47. Qi Y, Liu C, Zhou J, Lou Q, Chen W, Dong J, Wei Y (2009) Single-frequency linearly polarized master-oscillator fiber power amplifier system and its application in high fill factor coherent beam combining. Appl Opt 48:5514
48. Ma Y, Zhou P, Wang X, Ma H, Xu X, Si L, Liu Z, Zhao Y (2010) Coherent beam combination with single-frequency dithering technique. Opt Lett 35:1308
49. Ma P, Zhou P, Wang X, Ma Y, Su R, Liu Z (2013) Influence of perturbative phase noise on active coherent polarization beam combining system. Opt Express 21:29666
50. Liu Z, Zhou P, Wang X, Ma Y, Xu X (2013) Kilowatt coherent beam combining of high-power Fiber amplifiers using single-frequency dithering techniques. In: Brignon A (ed) Coherent laser beam combining. Wiley-VCH, Weinheim, p 75
51. Ma Y, Wang X, Leng J, Xiao H, Dong X, Zhu J, Du W, Zhou P, Xu X, Si L (2011) Coherent beam combination of 1.08 kW fiber amplifier array using single-frequency dithering technique. Opt Lett 36:951
52. Su R, Zhou P, Wang X, Ma Y, Xu X (2012) Active coherent beam combination of two high-power single-frequency nanosecond fiber amplifiers. Opt Lett 37:497

53. Su R, Zhou P, Wang X, Ma P, Xu X (2013) Actively coherent beam combining of two single-frequency 1083 nm nanosecond Fiber amplifiers in low-repetition-rate. IEEE Photon Technol Lett 25:1485
54. Lombard L, Azarian A, Cadoret K, Bourdon P, Goular D, Canat G, Jolivet V, Jaouën Y, Vasseur O (2011) Coherent beam combination of narrow-linewidth 1.5 μm fiber amplifiers in a long-pulse regime. Opt Lett 36:523
55. Wang X, Zhou P, Wang X, Ma Y, Su R, Xiao H, Si L, Liu Z (2014) 108 W coherent beam combining of two single-frequency Tm-doped fiber MOPAs. Laser Phys Lett 11:105101

Chapter 10
Conclusion and Outlook

Fiber lasers that emit monochromatic light have been intensively investigated owing to its high purity in optical spectrum and the resulting significant width of the scope of applications that are currently accessing and could access this type of laser source. The main properties that render the single-frequency fiber laser popular are its inherent low noise and narrow linewidth, as well as the all-fiber format that makes the system flexible and reliable. Based on a generally fiber laser, single-frequency lasing can be realized given that the employed filtering element is narrow enough, while the optical gain mechanism can be fundamental transition in rare earth ions or fiber nonlinear effects or an association of both. The narrowband filtering mechanism can be various on the basis of optical fibers, leading to various kind of laser cavity configurations. The laser cavity can be also manipulated to achieve desired performances such as linear polarization operation, lower noise, narrower linewidth, wider tunability, frequency modulation, Q-switched pulsing output, etc. In addition, the invention of highly rare earth ion-doped multicomponent soft glass fiber enables the realization of high-power operation in a compact short-cavity laser cavity, while maintaining or even improving other performing indexes of the single-frequency laser. Finally, higher laser power can be obtained by implementing the well-developed master oscillator fiber amplifier and subsequent laser coherent beam combining.

In the future, research on single-frequency fiber lasers will continue, mainly motivated by further improving the existing application performances and finding new applications. One of the topics will be extending the operating wavelength to the mid-infrared band and the visible band, with the development of novel rare earth ion-doped fibers, nonlinearity fibers, and related passive fiber components. Besides, continuously improving the individual or combined properties of the laser such as output power, stability, noise, linewidth, polarization, etc. would be also the main topic in studying of single-frequency fiber lasers to meet the application requirements. Additionally, fiber lasers in micro-/nanodimensions enabled by high-gain

© Springer Nature Singapore Pte Ltd. 2019

Z. Yang et al., *Single-Frequency Fiber Lasers*, Optical and Fiber Communications Reports 8, https://doi.org/10.1007/978-981-13-6080-0_10

active/passive fibers are another promising research topic that aims application in highly integrated situations such as on-chip laser source. Finally, with the ongoing development of relevant science and technology, new mechanisms for single-frequency operation in optical fiber are likely to emerge.